

# University of Southampton Research Repository ePrints Soton

Copyright © and Moral Rights for this thesis are retained by the author and/or other copyright owners. A copy can be downloaded for personal non-commercial research or study, without prior permission or charge. This thesis cannot be reproduced or quoted extensively from without first obtaining permission in writing from the copyright holder/s. The content must not be changed in any way or sold commercially in any format or medium without the formal permission of the copyright holders.

When referring to this work, full bibliographic details including the author, title, awarding institution and date of the thesis must be given e.g.

AUTHOR (year of submission) "Full thesis title", University of Southampton, name of the University School or Department, PhD Thesis, pagination

## UNIVERSITY OF SOUTHAMPTON

# 

## On the effect of surface morphology on wall turbulence

by

## Marco Placidi



Thesis for the degree of Doctor of Philosophy

June 2015

#### UNIVERSITY OF SOUTHAMPTON

#### ABSTRACT

# FACULTY OF ENGINEERING AND THE ENVIRONMENT Aerodynamics and Flight Mechanics

#### Doctor of Philosophy

# ON THE EFFECT OF SURFACE MORPHOLOGY ON WALL TURBULENCE by Marco Placidi

This thesis presents an extensive experimental data set that systematically examines the impact of surface morphology on wall-flows and could serve as benchmark data for validation of numerical simulations and other drag-prediction models. Experiments were conducted in the fully-rough regime on surfaces with large relative roughness height  $(h/\delta \approx$ 0.1). The surfaces were generated by distributed LEGO™ bricks of uniform height, arranged in different configurations. Measurements were made with both floating-element drag-balance and high-resolution 2D and 3D particle image velocimetry on six configurations with different frontal solidity,  $\lambda_F$ , at fixed plan solidity,  $\lambda_P$ , and vice versa, for a total of twelve rough-wall cases. Results show, for the first time, the individual effect of frontal and plan solidities on various quantities in a controlled experiment. The bulk drag behaviour is shown to be different for variation of the solidities. This reaches a peak value for  $\lambda_F = 0.21$ , while it monotonically decreases with increasing  $\lambda_P$  in contrast to previous results obtained by examining the flow over cube roughness, where the effects of the solidities are coupled. The upper boundary of Townsend's similarity hypothesis is also investigated. While mean velocity profiles are found to conform to outer-layer similarity, the higher-order quantities show a lack of collapse for almost all cases considered. This suggests that Townsend's hypothesis, for these rough surfaces with a high relative roughness height  $(h/\delta \approx 0.1)$  does not hold - this conflicts with previous results obtained on simplified cube roughness. The use of proper orthogonal decomposition to infer spatial similarity of flows over different wall morphologies is also demonstrated, where some universal characteristics of the turbulence across rough-walls are identified. Hairpin vortex packets' inclination is confirmed to be insensitive to a change in the frontal and plan solidities and so are two-point velocity correlations in both streamwise and wall-normal directions. Moreover, POD modes are indistinguishable in both shape and size across the different roughness morphologies. These findings strongly suggest that although the spatial structure of the turbulence is universal, irrespective of the surface morphology, its strength is modulated by the wall's conditions.

# Contents

Li	st of	Figures	ix
Li	st of	Tables	⁄ii
D	eclar	ation of Authorship x	ix
$\mathbf{A}$	ckno	wledgements	хi
N	omer	nclature xx	iii
1	Intr	roduction	1
	1.1	Introduction	1
	1.2	Motivation	2
	1.3	Research objectives and approach	4
	1.4	Thesis outline	5
	1.5	Novel contributions and publications	5
2	Exp	perimental details and methodology	7
	2.1	Experimental facility	7
	2.2	Roughness morphology characterisation	8
	2.3	Current roughness morphology	11
	2.4	Particle image velocimetry	11
		2.4.1 2D planar PIV	13
		2.4.2 3D stereoscopic PIV	14
		2.4.2.1 3D PIV vector validation	15
		2.4.3 PIV data resolution	16
	2.5	Floating-element drag-balance	17
		2.5.1 The calibration unit	19
		2.5.1.1 Load cell calibration	20
		2.5.1.2 Mechanical system calibration	20
	2.6	Uncertainty estimation	21
		2.6.1 PIV bias estimation	21
		2.6.2 PIV statistical uncertainty	22
		2.6.3 Floating-element drag-balance uncertainty	22
	2.7	Smooth-wall turbulent boundary layer	23
3	Effe	ect of surface morphology on aerodynamic parameters and the rough-	
			25

vi

	3.1	Introd	luction and background	. 25
	3.2		ct estimate of skin-friction	
	3.3	Deter	mination of aerodynamic parameters	. 30
	3.4	Prope	er orthogonal decomposition	. 30
	3.5	Result	ts and discussion	. 31
		3.5.1	Effect of surface morphology on aerodynamic parameters	. 31
		3.5.2	Effect of surface morphology on the depth of the RSL	. 39
		3.5.3	Street and building profiles	. 41
		3.5.4	Effect of surface morphology on the structure of the RSL	. 43
		3.5.5	Effect of surface morphology on energy distribution across scales	. 45
	3.6	Concl	usions	. 47
4	Effe		surface morphology on the turbulence statistics	49
	4.1		luction and background	
	4.2	-	alent sand roughness	
	4.3	Result	ts and discussion	
		4.3.1	Assessing the flow homogeneity	
		4.3.2	Fully developed boundary layer	
		4.3.3	Outer-layer similarity	
		4.3.4	Quadrant analysis	
		4.3.5	POD modes shape and energy content	
		4.3.6	POD of isolated velocity fluctuations	
		4.3.7	Reduced model	
		4.3.8	Influence of roughness' pattern	
		4.3.9	Influence of roughness' geometry	
	4.4	Concl	usions	. 76
5			surface morphology on the arrangement of the turbulence	79
	5.1		luction and background	
	5.2	•	point correlation	
	5.3		ng strength criteria	
	5.4		ts and discussion	
		5.4.1	Velocity correlations	
		5.4.2	Velocity correlation length scales	
		5.4.3	Population trends of vortices	
		5.4.4	Swirling strength correlations	
	5.5	Concl	usions	. 107
6			iscussion and conclusions	109
	6.1		nary of the major findings	
		6.1.1	The bulk quantities	
		6.1.2	The roughness sublayer	
		6.1.3	The validity of Townsend's similarity hypothesis	
		6.1.4	The roughness characterisation	
		6.1.5	The spatial arrangement of the turbulence	
	6.0	6.1.6	The energy distribution across scales	
	6.2	Limita	ations and shortcomings	. 112

Contents

	6.3	Recommendations for future work
$\mathbf{A}$	Smo	ooth-wall
	A.1	Introduction
	A.2	Experimental facility and details
	A.3	Results and discussion
		A.3.1 Velocity correlations
		A.3.2 Velocity correlation length scales
		A.3.3 Swirling strength analysis
		A.3.4 Population trends of vortices
		A.3.5 POD modes shape
		A.3.6 POD modes energy content
	A.4	Conclusions
В	Ster	reoscopic data validation 123
	B.1	Everson and Sirovich's method
Re	efere	nces 125

# List of Figures

1.1	Contour plot of Macdonald's prediction of the roughness length behaviour as a function of $\lambda_F$ and $\lambda_P$ calculated using the expressions presented in Macdonald (1998) with $C_d = 1.2$ , $\kappa = 0.41$ , $\beta = 1$ and $A = 4.43$ (refer to § 3.1 for further details). Colorbar shows $y_0/h$ . Dashed line represents $\lambda_F \equiv \lambda_P$ (cubes), dot-dashed line represents variation of $\lambda_P$ at fixed $\lambda_F$ and dotted line stands for variation of $\lambda_F$ at fixed $\lambda_P$ . Filled symbols indicate the current experiment while empty symbols indicate respectively $\circ$ Kanda et al. (2004), $\diamond$ Hagishima et al. (2009) and $\square$ Leonardi and Castro (2010)	4
2.1	Wind tunnel schematic	8
2.2	Definition of frontal and plan solidities. Black lines identify a single repeated unit, grey lines show how adjacent units are linked together to	
	build the wall morphology. Inspired by Grimmond and Oke (1999)	9
2.3	Equivalent Sand Roughness, $h_s$ , for various surfaces versus the solidity,	
	$\lambda_F$ , corrected with empirical drag coefficient. Open symbols, rounded	
	elements (spheres, cones, $C_d = 0.3$ ; spherical segments, $C_d = 0.13$ ) from	
	Schlichting (1979). For all others, $C_d = 1.25$ . Filled triangle up, span-	
	wise fences (Schlichting, 1979); triangle down, spanwise fences (Webb	
	et al., 1971); +, spanwise cylinders (Tani, 1988); x, spanwise square bars	
	(Bandyopadhyay, 1987). The dashed lines have logarithmic slopes +1 and -2. Modified from Jimenez (2004)	1(
2.4	A conceptual representation of the relationship of the aerodynamic rough-	1(
	ness length and the displacement height to the plan and frontal area	
	density ratios. Modified from Grimmond and Oke (1999). ©American	
	Meteorological Society. Used with permission	10
2.5	(a) LEGO <sup>TM</sup> brick geometry, (b) $(x, z)$ plane view of the roughness ele-	
	ments' patterns with varying $\lambda_F$ at $\lambda_P = const = 0.27$ (left) and rough-	
	ness elements' patterns with varying $\lambda_P$ at $\lambda_F = const = 0.15$ (right).	
	Dashed and dash-dotted lines in (b) indicate the position of the laser sheet	
	during the measurements with the respect of each repeated unit for the	
	2D and 3D setup respectively. Dimensions are not in scale for ease of readability. Flow is top to bottom	12
2.6	Schematic view of the 2D planar PIV setup. Dimensions are not in scale	12
2.0	for ease of readability.	14
2.7	Schematic view of the 3D stereoscopic PIV setup. Dimensions are not in	
	scale for ease of readability.	16

List of Figures

2.8	Schematic of the floating-element drag-balance. Components: (1) measurement patch, (2) two-arm lever system, (3) knife edge, (4) precision scale, (5) counterbalance weights, (6) load-transfer adjustment pin, (7) H-frame containing the scale, (8) base structure, (9) fine-adjustment feet, (10) rough-adjustment feet, (11) Pitot tube, (12) sealed box Calibration curves for (a) the load cell and (b) the mechanical arm (the	19
2.10	10 $g$ preload has been subtracted for clarity)	21 23
3.1	Schematic representation of the effect of surface morphology on the law of the wall. $\Delta U^+$ is the roughness function, $\kappa$ is the von Kármán constant and $d$ is the zero-plane displacement. Inspired by Varano (2010)	26
3.2	(a) Contour plot of the Macdonald's (1998) prediction of the roughness length behaviour as a function of $\lambda_F$ and $\lambda_P$ calculated using the expressions presented in Macdonald (1998) with $C_d=1.2$ , $\kappa=0.41$ , $\beta=1$ and $A=4.43$ . Colorbar shows $y_0/h$ . Dashed line represents $\lambda_F\equiv\lambda_P$ (cubes), dot-dashed line represents variation of $\lambda_P$ at fixed $\lambda_F$ and dotted line stands for variation of $\lambda_F$ at fixed $\lambda_P$ . Filled symbols indicate the current experiment while empty symbols indicate respectively $\circ$ Kanda et al. (2004), $\diamondsuit$ Hagishima et al. (2009) and $\square$ Leonardi and Castro (2010). A	
3.3	cut along the dashed line in figure $(a)$ is presented in $(b)$	28
3.4	Skin friction coefficient, $C_f$ , as a function of the Reynolds number, for (a) $\lambda_F$ ( $\lambda_P = const = 0.27$ ) and (b) $\lambda_P$ ( $\lambda_F = const = 0.15$ )	33
3.5	Variation of $C_f$ as a function of $\theta/y_0$ for (a) indirect method and (b) direct measurement. Dot and dashed-dotted curves refer to the standard two-parameter family results with wake strength of $\Pi=0.55$ and 0.7. Current experiment (CE) refers to values obtained by floating-element drag-balance (solid marks) and via the means of equation 3.3 (empty marks). The roughness length, $y_0$ , is calculated via a least-square-fit procedure for $1.5h < y < 0.2\delta$	33
3.6	Skin friction measurements, for sparse (top), medium-packed (centre) and dense regimes (bottom) as a function of $\lambda_F$ ( $\lambda_P = const = 0.27$ ) on the left and $\lambda_P$ ( $\lambda_F = const = 0.15$ ) on the right. Drag-balance results are compared with 2D and 3D indirect skin friction estimation (i.e. equation 3.3). A 10% error bar on the drag-balance data is included. Every five vectors is used for clarity	34
3.7	Mean velocity profiles in inner scales as a function of (a) $\lambda_F$ ( $\lambda_P = const = 0.27$ ) and (b) $\lambda_P$ ( $\lambda_F = const = 0.15$ ). Markers are spaced every five vectors for clarity	35
3.8	Normalised roughness length, $y_0/h$ , as a function of (a) $\lambda_F$ and (b) $\lambda_P$ . Current experiment refers to values obtained by log-law least-square fit within $1.5h < y < 0.2\delta$	36
3.9	Normalised zero-plane displacement, $d/h$ , as a function of $(a)$ $\lambda_F$ and $(b)$ $\lambda_P$ . Current experiment refers to values obtained by log-law least-square	
	fit within $1.5h < y < 0.2\delta$	38

List of Figures xi

3.10	Different elements' field patterns and associated flow regimes for increasing $\lambda_P$ . LF1 (left), LF3 (centre) and LF5 (right). Symbols $\odot$ stand for	
	arrows pointing towards the reader and symbolise path lines of particles that deviate upward, symbols $\otimes$ stand for path lines of particles that	
9 1 1	deviate downward. Flow is left to right	38
3.11	ing $\lambda_P$ . LP1 (left), LP3 (centre) and LP6 (right). Symbols $\odot$ stand for arrows pointing towards the reader and symbolise path lines of particles that deviate upward, symbols $\otimes$ stand for path lines of particles that deviate downward. Flow is left to right. Light and dark grey areas in $(a)$ ,	
3.12	(b) and (c) indicate subsequent elements' repetitive units	39
	medium-packed (centre) and dense regimes (bottom) as a function of $\lambda_F$ ( $\lambda_P = const = 0.27$ ) on the left and $\lambda_P$ ( $\lambda_F = const = 0.15$ ) on the right. Lowest contour level $U/U_e = 0.5$ , contour spacing of 0.05. Bricks in the measurement plane are represented in full black, whilst bricks out of the measurement plane (in the same repeated unit) are identified by	
	dashed lines. The mean flow is into the page. Dark and light grey areas are discussed in $\S$ 3.5.3	40
3.13	Normalised Reynolds shear stress profiles, $-\overline{u'v'}/U_e^2$ , for sparse (top), medium-packed (centre) and dense regimes (bottom) as a function of $\lambda_F$	
	$(\lambda_P = const = 0.27)$ on the left and $\lambda_P$ ( $\lambda_F = const = 0.15$ ) on the right. Grey solid symbols represent the shear stress data (only one in every five vectors is shown for clarity), dashed black line shows $y = h$ (canopy layer)	
	whilst dotted and solid black lines represent the extent of the RSL and	
9 1 4	ISL respectively.	42
3.14	Building and street streamwise mean velocity profiles, for sparse (top), medium-packed (centre) and dense regimes (bottom) as a function of $\lambda_F$ ( $\lambda_P = const = 0.27$ ) on the left and $\lambda_P$ ( $\lambda_F = const = 0.15$ ) on the right.	
0.15	Grey lines indicate different spanwise locations	44
3.15	First four low-order POD modes in the roughness sublayer for (a-d) sparse regime and (e-h) dense frontal solidity regime. Flow is left to right. POD modes are calculated on the combined $(u', v')$ field	45
3.16	First four low-order POD modes in the roughness sublayer for (a-d) sparse regime and (e-h) dense plan solidity regime. Flow is left to right. POD	
	modes are calculated on the combined $(u', v')$ field	46
4.1	(a) Comparison of mean velocity defect profiles across 2D and 3D PIV measurements. (b) Wall-normal variation of streamwise (black), wall-normal (red) turbulence intensities and Reynolds shear stress (blue). 2D	
	and 3D PIV measurements are represented by filled and empty symbols	<b>F</b> 0
4.2	respectively. Markers are spaced every five vectors for clarity Schematic diagram of the various layers over a step-change in roughness.	53
	Original from Cheng and Castro (2002a). (1) Upstream boundary layer, (3) transition region, (4) outer region of the internal boundary layer, RSL	
19	indicates the roughness sublayer of the internal boundary layer	54
4.3	Mean velocity profiles in defect form as a function of (a) $\lambda_F$ ( $\lambda_P = const = 0.27$ ) and (b) $\lambda_P$ ( $\lambda_F = const = 0.15$ ). Markers are spaced every five vectors for clarity	55
		-

xii List of Figures

4.4	PDFs of $u'$ events contributing to the Reynolds stress for $y = 1h$ (top) and $y = 3h$ (bottom) as a function of $\lambda_F$ ( $\lambda_P = const = 0.27$ ) on the left and $\lambda_P$ ( $\lambda_F = const = 0.15$ ) on the right	56
4.5	PDFs of $v'$ events contributing to the Reynolds stress for $y = 1h$ (top) and $y = 3h$ (bottom) as a function of $\lambda_F$ ( $\lambda_P = const = 0.27$ ) on the left	90
	and $\lambda_P$ ( $\lambda_F = const = 0.15$ ) on the right	57
4.6	Wall-normal variation of streamwise turbulence intensity, $\overline{u'u'}/U_{\tau}^2$ , and wall-normal turbulence intensity, $\overline{v'v'}/U_{\tau}^2$ , as a function of (a) $\lambda_F$ ( $\lambda_f = const = 0.27$ ) and (b) $\lambda_P$ ( $\lambda_f = const = 0.15$ ). Markers are spaced every	F 17
4 7	five vectors for clarity.	57
4.7	PDFs of $u'v'$ events contributing to the Reynolds stress for $y = 1h$ (top) and $y = 3h$ (bottom) as a function of $\lambda_F$ ( $\lambda_P = const = 0.27$ ) on the left and $\lambda_P$ ( $\lambda_F = const = 0.15$ ) on the right	58
4.8	Wall-normal variation of Reynolds shear stress, $-\overline{u'v'}/U_{\tau}^2$ , as a function	
	of (a) $\lambda_F$ ( $\lambda_P = const = 0.27$ ) and (b) $\lambda_P$ ( $\lambda_F = const = 0.15$ ). Markers	
	are spaced every five vectors for clarity	59
4.9	Diagnostic plot for the different rough surfaces as a function of (a) $\lambda_F$ ( $\lambda_P = const = 0.27$ ) and (b) $\lambda_P$ ( $\lambda_F = const = 0.15$ ). The thick solid line represent the fully-rough regime, as from Castro et al. (2013), while the dashed line comes from the smooth-wall limit, as reported by Alfredsson	
	et al. (2011). Markers are spaced every five vectors for clarity	60
4.10	Normalised wall-normal variation of Reynolds shear stress, $-\overline{u'v'}/K$ , as a	
	function of (a) $\lambda_F$ ( $\lambda_P = const = 0.27$ ) and (b) $\lambda_P$ ( $\lambda_F = const = 0.15$ ).	
	Markers are spaced every five vectors for clarity	62
4.11	Wall-normal variation of $Q_2$ (top) and $Q_4$ (bottom) events for $H=2.5$ as	
	a function of $\lambda_F$ ( $\lambda_P = const = 0.27$ ) on the left and $\lambda_P$ ( $\lambda_F = const = 0.27$ )	
	0.15) on the right. Markers are spaced every five vectors for clarity	63
4.12	Percentage contributions to $\overline{u'v'}$ for $H=2.5$ from $Q_2$ (top), $Q_4$ (center)	
	events and their ratio (bottom) as a function of $\lambda_F$ ( $\lambda_P = const = 0.27$ ) on the left and $\lambda_P$ ( $\lambda_F = const = 0.15$ ) on the right. Markers are spaced	
	every five vectors for clarity	64
4.13	First five low-order POD modes for increasing $\lambda_F$ ( $\lambda_P = const = 0.27$ ).	01
	Cases: LF2 (left), LF5 (centre-left), LP2 (centre-right), LP5 (right). Flow	
	is left to right. POD modes are calculated on the combined $(u', v')$ con-	
	fined to the near-wall region	67
4.14	Correlation coefficient, $R_{m_i m_i}$ as a function of (a) $\lambda_F$ ( $\lambda_P = const = 0.27$ )	
	and (b) $\lambda_P$ ( $\lambda_F = const = 0.15$ ). POD modes are calculated on the	0.0
	combined $(u', v')$ field. Grey lines indicate the trend	68
4.15	(top) FTKE, $E_i$ , and (bottom) CTKE content, $\sum_{i=1}^n E_i$ , versus mode	
	number as a function of (left) $\lambda_F$ ( $\lambda_f = const = 0.27$ ) and (right) $\lambda_P$	
	$(\lambda_f = const = 0.15)$ . POD modes are calculated on the combined $(u', v')$ field.	69
4 16	First five low-order POD modes for increasing $\lambda_F$ ( $\lambda_P = const = 0.27$ ).	0.5
1.10	Cases: LF2 (left), LF5 (centre-left), LP2 (centre-right), LP5 (right). POD	
	modes are calculated on the $(v')$ . Flow is left to right	71
4.17	Reynolds stresses contribution from LS (black) and SS (grey) velocity	
	fields. Streamwise velocity fluctuations, $u'u'/U_{\tau}^2$ , as a function of $\lambda_F$	
	$(\lambda_P = const = 0.27)$ on the left and $\lambda_P$ $(\lambda_F = const = 0.15)$ on the right.	
	Grey symbols follow the same convention as the black	73

List of Figures xiii

<ul><li>4.18</li><li>4.19</li></ul>	(Top) mean velocity profiles in $(a)$ inner scales and $(b)$ defect form at $\lambda_F = 0.15$ and $\lambda_P = 0.27$ . (Bottom) wall-normal variation of $(a)$ streamwise, $\overline{u'u'}/U_\tau^2$ , wall-normal turbulence intensities, $\overline{v'v'}/U_\tau^2$ , and $(b)$ Reynolds shear stress, $-\overline{u'v'}/U_\tau^2$ , at $\lambda_F = 0.15$ and $\lambda_P = 0.27$ . Different roughness patterns. Markers are spaced every five vectors for clarity (Top) mean velocity profiles in $(a)$ inner scales and $(b)$ defect form at $\lambda_F = 0.15$ and $\lambda_P = 0.27$ . (Bottom) wall-normal variation of $(a)$ streamwise, $\overline{u'u'}/U_\tau^2$ , wall-normal turbulence intensities, $\overline{v'v'}/U_\tau^2$ , and $(b)$ Reynolds shear stress, $-\overline{u'v'}/U_\tau^2$ . Markers are spaced every five vectors for clarity.	75 76
<b>.</b> .		10
5.1	Snapshots of (a) Instantaneous streamwise, (b) wall-normal and (c) Reynolds shear stress fluctuations. Colorbar represents the normalised intensities. Flow is left to right. Example case LF4	86
5.2	Galilean decomposition with $U_c = 0.8U\infty$ applied to figure 5.1(a). Contour of streamwise velocity fluctuations are also shown in the background. Flow is left to right. Example case LF4	87
5.3	Two-point correlation of streamwise $(a)$ , wall-normal $(b)$ and Reynolds shear stress $(c)$ fluctuations. Colorbar represents the normalised correlation coefficient, $R_{u'u'}$ , $R_{v'v'}$ and $R_{u'v'}$ . Flow is left to right. Example case LF4	88
5.4	Streamwise slices through auto-correlation points of $R_{u'u'}$ (top), $R_{v'v'}$ (centre) and $R_{u'v'}$ (bottom) as a function of $\lambda_F$ ( $\lambda_P = const = 0.27$ ) on the left and $\lambda_P$ ( $\lambda_F = const = 0.15$ ) on the right. Markers are spaced	
5.5	every five vectors for clarity	89
5.6	every five vectors for clarity	91
5.7	as a function of $\lambda_F$ ( $\lambda_P = const = 0.27$ ) on the left and $\lambda_P$ ( $\lambda_F = const = 0.15$ ) on the right. Flow is left to right. Examples cases LF2 and LP2 Example of contours of $R_{u'v'}$ (top), $R_{u'w'}$ (centre) and $R_{v'w'}$ (bottom) in the $(y, z)$ plane, as a function of $\lambda_F$ ( $\lambda_P = const = 0.27$ ) on the left and $\lambda_P$ ( $\lambda_F = const = 0.15$ ) on the right. Flow is left to right. Examples	94
5.8	cases LF2 and LP2	95
	$R_{u'v'}$ (from top to bottom) as a function of $\lambda_F$ ( $\lambda_P = const = 0.27$ ) on the left and $\lambda_P$ ( $\lambda_F = const = 0.15$ ) on the right. Flow is left to right. Markers are spaced every five vectors for clarity	96
5.9	Wall-normal slices through auto-correlation points of $R_{u'u'}$ , $R_{v'v'}$ , $R_{w'w'}$ and $R_{u'v'}$ (from top to bottom) as a function of $\lambda_F$ ( $\lambda_P = const = 0.27$ ) on the left and $\lambda_P$ ( $\lambda_F = const = 0.15$ ) on the right. Flow is left to right.	<i>5</i> 0
5.10	Markers are spaced every five vectors for clarity	97
	$R_{v'v'} = 0.5$ and $R_{u'v'} = 0.15$ contours as a function of $\lambda_F$ ( $\lambda_P = const = 0.27$ ) on the left and $\lambda_P$ ( $\lambda_F = const = 0.15$ ) on the right. Markers are spaced every five vectors for clarity	98

xiv List of Figures

5.11	Wall-normal variation of wall-normal length scales based on $R_{u'u'} = 0.5$ ,	
	$R_{v'v'} = 0.5$ and $R_{u'v'} = -0.15$ contours as a function of (a) $\lambda_F$ ( $\lambda_f = 0.27$ ) and (b) $\lambda_F$ ( $\lambda_F = 0.15$ ). Markovs are spaced every	
	$const = 0.27$ ) and (b) $\lambda_P$ ( $\lambda_f = const = 0.15$ ). Markers are spaced every	99
5 19	five vectors for clarity	98
5.12		
	for (a) frontal and (b) plan solidities. (bottom) Wall-normal variation trends of wall-normal correlation length scales for (c) frontal and (d) plan	
		101
5 12	Population vortex trend in the $(x,y)$ plane. (Top) Percentage of pro-	101
5.15	grade (black) and retrograde (grey) vortices, (bottom) strength of pro-	
	grade (black) and retrograde (grey) vortices, (bottom) strength of prograde (black) and retrograde (grey) vortices as a function of (left) $\lambda_F$	
	( $\lambda_P = const = 0.27$ ) and (right) $\lambda_P$ ( $\lambda_f = const = 0.15$ ). Grey symbols	
		102
5 14	Population vortex trends in the $(y, z)$ plane. (Top) Percentage of pro-	102
0.11	grade (black) and retrograde (grey) vortex, (bottom) strength of pro-	
	grade (black) and retrograde (grey) vortex, as a function of (left) $\lambda_F$	
	$(\lambda_f = const = 0.27)$ and (right) $\lambda_P$ ( $\lambda_f = const = 0.15$ ). Grey symbols	
		103
5.15	Conditioned population vortex trends in the (a) $(x,y)$ and (b) $(y,z)$	
	planes. Percentage of prograde (black) and retrograde (grey) vortex, as a	
	function of $\lambda_F$ ( $\lambda_f = const = 0.27$ ). Grey symbols follow the convention	
		104
5.16	Example of swirling strength correlation coefficient, $R_{\Lambda\Lambda}$ , (a) in the $(x,y)$	
	plane and (b) in the $(y, z)$ plane. Outermost contour $R_{\Lambda\Lambda} = 0.1$ , contour	
	spacing 0.1. Solid lines indicate cuts through the wall-normal location	
	while dashed lines indicate cuts through the auto-correlation along the	
	streamwise direction. Example case LF3	105
5.17	(Top) Streamwise and (bottom) wall-normal slices through auto-correlation	
	points of $R_{\Lambda\Lambda}$ contours in the $(y,z)$ plane as a function of $\lambda_F$ ( $\lambda_f =$	
	$const = 0.27$ ) on the left and $\lambda_P$ ( $\lambda_f = const = 0.15$ ) on the right.	
	Markers are spaced every five vectors for clarity	106
5.18	Example of contours of (a) $R_{\Lambda u'}$ and (b) $R_{\Lambda v'}$ in the $(x, y)$ plane centred at	
	$y/\delta = 0.4$ . Contour magnitudes $R_{\Lambda u'} = R_{\Lambda v'} = R_{\Lambda w'} = 0.01, 0.03, 0.07, 0.1;$	1.05
	contour signs black, negative; grey, positive. Examples case LF2	107
A.1	Two-point correlation of $(a)$ streamwise, $(b)$ wall-normal and $(c)$ Reynolds	
	shear stress fluctuations for smooth-wall case. Colorbar represents the	
	normalised correlation coefficient, $R_{u'u'}$ , $R_{v'v'}$ and $R_{u'v'}$ . Flow is left to	
	right	116
A.2	Streamwise (left) and wall-normal (right) variation of the length scales	
	based on $R_{u'u'} = 0.5$ , $R_{v'v'} = 0.5$ and $R_{u'v'} = 0.15$ contours (top, centre	
	and bottom respectively) for smooth-wall case	118
A.3	(a) Swirling strength correlation coefficient, $R_{\Lambda\Lambda}$ , for smooth-wall case.	
	Outermost contour $R_{\Lambda\Lambda} = 0.1$ , contour spacing 0.1. Contours of (b) $R_{\Lambda u'}$	
	and (c) $R_{\Lambda v'}$ centred at $y/\delta = 0.4$ for smooth-wall case. Contour mag-	
	nitudes $R_{\Lambda u'} = R_{\Lambda v'} = 0.01, 0.03, 0.07, 0.1$ ; contour signs black, positive;	
	grey, negative	119
A.4	Population vortex trend in the $(x,y)$ plane. (a) Percentage of prograde	
	(black) and retrograde (grey) vortex, (b) strength of prograde (black) and	
	retrograde (grey) vortices for smooth-wall case	119

List of Figures xv

A.5	First five low-order POD modes for smooth-wall case. POD modes are calculated on the combined $(u', v')$ field (left), solely upon $(u')$ field (centre) and solely upon $(v')$ field (right). Flow is left to right	121
B.1	(a) Streamwise velocity vector field from PIV with spurious vectors. (b) "Gappy" vector field where the spurious vectors are removed after applying the mask. (c) Reconstructed vector field after Everson and Sirovich's (1995) procedure is applied. Flow is left to right. Example case LF5	124

# List of Tables

2.1 2.2	2D and 3D PIV Parameters	17 22
3.1	Relevant experimental parameters for frontal and plan solidities variation. The aerodynamic parameters are calculated through a log-law fit with $\kappa=0.38$ in the range $1.5h \leq y \leq 0.2\delta$ . $Ue$ values reported herein are relative to the PIV results, however, the imposed $Ue$ for floating-element drag-balance tests were set within a 1.5% difference	35
3.2	Fractional TKE, $E_i$ and cumulative TKE $\sum_{i=1}^n E_i$ content versus mode number. $0.5\sum_{i=1}^n E_i$ refers instead to the number of modes necessary to resolve the 50% of the turbulent kinetic energy contained in the flow. POD modes are calculated on the combined $(u', v')$ field only within the RSL	47
4.1	Fractional TKE, $E_i$ and cumulative TKE $\sum_{i=1}^n E_i$ content versus mode number. $0.5\sum_{i=1}^n E_i$ refers instead to the number of modes necessary to resolve the 50% of the turbulent kinetic energy contained in the flow.	
4.2	POD modes are calculated on the combined $(u', v')$ field Fractional TKE, $E_i$ and cumulative TKE $\sum_{i=1}^n E_i$ content versus mode number. $0.5\sum_{i=1}^n E_i$ refers instead to the number of modes necessary to resolve the 50% of the turbulent kinetic energy contained in the flow. POD modes are calculated on the $(v')$ field only	69 72
5.1	$R_{u'u'}$ inclination angles, $\alpha_{R_{u'u'}}$ , as a function of the surface morphologies.	88
5.2	$R_{\Lambda u'}$ inclination angles, $\alpha_{R_{\Lambda u'}}$ , as a function of the surface morphologies	107
A.1	case	117
A.2	Fractional TKE, $E_i$ and cumulative TKE $\sum_{i=1}^{n} E_i$ content versus mode number. $0.5\sum_{i=1}^{n} E_i$ refers instead to the number of modes necessary to resolve the 50% of the turbulent kinetic energy contained in the flow	120

## Declaration of Authorship

I, Marco Placidi, declare that the thesis entitled On the effect of surface morphology on wall turbulence and the work presented in the thesis are both my own, and have been generated by me as the result of my own original research. I confirm that:

- this work was done wholly or mainly while in candidature for a research degree at this University;
- where any part of this thesis has previously been submitted for a degree or any other qualification at this University or any other institution, this has been clearly stated:
- where I have consulted the published work of others, this is always clearly attributed;
- where I have quoted from the work of others, the source is always given. With the exception of such quotations, this thesis is entirely my own work;
- I have acknowledged all main sources of help;
- where the thesis is based on work done by myself jointly with others, I have made clear exactly what was done by others and what I have contributed myself;
- parts of this work have been published as: (Placidi and Ganapathisubramani, 2013, 2015b,a)

Signed:	 	 	 	
~-6	 	 	 	
Date:	 	 	 	

## Acknowledgements

First, and foremost, I would like to express my gratitude to my supervisor Prof. Bharath Ganapathisubramani for his help and unwavering support throughout my time spent at Southampton University. I consider myself very privileged to have been able to work so closely with Bharath while, at that point, he was establishing his new research group. I am indebted to him for his time and constant source of inspiration, motivation and guidance both in and outside of the lab. He has always encouraged me to better my research and to develop my academic career beyond the Ph.D.

I am also deeply grateful to Dr. Roeland de Kat who took me under his wing in the long and difficult process of learning PIV. He dedicated a lot of his time to me in my first year, and I will not forget the many conversations over lunch or coffee. He has been an outstanding academic role model and he has deeply shaped my research. I also want to express my gratitude to both Dr. Roeland de Kat and Dr. Grégoire Fourrié for providing me with the smooth-wall data contained in appendix A.

I must also acknowledge my sponsors for their support, without which I could not have completed this research. I want to thank the Lloyds Register Foundation, for their financial support over the past three years. I also would like to acknowledge the Royal Aeronautical Society for the extra help they have given me via both the Centennial Scholarship Award and the Aerospace Speaker Travel Grant.

This work would never have come to fruition without many of the great people I met in Southampton. I have been extremely lucky to have shared this long journey with you all and I cannot express my gratitude enough.

Finally, I would like to thank my parents and brother for their love, support and patience over the last few years.

# Nomenclature

### **Greek Symbols**

 $\alpha_{R_{\Lambda u'}}$  Inclination angle of correlation coefficient of signed-swirling strength and streamwise velocity fluctuations

 $\alpha_{R_{n'n'}}$  Inclination angle of streamwise velocity fluctuations coefficient

 $\beta$  Constant in Macdonald's equation

 $\Delta t$  Time delay between image pair

 $\Delta U^+$  Roughness function

 $\Delta$  Clauser scaling parameter =  $\frac{\delta^* Ue}{U_{\tau}}$ 

 $\delta$  Boundary layer thickness

 $\delta^*$  Displacement thickness

 $\epsilon_{2D}$  2D data set overall uncertainty

 $\epsilon_{3D}$  3D data set overall uncertainty

 $\epsilon_{flip}$  Uncertainty on the load sensor rotation

 $\epsilon_{LC}$  Uncertainty on the load sensor calibration

 $\epsilon_{MA}$  Uncertainty on the mechanical arm calibration

 $\epsilon_R$  Uncertainty on the floating-element drag-balance reproducibility

 $\eta$  Kolmogorov length scale

I Identity matrix

 $\Lambda$  Diagonal eigenvalues matrix (Proper orthogonal decomposition)

 $\Lambda_{ci}$  Vorticity-signed swirling strength

 $\lambda_{ci}$  Imaginary part of the complex pair of eigenvalues of the local velocity gradient tensor  $\overline{\overline{D}}(\lambda)$ 

xxiv Momenclature

 $\lambda_{cr}$  Real part of the complex pair of eigenvalues of the local velocity gradient tensor  $\overline{\overline{D}}(\lambda)$ 

- $\lambda_F$  Frontal solidity
- $\lambda_P$  Plan solidity
- $\lambda_r$  Real eigenvalue of the local velocity gradient tensor  $\overline{\overline{D}}(\lambda)$
- $\mu$  Air dynamic viscosity
- $\nu$  Air kinematic viscosity
- $\Phi$  Proper orthogonal decomposition basis
- $\phi_i$  Proper orthogonal decomposition modes
- $\Pi$  Wake parameter
- $\rho$  Air density
- $\sigma_A$  Standard deviation of A
- $\tau_w$  Wall total stress
- $\theta$  Momentum thickness

#### Roman Symbols

- **K** Acceleration parameter =  $(\nu/U_e^2)[dU_e/dx]$
- $\kappa$  von Kármán constant
- $\overline{D}(\lambda)$  Local velocity gradient tensor
- $\overline{h}$  Mean roughness height
- U Column-wise-arranged matrix containing the velocity fields
- v Imaginary part of the complex pair of eigenvectors of the local velocity gradient tensor  $\overline{\overline{D}}(\lambda)$
- ${f v}_{cr}$  Real part of the complex pair of eigenvectors of the local velocity gradient tensor  $\overline{\overline{D}}(\lambda)$
- $\mathbf{v}_r$  Real eigenvector of the local velocity gradient tensor  $\overline{\overline{D}}(\lambda)$
- A Constant in Macdonald's equation
- $A_F$  Element frontal projected area
- $A_P$  Element plan area
- $A_T$  Element unit-wall area

Momenclature xxv

- B Smooth-wall intercept
- $C_d$  Drag coefficient
- $C_f$  Skin Friction coefficient =  $2(U_\tau/U_\infty)^2$
- d Zero-plane displacement
- $f_{\#}$  Lens f-number
- H Hyperbolic hole size (Quadrant analysis)
- h Roughness height
- $h_s$  Equivalent sand roughness
- K Total turbulent kinetic energy =  $1/2(\overline{u'^2} + \overline{v'^2})$
- $l_{2D}^{+}$  2D data set resolution
- $l_{3D}^{+}$  3D data set resolution
- $Lx_{u'u'}$  Streamwise correlation length of streamwise velocity fluctuations
- $Lx_{u'v'}$  Streamwise correlation length of Reynolds shear stress
- $Lx_{v'v'}$  Streamwise correlation length of wall-normal velocity fluctuations
- $Ly_{u'u'}$  Wall-normal correlation length of streamwise velocity fluctuations
- $Ly_{u'v'}$  Wall-normal correlation length of Reynolds shear stress
- $Ly_{v'v'}$  Wall-normal correlation length of wall-normal velocity fluctuations
- $Q_2$  Second Quadrant (ejections: u' < 0 & v' > 0)
- $Q_4$  Fourth Quadrant (sweeps: u' > 0 & v' < 0)
- $R_{\Lambda u'}$  Correlation coefficient of signed-swirling strength and streamwise velocity fluctuations
- $R_{\Lambda v'}$  Correlation coefficient of signed-swirling strength and wall-normal velocity fluctuations
- $R_{AB}$  Correlation coefficient of A and B variables
- $R_{u'u'}$  Correlation coefficient of streamwise velocity fluctuations
- $R_{u'v'}$  Correlation coefficient of Reynolds shear stress
- $R_{u'w'}$  Correlation coefficient of streamwise-spanwise velocity fluctuations
- $R_{v'v'}$  Correlation coefficient of wall-normal velocity fluctuations

xxvi Momenclature

 $R_{v'w'}$  Correlation coefficient of wall-normal-spanwise velocity fluctuations

- $Re_h$  Roughness-height Reynolds number =  $\frac{U_{\infty}h}{\nu}$
- $Re_{\tau}$  Friction velocity Reynolds number =  $\frac{U_{\tau}\delta}{\nu}$
- $S_i$  Quadrant analysis discriminant
- U Mean velocity component along the x axis
- u Instantaneous velocity component along the x axis
- u' Fluctuating velocity component along the x axis
- $u_c'$  Galilean fluctuating velocity
- $U^+$  Non-dimensional velocity along the x axis =  $U/U_{\tau}$
- $U_{\infty}$  Freestream velocity component along the x axis
- $U_c$  Convection velocity
- $U_{\tau}$  Friction velocity =  $\sqrt{\tau_w/\rho}$
- Ue Edge velocity at  $y = \delta$
- V Mean velocity component along the y axis
- v Instantaneous velocity component along the y axis
- v' Fluctuating velocity component along the y axis
- W Mean velocity component along the z axis
- W Spanwise extent of one repeated unit
- w Instantaneous velocity component along the z axis
- w' Fluctuating velocity component along the z axis
- $W_c$  Average streamwise spacing between roughness elements
- x Streamwise direction
- $X_F$  Fetch required to regain equilibrium
- y Wall-normal direction
- $y^+$  Non-dimensional distance from the wall =  $yU_\tau/\nu$
- $y_0$  Roughness length
- $y_{ref}$  Reference wall-normal height (correlations)
- z Spanwise direction
- $U_e^+$  Non-dimensional  $U_e$  velocity =  $U_e/U_\tau$

# Acronyms

**CCD** Charge-Coupled Device. 13

CTKE Cumulative Turbulent Kinetic Energy. 46

**FOV** Field Of View. 13

FTKE Fractional Turbulent Kinetic Energy. 45

HMPs High-Momentum Pathways. 43

IBL Internal Boundary Layer. 53

ISL Inertial SubLayer. 41

LMPs Low-Momentum Pathways. 43

LS Large-Scales. 73

LSMs Large-Scale Motions. 79

PDFs Probability Density Functions. 55

PIV Particle Image Velocimetry. 11

POD Proper Orthogonal Decomposition. 30

RSL Roughness SubLayer. 39

 ${f SS}$  Small-Scales. 73

TBLs Turbulent Boundary Layers. 79

**TKE** Turbulent Kinetic Energy. 45

UBL Upstream Boundary Layer. 53

VLSMs Very-Large-Scale Motions. 79

**ZPG** Zero-Pressure-Gradient. 7

# Chapter 1

# Introduction

### 1.1 Introduction

Surface roughness is found in abundance in natural environments and plays an important role in a variety of practical and engineering applications. In particular, the earliest studies on turbulent boundary layers over rough surfaces date back to the investigation of roughened-wall pipes in the mid nineteenth century (Hagen 1854; Darcy 1858). Later on, Nikuradse (1933) examined the effect of roughness on frictional losses in pipes due to both vegetation and biofouling, building the pillar on which most of the current knowledge and research output are based. Nikuradse's approach is based on high density rough-walls characterised by closely-packed sand-grain roughness. However, more often than not, the morphologies that engineers deal with are not necessarily densely populated roughness environments. The effect of biofouling, which has always interested the maritime community, is a classic example. Ships' performance is, in fact, influenced by roughness in the form of biofouling (King, 1982). This is due to barnacle growth on the hull, which is often found to be not evenly distributed but rather intermittent across the surface (Schultz and Swain, 1999; Schultz and Flack, 2005; Schultz, 2004, 2007). There is a paucity of literature available on the effects of sparse distribution of roughness (Ganapathisubramani and Schultz, 2011).

Historically, another important investigative input into rough-walls has derived from the aeronautical industry. In aeronautics, the accretion of ice on aircraft wings and its effect on boundary layer separation, which can result in stall, is an aspect of great importance (Matheis and Rothmayer, 2004). The drag and the heat transfer on an aircraft are also influenced by the surface morphology of both the wings and the fuselage. In this respect, roughened surfaces can be used to enhance heat transfer or be employed to delay boundary layer separation and transition (Reed and Saric, 1996). In the case of a large commercial airliner, up to 50% of the thrust produced by the engines is used to overcome turbulent skin friction drag (Poll, 1985; Ganapathisubramani et al., 2005).

Moreover, the effect of wear roughened turbine blades in turbo-machinery has also been thoroughly investigated, as it is known to be linked to severe performance degradation (Acharya et al., 1986; Wu and Christensen, 2010; Bons et al., 2001; Mejia-Alvarez and Christensen, 2013).

Regularly distributed discrete roughness also plays an important role in diverse energy and civil engineering applications, such as: pollutant dispersion modelling (Bottema, 1996), wind energy farming (Millward-Hopkins et al., 2012) and wind load calculations (Crago et al., 2012). In recent years, driven by innovation in architecture, city planner designs have become more complex and tend to incorporate climate and air quality control concepts (Calhoun et al., 2004; Zaki et al., 2011). Other aspects influenced by the surface morphology are changes to local climate (Arnfield, 2003) and the effect of heterogeneous surroundings on pollutant dispersion in urban areas and the consequent public health concerns (Khanduri et al., 2003; Britter and Hanna, 2003; Dabberdt et al., 2000). Lastly, and arguably most importantly, meteorologists also wish to understand and predict the effect of roughness on the atmospheric boundary layer for urban and forest meteorology, climate change and ultimately, weather prediction (Best et al., 2006).

In general terms, a rough surface generates a higher skin friction compared to a smooth-wall. However, bio-inspired observations on the skin of fast swimming sharks, which is characterised by three-dimensional rib patterns (riblets), has raised the possibility that a particular roughened surface morphology can improve performance (Goldstein et al., 1995). Indeed, examples of drag reduction due to riblets of up to 10% have been well documented (Bechert et al., 1997, 2000; Garcia-Mayoral and Jimenez, 2011).

Although a variety of applications rely upon an understanding of boundary layers over rough surfaces, the focus of this work is, in particular, on flows over high relative roughness ( $h/\delta \approx 0.1$ ). These conditions are a good representation of atmospheric boundary layers that develop over densely populated areas. Here, the urban boundary layer (i.e. the lowest portion of the Earth's atmosphere) is typically of the order of hundreds of metres (Padhra, 2010), with the highest buildings reaching about a tenth of this height. Similar scales also characterise the boundary layers that develop on medium-size ships' hulls in the presence of biofouling and barnacles growth (King, 1982; Schultz, 2007).

#### 1.2 Motivation

Despite the clear and undeniable importance of this topic, rough-walls are much less understood than their smooth-wall counterpart (Jimenez, 2004). For this reason, turbulent boundary layers on rough-walls have been the object of extensive studies. Nevertheless, to date, the effect of surface morphology remains only partially understood, and a number of fundamental questions have not yet received attention. For example, it is still unclear which and how many parameters are necessary to uniquely identify a rough-wall

and describe its properties, or to what extent the turbulence is effected by the wall morphology. A universal agreement upon the validity of Townsend's (1976) similarity hypothesis and its limits is still elusive. In this regard, Volino et al. (2007) pointed out that given the similarity hypothesis, the prospect of a more extended structural universality between rough and smooth-walls and hence between all roughness morphologies (the concern of this thesis) is promising. Nevertheless, although numerous studies have shown similarity of pointwise mean and high-order statistics, very few studies have attempted a more thorough comparison of 2D and 3D spatial structures across wall morphologies. These studies have reported conflicting evidence (Krogstad and Antonia, 1994; Volino et al., 2007, 2009, 2011; Ganapathisubramani and Schultz, 2011).

In industrial applications, the most important topic in the study of turbulent boundary layer over rough-walls is the necessity to quantify and relate the drag generated by a surface to its wall morphology, so that skin friction prediction models can be generated. Despite there being no shortage of detailed explorations upon specific types of roughness (Wu and Christensen, 2007; Castro, 2007; Amir and Castro, 2011, amongst others), when experimental evidences have been gathered and reviewed, the results have been a comparison of data sets from disparate sources, with significantly different boundary conditions and geometrically different roughness elements (Macdonald, 1998; Grimmond and Oke, 1999; Jimenez, 2004). An example of a morphometric drag-prediction method, Macdonald (1998), is given in figure 1.1 (see further details in § 3.1). Here, a map of the predicted drag (i.e.  $y_0/h$ ) as a function of the wall geometry (i.e.  $\lambda_F$ ,  $\lambda_P$ ) is shown.

Although attempts have been made to systematically study the impact of increasingly varied surface morphology, predominantly in numerical simulations due to the huge effort required to compile a significant experimental data set, these have mainly considered idealised cube roughness (Kanda et al., 2004; Hagishima et al., 2009; Leonardi and Castro, 2010). These investigations are reported with open symbols in figure 1.1. Although the meaning of  $\lambda_F$  and  $\lambda_P$  will be further discussed in section 2.2, the reader should at this stage note that for cube roughness  $\lambda_F = \lambda_P$ . Therefore, it is unclear how accurate these drag-prediction studies are for different, more general, roughness geometries for which  $\lambda_F \neq \lambda_P$  (i.e. outside the dashed line in figure 1.1). As a result, a complete and stand alone experimental piece of work based on non-simplified roughness (i.e. noncubical) is unavailable. Additionally, Castro (2007) pointed out that, although there is substantial literature on rough-wall flows and there have been a number of attempts to develop useful correlations relating the surface friction to the boundary layer parameters over a wide range of surface roughness, such correlations have mainly considered only small relative roughness height,  $(h/\delta)$ , and it is not known how adequate they are at larger  $h/\delta$ .

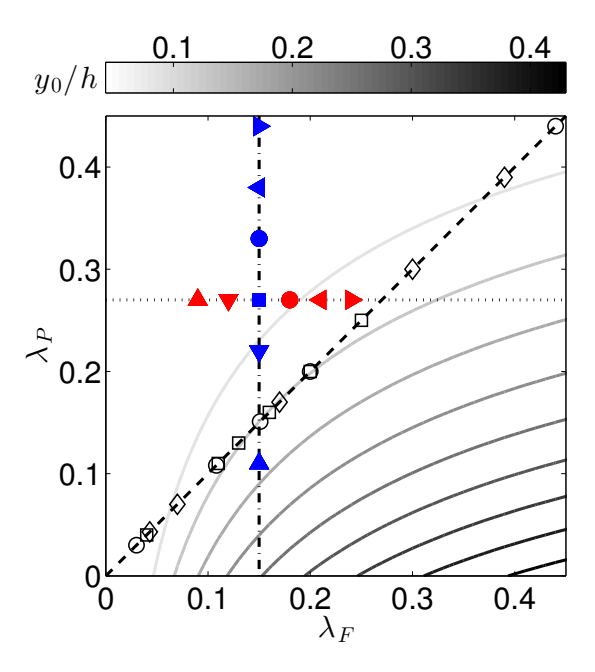


Figure 1.1: Contour plot of Macdonald's prediction of the roughness length behaviour as a function of  $\lambda_F$  and  $\lambda_P$  calculated using the expressions presented in Macdonald (1998) with  $C_d = 1.2$ ,  $\kappa = 0.41$ ,  $\beta = 1$  and A = 4.43 (refer to § 3.1 for further details). Colorbar shows  $y_0/h$ . Dashed line represents  $\lambda_F \equiv \lambda_P$  (cubes), dot-dashed line represents variation of  $\lambda_P$  at fixed  $\lambda_F$  and dotted line stands for variation of  $\lambda_F$  at fixed  $\lambda_P$ . Filled symbols indicate the current experiment while empty symbols indicate respectively  $\circ$  Kanda et al. (2004),  $\diamond$  Hagishima et al. (2009) and  $\square$  Leonardi and Castro (2010).

# 1.3 Research objectives and approach

The primary goals of this thesis are to address the following:

- investigate the individual effects of  $\lambda_F$  and  $\lambda_P$  on the bulk quantities (i.e. the drag) and the aerodynamic parameters (i.e.  $y_0$  and d);
- quantify the effect of the surface morphology on the depth of the roughness sublayer and its structure;
- explore the validity of Townsend's similarity hypothesis at  $h/\delta \approx 0.1$  over a broad range of surface morphologies (i.e. from sparse to dense regimes);
- investigate the spatial universality of the wall turbulence (i.e. vortex organisation, velocity correlations length scales, etc);
- quantify the turbulent kinetic energy distribution across the scales of the turbulence in rough-wall boundary layers.

With these aims in mind, it is firstly necessary to decouple the effect of these two density parameters ( $\lambda_F$  and  $\lambda_P$ ), allowing each to be varied independently. Secondly, to enhance

the importance of the results, a systematic approach, which would cover a broad range of surface morphologies is necessary. Finally, combining different experimental techniques is required for the purpose of this study. The focus of this thesis is to examine the individual effects of  $\lambda_F$  and  $\lambda_P$  at a constant high relative roughness height  $(h/\delta \approx 0.1)$ on drag and the 3D structure of the turbulence. In order to do so, a systematic series of experiments were carried out by varying  $\lambda_F$  at a fixed  $\lambda_P$  and vice versa. The cases examined herein are highlighted in figure 1.1 by filled symbols. The different surface morphologies were generated by regularly distributed LEGO<sup>™</sup> bricks of uniform height, arranged in different configurations covering the entire range of solidities (from sparse to dense regimes). A total of twelve different configurations of systematically varied rough surfaces were tested using high-resolution 2D planar and 3D stereoscopic particle image velocimetry in both the streamwise-wall-normal (x, y) and wall-normal-spanwise (y,z) planes. Direct floating-element drag-balance measurements are also performed to determine the skin friction generated by these different surfaces. This combined effort enables us to not only isolate the effects of  $\lambda_P$  and  $\lambda_F$  on the drag but also to examine the spatial structure of the turbulence above non-cubical roughness. The results of this study can contribute to the creation of a more accurate skin friction prediction model. The emphasis of this research is on fully-rough surfaces with  $h/\delta \approx 0.1$  and it is particularly tailored towards the roughness and inertial sublayers.

#### 1.4 Thesis outline

Building on the background to the study presented herein, chapter 2 describes the methodology, the experimental facility and techniques used throughout this investigation. Chapters 3 to 5 present and discuss the experimental results. The effect of surface morphology on bulk quantities (i.e. drag and aerodynamic parameters) is presented in chapter 3 together with analysis of the extent of the roughness sublayer region and its organisation. The turbulence statistics and the validity of outer-layer similarity are then the object of chapter 4. Finally, chapter 5 discusses the 2D and 3D spatial organisation of the turbulence. Chapter 6 contains a summary of the major findings, draws the final conclusions, and provides directions for future work. Appendix A includes results from a smooth-wall boundary layer at a comparable Reynolds number, here included for completeness. Appendix B describes the 3D vector validation procedure in more detail.

# 1.5 Novel contributions and publications

Parts of this work are discussed in the following publications:

Placidi, M. & Ganapathisubramani, B., (2015b). Effects of large roughness on aero-dynamic parameters and the roughness sublayer in turbulent boundary layers. *Under* 

consideration for publication in Journal of Fluid Mechanics.

Placidi, M. & Ganapathisubramani, B., (2015a). Effect of large surface roughness on flow statistics in turbulent boundary layer. *Under consideration for publication in Journal of Fluid Mechanics*.

In addition, some elements of this work have been presented in the following conferences:

Placidi, M. & Ganapathisubramani, B., (2015). Surface-morphology-induced energy redistribution in turbulent boundary layers. In 9th International Symposium On Turbulence and Shear Flow Phenomena, Melbourne, Australia June-July 30-3. In preparation.

Placidi, M. & Ganapathisubramani, B., (2014). Effect of surface morphology on drag and roughness sublayer in flows over regular roughness elements. In 67th Annual Meeting of APS Division of Fluid Dynamics, San Francisco, California November 23-25.

Placidi, M. & Ganapathisubramani, B., (2014). On the effects of surface morphology on the structure of wall-turbulence. In *interdisciplinary Turbulence initiative*, *Bertinoro*, *Italy September 21-24*.

Placidi, M. & Ganapathisubramani, B., (2013). Investigation of wall-bounded turbulence over regularly distributed roughness. In 8th International Symposium On Turbulence and Shear Flow Phenomena, Poitiers, France August 28-30.

Placidi, M. & Ganapathisubramani, B., (2012). Investigation of wall-bounded turbulence over sparsely distributed roughness. In 65th Annual Meeting of APS Division of Fluid Dynamics, San Diego, California November 18-20.

Placidi, M. & Ganapathisubramani, B., (2011). Investigation of wall-bounded turbulence over sparsely distributed roughness. In 64th Annual Meeting of APS Division of Fluid Dynamics, Baltimore, Maryland November 20-22.

# Chapter 2

# Experimental details and methodology

This chapter describes the facility, the methodology and the experimental techniques used throughout the course of this investigation. The facility is introduced in  $\S$  2.1, then the roughness characterisation and the surfaces examined herein are described and discussed in  $\S$  2.2 and  $\S$  2.3 respectively. The second half of the current chapter addresses the different experimental techniques employed in this study. In particular, the 2D and 3D particle image velocimetry setups are discussed in  $\S$  2.4, whilst the floating-element drag-balance is the focus of  $\S$  2.5. To conclude, an uncertainty analysis is presented in  $\S$  2.6.

# 2.1 Experimental facility

The experiments were carried out in a suction wind tunnel at the University of Southampton, shown in figure 2.1. The same facility has been used for previous rough-wall studies such as: Castro 2007; Reynolds and Castro 2008; Amir and Castro 2011; Claus et al. 2012. The tunnel has a working section of 4.5 m in length, with a 0.9  $m \times 0.6$  m cross-section. The freestream turbulence intensity in the tunnel has been verified through hot wire anemometry measurements, to be homogenous across the cross-section and less than 0.3%. In this study, (x,y,z) are the streamwise, wall-normal and spanwise directions (orientated as in figure 2.1), with the plane y=0 being the bottom surface of the baseboard onto which the roughness elements were located, as shown in figure 2.5(a). The mean and fluctuating velocities along these three directions are denoted as (U,V,W) and (u',v',w'), respectively, while (u,v,w) are the corresponding instantaneous velocities. Experiments were conducted in nominally Zero-Pressure-Gradient (ZPG) as the acceleration parameter  $(K=(\nu/U_e^2)[dU_e/dx])$  was less than  $5\times 10^{-8}$ . Measurements were taken at approximately 4 m downstream along the test section (i.e.

in the centre of section 4 in figure 2.1). The test section is equipped with glass sidewalls and a glass ceiling to provide high-quality optical access during the measurements. The bottom wall of the tunnel was instead designed and manufactured to allocate a slot for the floating-element drag-balance measurements.

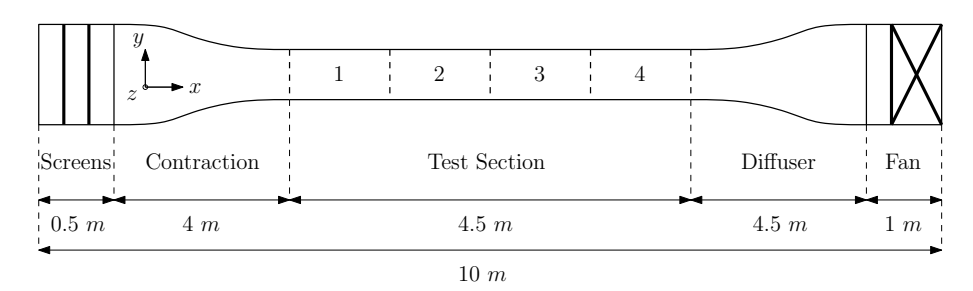


Figure 2.1: Wind tunnel schematic.

## 2.2 Roughness morphology characterisation

As briefly introduced in chapter 1, early experimental studies of rough surfaces were focused on high-density rough-walls. These surfaces were typically obtained by covering the wind tunnel floor with different grit sand papers, where the drag generated by those was measured. Therefore, for a high-density rough-wall, comparing it to its equivalent experimentally known sand-paper-covered wall was logical. In this fashion, a good parameter was found by Nikuradse (1933) to be the "equivalent sand roughness".  $h_s$ . The difficulty in applying this approach to practical cases lies in the fact that the value of  $h_s$  to be ascribed to a given surface is unknown a priori, hence the necessity to collect experimental data to effectively predict the bulk drag. This limitation deems this method unfeasible for use in the design stage. The roughness obtained by Nikuradse (1933) with sand paper can be said to be at maximum density, because the grains of sand were glued to the wall as closely to each other as possible. Although this concept is still largely used today for describing highly dense rough-walls, in many practical applications the density of the roughness on the walls is considerably lower than Nikuradse's case. Thus, such surfaces can no longer be described by his formulation. The last few decades have seen methods based on density parameters known as solidities come to the fore. Since Schlichting (1937), the tendency has been to characterise the effect of regularly distributed roughness using frontal and plan solidities. Later studies have also confirmed that a rough-wall (with regular roughness) can be optimally described using these two parameters (Theurer et al. 1992; Grimmond and Oke 1999). Referring to figure 2.2, the frontal solidity is defined as the total projected frontal area of the roughness elements per unit wall-parallel area  $(\lambda_F = \frac{A_F}{A_T})$ , while the plan solidity is, instead, the ratio between the plan area and the unit wall-parallel area  $(\lambda_P = \frac{A_P}{A_T})$ . These definitions rely upon uniform height roughness elements. For cases in which the obstacles' height

is heterogeneous, the mean roughness height,  $\overline{h}$ , is often used in defining the solidities (Grimmond and Oke, 1999).

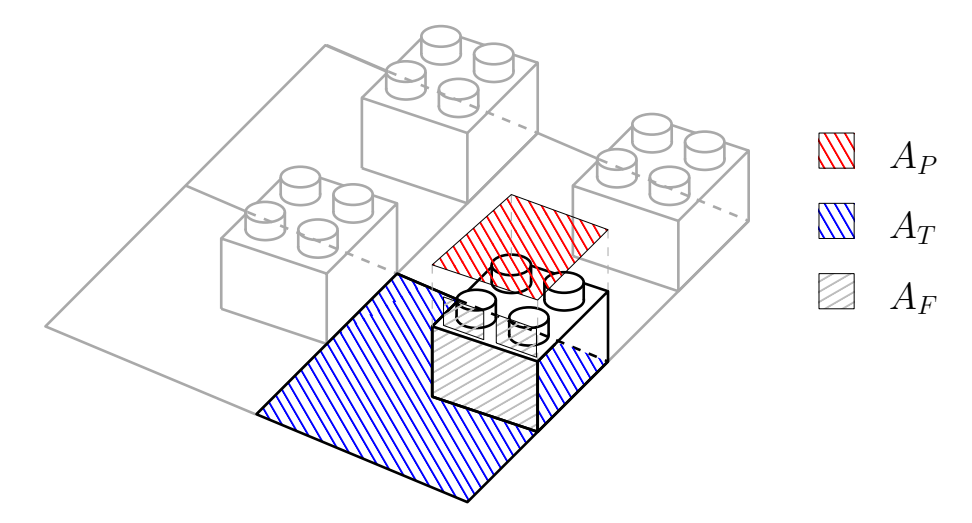


Figure 2.2: Definition of frontal and plan solidities. Black lines identify a single repeated unit, grey lines show how adjacent units are linked together to build the wall morphology. Inspired by Grimmond and Oke (1999).

Various studies have examined the effect of surface morphology on drag, and attempted to find correlations for  $y_0 = f(\lambda_F, \lambda_P)$ . This quantity will be further discussed in section 3.1. However, at this stage it is sufficient to know that it is closely linked with the drag. Jimenez (2004) compiled results from a series of experiments and showed the presence of two regions - the sparse regime (for  $\lambda_F \ll 0.15$ ) for which the effect of roughness increases with solidity, and the dense regime (for  $\lambda_F \gg 0.15$ ), for which it decreases. This is because, as the density increases so does the drag generated by the surface, up to the point where adding new elements merely serves to reduce their effectiveness due to mutual sheltering, hence, the bulk drag starts to decrease (Grimmond and Oke, 1999). The effects of the two different regimes are shown in figure 2.3, where a peak in the non-dimensional drag coefficient (here expressed as  $\frac{h_s}{C_D h}$ ) is visible around  $\lambda_F \approx 0.15$ .

However, the effect of plan solidity on bulk drag is not clear from the latter. Grimmond and Oke (1999) also included the plan solidity in their previous review. Figure 2.4 shows how  $y_0/h$  varies as a function of both solidities. The variation of the latter involves an increase for sparse area densities, followed by a decrease for higher area densities, in both  $\lambda_F$  and  $\lambda_P$ . It is important to highlight that the critical value for the predicted peak in drag occurs at different values of plan and frontal solidities. The cut-off between the regimes is reported to be  $\lambda_F \approx 0.15$  and  $\lambda_P \approx 0.35$ . These suggested values (Jimenez (2004) and Grimmond and Oke (1999)) are used as baselines for the design of the surface morphologies examined herein.

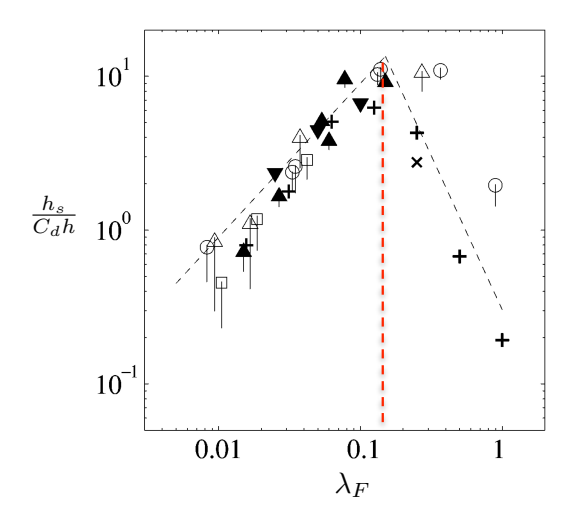


Figure 2.3: Equivalent Sand Roughness,  $h_s$ , for various surfaces versus the solidity,  $\lambda_F$ , corrected with empirical drag coefficient. Open symbols, rounded elements (spheres, cones,  $C_d = 0.3$ ; spherical segments,  $C_d = 0.13$ ) from Schlichting (1979). For all others,  $C_d = 1.25$ . Filled triangle up, spanwise fences (Schlichting, 1979); triangle down, spanwise fences (Webb et al., 1971); +, spanwise cylinders (Tani, 1988); x, spanwise square bars (Bandyopadhyay, 1987). The dashed lines have logarithmic slopes +1 and -2. Modified from Jimenez (2004).

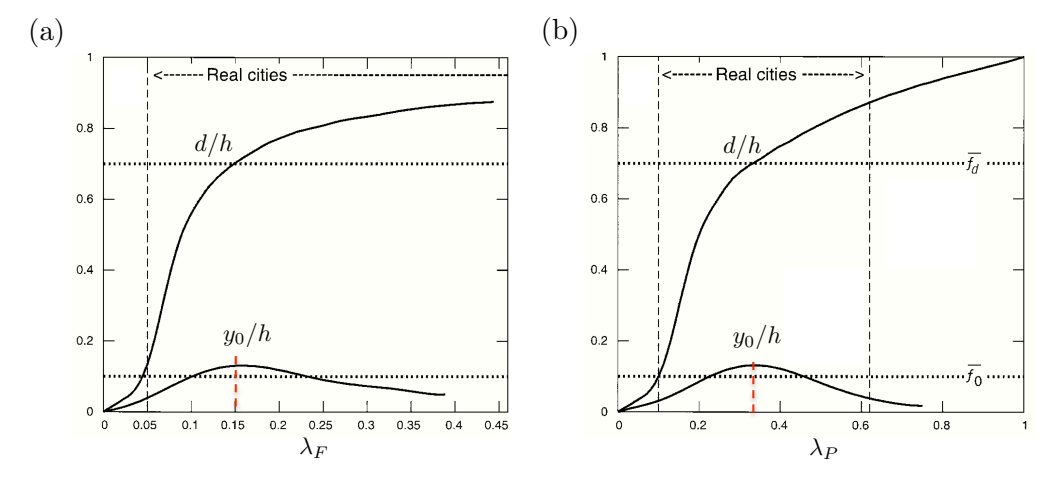


Figure 2.4: A conceptual representation of the relationship of the aerodynamic roughness length and the displacement height to the plan and frontal area density ratios. Modified from Grimmond and Oke (1999). ©American Meteorological Society. Used with permission.

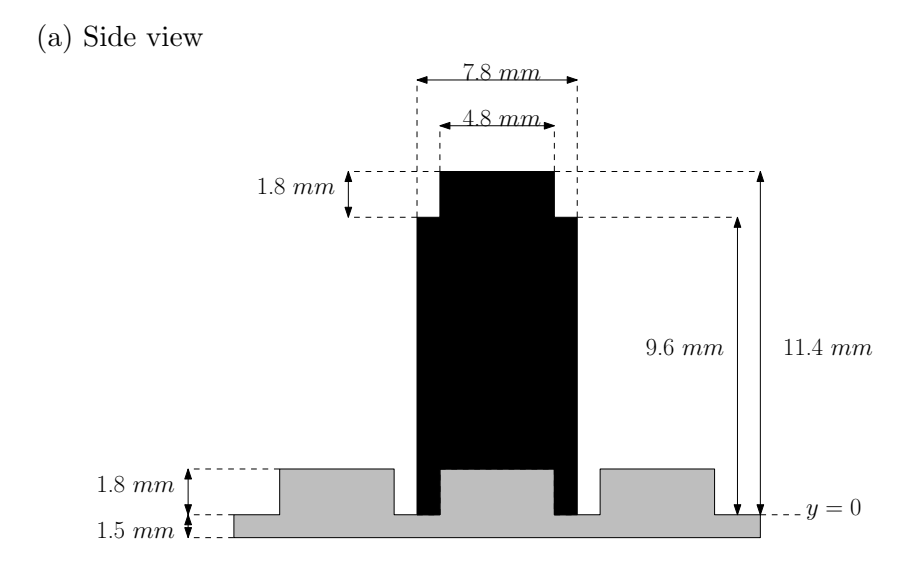
#### 2.3 Current roughness morphology

For rough surfaces, this study used LEGO<sup>TM</sup> baseboards onto which LEGO<sup>TM</sup> bricks (or blocks) were distributed in different patterns. Twelve different patterns were adopted to systematically examine the individual effects of frontal and plan solidities on the structure of the turbulence. Figure 2.5 shows the geometry of a LEGO<sup>TM</sup> element and the basic repetitive units adopted to generate the different patterns in analysis (variation of frontal and plan solidities in figure 2.5(b) left and right respectively). A single dark square in the top view is a single LEGO<sup>TM</sup>brick. This brick has a streamwise×spanwise dimension of 7.8  $mm \times 7.8$  mm and its height is h = 11.4 mm (which includes the pin at the top), as shown in figure 2.5(a). Patterns LF1 to LF6 represent cases for which the frontal solidity is varied at a fixed plan solidity whereas, in cases LP1 to LP6 the plan solidity is varied at fixed frontal solidity. These variations follow the dotted and dot-dashed lines in figure 1.1. The different cases were designed on the basis of previous studies that show the location of the peaks in  $y_0$  (Grimmond and Oke, 1999; Jimenez, 2004).

Progressive repositioning of the downstream roughness elements in the sheltered regions of the upstream obstacles, has allowed us to achieve variations in plan solidity at fixed frontal solidity. The same sheltering principle is applied to obtain the cases with varying  $\lambda_F$  at fixed  $\lambda_P$ . The filled symbols in figure 1.1 indicate the cases studied in this thesis. The unit wall-parallel area of each repetitive unit was kept fixed at  $70.2 \text{ } mm \times 39 \text{ } mm$  and  $46.8 \text{ } mm \times 46.8 \text{ } mm$  for the frontal and plan variation cases respectively. In evaluating  $\lambda_F$  and  $\lambda_P$ , the complete LEGO<sup>TM</sup> bricks have been considered (including the pins on top of the blocks as highlighted in figure 2.2). The flow was developed initially over the baseboard for 1.7 m and a further 2.3 m over the bricks to guarantee that the boundary layer reaches equilibrium with this new surface (as discussed in § 4.3.2). The leading edge just downstream of the contraction exit was fitted with a 300 mm aluminium "lead-in" ramp angled at approximately 3°. This ramp was designed to prevent the flow exiting the contraction impacting directly upon the front of the roughness plate and elements. Instead, it lifts up delicately to the roughness height (Castro, 2007) to allow a homogeneous development on this raised surface (at y = 1.8 in figure 2.5(a)).

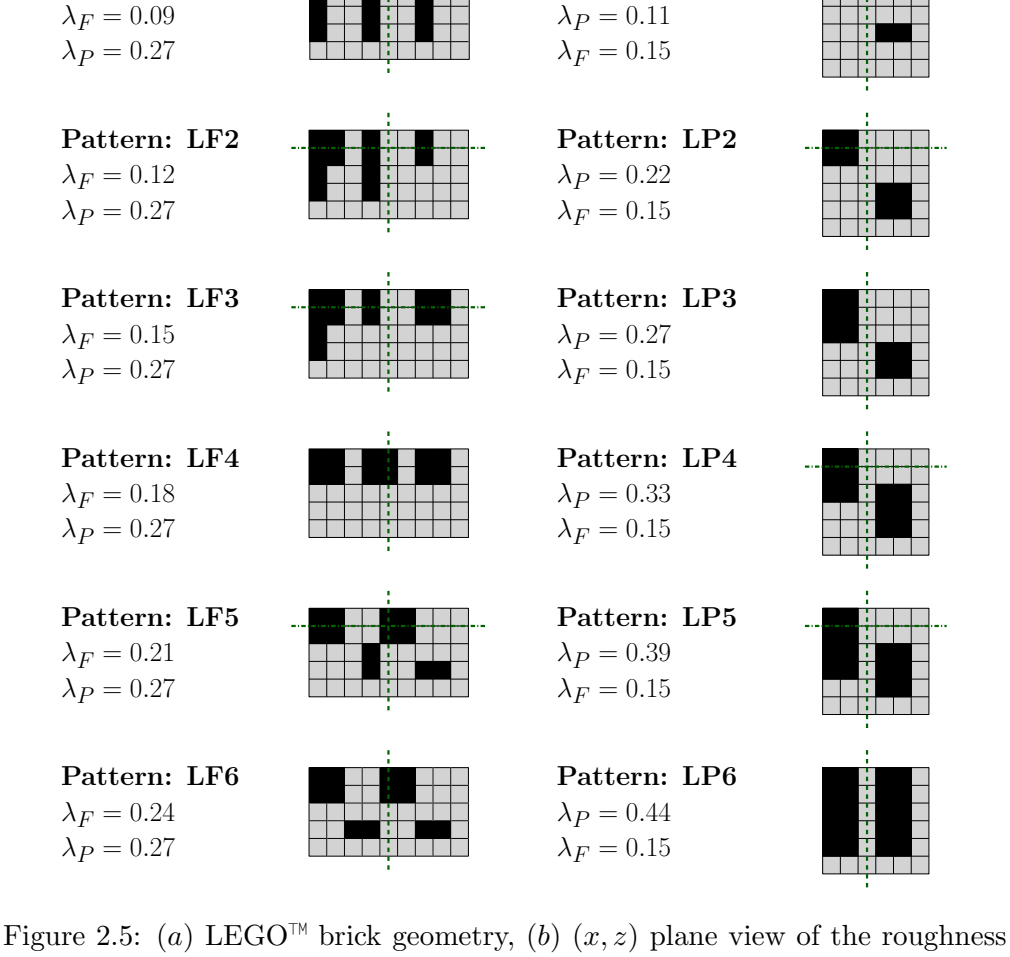
# 2.4 Particle image velocimetry

This section discusses the main experimental technique used throughout this investigation: Particle Image Velocimetry (PIV). Both 2D and 3D PIV are employed in this work. The 2D setup is described, with details on the 3D case subsequently presented. The reader is referred to Westerweel 1997; Raffel et al. 1998 and Adrian and Westerweel (2011) for further details on this measurement technique.



(b) Top View (basic square unit:  $7.8 \times 7.8 \ mm^2$ )

Pattern: LF1



Pattern: LP1

Figure 2.5: (a) LEGO<sup>TH</sup> brick geometry, (b) (x, z) plane view of the roughness elements' patterns with varying  $\lambda_F$  at  $\lambda_P = const = 0.27$  (left) and roughness elements' patterns with varying  $\lambda_P$  at  $\lambda_F = const = 0.15$  (right). Dashed and dash-dotted lines in (b) indicate the position of the laser sheet during the measurements with the respect of each repeated unit for the 2D and 3D setup respectively. Dimensions are not in scale for ease of readability. Flow is top to bottom.

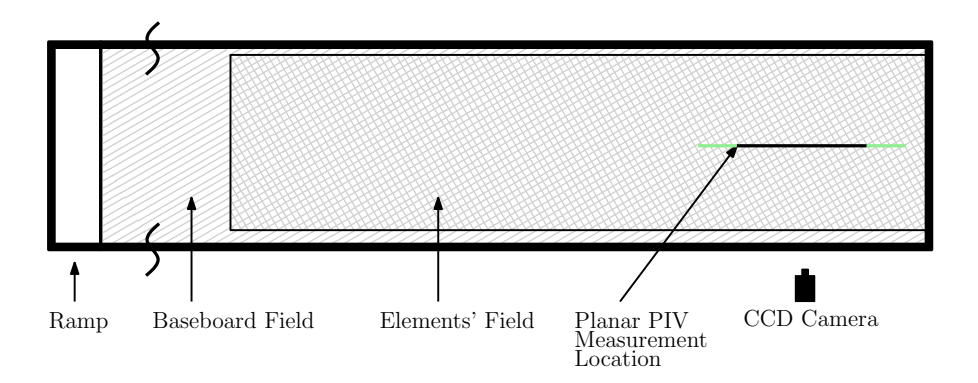
#### 2.4.1 2D planar PIV

PIV measurements were taken for all patterns at a freestream velocity,  $U_{\infty}$  of 11.5 m/s. The test location was at the same streamwise location as the skin-friction measurements (approximately 4 m downstream). As will be shown in section 3.5.1, at this freestream velocity, the flow over all surfaces is considered to meet fully-rough conditions to within the uncertainty of the skin-friction measurements. The flow was seeded with vaporised glycol-water solution particles (1  $\mu m$  in diameter) illuminated with a laser sheet produced by a pulsed New Wave Nd:YAG laser system operating at 200 mJ. A system of two spherical lenses (plano-convex -50 and plano-concave +100) was used to focus the laser sheet. A plano-concave cylindrical lens with a focal length of -30 mm was then employed to expand the laser beam into a sheet of a thickness of approximately 0.7 mm throughout the entire Field Of View (FOV). The position of the laser sheet with respect to the roughness configuration is indicated by dashed lines in figure 2.5(b).

Streamwise wall-normal (x,y) planes were acquired at the spanwise centreline of the test section by a 16 M pixel high resolution camera equipped with Nikon 105 mm f/8 lenses, at a fixed sampling frequency of 0.8 Hz. This was so that statistically uncorrelated measurements were acquired for each image pair. For each run, 2000 image pairs were acquired and processed with DaVis 8.0 software. The setup allowed a field of view of 200  $mm \times 136$  mm (approximately  $1.8\delta \times 1.3\delta$  streamwise-wall-normal for each roughness configurations). Velocity vectors were obtained using  $16\times16$  pixel final interrogation windows with 50% overlap. The resulting spatial resolution is approximately 0.7  $mm \times 0.7$  mm for all cases and successive vectors are spaced at half that distance (due to 50% overlap). Images were preprocessed with an averaged minimum intensity background subtraction. Following this procedure, a field of 98-99% good vectors was achieved, minimising the need of interpolation (when necessary a local mean interpolation was used). The time delay between laser pulses, across all the cases, was chosen such that the pixel displacement in the freestream was approximately 15 pixels, for reason discussed in section 2.6.1.

Figure 2.6 shows a schematic of the planar PIV experimental setup. This shows the light source positioned above the tunnel - therefore a 45° mirror was used to deflect the light into the measurement location. The latter, together with the rest of the optical equipment, was positioned above the tunnel onto a solid-structure-mounted rail. This was embedded in the lab floor to avoid transmission of tunnel vibrations to the instrumentation. The Charge-Coupled Device (CCD) camera was positioned on the side of the tunnel onto the same rigid structure to minimise its vibrations, and it was oriented to image the object plane at 90°. The resolution of the current data sets range from between 28 to 42 wall-units, due to differences in the skin friction velocities generated by the different surface morphologies. The different local resolution has a tangible effect on the turbulence statistics, in particular on the higher order quantities. Therefore, the

#### (a) Top view



#### (b) Side View

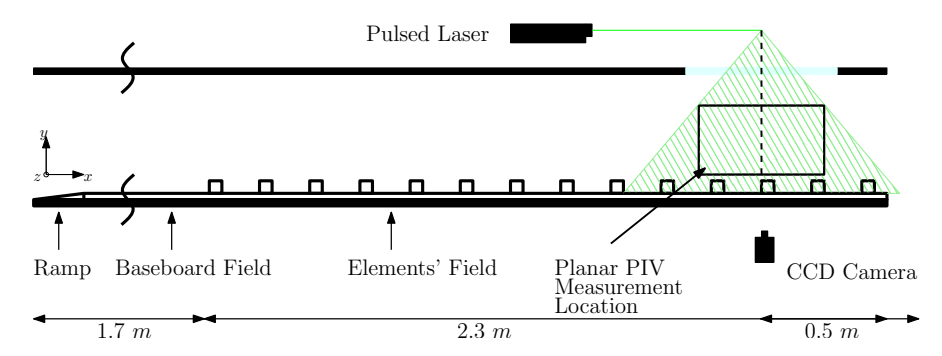


Figure 2.6: Schematic view of the 2D planar PIV setup. Dimensions are not in scale for ease of readability.

results presented in the following sections are obtained after all data sets have been filtered with a low-pass Gaussian filter designed to match the local resolution at  $l_{2D}^{+}=45$ . It must be noted that this filtered spatial resolution is comparable (if not better) than previous cross-wire and PIV based measurements presented in the literature.

#### 2.4.2 3D stereoscopic PIV

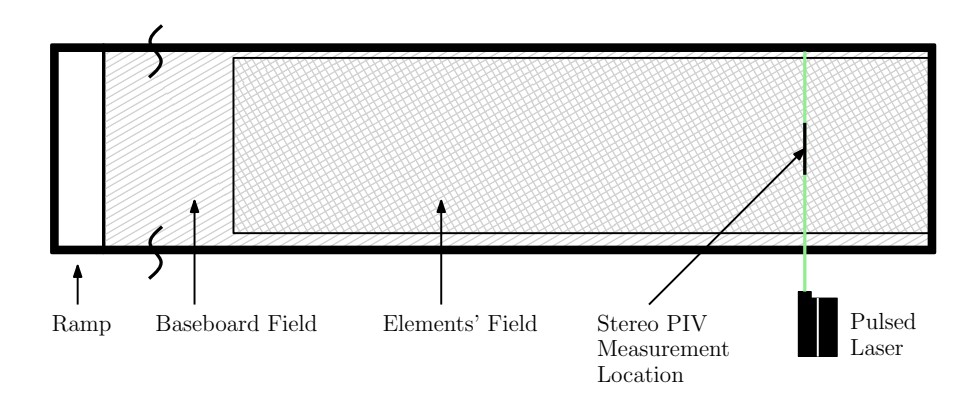
Given the high relative roughness height  $(h/\delta \approx 0.1)$ , spanwise flow heterogeneity is to be expected within the roughness sublayer. To investigate this, stereoscopic PIV measurements were also carried out in wall-normal-spanwise (y,z) plane, at roughly the same location as the 2D measurements. Two cameras with the same specifications as for the 2D measurements were used to acquire 1500 digital image pairs (instead of 2000 as for the 2D case) to reduce the data storage space at a cost of statistical convergency. Figure 2.7 shows a schematic of the stereoscopic PIV setup. The two cameras were positioned above the tunnel looking through an optical perspex ceiling, whilst the laser sheet was shone from the side. A FOV covering a minimum of two spanwise repeated-units  $(1.5\delta \times 1.5\delta$  spanwise-wall-normal) was resolved. A 1.5mm thick laser sheet (pulsed New Wave Nd:YAG) was used to illuminate the particles (glycol-water solution) and

the time delay between the laser pulses had to be reduced accordingly, so that the particles would not leave the laser sheet plane ( $\Delta t = 20 \mu s$ ). This reduced  $\Delta t$  has an influence on the averaged pixel displacement of the particles, and hence on the uncertainty (see section 2.6.1). Measurements were carried out across six cases only: LF2, LF3, LF5 and LP2, LP4, LP5 as these represent conditions for sparse, medium-packed and dense solidity regimes. The cameras were oriented at an angle of approximately 25° to the measurement plane axis, which is appropriate to accurately resolving the out-of-plane velocity component (Raffel et al., 1998). Scheimpflug adaptors were mounted on the lenses to help maintain focus across the entire field of view by orienting the lens plane at an angle to the image plane as discussed in Raffel et al. (1998). Although this configuration maximises the focus on the measurement plane, it comes at a cost of introducing a strong perspective distortion and a magnification that varies across the FOV. This distortion can, however, effectively be corrected via a two-plane calibration (Westerweel, 1997). A two-plane calibration target was used for calibration, and self-calibration using Davis 8.0 was applied to improve the quality of the final velocity field (typically up to 2-pixel correction was applied). Similar analysis to the 2D case was carried out in DaVis 8.0. Velocity vectors were obtained using  $32 \times 32$  pixel<sup>2</sup> final interrogation windows with 50% overlap. This resolution is coarser than the planar PIV measurement; however, given the nature of measurements (i.e. flow perpendicular to laser sheet) and the thickness of the laser sheet, this interrogation window size is deemed sufficient. The worst case resolution  $(l_{3D}^+)$  across the different cases was approximately 120 wall-units, therefore, for the same reasons previously discussed, the 3D data set has been filtered to match the local resolution across cases at  $l_{3D}^+=125$ . This is coarser than the 2D measurements due to the increased thickness of the laser sheet, increased size of the interrogation window, and the larger field of view. To conclude, table 2.1 summarises some of the most relevant 2D and 3D PIV parameters.

#### 2.4.2.1 3D PIV vector validation

Due to the cameras' positions, high angles characterise the stereoscopic imaging. For this reason, although great care has been put into minimising the light reflection by the means of a combination of rhodamine paint and matt black paint, some of the legoboard pins can still be seen in the background of each image. These pins were responsible for the generation of spurious vectors. A combination of minimum background subtraction, image intensity normalisation, followed by vector validation has been applied in DaVis 8.0 to minimise this problem. Nevertheless, some residual spurious vectors could easily be identified when plotting statistics in contour plots. Therefore, additional vector validation techniques had to be employed. A reconstruction methodology based on "gappy" proper orthogonal decomposition has been followed, as described in Raben et al. (2012). The reader is referred to appendix B for further details. Across the entire FOV, the reconstruction was only applied to less than 2.5% of the vectors, to minimise

#### (a) Top view



#### (b) Side View

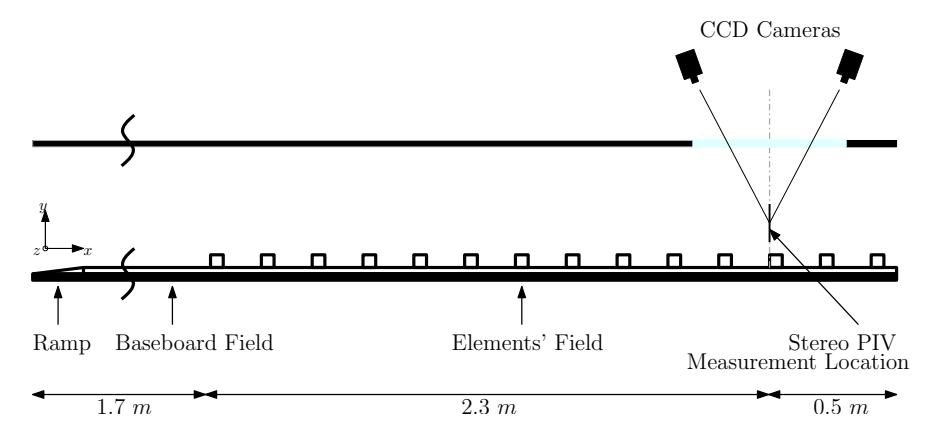


Figure 2.7: Schematic view of the 3D stereoscopic PIV setup. Dimensions are not in scale for ease of readability.

the use of interpolation. Even after the validation procedure, due to severe reflection, the FOV below  $y=25\ mm$  had to be discarded. Nevertheless, the 2D data set suggests that this region is still well below the RSL boundary, therefore, vital information can still be gathered from this reduced FOV. Furthermore, the focus of this thesis is the bulk behaviour of the flow and the large scale turbulence coherency across scales, which can still be inferred despite the limitation of the 3D measurements.

#### 2.4.3 PIV data resolution

The smallest scales in the flow can be assumed to be of the order of the Kolmogorov length scale. An estimate of this scale can be calculated, following Kolmogorov (1941), as:

$$\eta = \left(\frac{\nu^3 \kappa y}{U_\tau^3}\right)^{1/4}.\tag{2.1}$$

Parameters	Planar	Stereoscopic			
FOV	$1.8\delta \times 1.3\delta$	$1.5\delta \times 1.5\delta$			
Initial Interrogation Area	$64 \text{ pixel} \times 64 \text{ pixel}$	$64 \text{ pixel} \times 64 \text{ pixel}$			
Final Interrogation Area	$16 \text{ pixel} \times 16 \text{ pixel}$	$32 \text{ pixel} \times 32 \text{ pixel}$			
Time in between pulses $\Delta T$	$60~\mu s$	$20~\mu s$			
Average Pixel Displacement	15 pixel	5 pixel			
Acquisition Frequency	$0.8~\mathrm{Hz}$	$0.8~\mathrm{Hz}$			
Initial Resolution	$14\text{-}21\ l_{2D}^{+}$	$50-60 \ l_{3D}^{+}$			
Filtered Resolution	$0.7 \ mm \times 0.7 \ mm \ (45 \ l_{2D}^{+})$	$1.5 \ mm \times 1.5 \ mm \ (125 \ l_{3D}^{+})$			
Final Vetor Spacing	0.35~mm	$0.75 \ mm$			
Interrogation Area Overlap	50%	50%			
No. Realisations	2000	1500			
Laser Power	200~mJ	200  mJ			
Laser Optics	(-50, +100) & -30 mm	(-50, +75) & -30 mm			
No. Camera	1	2			
Camera Resolution	$16 \mathrm{Mp}$	$16\mathrm{Mp}$			
$f_{\#}$	8	2			
Camera Lens	Nikon $105 \ mm$	Nikon $105 \ mm$			
Camera Angle	0	$25^{\circ}$			

Table 2.1: 2D and 3D PIV Parameters.

This gives a Kolmorogov length scale,  $\eta$ , of the order of 0.1 mm or  $l_{2D}^+ \approx 4-6$  based upon the different skin friction velocities and at a wall-normal location  $y/\delta \approx 0.4$ . Therefore, the 2D data set is resolved, in the worst case, down to approximately 7 times the Kolmogorov's length scale (based on  $l_{2D}^+ = 45$ ). Although this is fairly large, as the aim of this study is mainly to investigate the large-scale flow features, this is not critical.

# 2.5 Floating-element drag-balance

Measuring the skin friction generated by a particular surface morphology is of fundamental importance in the study of boundary layers and it is invaluable for a variety of practical applications. Although it is typically very difficult to measure the wall friction in smooth-wall cases (i.e. pure viscous drag), the presence of the roughness elements and the additional pressure drag they generate, makes the direct measurement more reliable and feasible in rough-wall cases (Krogstad and Efros, 2010). Nonetheless, because of the general difficulties in measuring the friction velocity, this is usually extrapolated via the Reynolds shear stresses or a log-law fit. Both these procedures inherently introduce a series of uncertainties which will be discussed further in due course. Therefore, when possible, a more accurate way to obtain the wall shear stress is to measure it directly. This can be effectively achieved by a mechanical force balance (Acharya et al., 1986;

Bechert et al., 1997, 2000). Comprehensive reviews of the direct methods for estimating the friction velocity can be found in Winter (1977) and more recently in Hakkinen (2004).

Although complex and unsteady, the characteristics of the flow around a cuboid bluff-body mounted in isolation on a flat surface are well understood (Lim et al., 2007, 2009). When arrays of such obstacles are distributed on a surface, as in the current case, the flow characterisation becomes much more difficult, mainly because the different obstacles interact with each other and they do not behave as if they were in isolation (Padhra, 2010). In particular, the wake generated by an obstacle upstream can impinge and interact with the subsequent obstacle, exposing it to a significantly different flow field. This results in the so called "bulk drag", which is very different from the summation of the single drags generated by each element if it were in isolation.

The drag generated by the different wall morphologies examined herein was directly measured via a floating-element drag-balance (which was based on the design of Krogstad and Efros 2010; Efros 2011). This balance was placed approximately 4 m downstream along the test section, corresponding to the PIV measurement location. Figure 2.8 shows a schematic of the setup. A measurement patch (1) replica of the testing surface is positioned in the tunnel floor through a cut hole; this element is mechanically connected to a two-arm lever system (2) which converts the horizontal stress acting at the wall into a wall-normal load. A 370  $mm \times 370$  mm patch of the roughness was mounted on the top of the vertical arm of the balance to act as a sensing element. Its relatively large size, compared to the original version (Krogstad and Efros, 2010), allows a number of repeated units to be included in the measurement patch. However, the pressure variation across the floating element is negligible  $\leq 3\%$  (Krogstad and Efros, 2010; Hakkinen, 2004). The lever system, which rests on a knife edge (3), allows mechanical amplification of the forces based on the mutual lengths of the arms. The normal load is then measured by a high-sensitivity off-the-shelf precision Ohaus scale (4) with a sensitivity of 0.01 q (Gold Series no. TAJ602/A). The measurement resolution, in the worst case, was typically  $2.5 \times 10^{-4}$  of the applied load. The knife edge is mounted on a H-shaped frame (7) which locates the scale. This prevents any accidental movement of the latter during measurements, as it is bolted onto a 12 mm steel plate connected to the base structure (8). This plate offers fine-tuning height adjustment as the latter rests on adjustable feet (9). The whole system rests on the lab floor via a heavy base structure to minimise structural vibrations. The measuring element was centred in a hole cut at the bottom of the wind tunnel floor surrounded by a 1 mm gap at the front and a 2 mm gap at the back of the plate to allow movement (i.e. readings onto the scale). Previous studies using a similar floating element concept have shown that the effect of the gap size (up to 3 mm) is within 2% uncertainty (Iyengar and Farell, 2001). It was important to prevent any possible airflow through this gap around the tile, as this would affect the measurements (Krogstad and Efros, 2010; Efros, 2011; Claus et al., 2012). As the present work is carried out in a suction wind tunnel, the static pressure inside the tunnel was

always significantly lower than the atmospheric pressure. This necessitated mounting the entire balance in a sealed box (12), so that the measured force was not influenced. The sealed box was made out of soft plastic sheet. The static pressure inside both the tunnel and the box were monitored to prevent pressure difference effects.

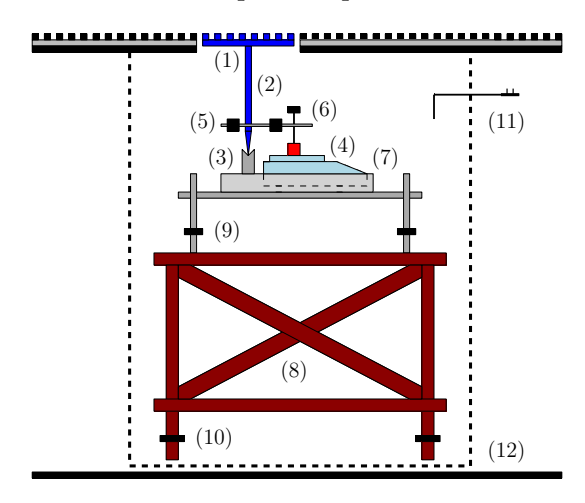


Figure 2.8: Schematic of the floating-element drag-balance. Components: (1) measurement patch, (2) two-arm lever system, (3) knife edge, (4) precision scale, (5) counterbalance weights, (6) load-transfer adjustment pin, (7) H-frame containing the scale, (8) base structure, (9) fine-adjustment feet, (10) rough-adjustment feet, (11) Pitot tube, (12) sealed box.

The measurements were found to be very sensitive to the vertical alignment of the measuring patch. This was obtained via a combination of different tunings. Two adjustable feet for rough and fine tuning were embedded within the sustaining structure. The initial balancing of the scale into the neutral position was obtained via the scale adjustable feet, the counter weights system (5) and the adjustable pin (6). Measurements were also found to be affected by vibration of the lab floor induced by close proximity movements which, therefore, had to be avoided. The numerous technical difficulties meant that obtaining repeatable results was difficult without caution, as previous studies in the same facility have highlighted (Claus et al., 2012). For these reasons each measurement was repeated multiple times and only converging runs were stored. Details of the calibration process follow, as it is the most striking difference with Krogstad and Efros' (2010) original design.

#### 2.5.1 The calibration unit

A calibration is required to convert the reading from the weighing scale into the corresponding shear stress at the wall. To do so, a Vishay load cell (model no. 1004) is employed. The load cell is rigidly fixed under the measuring patch. A manually operated linear traverse is embedded into the tunnel floor to allow pushing against the load cell. This records the load magnitude, and transmits it to the precision scale (via

rigid-body connection). The scale's reading is simultaneously acquired. The load cell is connected to a bespoke amplifier which converts the mV outputs into values of order of few V. This circuit amplifier also controls the "zero", i.e. can introduce an offset in the reading. The analog signal is then transmitted via a BNC cable to a NI DAQ (NI USB-6212). The scale readings are instead acquired by a computer via a serial-port connection. The acquisition was obtained via a combination of session-based interface and serial port based Matlab<sup>TM</sup> codes written for this purpose. The calibration of the system relies on two different steps. Firstly, the load cell has to be calibrated to create a reference curve for its reading against a known load. Secondly, the mechanical system has to be calibrated to verify that it transfers the load linearly with the imposed geometric amplification. The first calibration is only necessary as the exact applied load, via the means of the linear traverse, is unknown, and hence had to be recorded. The two calibration procedures are next described.

#### 2.5.1.1 Load cell calibration

This is obtained by positioning the load cell in a flat position on the tunnel floor and loading it with different known weights. Weights between 2 g and 250 g are used to calibrate the load cell over its entire range. This results in a first curve of known weights as a function of the sensor output, as in figure 2.9(a). The load cell is then installed in the measurement position, which involves the sensor being rotated  $90^{\circ}$ . This operation introduces an offset in the reading, which can be quantified acquiring its newly defined zero. The result is a shifting of the calibration curve (due to this new offset), although its slope does not change (i.e. variations within 1%), as shown by the dashed line in figure 2.9(a). The load cell was also calibrated in situ (with a pulley system) to verify its behaviour and the described calibration.

#### 2.5.1.2 Mechanical system calibration

Once the load cell is calibrated and installed under the measuring patch, loads are applied upon it, via a manually operated linear traverse. These loads are recorded by the load cell and transmitted to the scale via the rigid mechanical arm. Simultaneously, the scale reading is acquired. A preload of around 10~g is used to offset the load cell and to avoid misleading readings due to its first contact with the linear traverse. Weights covering the expected measurement range are used in this process. This second calibration results in a wall stress as a function of the scale reading curve, as shown in figure 2.9(b). A system's linear response with very little scatter was found, as in Krogstad and Efros (2010).

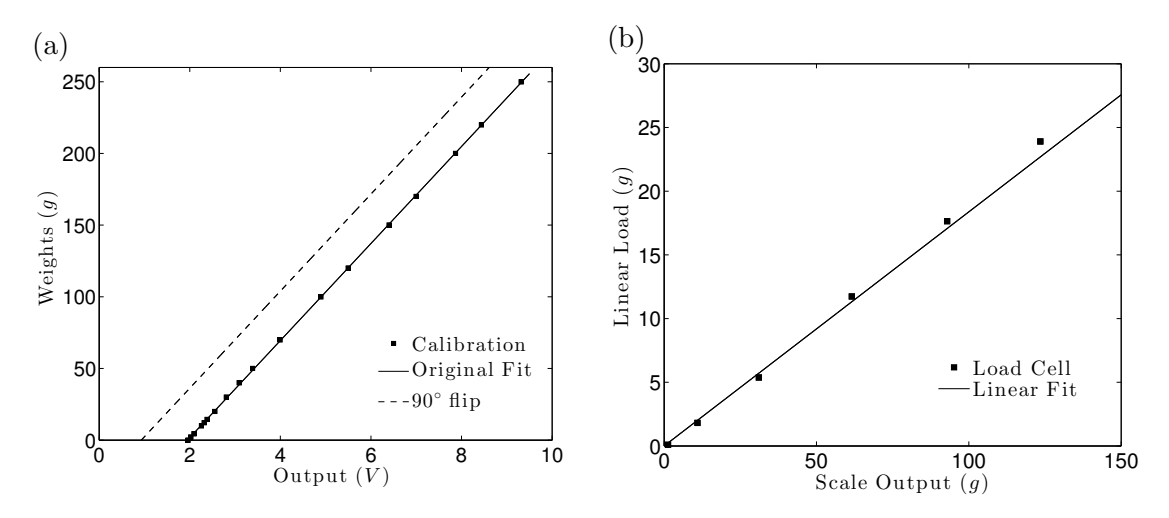


Figure 2.9: Calibration curves for (a) the load cell and (b) the mechanical arm (the 10 g preload has been subtracted for clarity).

#### 2.6 Uncertainty estimation

This section addresses the uncertainty estimation affecting the results of this thesis. Firstly, uncertainty affecting the PIV is discussed. Secondly, the uncertainty on the floating-element drag-balance measurement is presented.

#### 2.6.1 PIV bias estimation

Prasad et al. (1992) demonstrated that when particle images are well resolved during digitalisation (i.e. absence of pixel locking), the uncertainty on the measured displacement (due to the Gaussian peak fit, used in the PIV cross-correlation algorithm) is usually small. The time delay between laser pulses across all the 2D cases was chosen such that the pixel displacement in the freestream was approximately 15 pixels. This ensures that the bias error of the PIV velocity measurements is less than 1% of the full-scale velocity (given that the sub-pixel determination has an uncertainty of about ±0.1 pixels - see Adrian and Westerweel 2011). However, for the 3D measurements, for which the mean pixel displacement in the freestream was reduced to 5 pixels, the bias error becomes of the order of 2% of the full scale velocity. In addition, the effects of pixel-locking (Christensen, 2004), for both cases have also been minimised, ensuring that the mean particle-image diameters exceeded two pixels. A more accurate estimation of the PIV bias error can be obtained following the procedure highlighted by Adrian and Westerweel (2011) in  $\S$  9.4.4; where the dimensional spatial correlation of the variance of the velocity fluctuations can be evaluated and its peak value for zero-lag extrapolated. Comparing this with its theoretical value (i.e. normal distribution) allows the estimation of the bias error. Following this procedure, the bias uncertainty on the variance of the streamwise and wall-normal fluctuations has been found to be less than 4.8% and 7.8% respectively.

#### 2.6.2 PIV statistical uncertainty

Since statistical analysis is largely employed, the uncertainty in this procedure has to be taken into account. Benedict and Gould (1996), among others, have discussed the uncertainty due to an ensemble of uncorrelated data observations, which represents a good estimate for the current PIV data sets. Following their methodology, assuming a normal distribution of the statistics and including a 95% confidence limit, the statistical uncertainty on the planar data set resulted in less than 1%, 5%, 8% and 10% for the mean velocity, the variance of the streamwise and wall-normal velocity fluctuations and the covariance of the velocity fluctuation respectively. For the stereoscopic data set, on the other hand, given the lower number of realisations, the uncertainty for the correspondent quantities was found to be 3%, 6%, 9% and 14%. Given that the bias uncertainty, previously discussed, is contained in the statistical one, the latter is considered to be the overall uncertainty affecting the PIV results. These values are in line with previous PIV-based studies on rough-wall turbulent flows (Wu and Christensen, 2007). Table 2.2 summarises the uncertainty affecting the PIV measurements.

Quantity	$\epsilon_{2D}$	$\epsilon_{3D}$
$\overline{U}$	1 %	3%
$u'^2$	5%	6%
$v'^2$	8%	9%
u'v'	10~%	14%

Table 2.2: PIV uncertainty for the 2D and 3D cases.

#### 2.6.3 Floating-element drag-balance uncertainty

The accuracy of a similar force balance system has been quoted to be within 3% (Krogstad and Efros 2010; Claus et al. 2012). Given the different calibration used herein, and the technical modifications to the original design, the uncertainty of the friction-balance must be re-evaluated. The latter is composed of different terms. The uncertainty on the measured force is estimated by performing two subsequent runs and evaluating the percentage error in the measured skin friction. All runs reported a scatter well below 3%, which is assumed to be the reproducibility of the results,  $\epsilon_R$ . An example of this procedure is given in figure 2.10. Different amplification factors and wind speeds were tested and all yielded similar results. In addition, given that two different calibration procedures are used, these have to be taken into account. Firstly, the uncertainty on the load cell,  $\epsilon_{LC}$ , is defined on how well a certain known weight can be reproduced following the calculated sensor calibration curve. Additionally, as previously discussed, mounting the sensor in the measurement location, involves a 90° rotation as it is mounted in a vertical position. This introduces an additional error, here called  $\epsilon_{flip}$ . Finally, the uncertainty on the mechanical arm calibration,  $\epsilon_{MA}$ , has to be included in the process. This is defined in a similar fashion to  $\epsilon_{LC}$ . Following a

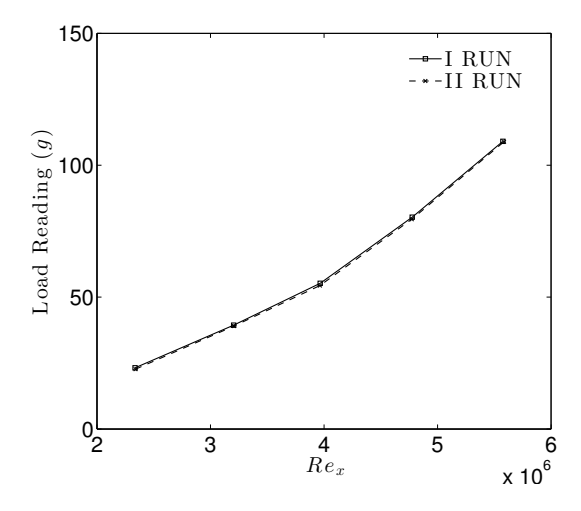


Figure 2.10: Scale reading as a function of the Reynolds number for convergent runs. Examples case LF4.

propagation error theory (Kline and McClintock, 1953), the overall uncertainty of the balance can be estimated as follows:

$$\epsilon = \sqrt{\epsilon_R^2 + \epsilon_{LC}^2 + \epsilon_{flip}^2 + \epsilon_{MA}^2} = \sqrt{3\%^2 + 2.5\%^2 + 1.5\%^2 + 2.5\%^2} \approx 5.2\%.$$
 (2.2)

This results in a overall uncertainty of approximately 5%.

# 2.7 Smooth-wall turbulent boundary layer

This thesis is concerned with comparing different types of rough-walls. However, how well these rough surfaces compare to the smooth-wall boundary layer is also of particular interest. For completeness, details and results for the smooth-wall case are reported in appendix A.

# Chapter 3

# Effect of surface morphology on aerodynamic parameters and the roughness sublayer

#### 3.1 Introduction and background

Characterising the effect of the surface roughness on the turbulence structure and hence on the bulk drag, is of vital importance for many applications. Conventionally, the study of wall-bounded flows is carried out based on the belief that the flow can be broken into two main different layers: the inner layer and the outer layer, each with its own characteristics and universal scaling laws (Clauser, 1954; Coles, 1956; Schlichting, 1979). The surface roughness is believed to directly affect the flow in the inner layer, whilst the outer layer is considered to be only indirectly influenced due to an increased skin friction (Schetz, 1993). It is well established that, compared to the law of the wall for smooth-walls, any rough surface morphology results in a downward shift in the logarithmic portion of the velocity profile. For a rough-wall boundary layer, the velocity profile in the log-region can be expressed as:

$$U^{+} = \frac{1}{\kappa} \ln \left( \frac{y - d}{y_0} \right) \equiv \frac{1}{\kappa} \ln (y - d)^{+} + B - \Delta U^{+}, \tag{3.1}$$

where  $\kappa$  is the von Kármán constant and B is the smooth-wall intercept. It is important to point out that the left-hand side expression is only valid in fully-rough conditions (i.e.  $y_0^+ > 2$ , as from Castro 2007), where viscous effects at the surface are negligible, as in the current study. The downward shift of the log-region is represented by the roughness length  $y_0$  in meteorology, or equivalently by the roughness function,  $\Delta U^+$ , in the engineering community. d is referred to as the zero-plane displacement, which

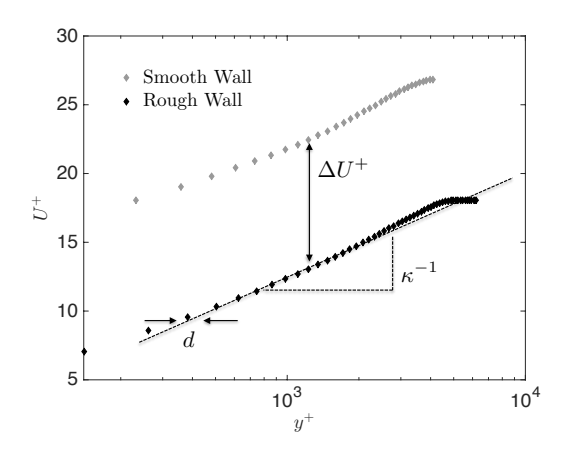


Figure 3.1: Schematic representation of the effect of surface morphology on the law of the wall.  $\Delta U^+$  is the roughness function,  $\kappa$  is the von Kármán constant and d is the zero-plane displacement. Inspired by Varano (2010).

Jackson (1981) proposed to be interpreted as the height at which the mean surface drag appears to act. This is usually a portion of the height of the roughness elements (Amir and Castro, 2011). A schematic representation of these two quantities, often referred to as "aerodynamic parameters", is given in figure 3.1. The  $^+$  superscript indicates quantities in inner scales (i.e. wall units), such that  $U^+ = U/U_\tau$  and  $y^+ = yU_\tau/\nu$ , where  $U_\tau$  is the skin friction velocity and  $\nu$  is the kinematic viscosity of the fluid. The skin friction velocity is defined as  $U_\tau = \sqrt{\tau_w/\rho}$ , where  $\tau_w$  is the total stress at the wall and  $\rho$  is the fluid density. Hence, the skin friction coefficient is given by  $C_f = 2 (U_\tau/U_\infty)^2$ . As previously discussed, a common way to characterise regularly distributed rough-walls is via two density parameters (Schlichting, 1937) - frontal and plan solidities (see figure 2.2). It is important to note that, based on this characterisation, both the aerodynamic parameters are highly dependent on the surface morphology so that, in the most general form,  $y_0 = f(\lambda_F, \lambda_P)$  and  $d = f(\lambda_F, \lambda_P)$ .

Various studies have examined the effect of surface morphology on drag, and attempted to find prediction methods for  $y_0 = f(\lambda_F, \lambda_P)$ . As previously discussed, these studies mainly classified the flow into sparse ( $\lambda_F < 0.15$ ), and dense ( $\lambda_F \ge 0.15$ ) regimes (Jimenez, 2004). Comprehensive reviews of different morphometric drag-prediction algorithms and an analysis of their accuracy can be found in Grimmond and Oke (1999), Macdonald (1998) and, more recently, in Millward-Hopkins et al. (2011) and Kanda et al. (2013). The main limitation of the above-mentioned studies is the fact that the suggested correlations  $y_0 = y_0(\lambda_F, \lambda_P)$  are calculated over a collection of data sets from disparate sources with significantly different boundary conditions and characterised by geometrically different roughness elements. Regardless, amongst the morphometric dragprediction methods, Macdonald's (1998) appears to be widely used as it incorporates a broader range of scenarios when compared to other methods (Grimmond and Oke 1999 and Millward-Hopkins et al. 2011).

Despite its limitations, Macdonald's (1998) predictions appear to be valid for a large range of surface densities, for both  $y_0$  and d. These correlations are given by

$$\frac{y_0}{h} = \left(1 - \frac{d}{h}\right) \exp\left[-\left(0.5\beta \frac{C_d}{\kappa^2} \left(1 - \frac{d}{h}\right) \lambda_F\right)^{-1/2}\right],$$

$$\frac{d}{h} = 1 + A^{-\lambda_P} \left(\lambda_P - 1\right),$$
(3.2)

where A and  $\beta$  are problem-dependent constants. It must be highlighted that Macdonald's method presents some obvious limitations. Firstly, it requires an a-priori knowledge of the drag coefficient of a single element,  $C_d$ , which is usually an unknown, especially in real urban areas characterised by complicated geometries. Secondly, the bulk drag is only considered dependent (geometrically) on frontal and plan solidities, therefore, this method does not account for situations in which  $\lambda_F$  and  $\lambda_P$  are matched, but where the element pattern is different. The importance of the roughness elements' distribution is undermined, implying that the two solidities are enough to fully characterise a rough-wall and its characteristic, which is yet to be proven. Finally, the influence of any other parameter on drag variation (i.e "street" width to block height, or similar) is completely neglected. Nevertheless, these correlations are often used during preliminary design stages. Figure 3.2(a) shows its prediction (from equation 3.2) for  $y_0$  as a function of  $\lambda_F$  and  $\lambda_P$ . Figure 3.2(b) shows its well-established empirical relationship between drag and  $\lambda_F$ , as reported in previous studies on rough-wall boundary layers (Jimenez, 2004). However, the effect of plan solidity on bulk quantities is not clear, and the effects of large roughness elements on these correlations remain unresolved.

Most previous studies that systematically explored the effect of surface morphology on drag were carried out with cubical roughness elements. These studies include both numerical and physical experiments (Cheng and Castro 2002b; Coceal and Belcher 2004; Kanda et al. 2004; Cheng et al. 2007; Hagishima et al. 2009; Santiago et al. 2008; Leonardi and Castro 2010 among various others). Open symbols in figure 3.2(a) show the cases examined in these studies. Any conclusion regarding the relationship between plan solidity and drag deduced from these studies is limited, since for cube roughness,  $\lambda_F$  is equal to  $\lambda_P$ . Similarly, any study on regular geometric staggered arrays of roughness for which the frontal and plan solidities are related by a mathematical relation (provided that there is no mutual sheltering between the elements) will lie on a similar curve to the dashed line in figure 3.2(a), but with a different slope. This means that the individual effect of one of these two parameters will remain undetected. Isolating the effect of the two solidities is only possible by following the dotted line and the dot-dashed line (or any alternative lines parallel to those), i.e., varying  $\lambda_F$  at a fixed  $\lambda_P$  and vice-versa.

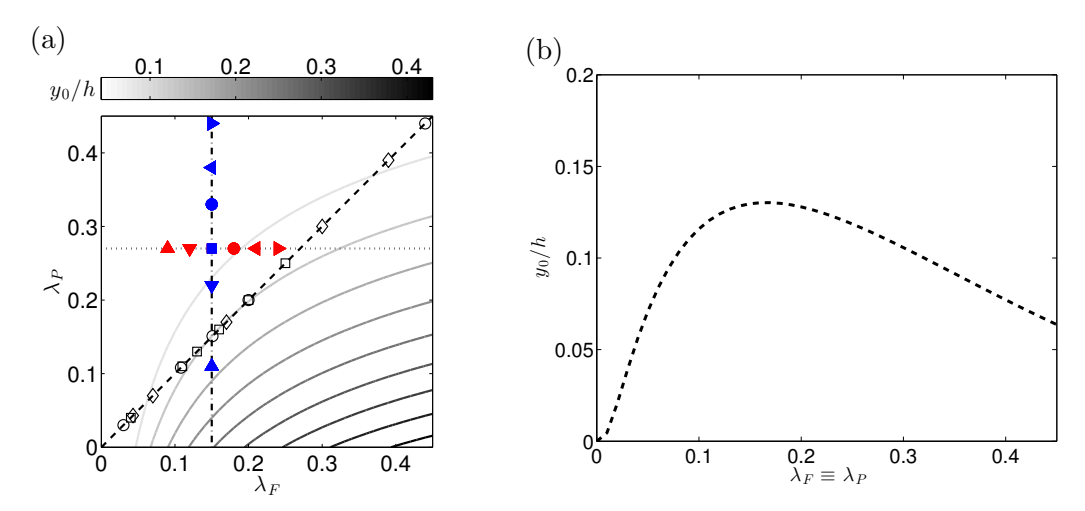


Figure 3.2: (a) Contour plot of the Macdonald's (1998) prediction of the roughness length behaviour as a function of  $\lambda_F$  and  $\lambda_P$  calculated using the expressions presented in Macdonald (1998) with  $C_d = 1.2$ ,  $\kappa = 0.41$ ,  $\beta = 1$  and A = 4.43. Colorbar shows  $y_0/h$ . Dashed line represents  $\lambda_F \equiv \lambda_P$  (cubes), dot-dashed line represents variation of  $\lambda_P$  at fixed  $\lambda_F$  and dotted line stands for variation of  $\lambda_F$  at fixed  $\lambda_P$ . Filled symbols indicate the current experiment while empty symbols indicate respectively  $\circ$  Kanda et al. (2004),  $\diamondsuit$  Hagishima et al. (2009) and  $\square$  Leonardi and Castro (2010). A cut along the dashed line in figure (a) is presented in (b).

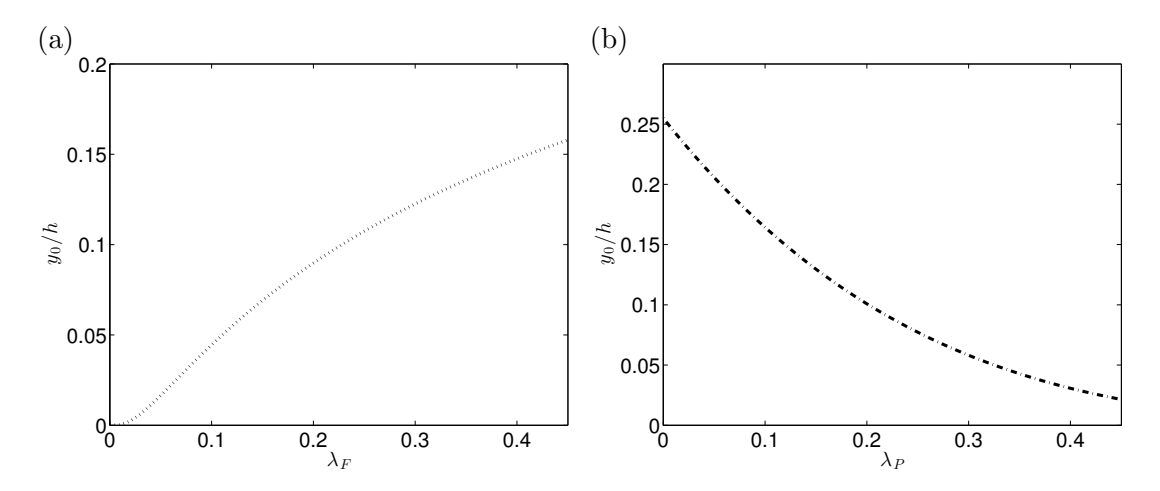


Figure 3.3: Cuts along the dotted and dot-dashed lines in figure 3.2(a). Predictions of the roughness length behaviour as a function of (a)  $\lambda_F$  at fixed  $\lambda_P$  and (b) vice versa.

These branches have not been explored before. Macdonald's (1998) predicted bulk drag behaviour for variation of  $\lambda_F$  at fixed  $\lambda_P$  (dotted line) is shown in figure 3.3(a), and similarly the behaviour for variation of  $\lambda_P$  at fixed  $\lambda_F$  (dot-dashed line) is shown in figure 3.3(b).

In this chapter, we explore the behaviour of the bulk drag along the dotted and dotdashed lines in figure 3.2(a) in turbulent boundary layers with relatively large roughness elements ( $h/\delta \approx 0.1$ ). This enables us to isolate the effects of  $\lambda_P$  and  $\lambda_F$  on the drag. The individual effects of frontal and plan solidities on the roughness sublayer region is also investigated. The entire regime of solidity (sparse to dense) is considered.

It should be emphasised that this thesis contains results only along the dotted and dotdashed lines in figure 3.2(a). These branches, although unexplored to date, only cover a small portion of the  $(\lambda_F, \lambda_P)$  plane. Therefore, the conclusion drawn herein should not be considered universal or valid for any combination of frontal and plan solidities. Moreover, although variations of frontal density are examined at fixed plan solidity (and vice versa), the effect of the two parameters can never be truly and completely decoupled as, by definition, any roughness is characterised by both a frontal and a plan blockage. The novelty of this study, however, is the fact that one solidity is varied at a time, keeping the other one fixed. This is referred to as a "decoupled effect".

#### 3.2 Indirect estimate of skin-friction

The skin friction velocity,  $U_{\tau}$ , is commonly assumed to be the average Reynolds shear stress in the log-region. In this thesis, we refer to this as the indirect method for determining skin-friction velocity. Cheng and Castro (2002b) in their experiments on different urban roughnesses (all with  $\lambda_F \equiv \lambda_P = 0.25$ ) demonstrated that an optimum estimation for the skin friction velocity can be obtained from spatially averaged Reynolds shear stress within both the roughness sublayer and the inertial sublayer. This shows that by spatially averaging over a roughness repeating unit, the logarithmic region can be extended down to the roughness sublayer. For all the morphologies examined herein, the average across the streamwise direction and over a single repetitive unit yielded, within experimental uncertainty, the same results. Cheng et al. (2007) also argued that for boundary-layer flows over staggered arrays of cubical elements, the  $\rho \overline{u'v'}$  underestimates the surface stress by some 25%. Therefore, a corrected estimate should be used, defined as (Reynolds and Castro, 2008):

$$U_{\tau} = 1.12\sqrt{-\overline{u'v'}} \Big|_{2 < y/h < 3};$$
 (3.3)

where the Reynolds shear stress is evaluated from the plateau region in the roughness sublayer (as in Flack et al. 2005 and Castro 2007). Both these above-mentioned approaches yield a  $U_{\tau}$  value that is within 5% of each other. This value is also similar to the skin friction velocity obtained by assuming it to be the maximum of the Reynolds shear stresses, as in other studies in the literature (Manes et al., 2011).

### 3.3 Determination of aerodynamic parameters

Once the skin friction velocity is calculated (either using the direct measurement from the drag-balance or the indirect estimate), a least-square-fit procedure was adopted to evaluate the zero-plane displacement, d and the roughness length,  $y_0$ . The log-layer is assumed to exist for  $1.5h \le y \le 0.2\delta$  as in Schultz and Flack (2005). The fitting procedures were carried out with  $\kappa = 0.38$  for all surfaces. This value is close to the value of  $\kappa$  suggested by Marusic et al. (2013), for high Reynolds number smooth-wall boundary layers, where  $\kappa = 0.39 \pm 0.02$ . A different choice of  $\kappa$  alters the numerical values of  $y_0$  and d but not the trends shown in the following sections. Accurate determination of both the skin friction and the aerodynamic parameters are important since they are typically used to normalise the velocity profiles. However, it should be noted that this task is not trivial. Firstly, the inertial region (i.e. log-law boundaries) must be identified (Segalini et al., 2013). Secondly, indirect estimation of the friction velocity is dependent on the choice for the von Kármán parameter (Castro, 2007; Zaunon et al., 2003; Segalini et al., 2013; Marusic et al., 2013). Thirdly, the fitting procedure is more problematic (i.e. it bears greater uncertainty) in rough-wall boundary layers than in smooth-surfaces. This is due to the fact that the location of the virtual origin, d, and the roughness function,  $\Delta U^+$ , are additional unknown (Acharya et al., 1986). Finally, the onset of the fully-rough regime is also difficult to pinpoint (Snyder and Castro, 2002).

# 3.4 Proper orthogonal decomposition

To explore the spatial characteristics and the behaviour of the flow and its dependence on wall morphology, a snapshot-based Proper Orthogonal Decomposition (POD) analysis has been carried out (Berkooz et al., 1993). This technique generates a basis for modal decomposition of ensembles of instantaneous fluctuating velocity fields and provides the most efficient way of identifying the motions which, on average, contain a majority of the turbulent kinetic energy in the flow. The POD was first introduced in turbulence analysis by Lumley (1970). Very briefly, this decomposition consists of essentially solving an eigenvalue problem. Following Pearson et al. (2013), given an ensemble of n velocity fields arranged in a column-wise matrix,  $\mathbf{U} \in \Re^{n \times p}$ , then the POD basis,  $\Phi \in \Re^{p \times n}$ , satisfies:

$$\begin{aligned} \max_{\phi} & \frac{\Phi^T \mathbf{U}}{\Phi^T \Phi} \\ \text{s.t.} & \Phi^T \Phi = \boldsymbol{I}. \end{aligned} \tag{3.4}$$

The columns of  $\Phi$  (i.e. the basis functions) are called POD modes and are identified by  $\phi_i \in \Re^p$ . These modes are obtained by solving the eigenvalue problem:

$$\mathbf{U}^T \mathbf{U} \Phi = \Lambda \Phi; \tag{3.5}$$

where  $\Lambda \in \Re^{n \times n}$  is a diagonal matrix containing the eigenvalues. Physically, Lumley (1970) pointed out that seeking  $\phi_i$  corresponds to maximising a certain function, here to be the flow energy content captured by each mode.

The energy contribution of the singular value across the modes, hence its shape, depends on the local spatial resolution of the data set, as discussed in Pearson et al. (2013) and Placidi and Ganapathisubramani (2015a). This is because the energy content of each  $\phi_i$  mode depends on the smallest resolved scale in the flow. As previously discussed, the global resolution of the current 2D data set ranges in between 30 to 40 wall-units, resulting in a variation of the Kármán number in the range of  $Re_{\tau} \approx 4900 - 7500$ . Therefore, a low-pass Gaussian filter, designed to match the local resolution at  $l_{2D}^+ = 45$  is applied. Moreover, the FOV across the different cases is also matched to allow meaningful comparisons. The results presented in the following sections were obtained performing the POD calculation over the combined (u', v') data.

#### 3.5 Results and discussion

Section 3.5.1 shows the effect of the surface morphology on the aerodynamic parameters. Sections 3.5.2 and 3.5.3 examine the effect of the wall morphology on the depth of the roughness sublayer. Finally,  $\S$  3.4 examines the global spatial structure of the flow over different types of roughness. The turbulent kinetic energy content at different flow scales is also investigated via proper orthogonal decomposition.

#### 3.5.1 Effect of surface morphology on aerodynamic parameters

Before examining the effect of the surface morphologies on aerodynamic parameters, it is useful to determine if these surfaces are fully-rough, in order to ensure that the results presented herein are solely due to the different roughness morphologies, rather than the product of a change in Reynolds number (i.e. viscous effects). There is general consensus in the literature that fully-rough conditions are attained when  $y_0^+ > 2$  (Castro 2007) or  $h_s^+ > 70$  (Flack et al. 2005). Here  $h_s$  is the equivalent sand-grain roughness as in Nikuradse (1933). Recent findings have cast doubt on these limits and pointed out that, depending on the surface morphology, values up to  $y_0^+ > 10$  might be necessary to guarantee the fully-rough conditions (Castro et al., 2013). In order to assess if the surfaces examined herein are in the fully-rough regime, the friction coefficient was measured with the drag-balance at different inflow velocities, and hence different Reynolds numbers. A velocity range between 11.5 to  $20 \ m/s$  was considered and the results are presented in figure 3.4(a) & (b) for the frontal and plan solidity cases respectively. It

is clear that the variation in the measured friction coefficient at different velocities is within the limits of uncertainty. It follows that, within the measurement uncertainty, all cases in both  $\lambda_F$  and  $\lambda_P$  are to be considered in the fully-rough regime, i.e. Reynolds number independent. Hence, if differences are observed in the aerodynamic parameters, these are purely an effect of surface morphology.

The skin friction results are discussed before the aerodynamic parameters are investigated. The validity of the indirect method for the skin friction determination can be established by comparing the results with the drag-balance measurements. The skin friction coefficient,  $C_f$ , as a function of the normalised momentum thickness,  $\theta/y_0$ , is shown in figure 3.5. Here, the momentum thickness is defined as  $\theta = \int_0^\delta \frac{U}{U_e} \left(1 - \frac{U}{U_e}\right) dy$ , whilst the displacement thickness as  $\delta^* = \int_0^\delta \left(1 - \frac{U}{U_e}\right) dy$ ;  $\delta$  is the boundary layer thickness and  $U_e$  is the corresponding edge velocity at  $y = \delta$ . The boundary layer thickness is defined as that distance from the wall where the velocity is the 99 % of the free stream velocity,  $U_{\infty}$ . The boundary layer parameters are, for each case, calculated by appropriate integrations of the wall-normal velocity profiles. In particular, following Castro (2007), the near-wall region in between  $y - d = y_0$  and the first measurement point ( $\approx 1.5h$ ) is modelled using an extension to the log-law.

Figure 3.5(a) shows results for the indirect method (via equation 3.3) and figure 3.5(b) using the direct method (i.e. floating-element drag-balance). This type of plot was first proposed by Castro (2007) and allow us to estimate if the current results agree with previous findings. Most of the results from rough-wall studies have been found to scatter around the two curves (for different values of wake parameter  $\Pi$ ) shown in figure 3.5 (Castro, 2007). It can be seen that our data (using both methods) are consistent with previous data in the literature. The indirect measurements results (via equation 3.3) compare well with the direct measurements (within 10%) given the uncertainty in determination of the skin-friction velocity (Acharya et al., 1986) and the log-law boundaries used to determine the roughness length (Segalini et al., 2013).

More quantitative information on the skin friction behaviour can be gathered plotting  $U_{\tau}$  across one spanwise repeated unit (0 < z/W < 1), where W is the spanwise unit extent) for the direct and indirect skin friction determination. This is shown in figure 3.6 for both frontal and plan solidity cases. The skin friction measured via floating-element drag-balance is plotted in grey and a 10% error bar is reported. The results obtained by applying equation 3.3 to the 2D and 3D data sets are also plotted (filled symbols) for comparison. It is comforting to see that, for all the cases, both PIV results tie in well (within 10% difference) with direct measurement. Although 10% difference might seem quite a significant number, the scatter found herein is of the same order of magnitude commonly excepted (Flack et al., 2005; Schultz and Flack, 2005; Volino et al., 2007; Wu and Christensen, 2007; Castro, 2007; Volino et al., 2009; Amir and Castro, 2011). Therefore, from this point on, the direct measure of the skin friction velocity (i.e. dragbalance) will be used to normalise the turbulence statistics. Relevant boundary-layer

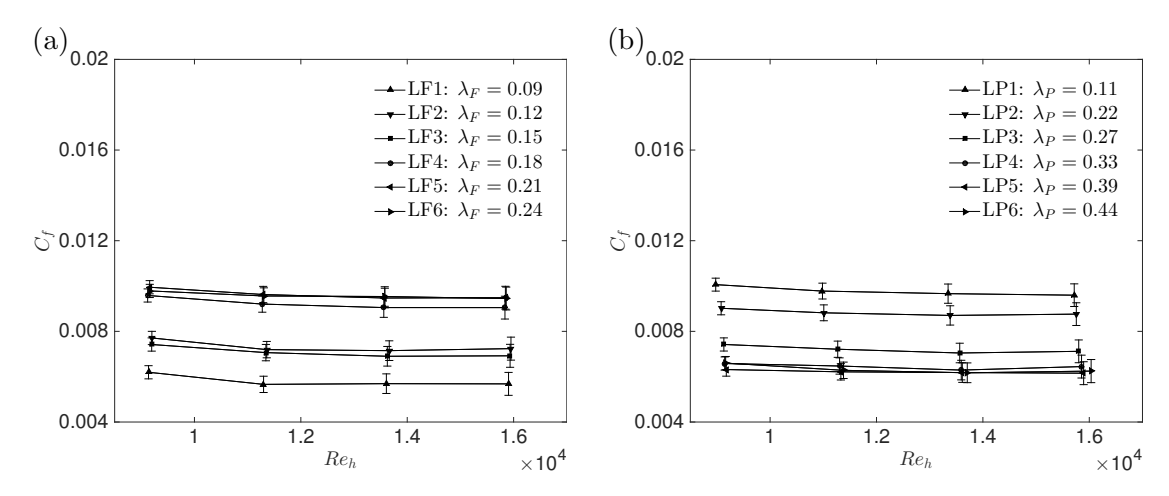


Figure 3.4: Skin friction coefficient,  $C_f$ , as a function of the Reynolds number, for (a)  $\lambda_F$  ( $\lambda_P = const = 0.27$ ) and (b)  $\lambda_P$  ( $\lambda_F = const = 0.15$ ).

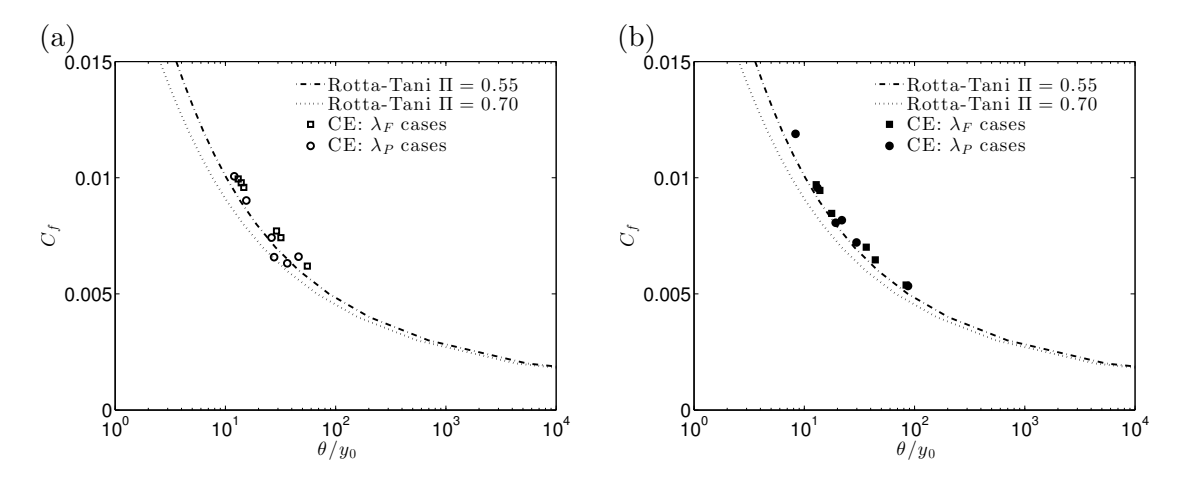


Figure 3.5: Variation of  $C_f$  as a function of  $\theta/y_0$  for (a) indirect method and (b) direct measurement. Dot and dashed-dotted curves refer to the standard two-parameter family results with wake strength of  $\Pi=0.55$  and 0.7. Current experiment (CE) refers to values obtained by floating-element drag-balance (solid marks) and via the means of equation 3.3 (empty marks). The roughness length,  $y_0$ , is calculated via a least-square-fit procedure for  $1.5h < y < 0.2\delta$ .

characteristics of all the cases are given in table 3.1. It can be seen from the table, that all cases have  $y_0^+ \ge 10$  and hence we conform to the revised estimates for fully-rough conditions (Castro et al., 2013).

Finally, having discussed the qualities used for normalisation, the focus can be shifted to discuss the velocity profiles and the aerodynamic parameters. Figure 3.7(a) shows the mean velocity profiles in inner scales for the different cases of  $\lambda_F$  at fixed  $\lambda_P$ . It can be seen that, compared to a smooth-wall case (equation 3.1 with d=0, B=5 and  $\Delta U^+=0$ ), the roughness is responsible for a uniform downward shift of the log-region, as expected. The plain baseboard case, referring to the wind tunnel floor being covered only with baseboard but no bricks, is also reported for comparison. It shows that the presence of the blocks (case LF1 to LF6) is indeed responsible for generating a further

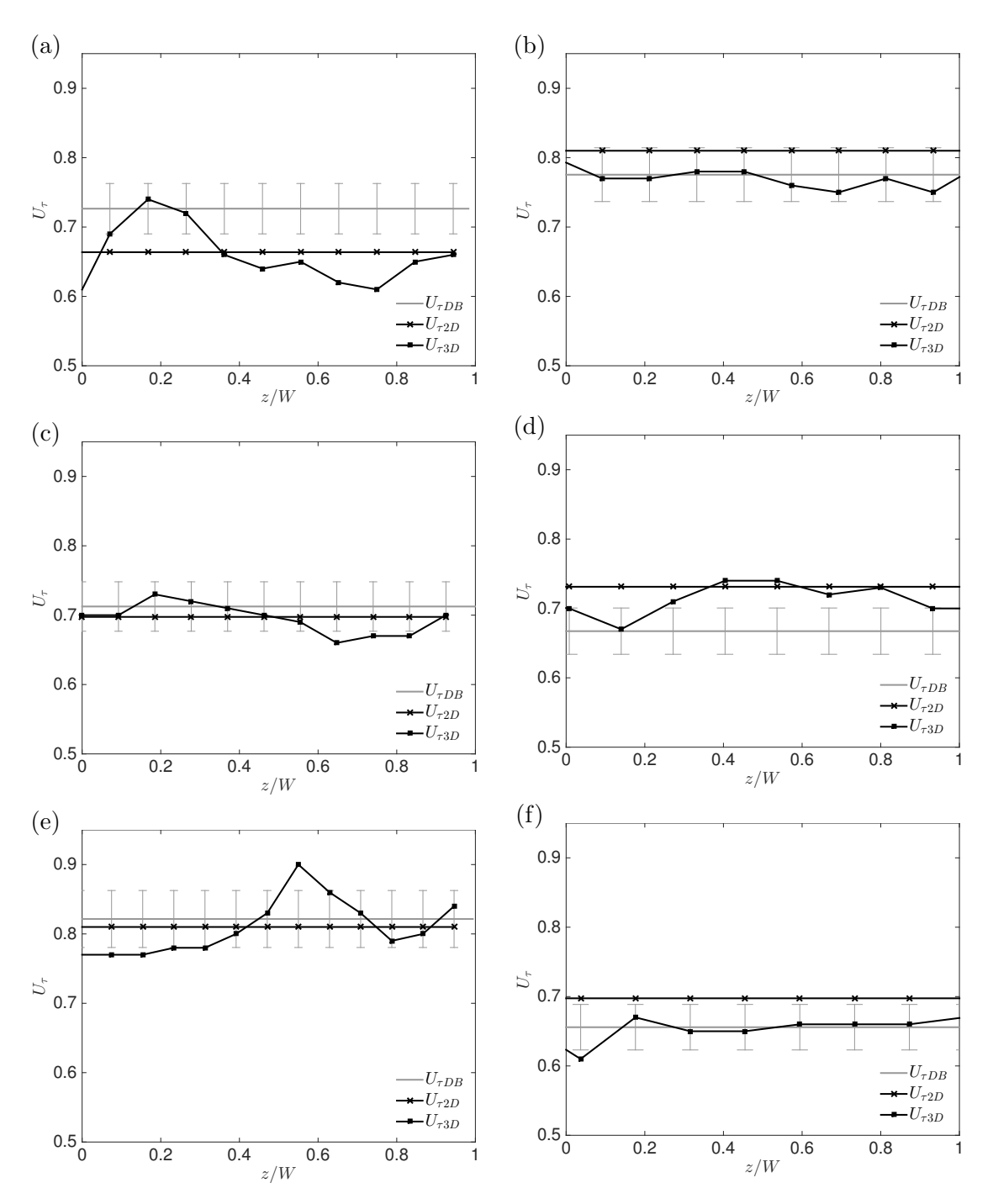


Figure 3.6: Skin friction measurements, for sparse (top), medium-packed (centre) and dense regimes (bottom) as a function of  $\lambda_F$  ( $\lambda_P = const = 0.27$ ) on the left and  $\lambda_P$  ( $\lambda_F = const = 0.15$ ) on the right. Drag-balance results are compared with 2D and 3D indirect skin friction estimation (i.e. equation 3.3). A 10% error bar on the drag-balance data is included. Every five vectors is used for clarity.

Data set	$\lambda_F$	$\lambda_P$	$\delta^*(mm)$	$\theta(mm)$	d(mm)	Ue(m/s)	$U_{\tau}(m/s)$	$Re_{\tau}$	$\delta/h$	$\delta/h_s$	$y_0^+$
LF1	0.09	0.27	19	13	11.2	11.57	0.65	5110	10	69	10
LF2	0.12	0.27	27	16	6.7	11.61	0.73	6313	11	31	28
LF3	0.15	0.27	26	16	9.1	11.65	0.71	6140	11	36	24
LF4	0.18	0.27	28	16	8.5	11.53	0.80	6919	11	16	61
LF5	0.21	0.27	32	18	7.0	11.63	0.82	7092	11	13	77
LF6	0.24	0.27	31	17	8.3	11.64	0.81	7005	11	14	69
LP1	0.15	0.11	35	19	5.7	11.54	0.81	7642	12	12	89
LP2	0.15	0.22	30	17	7.7	11.57	0.78	6746	11	16	60
LP3	0.15	0.27	28	16	11.4	11.58	0.71	6140	11	30	29
LP4	0.15	0.33	27	16	10.4	11.50	0.67	5794	11	31	26
LP5	0.15	0.39	24	15	11.1	11.49	0.66	5189	10	39	18
LP6	0.15	0.44	21	13	11.1	11.42	0.67	5268	10	54	14

Table 3.1: Relevant experimental parameters for frontal and plan solidities variation. The aerodynamic parameters are calculated through a log-law fit with  $\kappa=0.38$  in the range  $1.5h \leq y \leq 0.2\delta$ . Ue values reported herein are relative to the PIV results, however, the imposed Ue for floating-element drag-balance tests were set within a 1.5% difference.

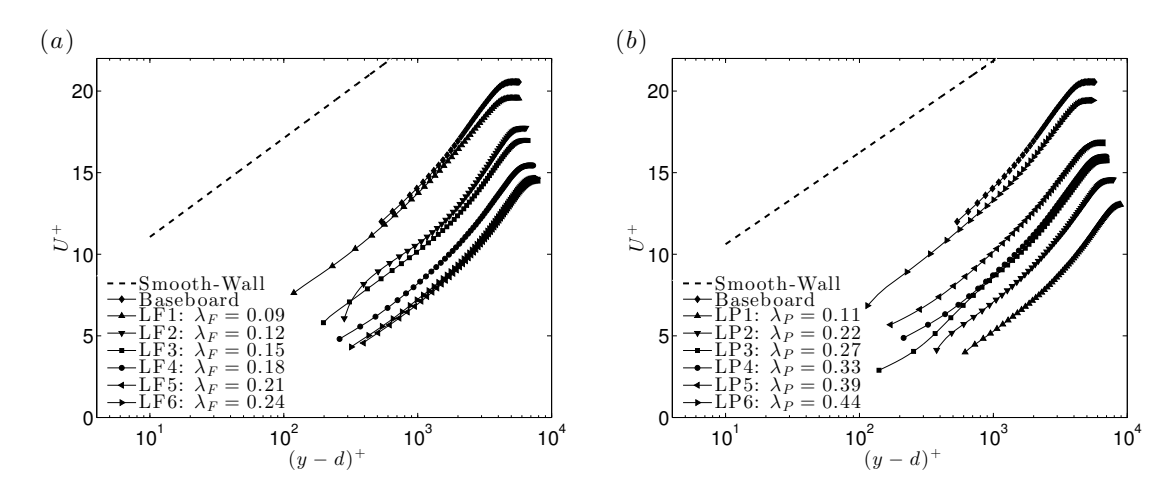


Figure 3.7: Mean velocity profiles in inner scales as a function of (a)  $\lambda_F$  ( $\lambda_P = const = 0.27$ ) and (b)  $\lambda_P$  ( $\lambda_F = const = 0.15$ ). Markers are spaced every five vectors for clarity.

shift of the log-law compared to the baseboard case. Figure 3.7(b) shows the behaviour of the mean velocity profiles for the different  $\lambda_P$  cases, where a similar downward shift of the log-law region is observed. To further quantify the effect of the surface morphology on the bulk drag, the roughness length can be calculated.

Figure 3.8 shows the normalised roughness length,  $y_0/h$ , as a function of both solidities. It is shown in figures 3.8(a) & (b) that the behaviour of roughness length as a function of frontal and plan solidity is drastically different. Figure 3.8(a) shows that the roughness length (which is related to the total drag) increases in the sparse regime, and indicates a marginal decrease after the peak for increased values of frontal solidity (as in Leonardi et al. (2003) and Leonardi and Castro (2010)). The bulk drag seems to reach a peak for  $\lambda_F = 0.21$  as opposed to  $\lambda_P \equiv \lambda_F \approx 0.15$  as in Hagishima et al. (2009), Leonardi and

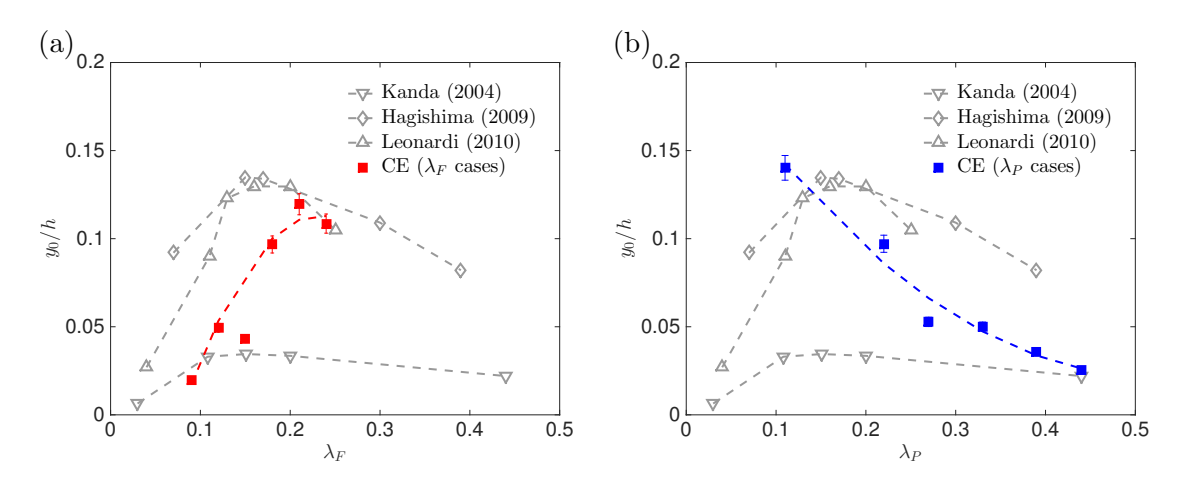


Figure 3.8: Normalised roughness length,  $y_0/h$ , as a function of (a)  $\lambda_F$  and (b)  $\lambda_P$ . Current experiment refers to values obtained by log-law least-square fit within  $1.5h < y < 0.2\delta$ .

Castro (2010) and Kanda et al. (2004) or  $\lambda_P \equiv \lambda_F \approx 0.16$  as in Santiago et al. (2008) and Coceal and Belcher (2004). These differences are perhaps not surprising giving the high uncertainty in the fitting procedure, which results in the visible scatter of the data for different studies in figure 3.8(a) even when values of similar frontal and plan solidity are considered. It must also be stressed that all the previous studies used cube roughness elements, for which  $\lambda_F \equiv \lambda_P$  (therefore they all lay on the dashed line in figure 3.2(a)), while in the current experiment the plan solidity has been kept constant. Additionally, the compared studies also have different  $h/\delta$  values. Finally, given that the current data set is a collection of discrete points, the reported peak at  $\lambda_F = 0.21$  only implies that the effective peak value should be located somewhere in the range  $\lambda_F = 0.18 - 0.24$ , which is consistent with previous findings. However, it is important to notice that the existence of this peak in the bulk drag is in disagreement with Macdonald's prediction, which prescribes a monotonic increase of the drag as the element's frontal density increases (see figure 3.3(a)). As previously emphasised, in the current experiment the influences of frontal and plan solidity have been decoupled keeping one of the two parameters fixed at a time. The behaviour of the bulk drag with plan solidity is shown in figure 3.8(b), and it reveals a completely different feature. The roughness length is found to monotonically decrease, as the plan density increases. It is not possible to compare this behaviour with previous studies (for which  $\lambda_F \equiv \lambda_P$ ), since in that case changes in one solidity parameter result in modifying the other one. However, the behaviour of  $y_0$  as a function of  $\lambda_P$  is in accordance with Macdonald's prediction in figure 3.3(b).

It is expected that the roughness length should increase as the elements' frontal density increases, reaching a peak beyond which it should decrease for further increase in roughness density. This prediction is verified in the case of frontal density variation, which shows a peak for  $\lambda_F = 0.21$ . An increase in frontal solidity (cases LF1 to LF6) increases the frontal blockage, reducing the free-space available for the flow, forcing it up and over the elements, and hence resulting in a drag increase. However, for plan solidity

cases, the bulk drag monotonically decreases with increasing  $\lambda_P$ . This could be due to the fact that a progressive increase of the plan area at fixed  $\lambda_F$ , and hence at fixed unit wall-parallel area (as in cases LP1 to LP6 in figure 3.2(b)), results in a transition from "k-type" to "d-type" roughness. This progressive transition results in a decrease in drag with increasing plan solidity. It must be noted that we use the "k-type" or "d-type" terms to relate to the flow mechanisms that are associated with these classifications. The flow behaviour between the roughness elements, following Grimmond and Oke (1999), depends upon the ratio between the roughness height, h, and the average streamwise spacing between elements,  $W_c$  (the width of the channel between subsequent elements). An "isolated flow regime" is expected when  $h/W_c < 0.3$ , a "wake interference regime" for  $0.3 < h/W_c < 0.65$  and a "skimming flow regime" for  $h/W_c > 0.65$ . It is easy to verify from figure 2.5(b) that, while the average spacing is almost constant for variations in  $\lambda_F$ , the same is not true for the  $\lambda_F$  cases. In the latter this spacing decreases from case LP1 to LP6. This is due to the necessity of keeping the unit wall-parallel area fixed, which enforces changes in plan solidity at fixed  $\lambda_F$ . Therefore cases LF1 to LF6 should all belong to the wake interference regime  $(h/W_c \approx 0.39)$ , while a transition between the isolated flow regime toward the skimming regimes is to be expected between cases LP1 and LP6  $(h/W_c$  ranging between 0.27 - 0.55).

It is certainly possible, under some circumstances, that an increase in frontal blockage can be in competition with the transition from "k-type" to "d-type" (i.e. changes in  $h/W_c$ ). In those cases, the bulk drag of different surfaces with different  $\lambda_F$  and  $\lambda_P$  can be a constant. Alternately, depending on the pattern of the repeating unit, the drag could even decrease with increasing  $\lambda_P$ . A sketch that describes the scenarios discussed above is shown in figures 3.10 and 3.11 respectively. Figures 3.10(a) to (c) show a progressive increase in  $\lambda_F$ , which is accompanied by a higher spanwise blockage in the flow. This results in the flow raising upward toward the top of the elements and over them, resulting in an increase in the bulk drag. Figure 3.11(d) to (f) shows a representation of  $\lambda_P$  change and the transition mechanism. Elements in subsequent repeated units becoming closer to each other, resulting in the formation of stable vortices in the grooves between the bricks. This ensures that the eddy shedding from the elements into the flow, is progressively more negligible. These stable recirculation vortices are effectively isolating the elements from the flow, which rides almost undisturbed over the canopy, resulting in a reduction of the bulk drag.

In addition to the roughness length, the values of the zero-plane displacement, d, as a function of frontal and plan solidities have also been calculated, and are shown in figures 3.9(a) & (b) respectively. Since a value of d > h would be physically meaningless (Jackson 1976), these values are forced to be d = h as in Iyengar and Farell (2001). It is clearly visible in figure 3.9(b) that the virtual origin increases with an increase in plan solidity till it approaches its asymptote for d = h. This behaviour is qualitatively consistent with previous studies, which have shown that the zero-plane displacement tends to assume larger values (i.e. d tends to h) as the plan solidity increases (Kanda et al.

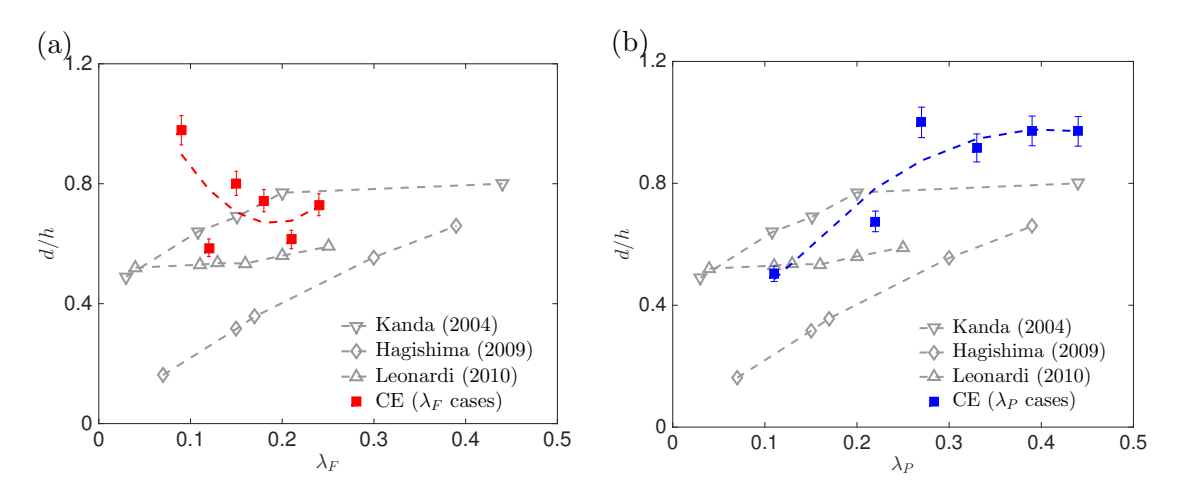


Figure 3.9: Normalised zero-plane displacement, d/h, as a function of (a)  $\lambda_F$  and (b)  $\lambda_P$ . Current experiment refers to values obtained by log-law least-square fit within  $1.5h < y < 0.2\delta$ .

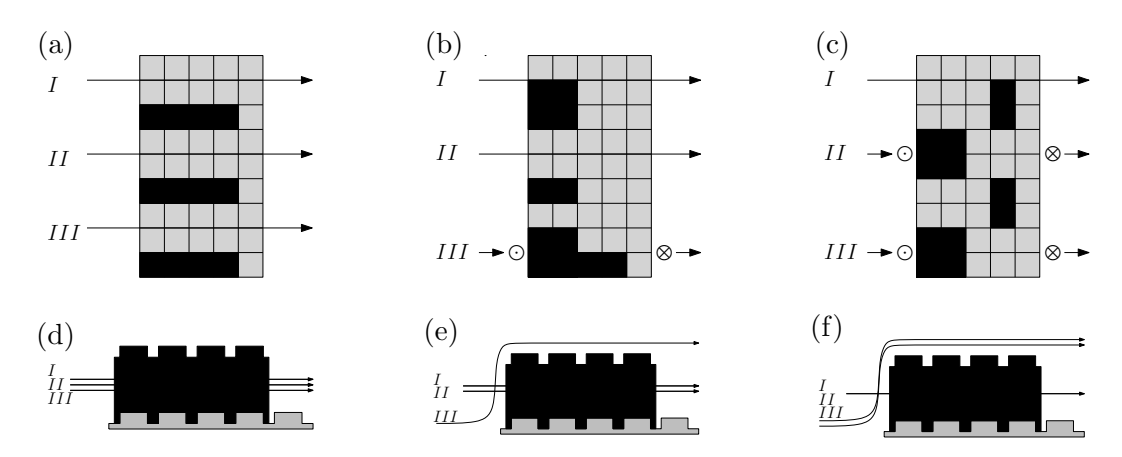


Figure 3.10: Different elements' field patterns and associated flow regimes for increasing  $\lambda_P$ . LF1 (left), LF3 (centre) and LF5 (right). Symbols  $\odot$  stand for arrows pointing towards the reader and symbolise path lines of particles that deviate upward, symbols  $\otimes$  stand for path lines of particles that deviate downward. Flow is left to right.

2004; Hagishima et al. 2009; Leonardi and Castro 2010). This trend is also consistent with the predictions from Macdonald (1998). However, an opposite trend is found in figure 3.9(a) for a frontal solidity variation, where the virtual origin decreases as  $\lambda_F$  increases. It must be noted that the trends followed by previous studies do not capture the conditions of the present experiment - the data was obtained over cubical array roughness and hence the behaviour with  $\lambda_F$  is exactly the same as for  $\lambda_P$ . Nonetheless, it must pointed out that the trend of the virtual origin variation, as a function of frontal solidity, conflicts with previous observations.

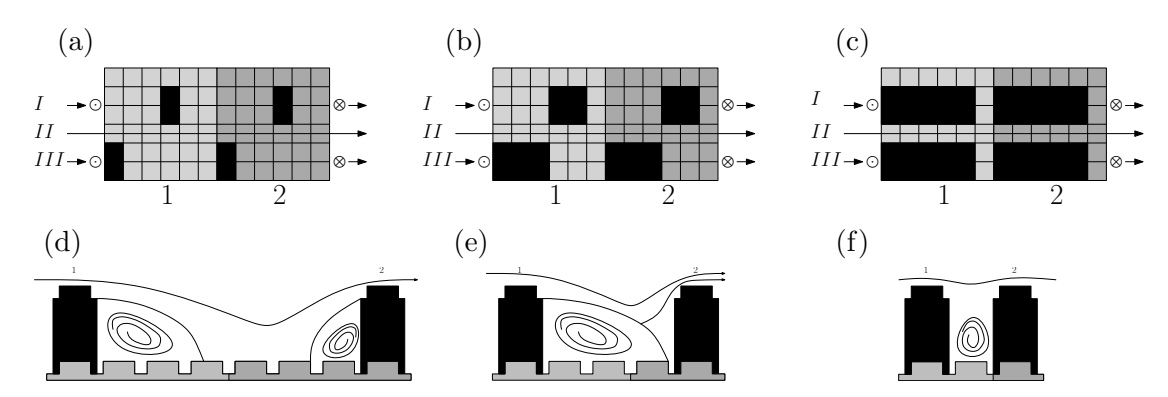


Figure 3.11: Different elements' field patterns and associated flow regimes for increasing  $\lambda_P$ . LP1 (left), LP3 (centre) and LP6 (right). Symbols  $\odot$  stand for arrows pointing towards the reader and symbolise path lines of particles that deviate upward, symbols  $\otimes$  stand for path lines of particles that deviate downward. Flow is left to right. Light and dark grey areas in (a), (b) and (c) indicate subsequent elements' repetitive units.

#### 3.5.2 Effect of surface morphology on the depth of the RSL

Given the high relative roughness height  $(h/\delta \approx 0.1)$ , flow heterogeneity along the spanwise direction is to be expected, at least within the roughness sublayer. This region has usually been identified to extend up to five roughness heights (Cheng and Castro, 2002a; Flack et al., 2007). To investigate the flow heterogeneity, results from stereoscopic PIV measurements in the wall-normal-spanwise (y, z) plane are presented. Contour plots of mean streamwise velocity are shown in figure 3.12 for both  $\lambda_F$  and  $\lambda_P$  cases on the left and right column, respectively. The extent of the field of view has been cropped so that two to three entire repeated units are contained in the presented graphs, hence allowing the effect of the edges of the single unit to be taken into account. To facilitate the interpretation of the figures, the bricks locations are also reported in the figure. Three/four bricks combined represent one repeated unit for the  $\lambda_F$  cases, whilst only two bricks combine to form the  $\lambda_P$  cases (as in figure 2.5(b)), keeping the overall size of the FOV roughly the same. Full black bricks stand for elements in the measurement plane, whilst dashed lines represent bricks out of the measurement plane, yet in the same repeated unit. For the frontal solidity cases (on the left), the mean flow distortion due to the elements' field is clearly visible for low values of y/h. This effect is much greater for the  $\lambda_F$  cases than for the  $\lambda_P$  cases (on the right). For all cases, the contour lines appear reasonably flat farther away from the crest of the roughness elements, suggesting a localised effect of the wall morphology. Moreover, very little differences in mean streamwise velocity across the span are found above 5h in height, which is therefore suggested to be the upper edge of the roughness sublayer.

To further examine the depth of the Roughness SubLayer (RSL), it is necessary to look at the Reynolds shear stress characteristics. In particular, following the literature (Raupach et al., 1991; Cheng et al., 2007; Cheng and Castro, 2002b), the RSL can

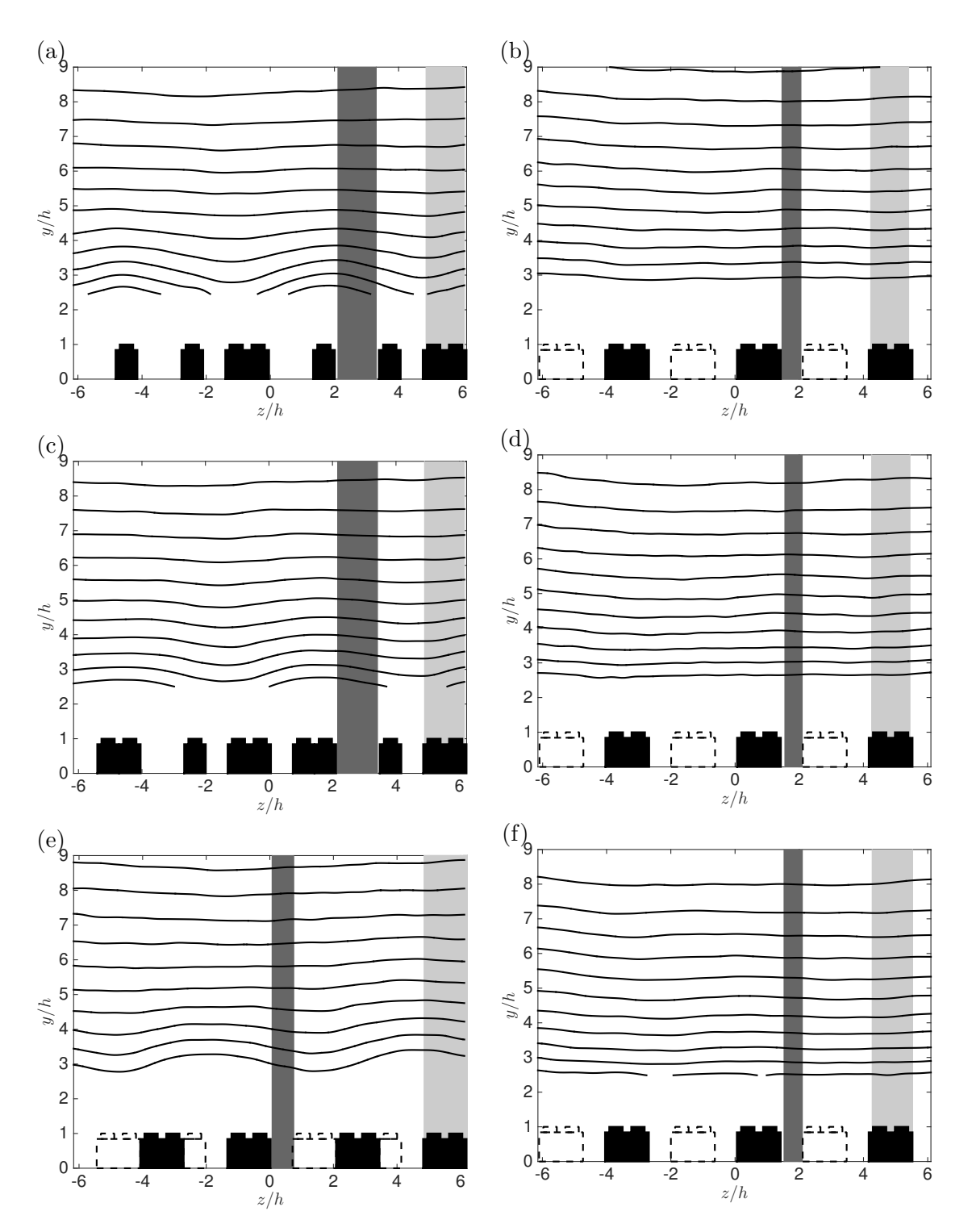


Figure 3.12: Mean streamwise velocity contours, U, in the (y,z) plane for sparse (top), medium-packed (centre) and dense regimes (bottom) as a function of  $\lambda_F$  ( $\lambda_P = const = 0.27$ ) on the left and  $\lambda_P$  ( $\lambda_F = const = 0.15$ ) on the right. Lowest contour level  $U/U_e = 0.5$ , contour spacing of 0.05. Bricks in the measurement plane are represented in full black, whilst bricks out of the measurement plane (in the same repeated unit) are identified by dashed lines. The mean flow is into the page. Dark and light grey areas are discussed in § 3.5.3.

be defined as where the spatially-spanwise-averaged wall-normal profiles converge (i.e.  $\partial (\overline{u'v'})/\partial z < 10\%$ ). Additionally, the Inertial SubLayer (ISL) can be taken to be the region where the vertical variation of the Reynolds shear stresses is below a certain threshold (here  $\partial (u'v')/\partial y < 5\%$ ). Figure 3.13 shows the depth of the above-mentioned regions within the boundary layer, for frontal and plan solidity variations on the left and right column, respectively. Grey solid marks indicate profiles along the spanwise direction across the entire FOV, which included more than one complete repeated unit. In all these graphs, the roughness height is defined from the bottom of the legoboard (i.e. the actual wall y=0). The height of the roughness elements is marked by a dashed black line and it is constant. For all cases, the extent of the RSL is found to be confined to  $\approx 5h$  which is consistent with previous findings (Flack et al., 2007). Moreover, for the frontal solidity cases ((a), (c)) and (e) the RSL seems to reach a minimum, to then increase again as the  $\lambda_F$  increases. Therefore, the extent of this region follows a reverse trend when compared to that of the bulk drag behaviour (in figure 3.8(a)). It seems that an increase in drag results in a decrease of the RSL depth and vice-versa. The same trend is found for the plan solidity cases (b), (d) and (f) where the extent of the RSL seems to increase with the solidity, whilst the drag was found to decrease (see figure 3.8(b)). It is important to note that, despite the fact that substantial differences can arise in dependency of the threshold used to define these regions, the trends across cases were found to be unaffected by the threshold's magnitude.

#### 3.5.3 Street and building profiles

Given the local character of the flow field in the near-canopy layer, as just discussed, it is interesting and important to estimate whether these differences across cases are confined to the RSL or if they extend to the outer layer. Figure 3.14 shows the streamwise velocity profiles across one complete spanwise repeated unit for both  $\lambda_F$  and  $\lambda_P$  cases (on the left and right column respectively). Each spanwise location vector is plotted in solid grey line. It is easy to see that, although differences across profiles are present in the near-wall region, the flow is self-similar in the outer region, for all cases. Significant differences within the RSL are particularly visible for the  $\lambda_F$  cases. These present much more pronounced variability across the entire range of solidity when compared to the plan variation, in accordance with findings in figure 3.13. When discussing the mean velocity profiles in figure 3.12, light and dark grey areas were highlighted. These represent profiles above "streets" and "buildings". The term "street" identifies spanwise locations above the channels in between the roughness elements whilst "building" is used for locations above the bricks. The spawise-averaged mean values across these light and dark shaded areas in figure 3.12 are also plotted in figure 3.14 in solid and dashed black lines respectively. It is important to note that the building and street profiles show fairly small differences in the outer layer. This is not only a proof of the self-similar character of the flow but also it means that these different locations generate similar

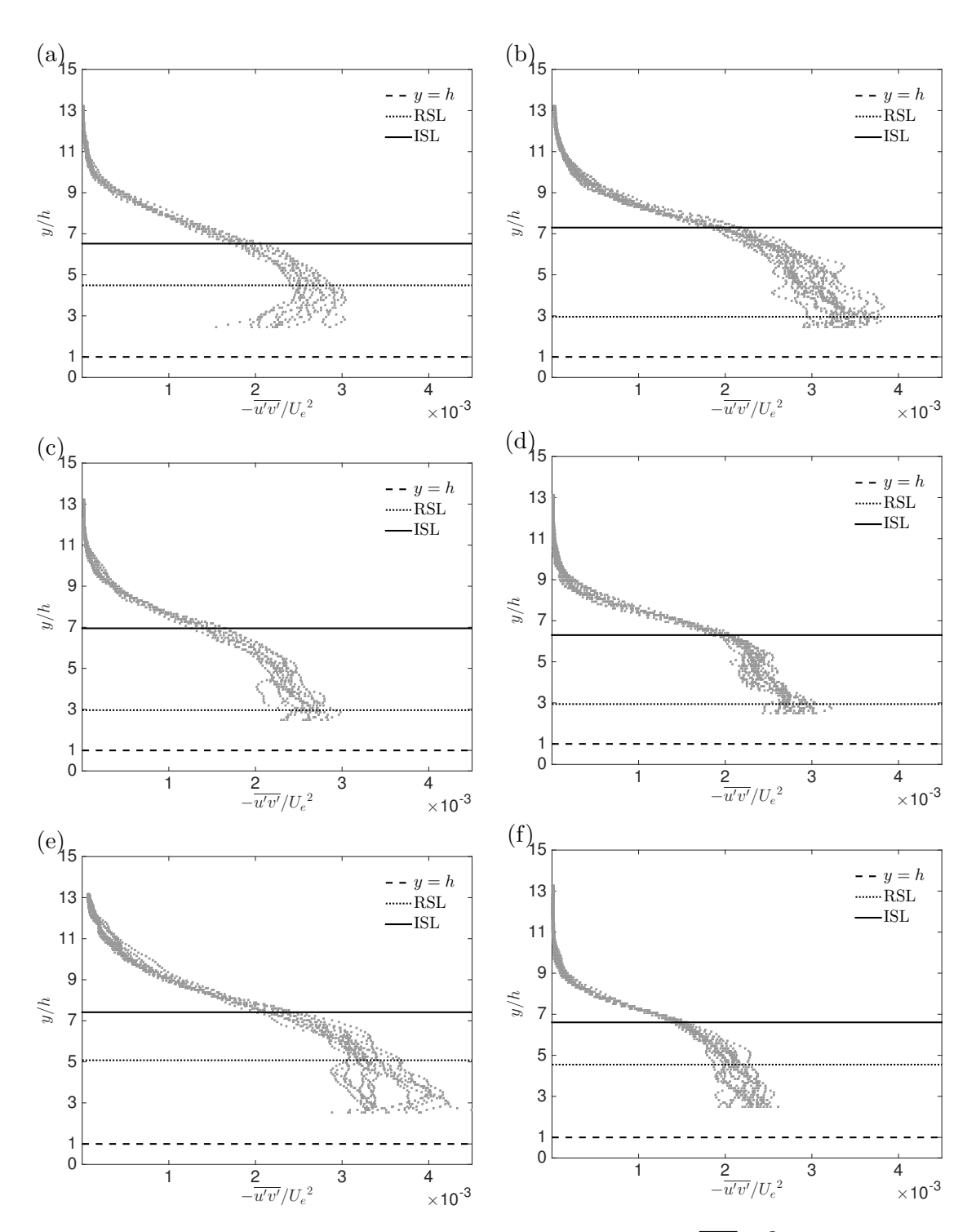


Figure 3.13: Normalised Reynolds shear stress profiles,  $-\overline{u'v'}/U_e^2$ , for sparse (top), medium-packed (centre) and dense regimes (bottom) as a function of  $\lambda_F$  ( $\lambda_P = const = 0.27$ ) on the left and  $\lambda_P$  ( $\lambda_F = const = 0.15$ ) on the right. Grey solid symbols represent the shear stress data (only one in every five vectors is shown for clarity), dashed black line shows y = h (canopy layer) whilst dotted and solid black lines represent the extent of the RSL and ISL respectively.

skin friction values. This is true across the entire wall-normal range for the  $\lambda_P$  cases, whilst for frontal solidity cases, it only holds in the outer region, where the flow gains homogeneity.

It is worth noting that recent studies (Mejia-Alvarez and Christensen, 2013; Barros and Christensen, 2014) have experimentally shown that mean flow heterogeneity exists in the spanwise-wall-normal plane of rough-wall turbulent boundary layers, particularly over a complex roughness which exhibited large-scale streamwise-elongated patches of elevated height. This heterogeneity extend outside the RSL all the way to the freestream. This phenomenon was reported to be due to the presence of spanwise-wall-normal mean secondary flow in the form of mean streamwise vorticity. This is associated with counterrotating boundary layer-scale circulations (Barros and Christensen, 2014). The latter induces regions of high and low-momentum (High-Momentum Pathways (HMPs) and Low-Momentum Pathways (LMPs) respectively). Such patterns are also in agreement with the behaviour found for flow over regular cubical roughness (Reynolds et al., 2007) and converging-diverging riblet-type surfaces (Nugroho et al., 2013). The mean-flow heterogeneity, in both cases, was here found to correspond to the periodic spanwise roughness spacing. However, although some of the cases examined herein resemble Barros and Christensen's (2014) geometry (in particular case LP6), the current investigation found no trace of this heterogeneity in the freestream. This is in disagreement with the aforementioned studies and it is perhaps due to the fact that the spanwise spacing between elements herein is not significant enough to induce this characteristic behaviour. Further exploration of this aspect is outside the scope of this work.

#### 3.5.4 Effect of surface morphology on the structure of the RSL

To further investigate the effect of the surface morphology in the near-canopy (or nearwall) layer, a POD analysis can be carried out only focusing on the roughness sublayer. As shown in the previous sections, this region appears to be where the roughness effect is confined. For this purpose, the POD analysis was carried out, where the FOV was restricted to the roughness sublayer:  $-0.6\delta < x < 0.6\delta$  in the streamwise and  $1.5h < 0.6\delta$ y < 5h in the wall-normal direction. The chosen vertical limit is based on the consensus in literature as to the extent of the roughness sublayer  $(y/h \approx 3-5)$  as in Flack et al. (2007)). Figure 3.15 show the result of this procedure for the frontal solidity cases. The top row, (a) to (d), shows results for the sparse regime (i.e. LF2) while the bottom row, (e) to (h), shows similar plots in the dense regime (i.e. LF5). The mode shapes appear to be qualitatively the same in these "near-canopy" fields. The only difference between the two regimes is that modes 3 and 4 switch their order between sparse and dense regimes. Mode 4 in the sparse regime seems to correspond to mode 3 in the dense, and vice-versa. This suggests that the relative energy content in mode 3 compared to mode 4, is higher in one case and is lower in the other. The mode number where this change in mode shape occurs is named the "cut-off" mode and can be taken to represent the breakdown

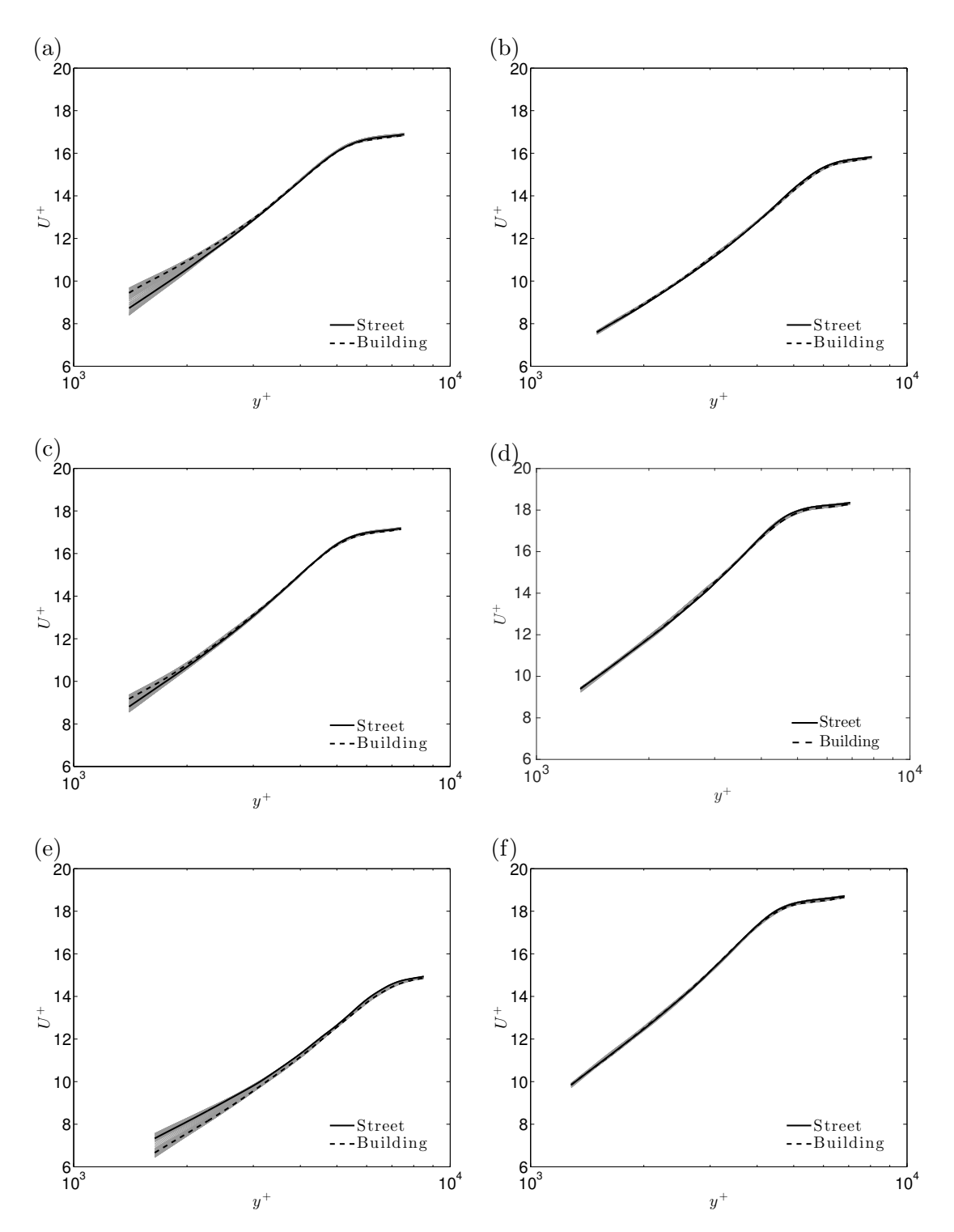


Figure 3.14: Building and street streamwise mean velocity profiles, for sparse (top), medium-packed (centre) and dense regimes (bottom) as a function of  $\lambda_F$  ( $\lambda_P = const = 0.27$ ) on the left and  $\lambda_P$  ( $\lambda_F = const = 0.15$ ) on the right. Grey lines indicate different spanwise locations.

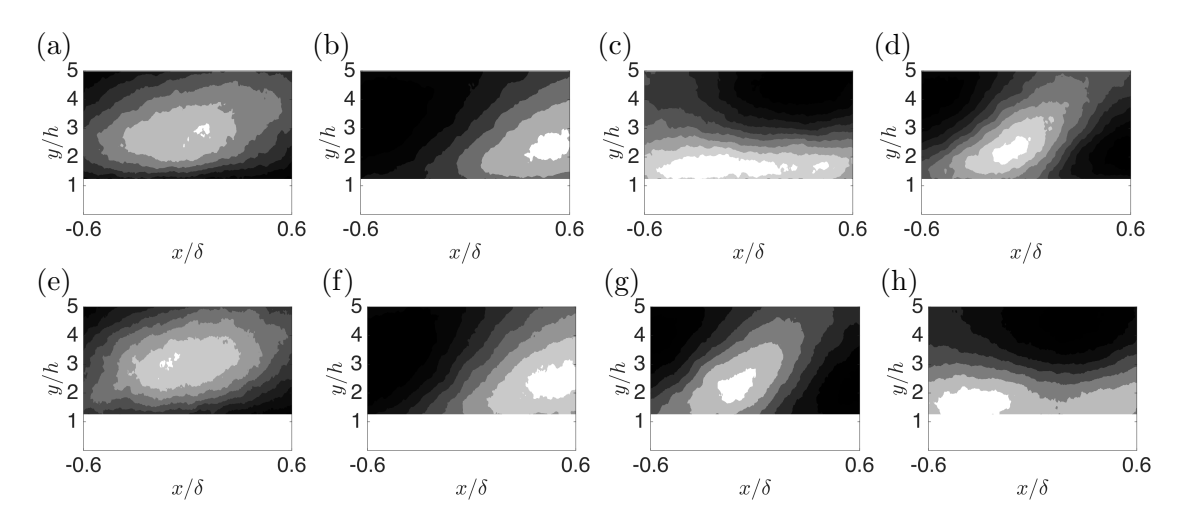


Figure 3.15: First four low-order POD modes in the roughness sublayer for (a-d) sparse regime and (e-h) dense frontal solidity regime. Flow is left to right. POD modes are calculated on the combined (u', v') field.

of the spatial similarity of the flow within the roughness sublayer. Physically, this modeshape-swap phenomenon means that a redistribution of energy across scales has taken place, so the energy relevant scales are different in size/shape for the different regimes. An increase in frontal solidity results in redistributing the energy towards scales that are inclined to the wall (mode 3 compared to mode 4). A similar POD analysis for the plan solidity cases is shown in figure 3.16. It is noticeable that the mode shapes appear similar to previously discussed  $\lambda_F$  cases and that for this solidity variation, the energy redistribution is absent, and hence the "cut off" mode does not appear. This suggests that there is a higher degree of spatial similarity in the energy containing motions in the roughness sublayer across the different plan solidities. These findings are consistent with the hypothesis presented in § 3.5.1. When the frontal solidity increases, the flow is progressively forced up and over the elements, hence a degradation of the local coherency is observed at high  $\lambda_F$  values, introducing energy into scales that are inclined to the wall - which is revealed by the appearance of the "cut-off" mode. This process is entirely absent for  $\lambda_P$  variations given that the frontal blockage is fixed as the flow over the canopy is not significantly altered, hence the "cut-off" mode does not appear in the RSL.

#### 3.5.5 Effect of surface morphology on energy distribution across scales

Table 3.2 shows the Fractional Turbulent Kinetic Energy (FTKE) contribution  $E_i$ , of the *i*th POD mode,  $\phi_i$ , to the total Turbulent Kinetic Energy (TKE) for the  $\lambda_F$  and  $\lambda_P$  cases. It can be seen that cases with lower  $\lambda_F$  tend to be characterised by lower energy content in the first POD mode. For example, mode 1 for the LF1 case contains only  $\approx 20\%$  of the total energy, while for the LF3 and LF6 cases, its content reaches  $\approx 22\%$ 

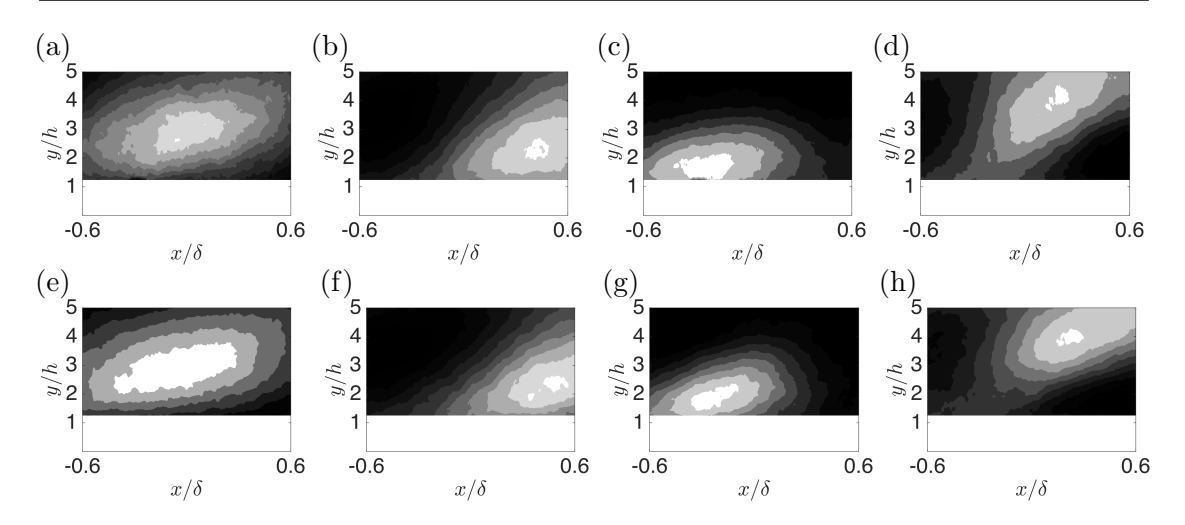


Figure 3.16: First four low-order POD modes in the roughness sublayer for (a-d) sparse regime and (e-h) dense plan solidity regime. Flow is left to right. POD modes are calculated on the combined (u', v') field.

and  $\approx 25\%$ , respectively. This seems to suggest that the effect of an increased frontal solidity would be to redistribute the energy toward the lowest-order POD modes and therefore the larger-scales. It can also be inferred that the plan solidity cases present an opposite trend, where the first mode for the sparse case contains almost 26% of the total TKE, while the contribution from the same mode for the medium and dense regimes (LP4 and LP6 cases for example) are only 21% and 22% respectively. It is also worth mentioning the peculiar behaviour of the LP3 case, which presents slightly different values for the modal energy. This is particularly visible in mode 3, which for LP3 contains 8% of the total TKE, whilst every other mode is characterised by 5-6%. This is due to reasons yet unknown.

The Cumulative Turbulent Kinetic Energy (CTKE) is also presented in table 3.2. The CTKE of the first four modes contributes to  $\approx 44\%$  of the total TKE for the densest case, LF6, while it only represent contributions of  $\approx 37\%$  for the sparsest case, LF1. This further confirms that an increased frontal solidity results in a redistribution of energy towards lower-order modes. The opposite is true for the plan solidity cases. Similar trends can also be inferred from the number of modes necessary to contribute to the 50% of the total turbulent kinetic energy which is progressively lower for increased  $\lambda_F$ , while it increases for an increased  $\lambda_P$ . The reader's attention is also drawn on the fact that more than  $\approx 600$  modes are needed to capture 95% of the resolved TKE from the (x,y) plane PIV measurements in both cases. This reflects the complexity of these flows, owing to the wide range of statistically important spatial scales present in the RSL at these Reynolds numbers. These observations strongly suggest that the effect of an increased frontal solidity is to redistribute the energy toward the highest-energy POD modes. This could be an indication of an increase in coherency of the turbulent structures in the denser regimes. The opposite trend is found, instead, for the

Data set	$E_1$	$E_2$	$E_3$	$E_4$	$\sum_{i=1}^{4} E_i$	$0.5\sum_{i=1}^{n} E_i$
LF1	20	8	5	4	37	10
LF2	22	9	6	4	41	8
LF3	22	10	5	4	41	8
LF4	23	9	5	4	41	8
LF5	25	10	5	5	44	6
LF6	25	9	5	5	44	6
LP1	26	10	5	4	45	6
LP2	22	10	5	4	40	8
LP3	19	8	8	4	39	9
LP4	21	9	5	4	39	9
LP5	22	8	5	4	39	9
LP6	22	9	5	4	39	9

Table 3.2: Fractional TKE,  $E_i$  and cumulative TKE  $\sum_{i=1}^n E_i$  content versus mode number.  $0.5\sum_{i=1}^n E_i$  refers instead to the number of modes necessary to resolve the 50% of the turbulent kinetic energy contained in the flow. POD modes are calculated on the combined (u', v') field only within the RSL.

plan solidity variation. Increasing  $\lambda_P$  redistributes the energy towards the higher-order modes, hence the smaller-scales.

#### 3.6 Conclusions

Results show, for the first time, the individual effect of frontal and plan solidities on various bulk quantities in a controlled experiment. The drag reaches a peak value for  $\lambda_F = 0.21$ , while it monotonically decreases with increasing  $\lambda_P$ . This is contrary to previous results obtained by examining the flow over cubical arrays, where the effects of  $\lambda_F$  and  $\lambda_P$  are coupled. This also suggests that morphometric studies purely based on the geometry of roughness elements (Macdonald, 1998) might not prove accurate. Further studies are required to identify appropriate correlations relating the geometry of the wall to the drag it generates.

An investigation into the depth of the roughness sublayer has revealed different behaviours for variation in frontal and plan solidities. The RSL depth, however, is found to follow the same trend in both cases - it appears to be inversely proportional to the roughness length (or bulk drag). A decrease in drag is usually accompanied by a thinning of the the RSL and vice-versa.

The use of proper orthogonal decomposition analysis to infer spatial similarity of flows over different wall morphologies was also demonstrated. The overall flow structure across the different roughness morphologies appears to be very similar. However the relative energy content in some energy-containing modes within the roughness sublayer changes

with increasing frontal solidity, while it remains the same with increasing plan solidity (i.e. absence of the "cut-off" mode).

The current chapter has shown that the depth of the roughness sublayer is found to be directly affected by the surface morphology. Consequently, differences across the spatial organisation of the turbulent structures in this region (1.5h < y < 5h) are reported, mainly via the appearance of the "cut-off" mode. In next chapter, the focus is shifted on whether or not these near-wall region differences can affect the statistics of the turbulence across the whole boundary layer thickness, and if so, to what extent.

## Chapter 4

## Effect of surface morphology on the turbulence statistics

#### 4.1 Introduction and background

Townsend (1976) first introduced the concept of outer-layer similarity that suggests that the structure of the turbulence (when appropriately scaled) is unaffected by the surface roughness at a sufficient distance from the wall. This hypothesis appears to be valid providing that the Reynolds Number is sufficiently high  $(hU_{\tau}/\nu >> 1)$  and that the mean height of the roughness elements characterising the surface, h, is small compared to the boundary layer thickness,  $\delta$ . This would imply that turbulent motions are independent of wall roughness, so that the topology and the details of the roughness itself do not impact the general structure of turbulence. The roughness then, would act merely to increase the surface stress without causing structural changes in the flow (Raupach, 1992). The first studies to offer experimental support of Townsend's similarity were conducted by Perry and Abell (1977), Andreopoulos and Bradshaw (1981) and Acharya et al. (1986); these revealed good collapse of the mean velocity defect profiles between smooth and rough-walls. Numerous further studies have also shown good agreement in proving the validity of Townsend's similarity in both mean velocity profiles and turbulence quantities (Perry and Li, 1990; Raupach, 1992; Schultz and Flack, 2005; Wu and Christensen, 2007; Volino et al., 2007; Castro, 2007; Wu and Christensen, 2010; Amir and Castro, 2011, amongst others).

However, some researchers cast doubts on the wall similarity hypothesis, stating that roughness effects can be observed well into the outer-layer (Krogstad and Antonia 1999; Keirsbulck et al. 2002; Tachie et al. 2004; Volino et al. 2009; Lee et al. 2010; Volino et al. 2011). When questioning the validity of outer-layer similarity, an important factor appears to be the three-dimensionality of the roughness morphology itself. Keirsbulck et al. (2002), Volino et al. (2009) and Volino et al. (2011) all reported differences in the

Reynolds stresses for 2D traverse bars when compared to smooth-walls. Furthermore, Krogstad et al. (1992), claimed that Townsend's similarity does not hold when  $h/\delta$  is large enough; the surface roughness, in fact, alters the velocity defect profile in both inner and outer-layer. They found, moreover, that spanwise velocity statistics outside the roughness sublayer differ from those measured above smooth-walls, as well as the normalised contributions to the Reynolds shear stress from the second and fourth quadrants  $(Q_2, Q_4)$ , which are higher.

Jimenez (2004) reviewed numerous studies on rough-wall boundary layers and suggested that the agreement or violation of Townsend's similarity depends on the relative roughness height. Violation of similarity appears for  $\delta/h < 40$  for the so-called "strong roughness", meaning that the typical roughness element height exceeds a few per cent of the boundary layer thickness. Other researchers also drew similar conclusions, suggesting slightly different critical values for  $h/\delta$ . Ligrani and Moffat (1985) stated that if the extent of the roughness sublayer is larger than the inner layer itself, then changes in the turbulent structure in the outer-layer are to be expected. Flack et al. (2005) have suggested that the important parameter for the validity of outer-layer similarity is ratio between the boundary layer thickness to the equivalent sand roughness. They suggested a critical value of  $\delta/h_s > 40$  for outer-layer similarity to be valid. Wu and Christensen (2007) also noted wall similarity, in both mean velocity profiles and Reynolds stresses, for roughness  $\delta/h = 28(<40)$  and  $\delta/h_s = 48(>40)$ , offering further support to the importance of the equivalent sand roughness formulation in assessing wall similarity. It is important to point out that Mejia-Alvarez and Christensen (2013) in a later study on the same roughness morphology, found that this surface has a tendency to promote channeling of the flow in the form of low-momentum pathways (LMPs) and high-momentum pathways (HMPs). These pathways influence the structure of the turbulence causing the persistence of spanwise heterogeneity across the entire boundary layer.

Castro (2007) found that rough surfaces that comprise cubes conforms to outer-layer similarity up to  $\delta/h \approx 5$  corresponding to a situation in which the mean roughness element height exceeds some 50% of the boundary-layer momentum thickness,  $\theta$ . Amir and Castro (2011) confirmed the validity of outer-layer similarity in the mean velocity profiles up to  $\delta/h \approx 5$ . They also reported an onset of  $\delta/h \approx 6.7$  for the Reynolds stresses to conform to the same hypothesis. Numerical simulations (Hagishima et al., 2009; Leonardi et al., 2003) have used cube roughness arranged in different patterns and have shown that outer-layer similarity might hold up to  $\delta/h \approx 6-8$ . This is in contrast with other studies with much smaller roughness (Bhaganagar et al., 2004; Bakken et al., 2005) that appeared to violate outer-layer similarity. As previously mentioned, most of the previous studies that systematically explored the effect of surface morphology on the flow behaviour were carried out with cube roughness. These studies include both numerical and physical experiments (Cheng and Castro 2002b; Coceal and Belcher 2004; Kanda et al. 2004; Cheng et al. 2007; Hagishima et al. 2009; Santiago et al. 2008; Leonardi and Castro 2010 among various others). It is important to note that cube

roughness is a special case for which  $\lambda_F \equiv \lambda_P$ . This means that these two parameters are coupled and effects of one or the other cannot be determined independently.

To our knowledge, only cube roughness studies have been able to push the onset for the validity of outer-layer similarity to up to  $h/\delta \approx 0.2$ . Perhaps, the cubes are a special case of regular roughness for which similarity holds. Therefore, the extent of roughness up to which outer-layer similarity holds is not entirely clear. It is also unclear whether the geometry of the roughness elements is important for outer-layer similarity.

#### 4.2 Equivalent sand roughness

As already mentioned, early experimental studies of rough surfaces were focused on high density rough-walls for which a good representation was found to be the equivalent sand roughness (Nikuradse, 1933). Given that some debate is still open on whether  $h/\delta$  or  $h_s/\delta$  is the driving parameter to asses the validity of Townsend's similarity, it is important to estimate the equivalent sand roughness for the surfaces examined herein. However, it must be noted that the latter is not the most appropriate way to characterise the current regular discrete roughness, particularly in the sparse regime. Nikuradse's (1933) equivalent sand roughness can be related to the roughness function,  $\Delta U^+$ , following the formulation of Schlichting (1979), and therefore to the roughness length,  $y_0$ , from Castro (2007), as follows:

$$\Delta U^{+} = \frac{1}{\kappa} \ln(h_s^{+}) - 3.5 = B + \frac{1}{\kappa} \ln(h^{+}) + \frac{1}{\kappa} \ln\left(\frac{y_0}{h}\right). \tag{4.1}$$

#### 4.3 Results and discussion

Section 4.3.1 compares results from the 2D and 3D PIV measurements to address the flow homogeneity. Next, section 4.3.2 discusses the fully development of the boundary layers in examination. Section 4.3.3 examines the validity of Townsend's outer-layer similarity for various mean and higher-order quantities across different surface roughness conditions. Section 4.3.4 provides a detailed quadrant analysis that sheds some light into the momentum transfers in these different flows. Section 4.3.5 presents results obtained via proper orthogonal decomposition. To conclude, the roughness characterisation based solely upon  $\lambda_F$  and  $\lambda_P$  is reviewed and important additional parameters to be considered are suggested in § 4.3.8 and § 4.3.9.

#### 4.3.1 Assessing the flow homogeneity

Before details on the turbulent statistics across different rough-walls are presented and discussed, it is important to highlight some of the characteristics of the flows herein examined. Figure 4.1 compares 2D and 3D PIV results across the FOV. Although only a particular case is presented here for the sake of brevity, the conclusions drawn herein are valid for all cases in examination. Figure 4.1(a) shows mean velocity profiles across the (y, z) plane in grey. It is clear that, despite some flow heterogeneity present in the roughness sublayer, very little difference is found in the mean streamwise velocity in the outer layer. Velocity profiles obtained via 2D PIV are also presented, and are found to be consistent (within 2%) with 3D measurements. This is important as it builds confidence that the planar PIV data set (slice of the spanwise FOV) is representative of the bulk flow behaviour and it is not dependent on the spanwise location. The normal stresses and the Reynolds shear stress for the 2D and 3D measurements are compared in figure 4.1(b). The collapse of the data sets across the whole wall-normal range, especially in the outer region, is very good. The difference between the two data sets can be regarded as dispersive stress<sup>1</sup> contribution (Raupach and Shaw, 1982). Therefore, any difference bigger than these dispersive contribution has to be considered due to the flow physics and not due to the location of measurement. The dispersive stresses contribution have also been calculated (although not shown here) for each of the statistics examined and were found to be negligible. These findings ensure that the turbulence statistics in the outerlayer are homogenous across the span, hence that the 2D results are representative of the bulk flow physics. Therefore, only results from the 2D measurements are presented in this chapter. This data set, in fact, is better resolved, has better statistical convergence and includes more wall morphologies than the 3D data.

Finally, before the effect of the surface morphologies on the turbulence statistics is discussed, some relevant boundary-layer characteristics (previously shown in table 3.1) are discussed. The calculated values for equivalent sand grain roughness are compared with the more appropriate roughness function and roughness length adopted in this thesis. It is easy to verify that the ratio  $\delta/h$  is roughly constant across all cases and assumes values in the range 10-12, which is much smaller than 40, and hence the current roughness is to be considered as "strong roughness" based on Jimenez's (2004) definition. This is important as the focus of this work is indeed exploring the upper limit of the roughness height and its relationship to outer-layer similarity. When the equivalent sand roughness is calculated, this also results in values for  $\delta/h_s < 40$  for almost all cases. In this respect, the current data set fails to adhere to both Jimenez's (2004) and Flack et al.'s (2005) characterisations of rough surfaces that are expected to conform to outer-layer similarity. However, they are within the limits proposed by Castro (2007) based on cube-roughness data.

<sup>&</sup>lt;sup>1</sup>When spatial averaging across the FOV is introduced, following Nikora et al.'s 2007 notation, the dispersive contribution is given by  $\tilde{U} = \langle U \rangle - U$ , where  $\langle U \rangle$  and U are the double-averaged and time-averaged contributions rspectively.

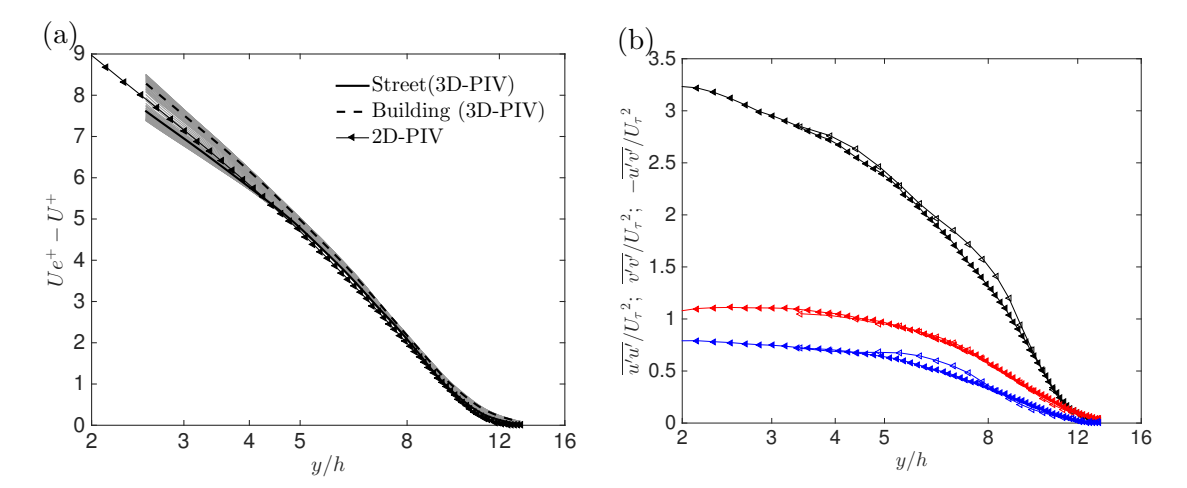


Figure 4.1: (a) Comparison of mean velocity defect profiles across 2D and 3D PIV measurements. (b) Wall-normal variation of streamwise (black), wall-normal (red) turbulence intensities and Reynolds shear stress (blue). 2D and 3D PIV measurements are represented by filled and empty symbols respectively. Markers are spaced every five vectors for clarity.

#### 4.3.2 Fully developed boundary layer

As the focus of the current investigation is on the bulk behaviour of fully-developed boundary layers over rough surfaces, it is important to verify that the cases examined herein are indeed fully-developed and that, at the measurement location, the boundary layers are in equilibrium with the surface underneath. For this purpose, in each case, a fetch of approximately  $20\delta$  upstream of the measurement location was designed to meet the fully-developed conditions (Castro, 2007). Nonetheless, as discussed in § 2.3, the flow was initially developed over a baseboard for 1.7 m and then a further 2.3 mover the LEGO™ bricks. The two surfaces are such that the ratio between the baseboard's protrusion and the bricks' height was  $h_1/h = 0.15$ . This sudden step-change in the roughness size generates an Internal Boundary Layer (IBL) that grows within the Upstream Boundary Layer (UBL). This phenomena is sketched in figure 4.2. Region  $(3) \cup (4)$  represents the IBL, which develops downstream of the surface discontinuity within the lover part of the UBL (1). Therefore, at first, only the lowest portion of the IBL (4) is in equilibrium with the new surface (i.e. the bricks), while the outer layer flow (2) retains characteristics determined by the upstream surface condition (i.e. the baseboard). This is equivalent to saying that region (2) is characteristic of obstacles of height  $h_1$ , whilst region (4) scales with the bricks' height h. These two regions are bridged by a transition region (3) in which the velocity profiles gradually change from that appropriate to the downstream roughness to that of the upstream one (Cheng and Castro, 2002a).  $X_F$  denotes the fetch necessary for the flow to regain equilibrium with the underlying surface after the step-change in roughness. Various studies have analysed the problem of step-change in roughness. The major findings (Jackson, 1976) can be summarised as follows: (i)  $X_F$  is essentially dependent of the larger roughness length,

in this case  $y_0$ ; (ii) neither the ratio of upstream to downstream roughness lengths  $(y_{01}/y_0)$ , nor that of boundary layer thickness to roughness element height,  $\delta/h$ , is in itself a significant parameter.

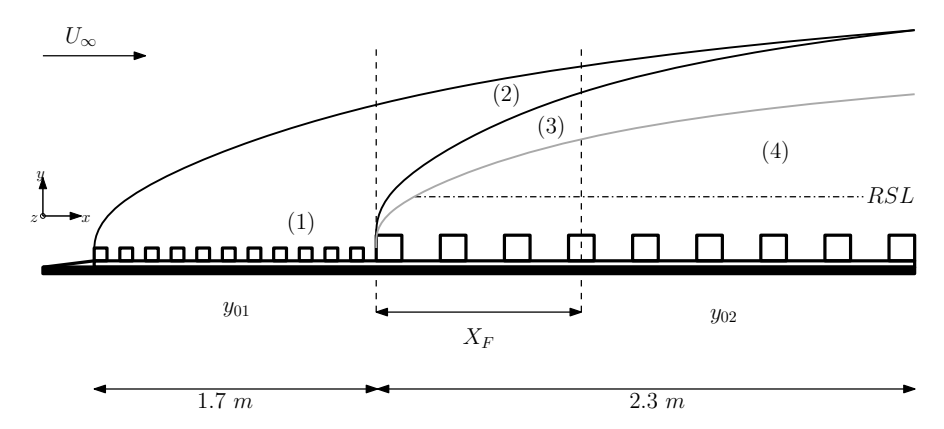


Figure 4.2: Schematic diagram of the various layers over a step-change in roughness. Original from Cheng and Castro (2002a). (1) Upstream boundary layer, (3) transition region, (4) outer region of the internal boundary layer, RSL indicates the roughness sublayer of the internal boundary layer.

Despite Wieringa (2014) predictions, Cheng and Castro (2002a) reported that a fetch of about  $300y_0$  is needed for the equilibrium layer to reach the upper limits of the roughness sublayer. Therefore, they pointed out that only significantly beyond that point a sensible thickness of the inertial region should be expected to match the underlying surface. Their prediction was found to be valid for step change in roughness with  $y_0/y_{01} \mathcal{O}(10)$ , which is of the same order of that of the current surfaces. When their prediction is applied herein, this results in  $X_F = 0.7 \ m$  (in the worse case, i.e. LP1). It is therefore reasonable to expect self-similarity in the mean statistics given that the measurement location was  $2 \ m$  downstream of the step-change in roughness, hence almost three times the required fetch for equilibrium. Therefore, the boundary layers examined herein are to be considered fully developed and in equilibrium with the brick-walls at the measurement location.

#### 4.3.3 Outer-layer similarity

Figure 4.3(a) shows the mean velocity profiles in defect form for the LF1 to LF6 cases. To normalise the wall-normal distance, the Clauser scaling parameter is used as in Castro (2007) and Amir and Castro (2011). This parameter is defined as  $\Delta = (\delta^* U_e)/U_\tau$ , where  $\delta^*$  is the displacement thickness, and  $U_e$  is the velocity at the edge of the boundary layer. The mean velocity profiles show a good agreement across all the different cases throughout the entire outer region. Figure 4.3(b) shows the equivalent figure for the plan solidity cases. Again, reasonable agreement across all the different cases is shown in the outer region (i.e.  $(y - d)/\Delta \ge 0.1$ ), although the quality of collapse is poorer compared to results for the frontal solidity cases and degrades closer to the wall. This suggests that

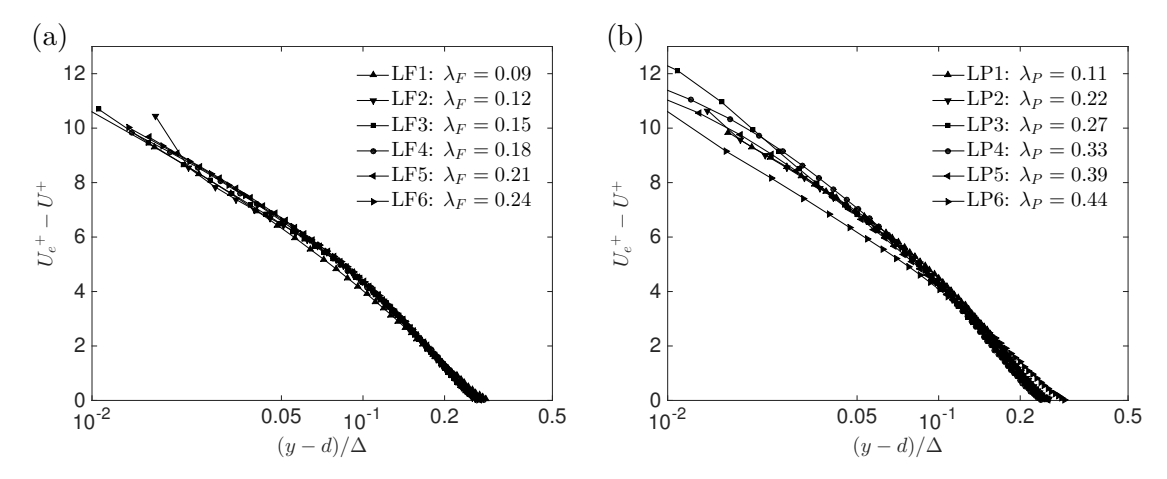


Figure 4.3: Mean velocity profiles in defect form as a function of (a)  $\lambda_F$  ( $\lambda_P = const = 0.27$ ) and (b)  $\lambda_P$  ( $\lambda_F = const = 0.15$ ). Markers are spaced every five vectors for clarity.

outer-layer similarity seemingly appears to break down with variations in plan solidity. It must be noted that the lack of collapse of the data is based on comparisons with other studies in the literature that claim collapse of data and the existence of outer-layer similarity. Although not shown here for brevity, the characteristics of the collapse (i.e. the spread in the data across different wall-normal locations and different cases) for the current experimental data set has been calculated and compared with previous studies (Amir and Castro, 2011). The spread in the current data has been found to be larger than the spread found in other studies indicating a lack of similarity. Similar comparisons were performed for all quantities reported in this study and the observations of presence/lack of similarity is based on these comparisons. Additionally, the spread of the statistics due to the dispersive stresses has also been taken into account - where a lack of collapse is claimed, this was found much larger than the dispersive contributions.

The variations in the velocity fluctuations with the surface morphology can be investigated by examining the Probability Density Functions (PDFs) of u' at different wall-normal locations (y=1h and y=3h). This is shown in figure 4.4 for both  $\lambda_F$  (left column) and  $\lambda_P$  (right column). The effect of different surface morphologies on the tails of the PDFs can be clearly seen. The tails are more compact across the frontal solidity cases ((a) and (c)) as opposed to plan solidity cases ((b) and (d)). This suggests that variations in  $\lambda_P$  would have a greater influence on the turbulence statistics. Furthermore, it is important to note that the differences are largest on top of the elements' crests for both cases ((a) & (b)) and they extend well into the outer region, as confirmed by PDFs at y=10h (not shown here for brevity). The effect of an increase in frontal solidity just above the elements field (figure 4.4(a)) seems to be a narrowing of both the positive and negative tails of the PDFs while the opposite is true in figure 4.4(b) for an increase in plan solidity.

Similar PDFs plots for the wall normal fluctuations v' are presented in figure 4.5(a) to

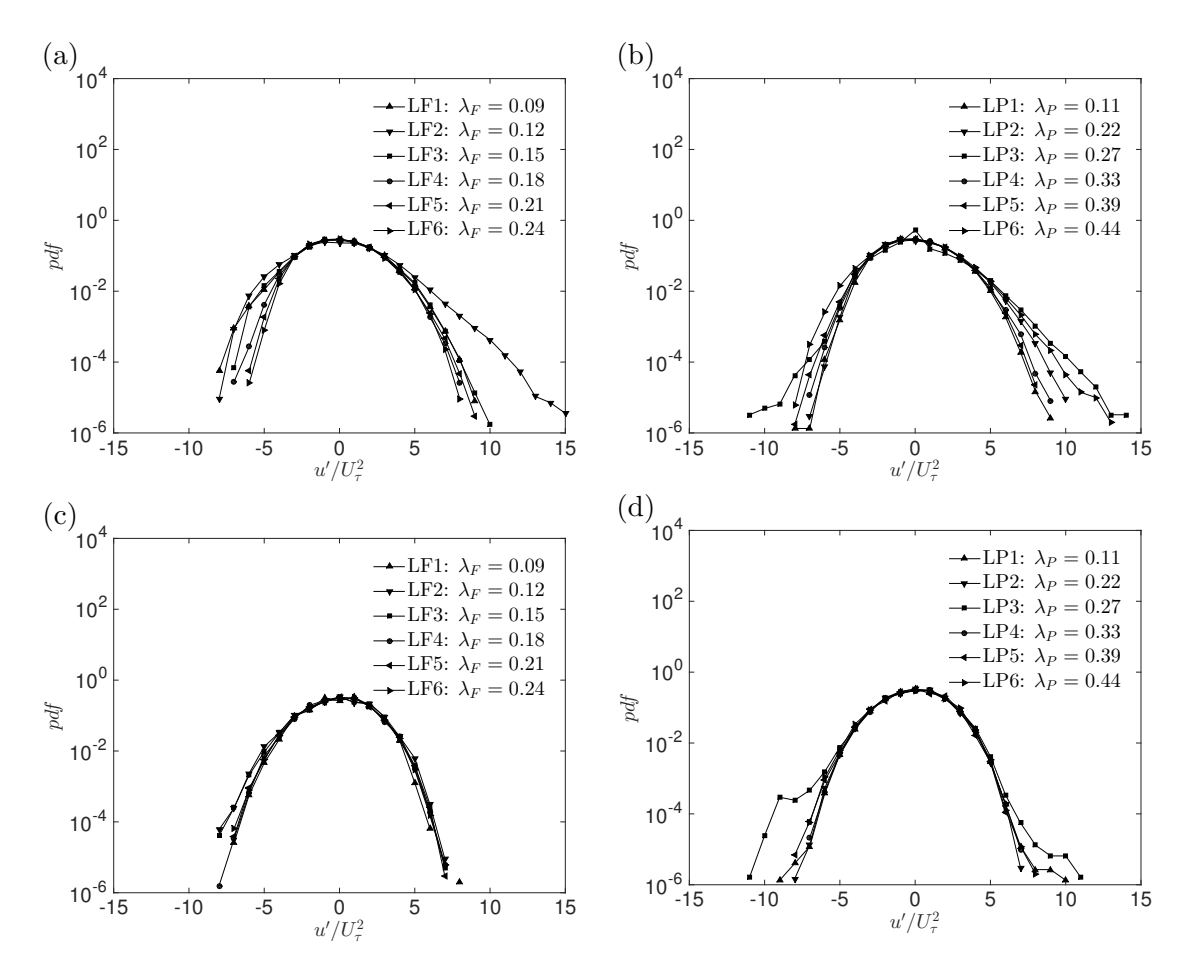


Figure 4.4: PDFs of u' events contributing to the Reynolds stress for y=1h (top) and y=3h (bottom) as a function of  $\lambda_F$  ( $\lambda_P=const=0.27$ ) on the left and  $\lambda_P$  ( $\lambda_F=const=0.15$ ) on the right.

(d). The variations in the tails for v' are less significant compared to u'. The plan solidity appears to have a greater influence on the tails of the PDFs (figure 4.5(b) and (d)) when compared to the frontal solidity. Although it is hard to infer, an increase in plan solidity results in narrower positive and negative tails of the PDFs. This indicates a reduction in strong positive and negative wall-normal velocity fluctuations at a given distance from the wall. Figure 4.6(a) shows the streamwise and the wall-normal velocity fluctuations for different values of  $\lambda_F$ . The streamwise turbulent intensities present a reasonable collapse of the data for  $(y-d)/\Delta > 0.2$ , whilst major differences appear closer to the wall. The LF1 and LF3 cases exhibit the largest differences and departure from the other cases for  $(y-d)/\Delta < 0.2$ . The wall-normal turbulence intensities show a better collapse throughout the entire range of wall-normal locations. Figure 4.6(b) shows the streamwise and the wall-normal velocity fluctuations for different values of  $\lambda_P$ . Both streamwise and wall-normal turbulence intensities show a clear lack of similarity across the whole range of wall-normal locations. These findings seem to confirm lack of similarity found in the previous studies, especially for low values of frontal solidities (Ganapathisubramani and Schultz, 2011) and in 2D roughness elements (Volino et al., 2009).

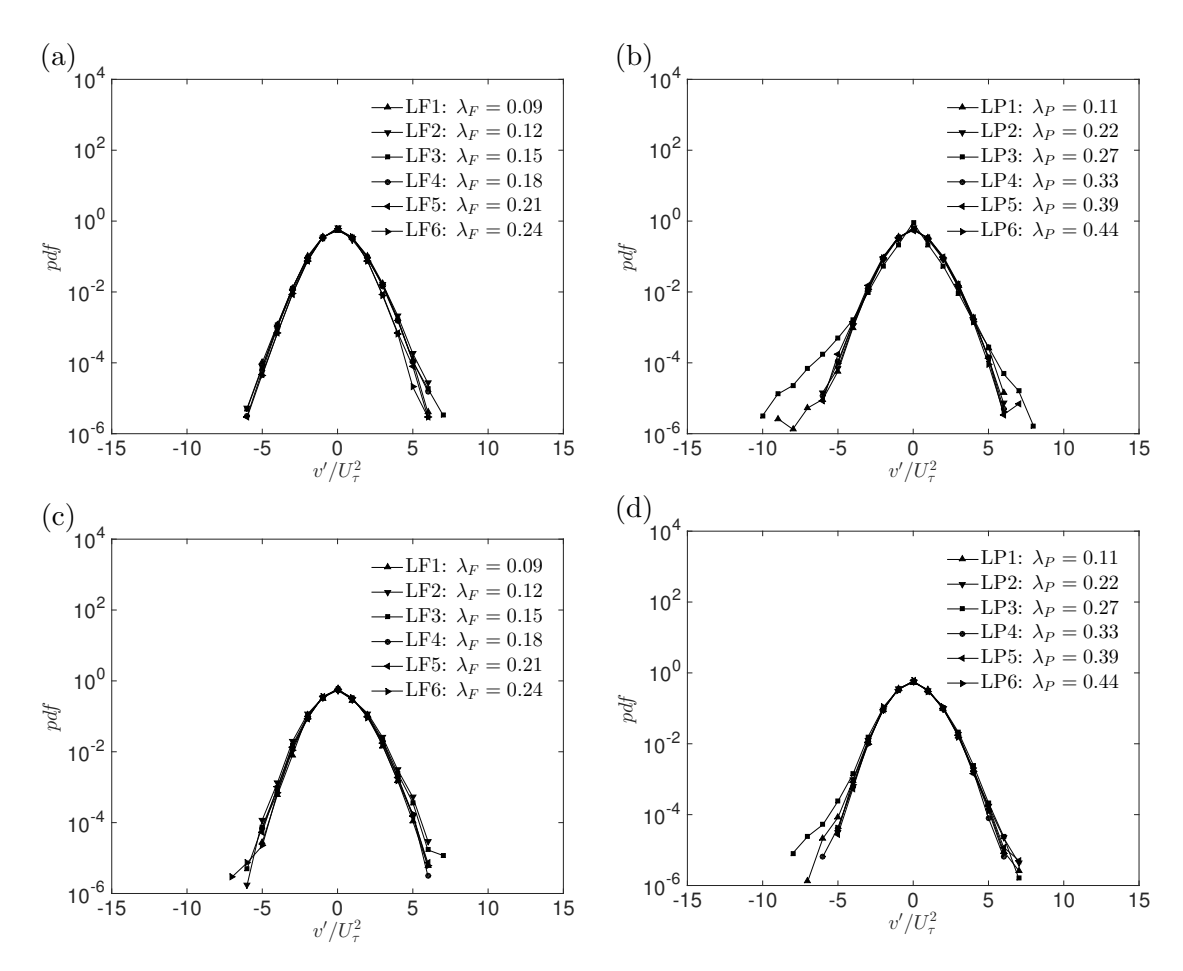


Figure 4.5: PDFs of v' events contributing to the Reynolds stress for y=1h (top) and y=3h (bottom) as a function of  $\lambda_F$  ( $\lambda_P=const=0.27$ ) on the left and  $\lambda_P$  ( $\lambda_F=const=0.15$ ) on the right.

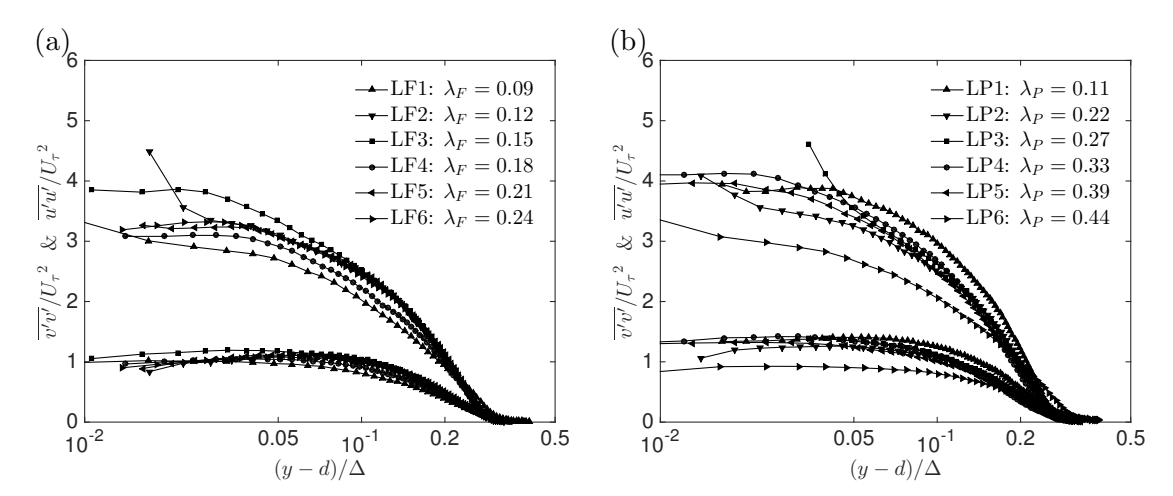


Figure 4.6: Wall-normal variation of streamwise turbulence intensity,  $\overline{u'u'}/U_{\tau}^2$ , and wall-normal turbulence intensity,  $\overline{v'v'}/U_{\tau}^2$ , as a function of (a)  $\lambda_F$  ( $\lambda_f = const = 0.27$ ) and (b)  $\lambda_P$  ( $\lambda_f = const = 0.15$ ). Markers are spaced every five vectors for clarity.

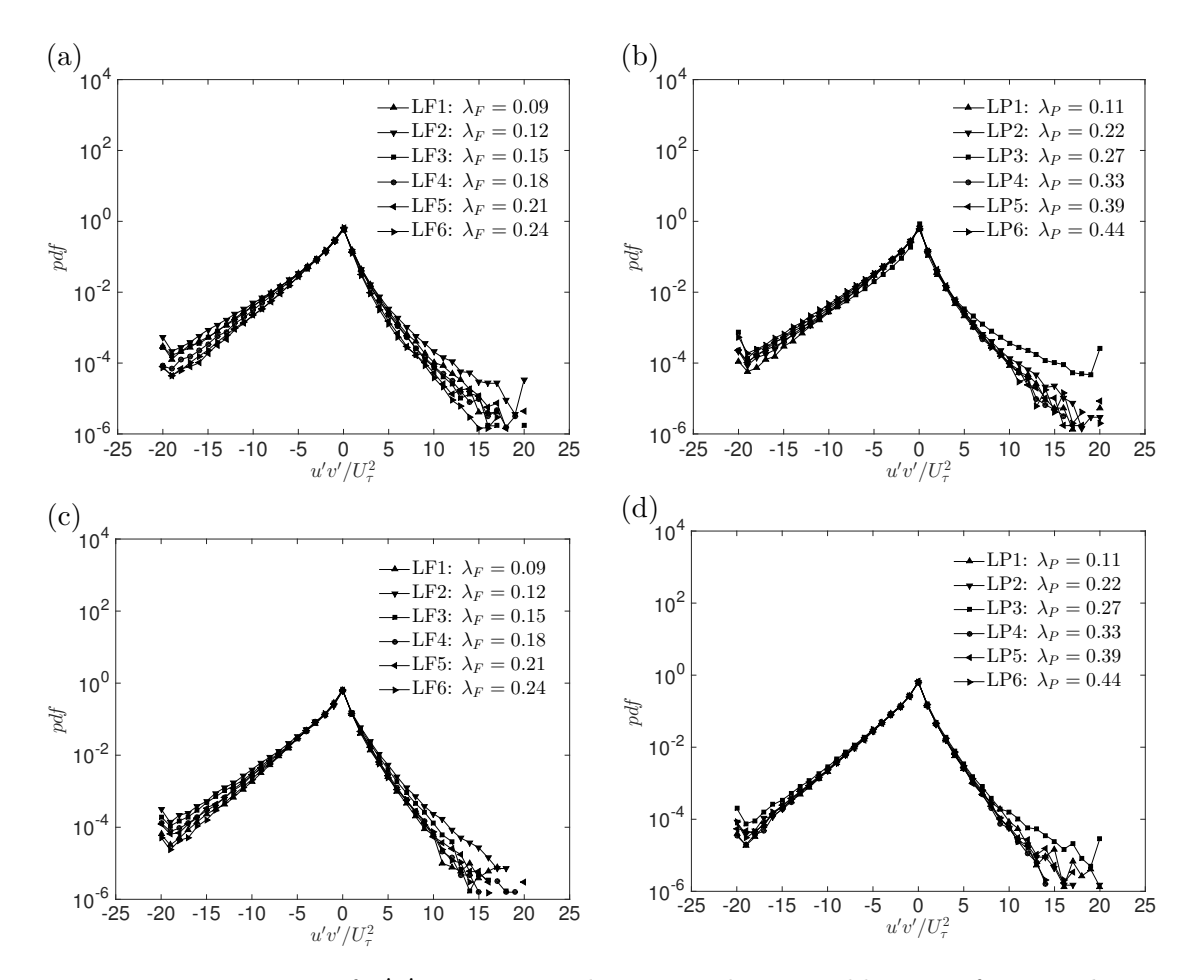


Figure 4.7: PDFs of u'v' events contributing to the Reynolds stress for y=1h (top) and y=3h (bottom) as a function of  $\lambda_F$  ( $\lambda_P=const=0.27$ ) on the left and  $\lambda_P$  ( $\lambda_F=const=0.15$ ) on the right.

The behaviour of the turbulent momentum flux and its modifications due to the surface morphology can be addressed by examining the PDFs of u'v'. Figure 4.7 shows the PDFs of u'v' events for both  $\lambda_F$  and  $\lambda_P$  variations at different wall-normal locations. As Licari and Christensen (2011) amongst others pointed out, generally u'v' PDFs are skewed toward negative values, primarily close to the wall and this is consistent with the negative sign of the Reynolds shear stress  $(\overline{u'v'})$ . This confirms that sweep and ejection events are on average the dominant contributions to the Reynolds shear stress compared to inward and outward interaction events.

Figures 4.7(a) and (c), shows that, close to the wall, an increase in frontal solidity results in a reduction of both positive and negative u'v' events. The effect of the plan solidity is shown on the right column of figure 4.7. Close to the wall, an increase in  $\lambda_P$  seems to enhance the negative u'v' events while damping the positive counterpart, as shown in figure 4.7(b) and (d).

Figures 4.8(a) & (b) present the Reynolds shear stress for the different  $\lambda_F$  and  $\lambda_P$  cases respectively. These are the first moments of the PDFs presented in figure 4.7. As indicated earlier, the Reynolds stress values seem to be affected by both the solidities;

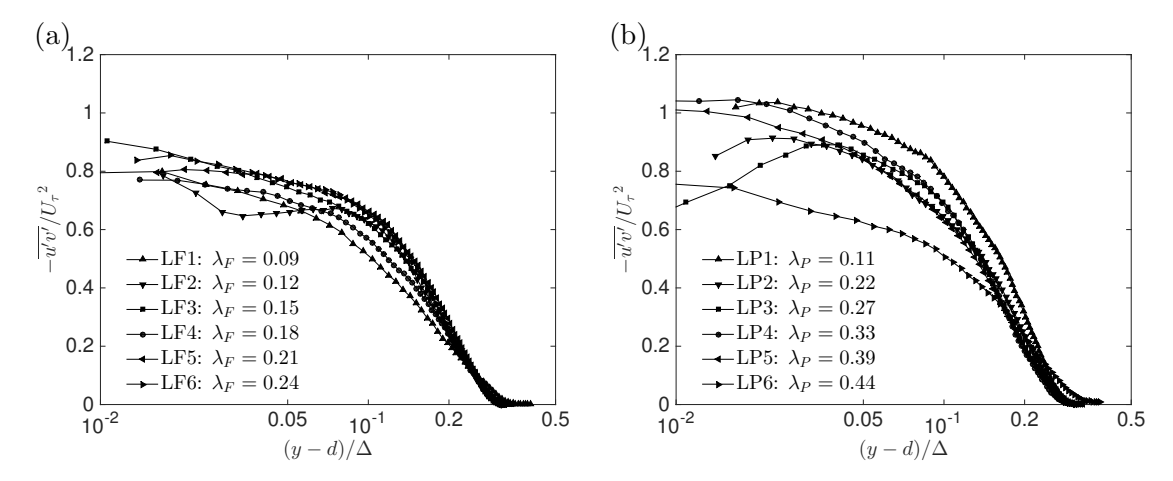


Figure 4.8: Wall-normal variation of Reynolds shear stress,  $-\overline{u'v'}/U_{\tau}^2$ , as a function of (a)  $\lambda_F$  ( $\lambda_P = const = 0.27$ ) and (b)  $\lambda_P$  ( $\lambda_F = const = 0.15$ ). Markers are spaced every five vectors for clarity.

this results in a lack of similarity throughout the entire  $(y-d)/\Delta$  range for both  $\lambda_F$  and  $\lambda_P$ . Particularly significant is the difference for the LP6 case, which shows lower turbulence stresses across almost the entire wall-normal range.

It is important to note that the results presented in the current section are affected by a significant uncertainty, as discussed in § 3.3. It must also be pointed out that a better collapse of the data sets could be achieved by tailoring the value of the von Kármán parameter. In particular, a technique based on minimising the slope of a rough-wall-modified indicator function (Nagib and Chauhan, 2008) can be adopted to estimate the optimal  $\kappa$  for each surface. This results in values of the von Kármán parameter well below the commonly suggested reference (Marusic et al., 2013). This approach also drastically contradicts the hypothesis of a constant  $\kappa$  for all rough-wall boundary layers, which is a topic outside the scope of this thesis. Moreover, as the roughness length is representative of the downshift of the log-region (when compared to the smooth-wall scenario), if comparison across different surface morphologies is to be made, the same value of  $\kappa$  is to be prescribed for all cases. Only then, the roughness length truly represents the offset of the log-region in respect to the same canonical smooth-wall. For this reason, in this study, the von Kármán parameter has been kept constant at  $\kappa = 0.38$ , as suggested by Marusic et al. (2013).

Thus far, the presence or lack of outer-layer similarity has been discussed according to the classical definition, i.e. the variation of mean and fluctuating quantities with appropriately scaled wall-normal distance. Recently, Castro et al. (2013) suggested an alternative way to examine the similarity of turbulence intensities, where they propose to use the "diagnostic plot" (Alfredsson and Örlü, 2010; Alfredsson et al., 2011). In their paper, they find that data obtained in the fully-rough regime appear to collapse in the outer-layer when this diagnostic plot form is used. Emphasis is also given to the fact that this method eliminates the uncertainty in determination of  $U_{\tau}$ , d as well as

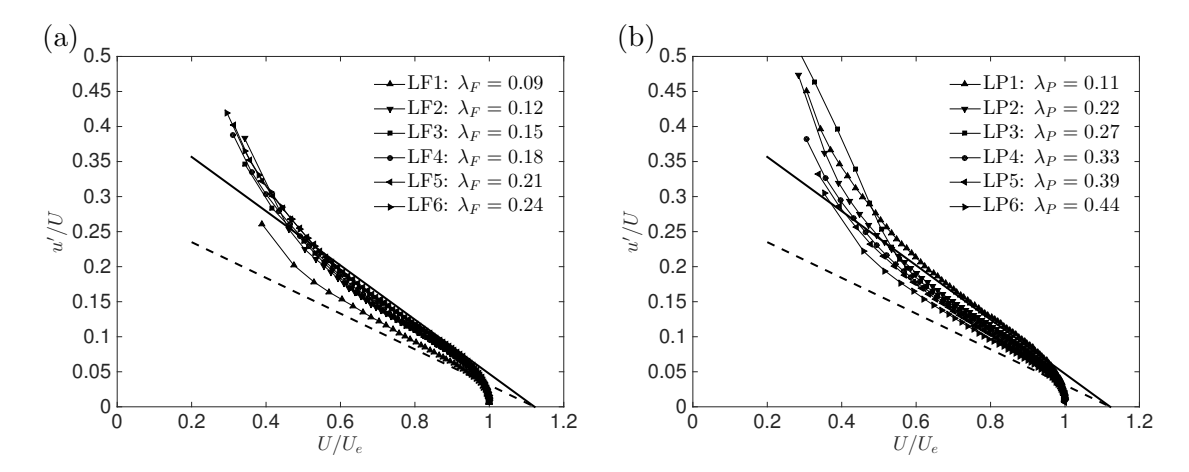


Figure 4.9: Diagnostic plot for the different rough surfaces as a function of (a)  $\lambda_F$  ( $\lambda_P = const = 0.27$ ) and (b)  $\lambda_P$  ( $\lambda_F = const = 0.15$ ). The thick solid line represent the fully-rough regime, as from Castro et al. (2013), while the dashed line comes from the smooth-wall limit, as reported by Alfredsson et al. (2011). Markers are spaced every five vectors for clarity.

the actual wall-normal position (y). Figure 4.9(a) and (b) presents the current data for  $\lambda_F$  and  $\lambda_P$  cases, respectively, in the "diagnostic plot" form (i.e. the variation of u'/U versus  $U/U_e$ , where  $U_e$  is the boundary layer edge velocity). Castro et al. (2013) pointed out that data in the fully-rough regime should collapse on the solid line shown in figure 4.9 (this line, which is a linear best fit from various data sets in the fully-rough regime, is taken from Castro et al. 2013). The figures also show the best fit in the outer-layer for a smooth-wall (dashed line). It can be seen from the figures that the collapse across the cases presented herein is poor. The lack of collapse is more pronounced in the  $\lambda_P$  cases (figure 4.9(b)), which is consistent with our findings based on classical scaling. This further lack of collapse in the diagnostic plot form, across the different cases, is seen as a further proof of a lack of outer-layer similarity in these flows.

Figures 4.9(a) & (b) also show that the data do not collapse on the trend line for the fully-rough regime. In fact, our data mainly lies between the smooth and the fully-rough trend lines. In their paper, Castro et al. (2013) argue that transitionally rough flows data should lie between these two lines. However, the current data set shows that the value for  $y_0^+$  is high (the lowest value is 10) for all the cases and is comparable to the values of  $y_0^+$  for cases that follow the fully-rough trend lines in their paper. Additionally, similar surfaces (cubes and random blocks with high  $h/\delta$ ) at similar freestream speeds and Reynolds numbers have been shown to be fully-rough (for example the data from Amir and Castro 2011). Finally, drag-balance results in the previous § 4.3.1 have shown that the flows over these surfaces is indeed in the fully-rough regime. The spatial resolution of the measurements in the current study is comparable to previous x-wire measurements and PIV measurements that show outer-layer similarity and hence the result is not an effect of resolution (especially in the outer-layer). Therefore, for all the reasons herein, the lack of collapse displayed by the current data with the previous trends is interpreted

as a lack of outer-layer similarity. This also raises the possibility that the fully-rough trend line in the diagnostic plot is, in fact, dependent on other parameters such as surface roughness morphology,  $h/\delta$ ,  $h^+$ ,  $\delta/y_0$  among others. The biggest difference between the data presented here and the data of Castro et al. (2013) is that the  $h/\delta$  in the current study is consistently around 0.1 (compared to much smaller values for various data sets in their paper). This suggests that the diagnostic plot (and the corresponding trend lines) is perhaps more sensitive to other surface parameters and the nature of the roughness for high values of  $h/\delta$ , as Castro et al. (2013) rightfully suggested. It is beyond the scope of the current study to examine the exact dependence of the diagnostic plot on these parameters.

It must also be noted that Castro et al. (2013) show that the rough-wall data can be collapsed onto the smooth-wall data by accounting for the roughness function,  $\Delta U$ . They re-define the parameters in the diagnostic plot as  $U'/U'_e$  ( $U' = U + \Delta U$  and  $U'_e = U'_e + \Delta U$ , where U is the local mean and  $U_e$  is the boundary layer edge velocity) instead of  $U/U_e$  (as in figure 4.9). However, this re-introduces the uncertainty in  $U_\tau$  as the latter is used to determine  $\Delta U$  (or equivalently  $\Delta U_n$  - see Castro et al. 2013 for details). They also examine outer-layer similarity in Reynolds shear stress by plotting  $-\overline{u'v'}^+$  against  $U'/U'_e$ . This also includes the uncertainty in determination of  $U_\tau$ . Given that the turbulence intensities across our different cases do not follow the trend shown in Castro et al. (2013), the utility in further exploration of outer-layer similarity along the lines of diagnostic plot is not clear. Although we do not discount the general utility and the merit of the method proposed by Castro et al. (2013), its value in the current circumstance is not apparent and the proposed universality of the curve for the fully-rough condition seems to fail in the current case.

Finally, figures 4.10(a) & (b) show the ratio of Reynolds shear stresses to total turbulent kinetic energy,  $K=1/2(\overline{u'^2}+\overline{v'^2})$  for different frontal and plan solidities cases respectively. This allows us to examine the influence of roughness topology on the efficiency of turbulence production (i.e. conversion of available potential energy into kinetic energy). From figure 4.10(a) a nominal trend is noticeable: an increased frontal solidity results in a larger Reynolds shear stresses compared with the turbulence energy. This is consistent with previous findings from Leonardi and Castro (2010). They suggested this behaviour to be an indication of an increase efficiency in turbulent production processes. The data in figure 4.10(b) show that the spread in this ratio with variations in plan solidity is minimal compared to the frontal solidity cases, particularly for  $0.05 \le (y-d)/\Delta \le 0.15$  where all the different plan solidity cases appear to collapse. This suggests that the efficiency in turbulent production is similar in the inertial layer regardless of changes in plan solidity.

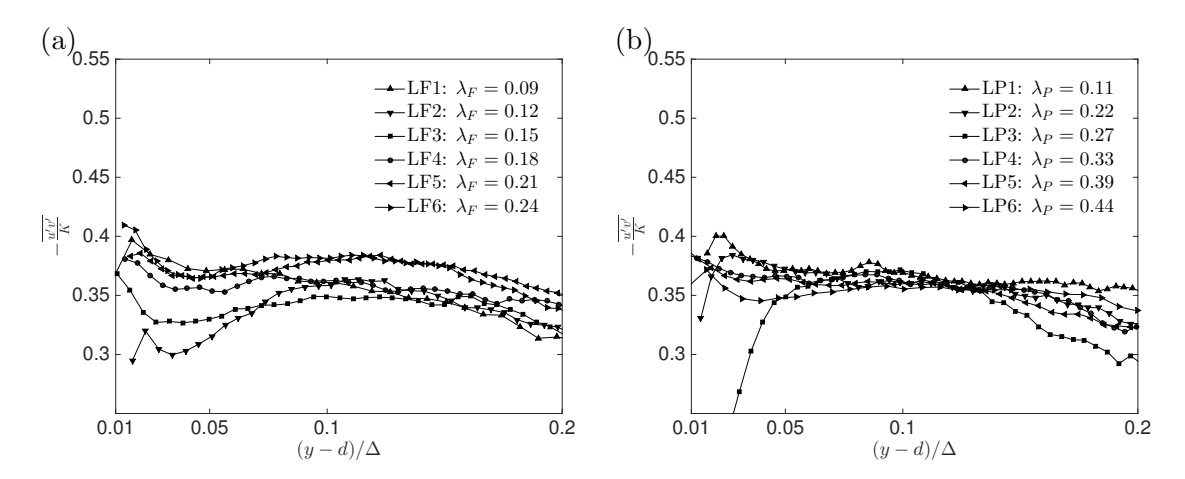


Figure 4.10: Normalised wall-normal variation of Reynolds shear stress,  $-\overline{u'v'}/K$ , as a function of (a)  $\lambda_F$  ( $\lambda_P = const = 0.27$ ) and (b)  $\lambda_P$  ( $\lambda_F = const = 0.15$ ). Markers are spaced every five vectors for clarity.

#### 4.3.4 Quadrant analysis

To further investigate the lack of similarity exhibited by the Reynolds shear stresses, a quadrant decomposition analysis has been carried out. This analysis is based on the hyperbolic hole size, H, following Lu and Willmarth (1973). Strong turbulent events are here conditioned into four quadrants in the (u', v') plane, in order to understand the significancy of these events to the momentum transfer following the criteria:

$$\frac{u_i'v_i'(H)}{u'v'} = \frac{1}{\overline{u'v'}} \lim_{T \to \infty} \frac{1}{T} \int_0^T u'v'(t) S_i(t, H) dt \qquad (i = 1, 2, 3, 4), \qquad (4.2)$$

where the subscript i refers to the ith quadrant and

$$S_i(x,t,H) = \begin{cases} 1, & |u'v'(x,t)| > Hu'v' \\ 0, & \text{otherwise.} \end{cases}$$
 (4.3)

and H is called the hyperbolic hole size. The second quadrant  $(Q_2: u' < 0 \& v' > 0)$ , representing the burst-like events or ejections, and the fourth quadrant  $(Q_4: u' > 0 \& v' < 0)$ , representing the sweeps contributions are the main object of the following investigation. Although a range of hyperbolic holes was investigated, only results for H = 2.5 are presented. Figure 4.11 shows the  $Q_2$  and  $Q_4$  contributions for  $\lambda_F$  and  $\lambda_P$  variation on the left and right respectively. In both cases, the  $Q_2$  and  $Q_4$  quadrants present some

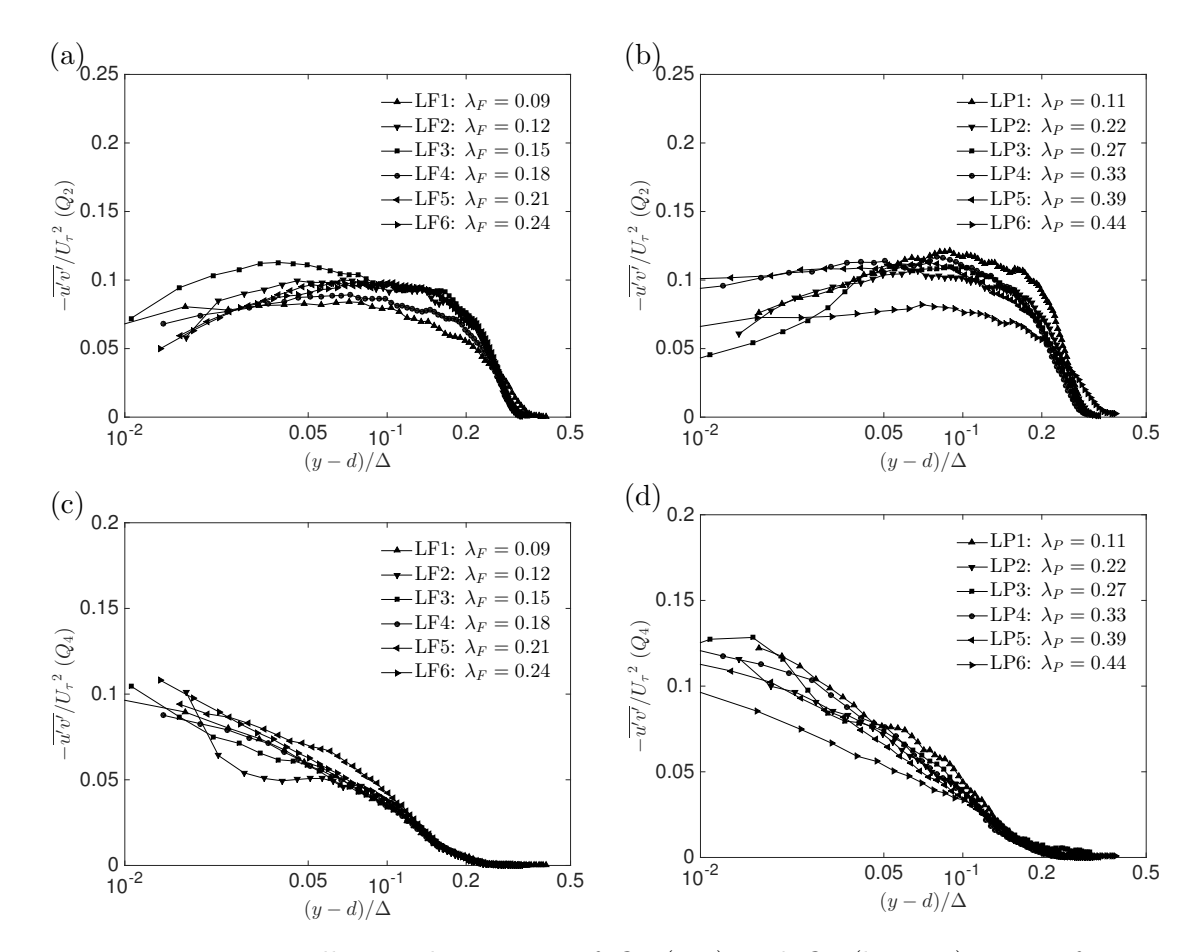


Figure 4.11: Wall-normal variation of  $Q_2$  (top) and  $Q_4$  (bottom) events for H=2.5 as a function of  $\lambda_F$  ( $\lambda_P=const=0.27$ ) on the left and  $\lambda_P$  ( $\lambda_F=const=0.15$ ) on the right. Markers are spaced every five vectors for clarity.

differences depending upon variation in the solidities. A comparison between the  $Q_2$  and  $Q_4$  activities for various surfaces suggests that the surface density of the roughness elements appear to impact the ejections more than the sweeps across all the cases. This is evident from the fact that the spread displayed in  $Q_2$  activity is, on average, larger compared to the spread in  $Q_4$  activity. Variation in plan solidity (figure 4.11(b) & (d)) exhibit similar behaviour to the  $\lambda_F$  cases, with differences observed across the entire  $(y-d)/\Delta$  range although a clear trend is difficult to infer. Perhaps not surprising, the LP6 cases, which showed lower u'v' in figure 4.8(b), also present lower trends for both  $Q_2$  and  $Q_4$  activities.

Further information on the shear-stress producing events can be accessed by examining the percentage contribution of sweeps and ejections. Figures 4.12(a) & (c) show the percentage contribution to the total shear stress provided by strong ejection and sweep events  $(Q_2$  and  $Q_4$  respectively) for the frontal solidity variations. For clarity, only cases LF1, LF3 and LF5 are shown, since the others follow the trends highlighted by those three cases. Both the  $Q_2$  and  $Q_4$  show a gradual increase in activity in the outer-layer, although closer to the wall, ejections are enhanced and sweeps are reduced with increasing values of the frontal solidity. Figure 4.12(e) shows the ratio  $Q_2/Q_4$  for

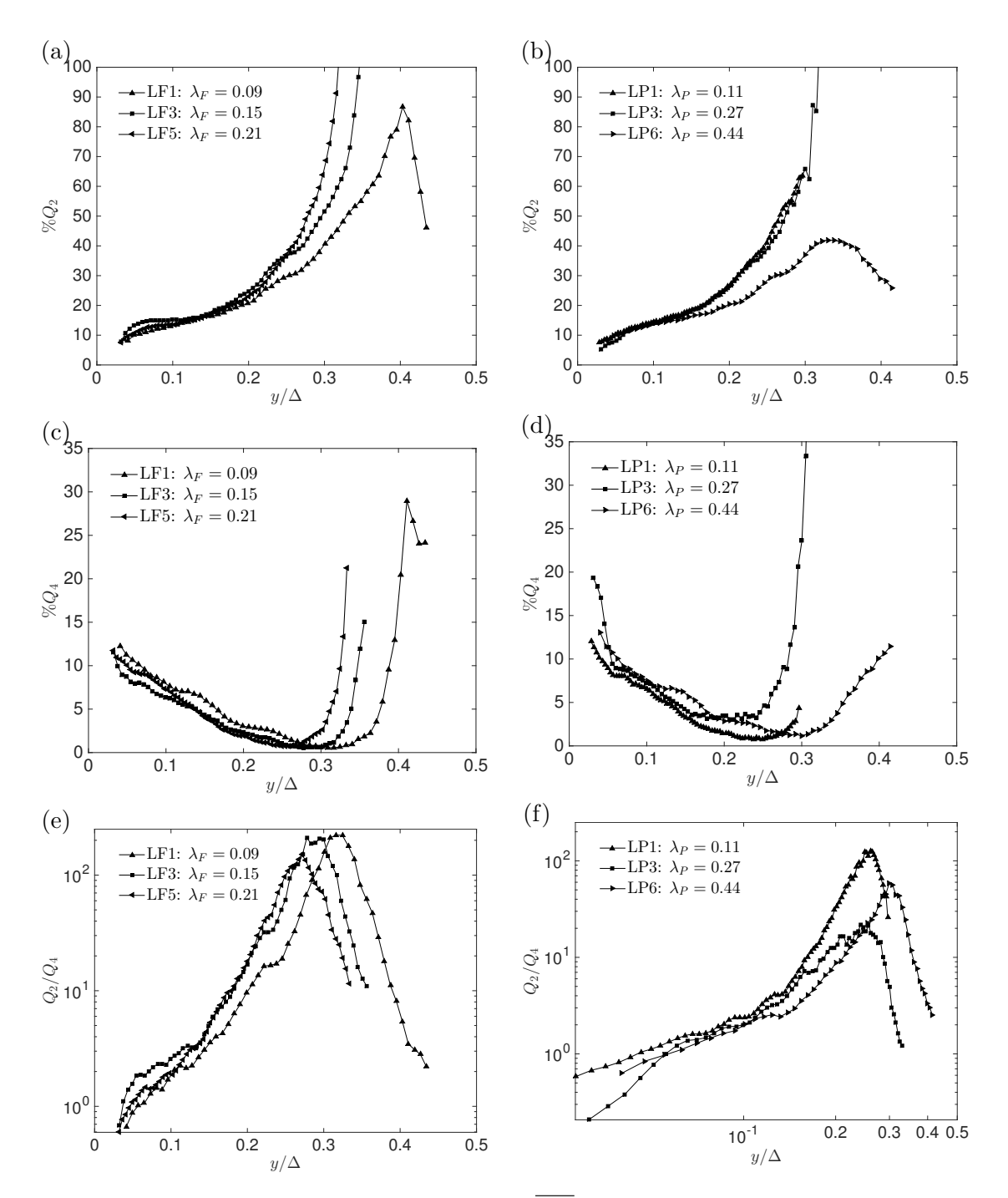


Figure 4.12: Percentage contributions to  $\overline{u'v'}$  for H=2.5 from  $Q_2$  (top),  $Q_4$  (center) events and their ratio (bottom) as a function of  $\lambda_F$  ( $\lambda_P=const=0.27$ ) on the left and  $\lambda_P$  ( $\lambda_F=const=0.15$ ) on the right. Markers are spaced every five vectors for clarity.

the different  $\lambda_F$  cases across different wall-normal locations. For a rough-wall boundary layer,  $Q_2$  events (ejections) consistently dominate  $Q_4$  events (sweeps) almost throughout the entire  $y/\Delta$  range. However, for  $y/\Delta < 0.05$ , it can be seen that this  $Q_2/Q_4$  ratio is less than unity for all the cases, suggesting that sweeps are dominant within the roughness sublayer. This is consistent with observations in previous studies such as Amir and Castro (2011) and Böhm et al. (2012). The  $Q_2/Q_4$  ratio has an local maxima in the outer region beyond which point this ratio starts decreasing. The wall-normal location where this local maximum occurs can be seen in figure 4.12(e). This location appears to decrease with increasing  $\lambda_F$ .

Figures 4.12(b), (d) & (f) show the preceding analysis carried out for plan solidity variations. As in the previous case for the sake of clarity, only three cases are shown. In contrast to the  $\lambda_F$  cases in figure 4.12(a) & (c), the  $Q_2$  and  $Q_4$  trends in figures 4.12(b) & (d) are opposite. Ejection and sweep activities show a gradual decrease and increase, respectively, in proximity of the wall with increasing value of the plan solidity. The differences closer to the wall are minimal for these cases. Farther away from the wall, both activities appear to decrease with increasing  $\lambda_P$ , although this trend is minimal just looking at the three cases herein presented. Figure 4.12(f) shows the ratio  $Q_2/Q_4$  for different plan solidity cases, which shows that the wall-normal location of the local maximum of this ratio increases with increasing  $\lambda_P$ , but, this increasing trend is marginal compared to the  $\lambda_F$  cases. Moreover, the absolute value of the ratio is much smaller for the  $\lambda_P$  cases compared to the  $\lambda_F$ .

The wall-normal location of the peak in the Q2/Q4 ratio can be interpreted as the extent to which the surface morphology affects the flow structure. If the origin of ejection type motions (caused by the roughness) is taken to be at the wall, then the location at which the sweeps start reversing the trend of ejections can be viewed as the point at which the ejections start to lose their strength. The results show that ejections start to lose their strength (compared to sweeps) closer to the wall for increasing  $\lambda_F$ . However, changes in  $\lambda_P$  makes a very marginal difference. This is consistent with observation that surfaces with sparsely distributed roughness generate vortical structures that have the ability (and freedom) to reach farther away from the wall. In denser distributions of roughness, vortical structures from adjacent elements might interfere with each other thereby reducing their ability to reach farther from the wall.

#### 4.3.5 POD modes shape and energy content

To further explore the spatial characteristics of the turbulence a snapshot based (POD) is next employed. Results presented herein have been filtered to match the local resolution at  $l_{2D}^+=45$ . The FOV across the different cases is also matched to the region  $-0.6\delta < x < 0.6\delta$  in the streamwise and  $1.5h \le y \le \delta$  in the wall-normal direction to allow for

meaningful comparisons. The result presented herein were obtained by performing the POD calculation over the combined (u', v') data.

Figure 4.13 shows contour plots of the shape of the first five (i.e. high energy) POD modes. Both frontal and plan solidities cases are plotted in the sparse and dense regime. The first two columns show frontal solidity cases in sparse (i.e. LF2) and dense regime (i.e. LF5) respectively. The same follows for plan solidity cases in columns three (i.e. LP2) and four (i.e. LP5). Focusing on the first column, regions of high and low streamwise momentum (or vice-versa) are highlighted in black and white respectively, although the colorbar is arbitrary. The shape of the most energetic mode (mode 1) is characterised by an elongated large-scale high (or low) momentum region. Mode 2 shows an inclined shear layer that separates a high-momentum region below it from a low-momentum region appearing above it (or vice-versa since the sign of the values is arbitrary and will depend on the eigenvalue itself). The structure of mode 3 is similar to mode 2 where the inclination of the shear layer is against the flow direction. Mode 4 is dominated by three distinctive regions: two localised high-momentum regions are separated by an elongated forward leaning streamwise low-momentum region. Finally, mode 5 presents four different alternating regions of low and high-speed. As Adrian et al. (2000a) discussed, while POD modes are not representative of the actual coherent structures present in the flow, but more of the energy of those structures, they do provide a qualitative glimpse of the dominant flow field associated with each mode and its variability from one mode to another. A trend of increasingly smaller structures for higher modes is generally found throughout all cases. Therefore, the most energetic modes tend to be associated with large-scale structure, whilst later modes are representative of increasingly smaller-scales.

This behaviour has been well-documented (Holmes et al., 1996). This trend can be visualised by plotting the correlation coefficient between the 1st-mode and the  $\phi_{i-th}$ -mode for the same ( $\lambda_F$  or  $\lambda_P$ ) case. Figure 4.14(a) & (b) show the result of this procedure for both the frontal and solidity cases. As expected, by definition, the correlation coefficient is unity for mode 1 (auto-correlation), while decreases for increasing order of the mode. This is true across all frontal and plan cases.

It can be clearly seen (in columns two to four in figure 4.13) that the modes characteristics are found to be consistent and indistinguishable in both shape and order across all surface morphologies regardless of the regime. This level of consistency is remarkable considering the different wall morphologies (see figure 2.5(b)) and is a testimony of a form of spatial universality of the turbulence structure over rough-walls. Note that the breakdown of the spatial similarity reported in the previous chapter for the RSL (via the appearance of the "cut-off" mode) is not present in the full-field modes, where the energy in the outer-region seemingly dominates the energy contained in the RSL. Nevertheless, when integrated across all the modes, the energy (in terms of stresses) does not conform to outer-layer similarity.

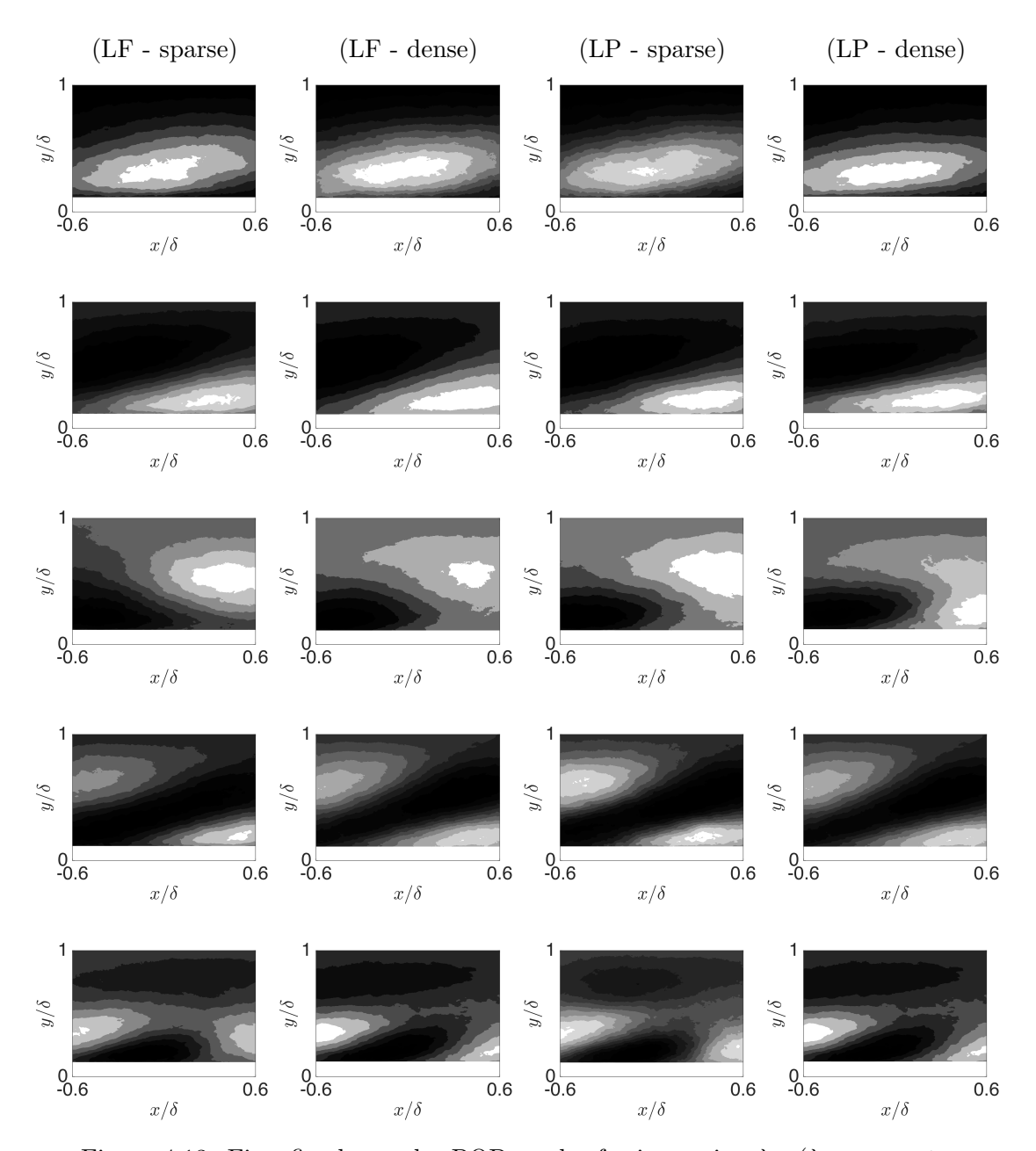


Figure 4.13: First five low-order POD modes for increasing  $\lambda_F$  ( $\lambda_P = const = 0.27$ ). Cases: LF2 (left), LF5 (centre-left), LP2 (centre-right), LP5 (right). Flow is left to right. POD modes are calculated on the combined (u', v') confined to the near-wall region.

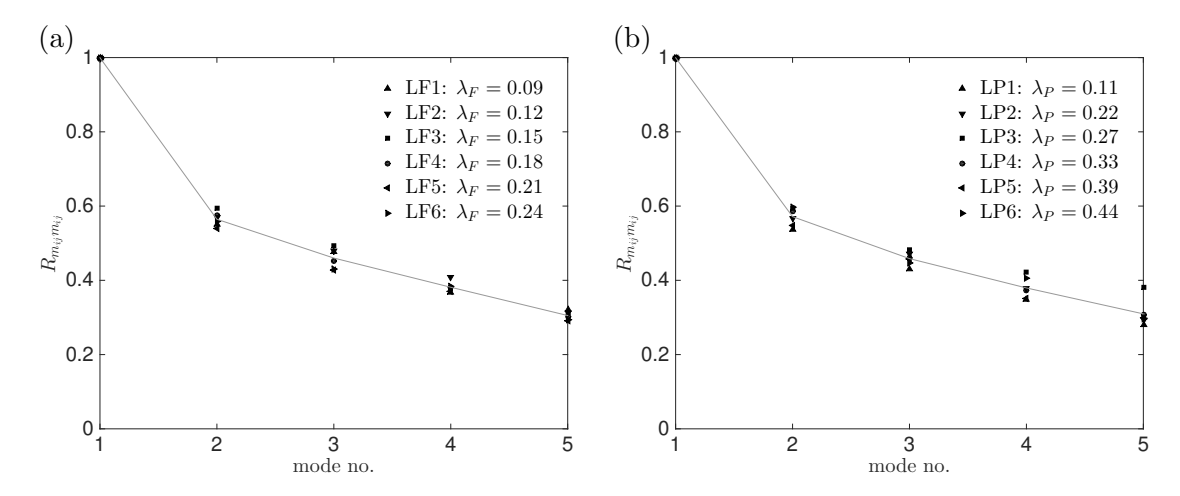


Figure 4.14: Correlation coefficient,  $R_{m_i m_i}$  as a function of (a)  $\lambda_F$  ( $\lambda_P = const = 0.27$ ) and (b)  $\lambda_P$  ( $\lambda_F = const = 0.15$ ). POD modes are calculated on the combined (u', v') field. Grey lines indicate the trend.

Figures 4.15(a) & (b) show the FTKE contribution  $E_i$ , of the *i*th POD mode,  $\phi_i$ , to the total TKE for the  $\lambda_F$  and  $\lambda_P$  cases respectively. The first order modes are the most energetic while the highest-order mode (mode 2000), contains the least energy. Figure 4.15(c) & (d) show the CTKE as a function of the modes number for the  $\lambda_F$  and  $\lambda_P$  cases respectively. The CKE reaches a unit value, correspondent to 100% of the energy when all modes are included. It is also clear that the  $\lambda_P$  variation appears to effect the energy budget less than the  $\lambda_F$ , as the right-hand side figure appears more compact across cases.

Table 4.1 shows the FTKE contribution to the total TKE for the  $\lambda_F$  and  $\lambda_P$  cases. It can be seen that cases with lower  $\lambda_F$  tend to be characterised by lower energy content in the first POD mode. For example, mode 1 for the LF1 case contains only  $\approx 15\%$ of the total energy, while for the LF3 and LF6 cases, its content reaches  $\approx 16\%$  and  $\approx 18\%$ , respectively. It can also be inferred that the plan solidity cases present an opposite trend, where the first mode for the sparse case contains almost 19% of the total TKE while the contribution of the same mode for the medium-packed and dense regimes (LP3 and LP6 cases for example) are only 14% and 16% respectively. The CTKE is also presented in table 4.1. The CTKE of the first five modes contributes to  $\approx 38\%$  of the total TKE for the densest case, LF6, while it only represent contributions of  $\approx 34\%$  for the sparsest case, LF1. This further confirms that an increased frontal solidity results in a redistribution of energy towards larger scales (or lower-order modes). The opposite is true for the plan solidity cases. Similar trends can also be inferred from the number of modes necessary to contribute to 50% of the total turbulent kinetic energy which is progressively lower for increased  $\lambda_F$ , while it increases for an increased  $\lambda_P$ . It is also worth noting that more than  $\approx 800$  modes are needed to capture 95% of the resolved TKE from the (x, y) plane PIV measurements in both cases. This reflects the complexity of these flows, owing to the wide range of statistically important spatial scales present at these Reynolds numbers.

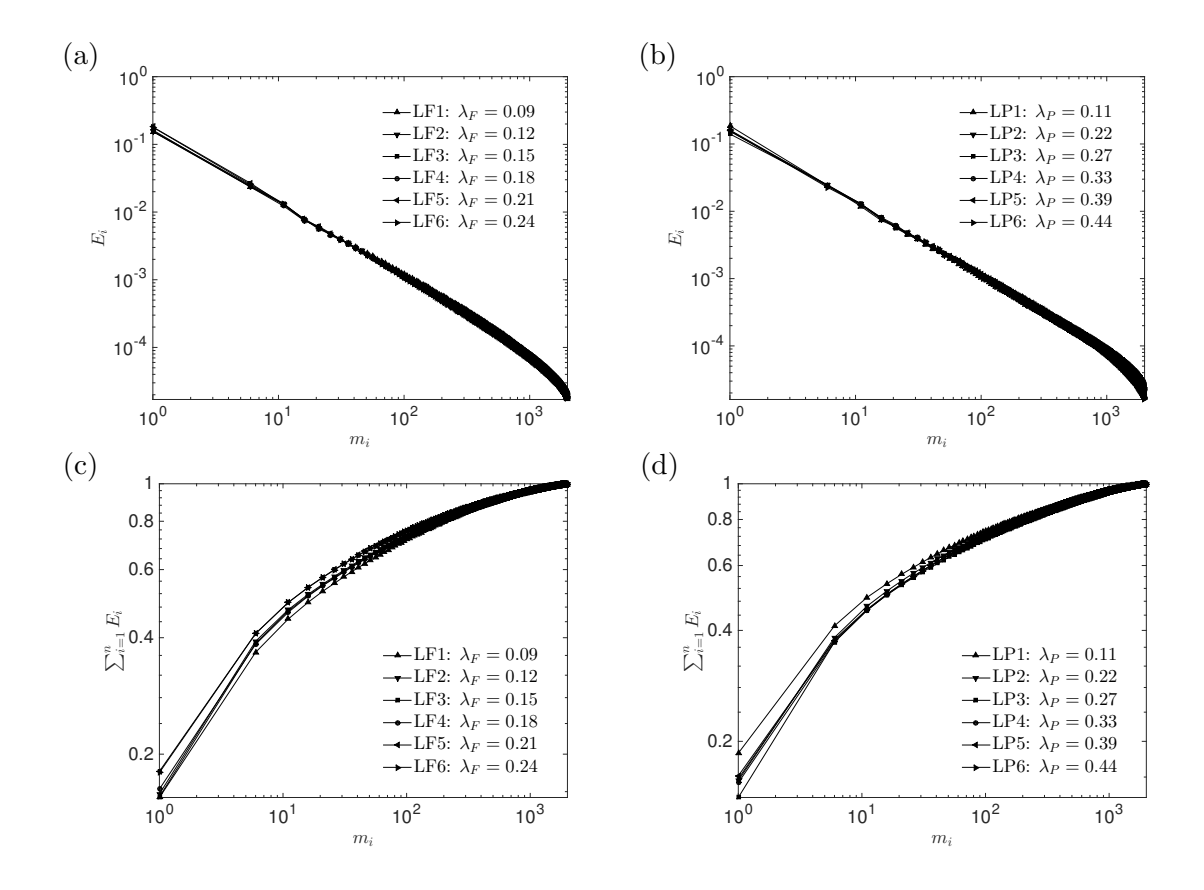


Figure 4.15: (top) FTKE,  $E_i$ , and (bottom) CTKE content,  $\sum_{i=1}^{n} E_i$ , versus mode number as a function of (left)  $\lambda_F$  ( $\lambda_f = const = 0.27$ ) and (right)  $\lambda_P$  ( $\lambda_f = const = 0.15$ ). POD modes are calculated on the combined (u', v') field.

Data set	$E_1$	$E_2$	$E_3$	$E_4$	$E_5$	$\sum_{i=1}^{5} E_i$	$0.5\sum_{i=1}^{n} E_i$
LF1	15	7	5	4	3	34	17
LF2	16	8	5	5	3	37	14
LF3	16	8	6	4	3	36	14
LF4	16	8	5	4	3	36	14
LF5	18	8	5	4	3	38	12
LF6	18	8	5	4	3	38	12
LP1	19	8	5	4	3	39	12
LP2	16	8	5	4	3	36	14
LP3	14	7	5	4	4	35	16
LP4	15	8	5	4	3	35	16
LP5	16	7	5	4	3	35	16
LP6	16	8	5	4	2	36	16

Table 4.1: Fractional TKE,  $E_i$  and cumulative TKE  $\sum_{i=1}^n E_i$  content versus mode number.  $0.5\sum_{i=1}^n E_i$  refers instead to the number of modes necessary to resolve the 50% of the turbulent kinetic energy contained in the flow. POD modes are calculated on the combined (u', v') field.

The preceding POD analysis together with the lack of collapse of turbulent statistics in the outer-layer discussed in section 4.3.3 seem to indicate that, although the spatial structure of the turbulence is maintained, the relative distribution of the energy and the overall energy content of the flow leads to the lack of similarity. For both solidity variations therefore, although the characteristic spatial scales of the flow seem to be maintained across all the different surface morphologies, these structures contribute, on average, to a different amount of turbulent kinetic energy. In this respect, it is interesting to report that this energy contribution appears to follow opposite trends for changes in frontal and plan solidities. An increase in  $\lambda_F$  shifts the energy toward the low-order modes (i.e. large scale), while the opposite is true for an increase in  $\lambda_P$ .

#### 4.3.6 POD of isolated velocity fluctuations

Having investigated the behaviour of the POD modes calculated from the (u', v') combined velocity field, further information for each velocity component can be obtained calculating the modes solely from the (u') or (v') fields. Similar boundaries as for the combined case are chosen for the vertical and horizontal extend of the FOV. When POD modes are calculated over the (u') field, for both  $\lambda_F$  and  $\lambda_P$ , their shapes are remarkably similar to those for the combined field in figure 4.13, and are hence omitted. This is to be expected as the combined field is constructed with the streamwise velocity first, it is therefore reasonable that this component results more represented in the first low-order POD shapes. It is perhaps more interesting to investigate the behaviour of the (v') field. This should be different from the previous case and can reveal new insight on the effect of surface morphology on the wall-normal structures. Figure 4.16 shows contour plots of the shape of the first five POD modes for an increase in both  $\lambda_F$  and  $\lambda_P$ , calculated solely upon this simplified wall-normal velocity field. It is striking that, although mode 1 results are similar to the previous cases (in figure 4.13), from mode 2 onward the POD modes have very different shapes compared to the previous result. It is perhaps not surprising that the mode structures for the wall-normal field are much smaller and compact, in agreement with snapshots of instantaneous wall-normal velocity fields, which are very localised, compact and small-scale dominated (as shown in due course in figure 5.3(b)). It must be also highlighted that for the wall-normal field we see the appearance of the critical "cut off" mode (as in section 3.5.4), despite the fact that the calculation is performed over the entire boundary layer thickness. This could be linked with the fact that the lack in spatial similarity discussed before, is strongly influenced by the flow in the near/canopy region. For the frontal solidity cases, a severe effect on the wall-normal velocity component is observed, therefore the POD structure are different, hence the "cut-off" mode appearance. The energy content of these structures is shown in table 4.2. Although the actual values of the FTKE and CTKE are different from the previous case, rightfully so, similar trends are reported.

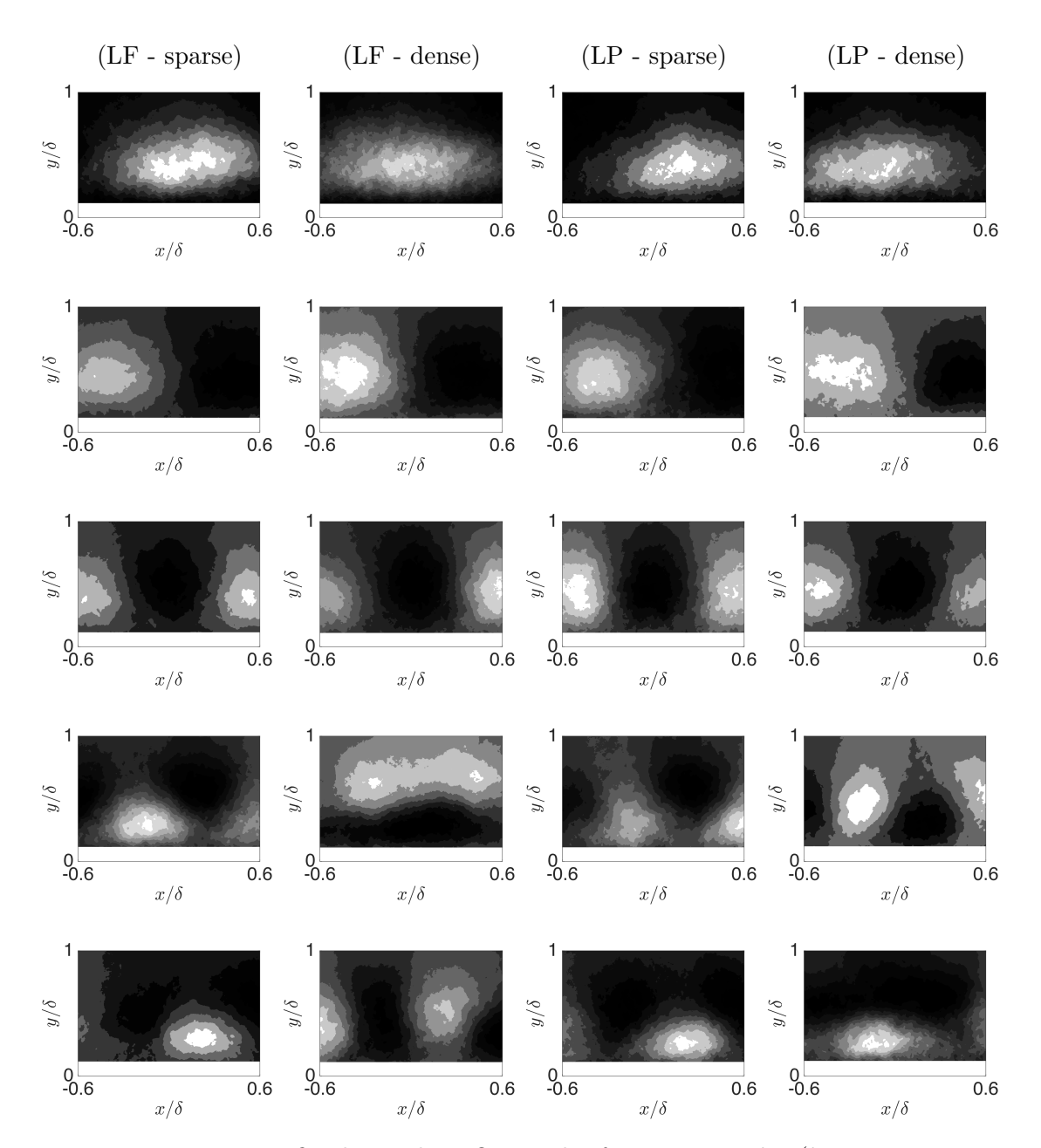


Figure 4.16: First five low-order POD modes for increasing  $\lambda_F$  ( $\lambda_P = const = 0.27$ ). Cases: LF2 (left), LF5 (centre-left), LP2 (centre-right), LP5 (right). POD modes are calculated on the (v'). Flow is left to right.

Data set	$E_1$	$E_2$	$E_3$	$E_4$	$E_5$	$\sum_{i=1}^{5} E_i$	$0.5\sum_{i=1}^{n} E_i$
LF1	5	4	3	2	2	17	48
LF2	6	5	4	3	3	20	38
LF3	6	5	4	3	2	19	42
LF4	6	5	4	3	2	19	43
LF5	7	5	4	3	3	22	31
LF6	7	5	4	3	3	21	33
LP1	7	6	4	3	3	22	33
LP2	6	5	4	3	3	20	38
LP3	6	5	4	3	3	19	44
LP4	5	4	3	2	2	18	45
LP5	5	4	3	2	2	18	47
LP6	5	4	3	2	2	18	48

Table 4.2: Fractional TKE,  $E_i$  and cumulative TKE  $\sum_{i=1}^n E_i$  content versus mode number.  $0.5\sum_{i=1}^n E_i$  refers instead to the number of modes necessary to resolve the 50% of the turbulent kinetic energy contained in the flow. POD modes are calculated on the (v') field only.

#### 4.3.7 Reduced model

To shed some light onto which particular size structures are responsible for the lack of similarity discussed herein, a reduced model based on the proper orthogonal decomposition was generated. The advantage in using the POD is that the basis functions can be used to low and high-pass filter instantaneous velocity realisations (Wu and Christensen, 2010; Wu, 2014). Low-order velocity (i.e. large-scale) are therefore generated by reconstructing each individual fluctuating velocity fields using the first most energetic  $\phi_{i-th}$ POD modes that guarantee to contain 50% of the TKE (Wu and Christensen, 2010). This number, although varies across the different cases, is a reasonable comparison, as it is based on the definition of POD basis. The residual between this low-order model and the original field is classified as the small-scale field (i.e. high-order). This residual, by definition, still contains the 50% of the energy, but this TKE contribution is spread over a much larger number of modes. Once both the low and high-order realisations are constructed, the vector fields can be averaged over the FOV and 2D statistics for the large and small-scales contributions to be estimated. This allows us to determine whether the breakdown of the similarity is due to large or small-scales contributions. In other words, whether the surface morphologies act to modify the behaviour of the large, small or both scales, inducing a lack of collapse in the turbulent statistics. The POD calculation is applied to a  $\delta \times \delta$  (streamwise-wall-normal) FOV. Previous studies (Wu and Christensen, 2010) used POD mode calculations performed over the combined (u',v') data. In the current flow conditions, the wall-normal velocity fluctuations are significantly lower in magnitude than the streamwise fluctuations. If POD modes were calculated over the combined (u', v') data, the (u') data would therefore be better represented, so that the energy of the streamwise fluctuations will mainly be locked into the

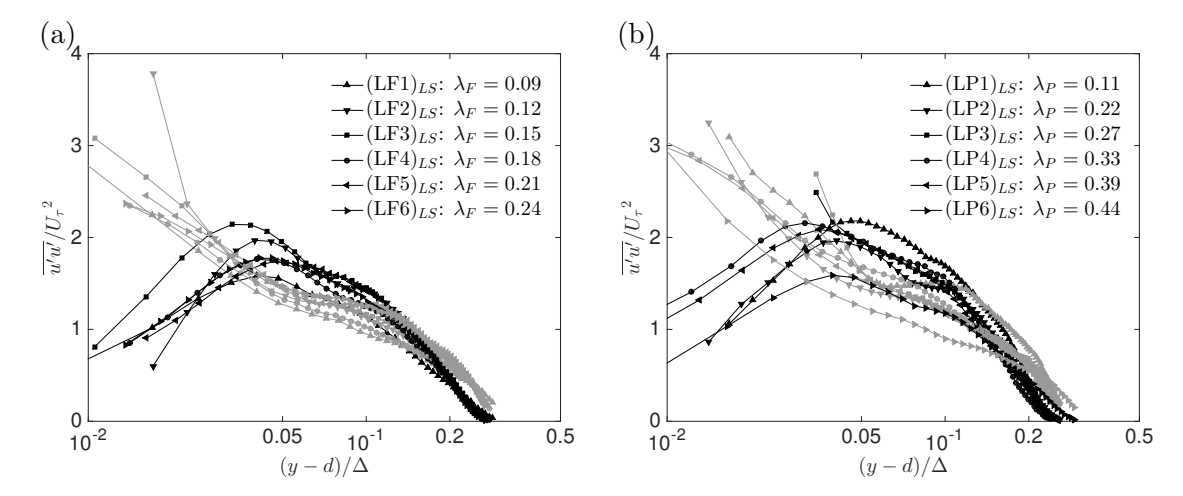


Figure 4.17: Reynolds stresses contribution from LS (black) and SS (grey) velocity fields. Streamwise velocity fluctuations,  $\overline{u'u'}/U_{\tau}^2$ , as a function of  $\lambda_F$  ( $\lambda_P = const = 0.27$ ) on the left and  $\lambda_P$  ( $\lambda_F = const = 0.15$ ) on the right. Grey symbols follow the same convention as the black.

low-order modes. To overcome this issue, the POD calculation is here performed on the (u') field, (v') field and (u',v') field separately for the streamwise, wall-normal and shear stress reduced model calculations. This procedure guaranties that the energy content of the low and high-order reductions are truly dependent on the velocity magnitudes, rather than on the decomposition.

Results of this procedures for the streamwise velocity,  $\overline{u'u'}/U_{\tau}^2$ , are presented in figure 4.17; the left side figure shows results for  $\lambda_F$  variation while the right hand side figure for the  $\lambda_P$  cases. In all cases, the higher-order model (i.e. Small-Scales (SS)) seems to be responsible for the most of the TKE close to the wall. These structure then lose importance in the log-region and are comparable to the contribution of the large scale in the outer region. The opposite behaviour is found for the Large-Scales (LS). These findings are in contrast with previous studies, where opposite trends were found for the LS and SS in the wall-normal and streamwise velocity fluctuations. Wu and Christensen (2010) reported that (for both smooth and rough-wall cases) only a small fraction of (v') field was carried by the larger spatial scales. This is believed to be an effect of the procedure they followed, which was applied on the combined (u', v') field.

For the surfaces examined herein it can be concluded that both the reduced and the residual model, i.e. both the large and small scale streamwise velocity fluctuations are responsible for a lack of collapse across the wall-normal range. Similar conclusions can be drawn examining the wall-normal velocity fluctuations and the Reynolds shear stresses, therefore these are here omitted. In other words, the breakdown of the similarity does not seem to be uniquely due to either of these structures. These findings indicate that the effect of surface morphology is reflected in both large and small-scale structures, which are both affected by the wall morphology.

#### 4.3.8 Influence of roughness' pattern

Thus far, only cases with varying  $\lambda_F$  at a fixed  $\lambda_P$  and vice-versa were compared. This relies on the assumption that the these two density parameters are sufficient to unequivocally describe a rough-wall and its properties. Nevertheless, it is worth exploring this roughness characterisation via investigating the bulk behaviour of two cases that have the same  $\lambda_F$  and  $\lambda_P$  but have different elements' pattern. This can be done by comparing case LF3 with LP3, both of which have the same frontal and plan solidities but different roughness elements' patterns (see figure 2.5(b)). The effect of pattern on the mean velocity profiles in inner scales for the two different cases is compared in figure 4.18(a). A clear difference is visible between the cases, where the LP3 case generates a higher momentum deficit and, therefore, higher drag. From table 3.1, it is clear that  $y_0^+$  is 29 for LP3 while it is only 24 for LF3. Therefore, the roughness length generated by a surface morphology seems to be dependent on both solidities and additionally, on the roughness pattern. This is in agreement with Cheng et al. (2007). Figure 4.18(b) presents the normalised mean velocity profiles in defect form. A reasonable collapse is revealed throughout the outer layer,  $(y-d)/\Delta > 0.05$ , suggesting the presence of similarity in the mean flow. Moreover, a similar collapse is obtained when comparing the streamwise and wall-normal turbulent fluctuations in figure 4.18(c). Finally, figure 4.18(d) investigates the Reynolds shear stresses and suggest that a significant lack of similarity is present for  $(y-d)/\Delta < 0.15$ , where the LP3 case shows considerably higher values of Reynolds stresses closer to the wall. Based on these preliminary results, we can conclude that the pattern of roughness plays an important role in fixing the bulk properties of the flow (i.e. drag) as well as in the validity of the outer-layer similarity.

#### 4.3.9 Influence of roughness' geometry

Preliminary tests were also carried out to evaluate whether or not the geometry of the roughness elements, used to build the different patterns, also has an influence upon the bulk behaviour of the flow. Although it is rather intuitive that different shaped elements would differently perturb the flow in their vicinity, the scope of these tests was to investigate in particular the log-law shift, and hence the skin friction generation. To do so, very similar patterns were used, although different element geometries (rectangular and cylindrical bricks) were adopted. The frontal and plan solidities were matched. The mean velocity profiles in inner and outer scales are presented in figure 4.19(a) and (b) respectively. The rectangular and cylindrical elements are found to generate a significantly different bulk drag. The difference in  $y_0$  for the two cases is around 20%, with the rectangular elements generating higher drag, perhaps not surprisingly. When plotting the mean velocity profiles in outer scale in figure 4.19(b), a remarkable collapse of the different surfaces is achieved over the entire  $(y-d)/\Delta$  range. Next, the streamwise and wall-normal turbulence intensities and the Reynolds shear stresses are

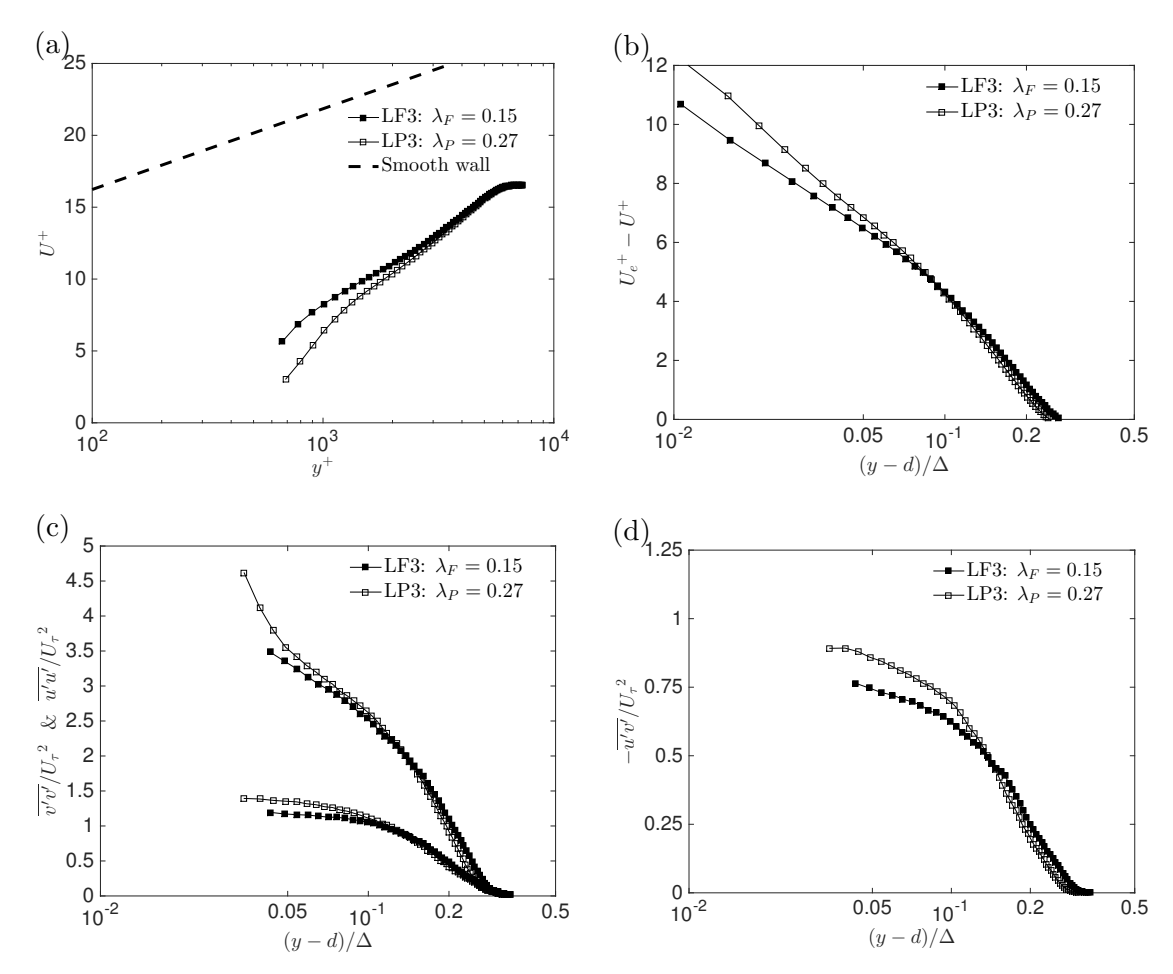


Figure 4.18: (Top) mean velocity profiles in (a) inner scales and (b) defect form at  $\lambda_F = 0.15$  and  $\lambda_P = 0.27$ . (Bottom) wall-normal variation of (a) streamwise,  $\overline{u'u'}/U_{\tau}^2$ , wall-normal turbulence intensities,  $\overline{v'v'}/U_{\tau}^2$ , and (b) Reynolds shear stress,  $-\overline{u'v'}/U_{\tau}^2$ , at  $\lambda_F = 0.15$  and  $\lambda_P = 0.27$ . Different roughness patterns. Markers are spaced every five vectors for clarity.

shown in figure 4.19(c) & (d) respectively. All these second order statistics show a good collapse across cases over the outer layer, i.e.  $(y-d)/\Delta > 0.05$ , although the streamwise velocity fluctuation present slightly higher differences particularly in the near-wall field.

To conclude, both the geometry and the distribution of the roughness elements are shown to significantly affect the bulk drag. The roughness' pattern, however, showed a greater influence on the turbulence statistics. Moreover, it is not clear what the mutual influence of the two parameters is, given that matching frontal and plan solidities with different elements' geometry also involves a change in the roughness' pattern. For the sake of brevity, this study will not focus on the direct effect of roughness geometry or pattern. Further research is necessary to investigate these aspects.

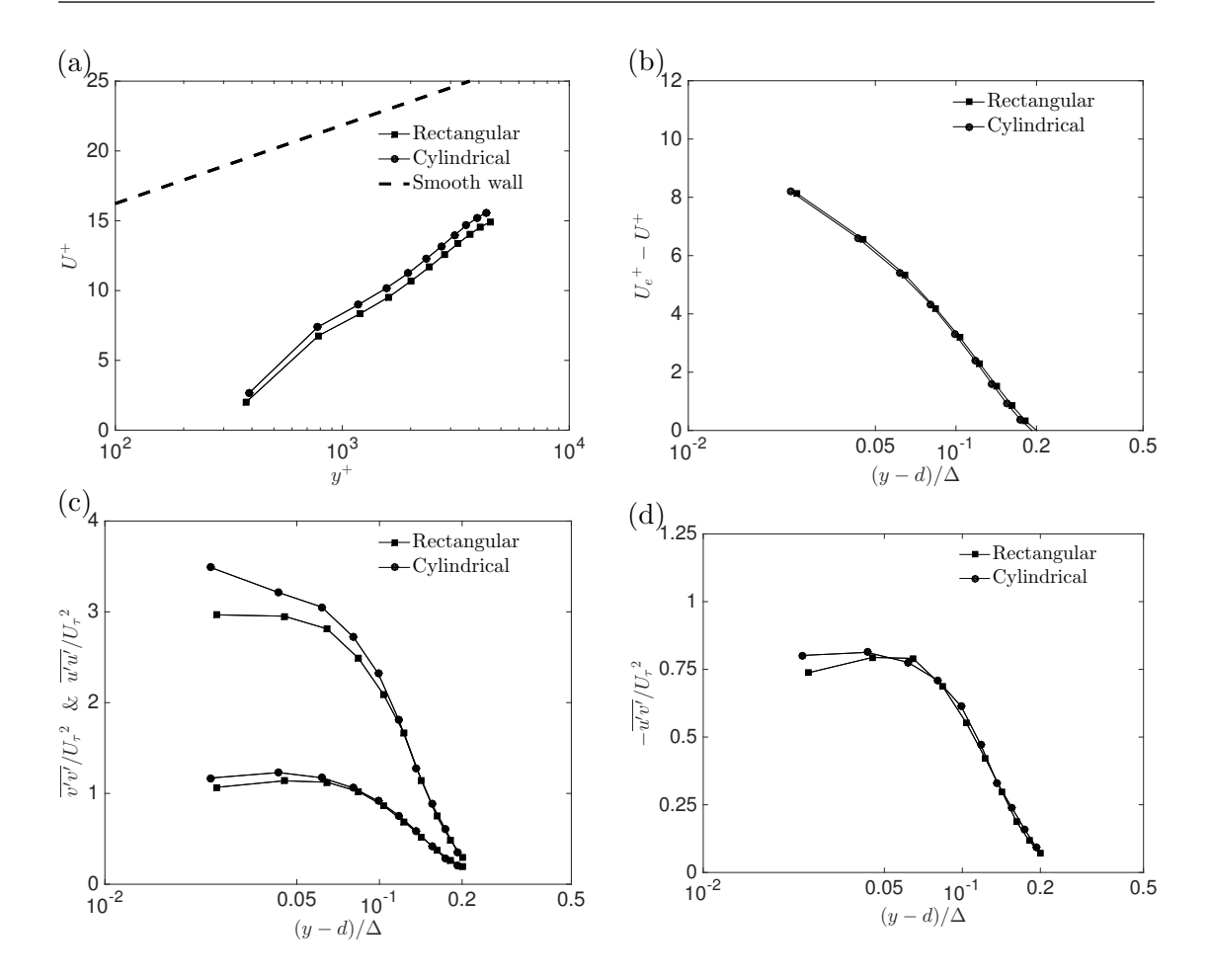


Figure 4.19: (Top) mean velocity profiles in (a) inner scales and (b) defect form at  $\lambda_F = 0.15$  and  $\lambda_P = 0.27$ . (Bottom) wall-normal variation of (a) streamwise,  $\overline{u'u'}/U_{\tau}^2$ , wall-normal turbulence intensities,  $\overline{v'v'}/U_{\tau}^2$ , and (b) Reynolds shear stress,  $-\overline{u'v'}/U_{\tau}^2$ . Markers are spaced every five vectors for clarity.

#### 4.4 Conclusions

The results presented in this chapter show the individual effect of frontal and plan solidities on the statistics of the turbulence. Mean velocity profiles in defect form conform to outer-layer similarity for different  $\lambda_F$  cases, while the collapse degrades marginally for different  $\lambda_P$  cases. This suggests that for given frontal blockage, the plan arrangement of the roughness can lead to violation of outer-layer similarity. The streamwise and wall-normal turbulent intensities as well as Reynolds shear stresses show a lack of outer-layer similarity for almost all cases considered. This suggests that for these rough surfaces with a relative height  $h/\delta \approx 0.1$ , the flow does not seem to follow outer-layer similarity, especially for higher-order quantities. This is in disagreement with the conclusions of Amir and Castro (2011) who suggested that outer-layer similarity is present up to  $h/\delta \approx 0.15$  for cube roughness. Therefore, the maximum relative roughness height for which outer-layer similarity hold depends not only on the ratios  $h/\delta$  and  $h_s/\delta$  as previously suggested (Jimenez, 2004; Flack et al., 2005), but also on the surface roughness

morphology. Quadrant analysis has also confirmed the higher sensitivity of turbulence statistics upon the solidities variations.

Proper orthogonal decomposition analysis shows that although the surfaces examined herein showed a lack in outer-layer similarity, some form of spatial universality of the flow is still present, as significantly different rough-walls exhibit virtually identical POD mode shapes and similar relative energy content. The different rough surfaces exhibit different absolute energy levels in the modes, in dependence on the solidities. This difference in energy distribution across scales could be a responsible for the breakdown of outer-layer similarity. The relative energy content in the POD modes strongly suggest that the effect of increasing  $\lambda_F$  is to redistribute a larger proportion of the energy to the highest energy POD modes (i.e. the larger-scales), while increasing  $\lambda_P$  redistributes the energy toward the smaller-scales (or higher-order POD modes).

Finally, a comparison between two surfaces with the same  $\lambda_F$  and  $\lambda_P$ , but with different element geometry/patterns is also presented. It is shown that the bulk drag is affected by both. Moreover, the turbulent organisation across cases seems to be dependent upon these two additional parameters. This strongly suggests that frontal and plan solidities along with the mean height of the roughness elements, might not be enough to fully characterise a rough-wall. Future studies are required to identify appropriate parameters which can then be incorporated in drag-prediction methods.

The current chapter has shown evidence of a lack of outer-layer similarity in the main turbulence statistics across the different surface morphologies examined herein. However, POD analysis has also revealed that the spatial organisation of the structure seems to persist across the same cases, as the POD mode shapes and sizes are consistent across the data sets. It was also shown that, although the POD modes are indistinguishable under visual inspection, their energy content is not only different across surface morphologies, but is also modulated in different ways by changes in frontal and plan solidities. It is therefore natural to investigate whether or not the surfaces in examination report further spatial similarity in the structure organisation. This is the focus of next chapter.

### Chapter 5

# Effect of surface morphology on the spatial arrangement of the turbulence

#### 5.1 Introduction and background

Chapters 3 and 4 presented evidence for a lack of spatial universality of the turbulence structures in Turbulent Boundary Layers (TBLs) both via POD modes shapes within the RSL, and the presence of distinct differences in the turbulent statistics in the outer-layer. However, the persistence of certain underlying characteristics of the turbulence organisation across the same walls was also highlighted, as the energetic POD modes shapes (calculated over the entire boundary layer thickness) were found to be identical across cases. It is therefore important, and necessary, to further investigate the spatial structure of the turbulence and its dependency on the surface features.

Early observations of TBLs indicated that streaks and vortices were found to be characteristic coherent structures of the near-wall region (Theodorsen, 1952; Hama, 1954). Farther away from the wall, the range of coherency in smooth-walls becomes hairpins, hairpin packets, Large-Scale Motions (LSMs) (Mejia-Alvarez and Christensen, 2013) and Very-Large-Scale Motions (VLSMs) (Kim and Adrian, 1999). The hairpin vortex (represented by an omega-shaped vortex with its legs close to the wall, while its head typically lifts up in the wall-normal direction) is usually considered a fundamental building block for coherent organisation. The physical basis of the formation of these structures is outside the scope of the current work. However, an exhaustive discussion can be found in Chong et al. (1990) and Zhou et al. (1999). In the current study, the term "hairpin vortex" is used to identify a series of different structures (hairpins, horseshoe, dog head or cane-shaped vortices) and randomly perturbed variants of these structures (Christensen and Adrian, 2001). Previous studies have found a systematic

vortex organisation in the outer-region in instantaneous snapshots of wall turbulence. The first experimentally-documented structures of this kind were visualised by Head and Bandyopadhyay (1981), whilst direct numerical simulations on this topic were originally conducted (at low Reynolds number) by Robinson (1991).

Subsequently, a range of studies has been carried out to document the organisation of vortical structures in TBLs. It has been shown that hairpin-like structures populate smooth-wall turbulent boundary layers at low and moderate Reynolds numbers and tend to align coherently to form large-scale structures termed "hairpin vortex packets" (Head and Bandyopadhyay, 1981; Adrian et al., 2000b; Christensen and Adrian, 2001; Ganapathisubramani et al., 2003; Tomkins and Adrian, 2003; Ganapathisubramani et al., 2005; Wu and Christensen, 2010). These packets are interpreted to work cooperatively (via mutual momentum transfer) to induce large regions of streamwise momentum deficit, thus providing a mechanism for the formation of the uniform momentum zones (Tomkins and Adrian, 2003). The importance of large-scale events in the outer region is significant, as the hairpin vortex packets have been found to contribute to a large fraction of the total stress in the boundary layer (Zhou et al., 1999; Kim and Adrian, 1999; Ganapathisubramani et al., 2003; Volino et al., 2007). Moreover, it was found that large and very large flow structures contribute to about 80% of the Reynolds stress in TBLs (Guala et al., 2012). Adrian et al. (2000a,b) also connected these hairpins to the spacing of bursts and streaks that characterise the inner-region of turbulent boundary layers. The main feature ascribed to hairpin packets are: (i) forward leading structure of streamwise velocity correlations and (ii) inclined regions of high and low-momentum (Tomkins and Adrian, 2003). It is still under discussion if, and to what extent, signatures in 2D velocity fields (as in the case of the current work and most of the experimental literature) are sufficient conditions to identify the existence of these packets. This topic is outside the scope of this thesis, therefore, more conservatively, this discussion refers to the inclination of the velocity correlations rather than to the vortex packets' orientation. Nevertheless, for smooth-wall boundary layers, typically this inclination of the streamwise velocity correlation has been found to be in the range of  $9-13^{\circ}$  (Christensen and Adrian, 2001; Adrian et al., 2000b; Flores et al., 2007, amongst others). Christensen et al. (2005) also found that not only the inclination of streamwise velocity correlations in a smooth channel flow is approximately constant around 11° but also that the latter was unaffected by the wall-normal location and Reynolds number.

A few studies have also supported the presence of similar hairpin-like structures in the outer layer of rough-wall TBLs. This is directly related to the concept of outer-layer similarity (discussed in chapter 4), representing effectively a 3D extension of the previous results. The quest for comparable structures between smooth and rough-wall boundary layers has developed into two main areas of interest - the inclination angle of the velocity correlations and the extent of the streamwise and wall-normal correlation length scales. When comparing the structure of smooth against rough-walls TBLs, unarguably the

most important finding is contained in Krogstad and Antonia (1994). Their results indicate that major structural differences are present, and that these were associated with the average inclination of the large-scale structures. They found that, over the smooth-wall case, this inclination was less than half that of woven-mesh-roughened-wall (10° against 38° respectively). Moreover, the longitudinal length scale was found to be considerably larger on a smooth than on a rough-wall. They summarised their findings as "it would appear that the primary effect of surface roughness is to change the shape of the large-scale motion, although we have evidence suggesting that the strength of this motion may also be increased". This study seems to present the most remarkable case in which the surface roughness was found to significantly affect the spatial structure of the turbulence.

Krogstad and Antonia's (1994) findings are in strong disagreement with Volino et al.'s (2007) results for a similar mesh-roughened wall in the fully-rough regime. In their study, they reported excellent agreement, both qualitatively and quantitatively, between their mesh case and the well-documented turbulence structure over smooth-wall TBLs. The inclination angle of the velocity correlation was found to be approximately  $13.2^{\circ} \pm 2.5^{\circ}$  for the smooth-wall case, against  $15.8^{\circ} \pm 3.3^{\circ}$  for the rough-wall. Slight differences were also noted between the two configurations, in terms of the velocity correlation lengths based on  $R_{v'v'}$ ,  $R_{u'v'}$  and  $R_{\Lambda\Lambda}$  that were found to be between 10% and 20% lower on the rough-wall. Any other quantity in examination resulted in good agreement. This strongly supports the validity of Townsend's similarity hypothesis.

Although the inclination angle of the large-scale motion was found to be largely unaffected by the wall morphology, Volino et al. (2009) demonstrated that the wall-normal and streamwise extent of the  $R_{u'u'}$  correlation was significantly enhanced by 2D roughness ( $\approx 39\%$  and  $\approx 42\%$  respectively when compared to a smooth-wall). Similar enhancement is reported for both  $R_{v'v'}$  and  $R_{u'v'}$ . This discrepancy is even bigger in the  $R_{\Lambda\Lambda}$  length scales, with differences reaching up to 64%. Similar conclusions were also reported in Volino et al. (2011), where large and small 2D spanwise bars and 3D cubes are reported to have an effect on the correlation length scales, with its significance decreasing from large bars to cubes - so from highly 2D to progressively 3D roughness. Further support for the similarity between smooth and rough-wall boundary layers comes from Nakagawa and Hanratty (2001), who found good agreement in the inclination angles of a boundary layer developed over sinusoidal wavy surfaces, when compared to reference smooth-wall cases. This agreement extends to both inclination of velocity correlations  $(\approx 9^{\circ})$  and correlation length scales (across both the streamwise and wall-normal directions). Wu and Christensen (2010) also reported reasonable similarities between rough and smooth-wall boundary layers. In particular the streamwise-elongated inclined nature of  $R_{u'u'}$  in the (x,y) plane, is found to be maintained in the rough-wall flow, as is the smaller-scale character of  $R_{v'v'}$ . The same similarity extends to the spanwisealternating, streamwise-elongated positive and negative momentum regions, previously reported in smooth-wall flows.

Given the results in the previous chapters, and the lack of outer-layer similarity of turbulent statistics across the different surface morphologies examined herein, this chapter aims to further investigate how the different surface morphologies influence the spatial organisation of the turbulence.

### 5.2 Two-point correlation

Two-point spatial correlations at the wall-normal location  $y_{ref}$  are evaluated as (Gana-pathisubramani et al., 2005):

$$R_{AB}(y_{ref}) = \frac{\overline{A(x, y_{ref})B(x + \Delta x, y_{ref} + \Delta y)}}{\sigma_A(y_{ref})\sigma_B(y_{ref} + \Delta y)} = \frac{COV(AB)}{\sigma_A\sigma_B};$$
 (5.1)

where A and B are the quantities of interest at the two locations, separated by  $\Delta y$  and  $\Delta x$  in the wall-normal and streamwise directions respectively.  $\sigma_A$  and  $\sigma_B$  are the standard deviations of A and B at  $y_{ref}$  and  $y_{ref} + \Delta y$  locations. More than 3000 independent realisations of PIV are needed for convergence within 1% (Christensen and Adrian, 2001; Ganapathisubramani et al., 2005), therefore, in this study, the instantaneous velocity fields have been zero-padded (with a length of  $0.25\delta$ ) to smoothen the edges.

## 5.3 Swirling strength criteria

Given that the vortex packets' organisation seems to be a persistent characteristic of the TBLs, irrespective of the surface morphology, it is useful to further investigate the nature of these vortical structures. Identification of vortices and coherent structures is an important task in TBLs, especially when one's aim is to understand and relate the effect of the surface morphology to the structure of the turbulence. In wall-bounded turbulent flows, strong shear layers populate the near-wall region and tends to mask turbulent eddies in vorticity maps (Adrian et al., 2000a); this problem has been resolved via adopting the swirling strength method (Chong et al. 1990; Zhou et al. 1999), which discriminates between vorticity due only to shear and vorticity resulting from rotation. This method requires the three-dimensional local velocity tensor, here  $\overline{\overline{D}}(\lambda)$  to be evaluated, and its eigenvalues to be calculated in the whole domain (i.e. for each of the FOV points). This local velocity gradient tensor, in Cartesian coordinates, can be decomposed as (Zhou et al., 1999):

$$\overline{\overline{D}}(\lambda) = [\mathbf{v}_r \mathbf{v}_{cr} \mathbf{v}_{ci}] \begin{bmatrix} \lambda_r \\ \lambda_{cr} \ \lambda_{ci} \\ -\lambda_{ci} \lambda_{cr} \end{bmatrix} [\mathbf{v}_r \mathbf{v}_{cr} \mathbf{v}_{ci}]^{-1};$$
 (5.2)

where  $\lambda_r$  is the real eigenvalue with corresponding eigenvector  $\mathbf{v}_r$ , and  $\lambda_{cr} \pm \lambda_{ci}i$  are the conjugate pair of the complex eigenvalues with complex eigenvectors  $\mathbf{v}_{cr} \pm \mathbf{v}_{ci}i$ . It can be shown that the flow locally is either stretched or compressed along  $\mathbf{v}_r$ , or it swirls in the  $(\mathbf{v}_{cr}, \mathbf{v}_{ci})$  plane. The imaginary part of the complex eigenvalue is the swirling strength,  $\lambda_{ci}^{-1}$ , which is only complex for spiralling or circular streamlines. Since the full 3D local velocity gradient tensor cannot be formed (due to the 2D nature of the measurements), the results described herein use a two-dimensional surrogate form of this tensor. This is defined as:

$$\overline{\overline{D}}(\lambda)_z = \begin{bmatrix} \frac{\partial u}{\partial x} \frac{\partial u}{\partial y} \\ \frac{\partial v}{\partial x} \frac{\partial v}{\partial y} \end{bmatrix}; \tag{5.3}$$

where spatial derivatives are computed using a central difference scheme, except at the boundaries where a forward/backward difference is applied. The swirling strength, by definition, does not have a sign, as it is the imaginary part of a complex-conjugate eigenvalue (and hence always positive). However, it can be given a rotational sign based upon the local vorticity (Wu and Christensen, 2006). This "signed swirling strength" is defined as:

$$\Lambda_{ci}(x,y) = \lambda_{ci}^2(x,y) \frac{\omega_z(x,y)}{|\omega_z(x,y)|}.$$
(5.4)

This allows us to distinguish between prograde/clockwise vortices ( $\Lambda_{ci} < 0$ ) in the same sense of the mean shear (i.e.  $\omega_z < 0$ ) and retrograde/counter-clockwise vortices (for which  $\omega_z > 0$  and  $\Lambda_{ci} > 0$ ). All of the above-mentioned definitions can also be used for spanwise-wall-normal plane measurements. The only difference is that there there will not be a distinction between prograde and retrograde vortices (although there is a clockwise and counter-clockwise sense of rotation) as there is no in-plane mean-shear in the (y, z) plane.

Generally isocontours of  $\lambda_{ci}^2$  are used to identify vortical structures (Zhou et al., 1999) purely to maintain dimensional consistency with both enstrophy and other previously used qualities (i.e. Q).

#### 5.4 Results and discussion

Measurements from both (x, y) and (y, z) planes are presented in this section. Velocity correlations are computed and compared in section 5.4.1, followed by inclination angles and the extent of the correlation in both wall-normal and streamwise directions in section 5.4.2. Section 5.4.3 further explores the nature of the vortices present in the boundary layers via a population trends study based on the swirling strength criteria. Correlations of the swirl are investigated in section 5.4.4. Finally, some conclusions are drawn.

Before presenting a statistical analysis of the structures, the instantaneous snapshots of velocity fluctuations are examined. Figure 5.1(a) shows instantaneous contours of streamwise fluctuations. The presence of a forward-leaning structure of alternating high and low-momentum regions can be seen. The inclination angle of this structure is approximately 14° in the direction of the flow. Although this is only valid for this particular instant, this appears to be a recurrent feature. Figure 5.1(b) shows the corresponding instantaneous wall-normal fluctuations (at the same instant). The wall-normal fluctuations appear more localised and do not show any particular form of large-scale organisation. Moreover, the characteristic structures seem to be considerably smaller for the wall-normal velocity than for the streamwise velocity. Figure 5.1(c) shows instantaneous contours of Reynolds shear stresses from the same snapshot. The dominancy of the negative character of the u'v' product (which persists when averaging is computed), and the presence of smaller structures that characterise the shear stresses (Ganapathisubramani and Schultz, 2011) are highlighted. The snapshots presented in figure 5.1 were deliberately chosen to show some of the features of the instantaneous flow field. However, they statistically represent the majority of the instantaneous images. To highlight some of the coherent structures present in the flow, different techniques can be used (Adrian et al., 2000a,b). The Galilean decomposition is a particularly efficient decomposition to visualise vortical structures. Here, small scales vortices are spatially enhanced by subtracting a constant convection velocity<sup>2</sup>,  $U_c$ , from the total instantaneous velocity, as follows:

$$u_c' = u - U_c. (5.5)$$

This decomposition results highlighting all the vortices that are moving at the velocity equal to the imposed convection velocity. Therefore, the choice of  $U_c$  can have a dramatic effect on the visualisation of the resulting fluctuating fields. Different optimal values are typically found, and these vary with wall-normal location. There is some consensus that a convection velocity of  $0.8U_{\infty}$  will highlight the vortices in the outer region. Figure 5.2

 $<sup>^2</sup>$ Although outside the scope of this work, recent years have seen increasing effort been put into finding a better definition for a convective velocity. The reader is referred to del Álamo and Jimenez (2009) for further details.

shows a typical instantaneous vector field after a Galilean decomposition ( $U_c = const = 0.8U_{\infty}$ ) is applied. Contours of instantaneous u' are also shown in the background. Alternating high and low-momentum regions, and some vortex cores (which Adrian et al. (2000a) suggested to be imprint of harpin packets), are shown. The inclination angle of these structures in this particular snapshot is approximately 14° in accordance with findings in figure 5.1. Given the vortex organisation in the outer region, these structures are bound to leave their imprint upon the statistics of the flow (Christensen and Adrian, 2001). The most striking of them all is often considered to be the shape of the correlation of streamwise velocity fluctuations in the (x, y) plane (Adrian et al., 2000b).

#### 5.4.1 Velocity correlations

To further explore the influence of the surface morphology on the characteristic structure of the turbulence, and to quantify its extent, it is useful to compute two-point velocity correlations. Figure 5.3(a) shows contours of the two-point correlations of streamwise fluctuating velocities. Although different wall-normal locations were investigated, only results at  $y_{ref} = 0.4\delta$  are presented in this figure. A large-scale forward-leading structure of positive correlation is clearly visible revealing a structural coherence. This is consistent with presence of vortex packets (Wu and Christensen, 2006; Ganapathisubramani et al., 2003, 2005; Dennis and Nickels, 2011; Volino et al., 2007, 2009). It is impossible, without time-resolved measurements, to address to what extent each of these individual vortices remain coherent. Nevertheless, statistically, this result confirms the presence of an elongated leaning structure whose extent is not expected to change with the wall boundary conditions. This is, in fact, a similar shape to the well-documented smoothwall case (see appendix A). The angle of inclination of this structure was found to be approximately  $14^{\circ}$ , which is consistent with the observations in the instantaneous fields (figure 5.1).

The two-point correlation of the wall-normal fluctuations,  $R_{v'v'}$  is presented in figure 5.3(b) (the reference height,  $y_{ref}$ , is the same as the for the  $R_{u'u'}$ ). The correlation structure indicates that the wall-normal fluctuations is compact in both streamwise and wall-normal directions. Again, this result is consistent with the corresponding instantaneous velocity field in figure 5.1(b). The streamwise extent of the correlation is much lower for  $R_{v'v'}$  than for  $R_{u'u'}$ , as previous studies have shown (Volino et al., 2007, 2009; Ganapathisubramani and Schultz, 2011, amongst others). This is not surprising given that the streamwise velocity depends on the convection speed of the hairpin packets, whereas the wall-normal velocity does not (Volino et al., 2007). Finally, two-point correlation of the Reynolds shear stress,  $R_{u'v'}$  (centred at  $y_{ref} = 0.4\delta$ ) is presented in figure 5.3(c). In agreement with both previous findings (Volino et al., 2007), and with instantaneous snapshot in figure 5.1(c), a backward-leaning structure of strong negative correlation is reported, the extent of which is larger than the wall-normal correlation,

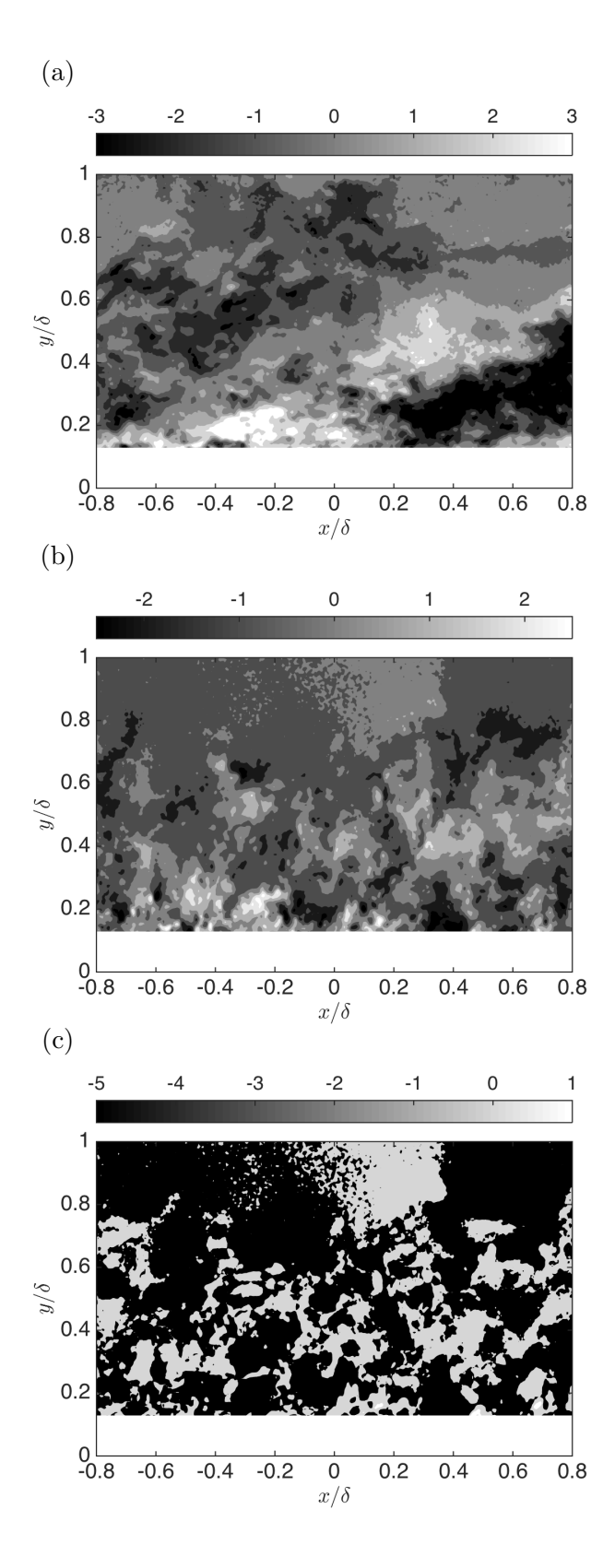


Figure 5.1: Snapshots of (a) Instantaneous streamwise, (b) wall-normal and (c) Reynolds shear stress fluctuations. Colorbar represents the normalised intensities. Flow is left to right. Example case LF4.

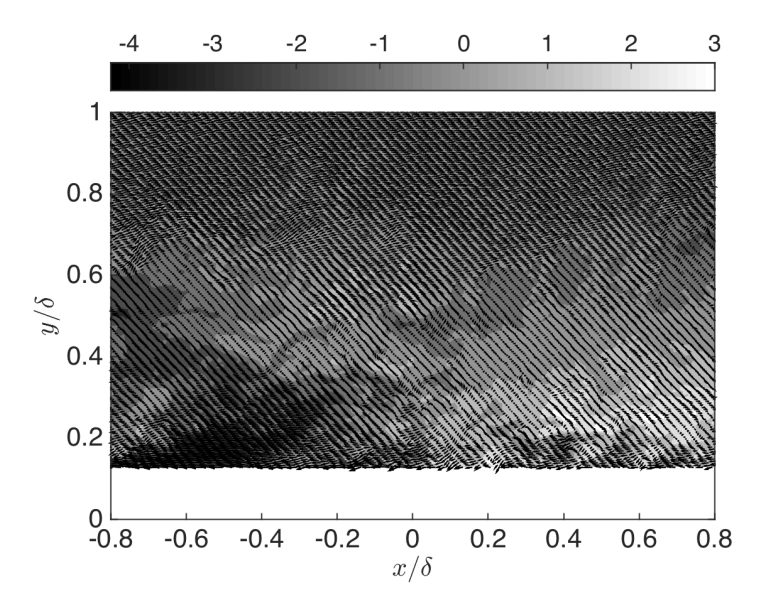


Figure 5.2: Galilean decomposition with  $U_c = 0.8U\infty$  applied to figure 5.1(a). Contour of streamwise velocity fluctuations are also shown in the background. Flow is left to right. Example case LF4.

but smaller than the streamwise coherence. It must also be stressed that, although these correlation shapes are calculated for a particular case (LF4), these findings are consistent across all cases examined herein, as the shape of the correlations do not change across the different roughness morphologies. It is also important to note that smooth-wall boundary layers are characterised by very similar attributes of these velocity correlations (see appendix A). These results compare well with previous studies (Volino et al., 2007, 2009; Ganapathisubramani and Schultz, 2011; Christensen et al., 2005; Head and Bandyopadhyay, 1981; Christensen and Adrian, 2001; Adrian et al., 2000b; Tomkins and Adrian, 2003; Nakagawa et al., 2003).

The inclination angle of the streamwise velocity correlation, which is often assumed to represent an estimate for the inclination angle of the outer-layer vortex packet organisation (Adrian et al., 2000b; Christensen et al., 2005), can be inferred by a least-square-fit procedure along the points furthest away from the auto-correlation peak at  $y = y_{ref}$ , along different contour lines. The fit is extracted along the following contour level: 0.5, 0.6, 0.7, 0.8, 0.9 (Christensen et al., 2005; Volino et al., 2007). Results are shown in table 5.1. The frontal solidity variation results in inclination angles in the range  $13 - 18^{\circ}$  and show slight sensitivity to the change in surface morphology, although a clear trend is difficult to infer. Instead, the plan solidity cases report inclination angles in a marginally lower range  $12-14^{\circ}$  and the results seem to be less influenced by the roughness morphology. This is in line with the behaviours discussed in chapter 3, where a frontal solidity increase corresponds to a flow that has to go up and over the elements, where this is not the case for the plan solidity variation. In this light, the results seem to suggest that vortex packets' inclinations could marginally depend on the nature of the roughness

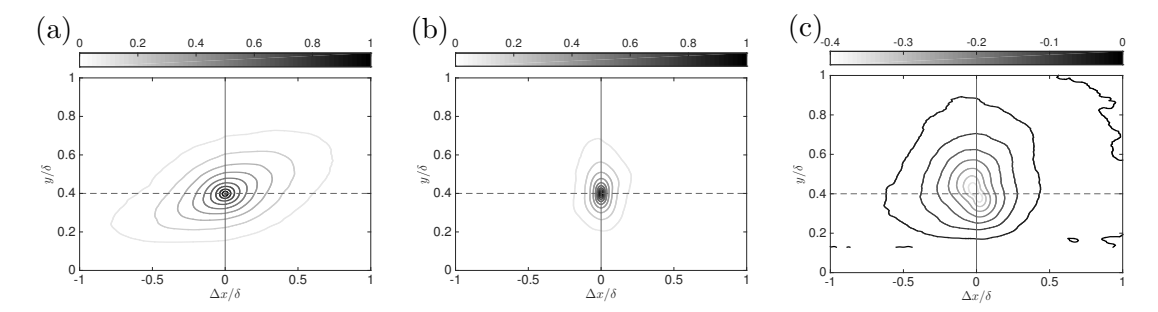


Figure 5.3: Two-point correlation of streamwise (a), wall-normal (b) and Reynolds shear stress (c) fluctuations. Colorbar represents the normalised correlation coefficient,  $R_{u'u'}$ ,  $R_{v'v'}$  and  $R_{u'v'}$ . Flow is left to right. Example case LF4.

Data set	$\alpha_{R_{u'u'}}$	Data set	$\alpha_{R_{u'u'}}$
LF1	13°	LP1	13°
LF2	$14^{\circ}$	LP2	$14^{\circ}$
LF3	$16^{\circ}$	LP3	$13^{\circ}$
LF4	$14^{\circ}$	LP4	$13^{\circ}$
LF5	18°	LP5	$12^{\circ}$
LF6	$15^{\circ}$	LP6	$13^{\circ}$

Table 5.1:  $R_{u'u'}$  inclination angles,  $\alpha_{R_{u'u'}}$ , as a function of the surface morphologies.

elements and the flow physics they induce. The current results are in line with previous findings on both smooth and rough-wall investigations, which have suggested similar order values for the characteristic inclination of the velocity correlations (Volino et al., 2007, 2009; Ganapathisubramani and Schultz, 2011; Christensen et al., 2005; Head and Bandyopadhyay, 1981; Christensen and Adrian, 2001; Adrian et al., 2000b; Tomkins and Adrian, 2003; Nakagawa et al., 2003).

The behaviour of the different walls can be further explored by taking a slice through the auto-correlation points for  $R_{u'u'}$ ,  $R_{v'v'}$  and  $R_{u'v'}$  in both streamwise and wall-normal directions. Figure 5.4(a) & (b) show the results of streamwise cuts across  $R_{u'u'}$  for  $\lambda_F$  and  $\lambda_P$  respectively. Both cases show a very good collapse. This indicates that the streamwise extent of elongated uniform momentum zones is not effected by the changes in surface morphology. Figure 5.4(c) to (f), shows streamwise cuts across  $R_{v'v'}$  and  $R_{u'v'}$  for the  $\lambda_F$  (left) and  $\lambda_P$  variation (right). These show similar collapse. Therefore, the extent of the streamwise coherence for all the Reynolds stresses is found to be largely insensitive to the surface morphology, when distances are scaled with the boundary layer thickness. This is an indication of outer-layer structural similarity, which is consistent with previous studies in the literature. However, it is in disagreement with the results in the previous chapter that showed a clear lack of similarity in the statistics for Reynolds stresses.

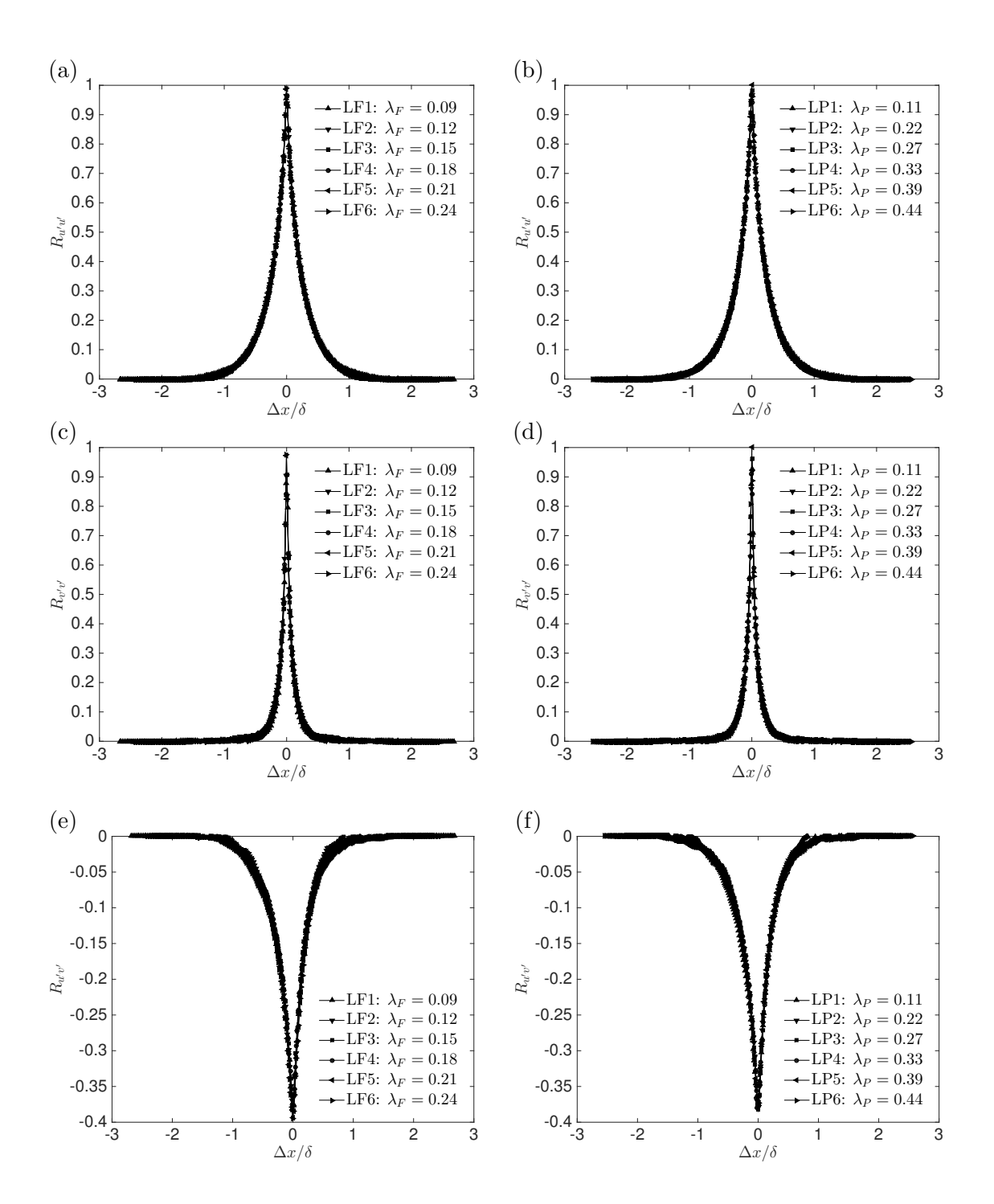


Figure 5.4: Streamwise slices through auto-correlation points of  $R_{u'u'}$  (top),  $R_{v'v'}$  (centre) and  $R_{u'v'}$  (bottom) as a function of  $\lambda_F$  ( $\lambda_P = const = 0.27$ ) on the left and  $\lambda_P$  ( $\lambda_F = const = 0.15$ ) on the right. Markers are spaced every five vectors for clarity.

Figure 5.5(a) & (b) show the results of wall-normal cuts across  $R_{u'u'}$  for  $\lambda_F$  and  $\lambda_P$ respectively. As Volino et al. (2007) has pointed out, the normalising quantities in  $R_{u'u'}$ (and similarly  $R_{v'v'}$  and  $R_{u'v'}$ ) become small near the boundary-layer edge due to the low free-stream turbulence resulting in higher uncertainty. For this reason, only data up to  $y/\delta = 0.7$  are presented. Examining figure 5.5(a), it is clear that the frontal solidity cases present a reasonable collapse across all cases, although this slightly deteriorates compared to the streamwise cuts in figure 5.4(a). These differences show that the wall-normal extent of the velocity coherence can be marginally affected by the surface morphology. This is particularly visible for  $0.1 < y/\delta < 0.3$  and  $0.5 < y/\delta < 0.7$  where an enhanced correlation is registered for an increase in frontal solidity. This shows that the increased blockage (accompanying the increase in  $\lambda_F$  from LF1 to LF6) stretches the coherence along the wall-normal direction. This effect is less pronounced in the  $\lambda_P$ cases, which for most cases appears to be more compact. This different behaviour could be due to the different mechanisms in frontal solidity, as opposed to plan solidity, as discussed in chapter 3. The behaviour for the plan solidity cases is similar across all cases expect for the LP1 case. This particular case shows a higher correlation over the entire wall-normal range. Although not conclusive, this could be due to the different relationship between vortices within the hairpin packets characterising this particularly sparse case. Adrian et al. (2000b) and Volino et al. (2007) both noticed that the interaction between larger (more mature hairpins in the outer flow) and smaller vortices, is found to be associated with the low-speed streaks in close proximity to the wall of a smooth-wall boundary layer. Therefore, the higher  $R_{u'u'}$  for the LP1 case may be indicative of this enhanced interaction over a wall with sparse roughness. On the other hand, the lower correlation value for the densest scenarios (i.g. LP6) could indicate the lack of elongated streaky structures near the canopy. Figure 5.5(c) & (d) present cuts through  $R_{v'v'}$  for the frontal and plan solidity cases. These show even smaller differences throughout all the cases, which is in agreement with previous studies that found no relevant differences in between smooth and 3D rough-wall cases (Volino et al., 2007, 2009). The trends are still maintained - an increase in  $\lambda_F$  results in an increase in coherence in the wall-normal extent, while the opposite is true for  $\lambda_P$  cases. Finally, cuts through  $R_{u'v'}$  are presented in figure 5.5(e) & (f). These also show a reasonable agreement considering the higher experimental uncertainty on the shear stresses. Nonetheless, the trends are similar to those observed in other correlations.

Following the same procedure, velocity correlation can also be calculated in the (y, z) plane - i.e. for the 3D case. To the best of the author's knowledge, this information has only been partially documented (Sillero et al., 2014), hence, a comparison with previous studies is not always available. Figure 5.6 presents correlations of the velocity fluctuation along the main directions for both frontal and solidity cases on the left and right respectively. The  $R_{u'u'}$  correlation in figure 5.6(a) & (b) shows a compact long wall-normal elongated structure, as previously documented (Sillero et al., 2014). The region of correlated data seems to be slightly more extended in the plan solidity cases

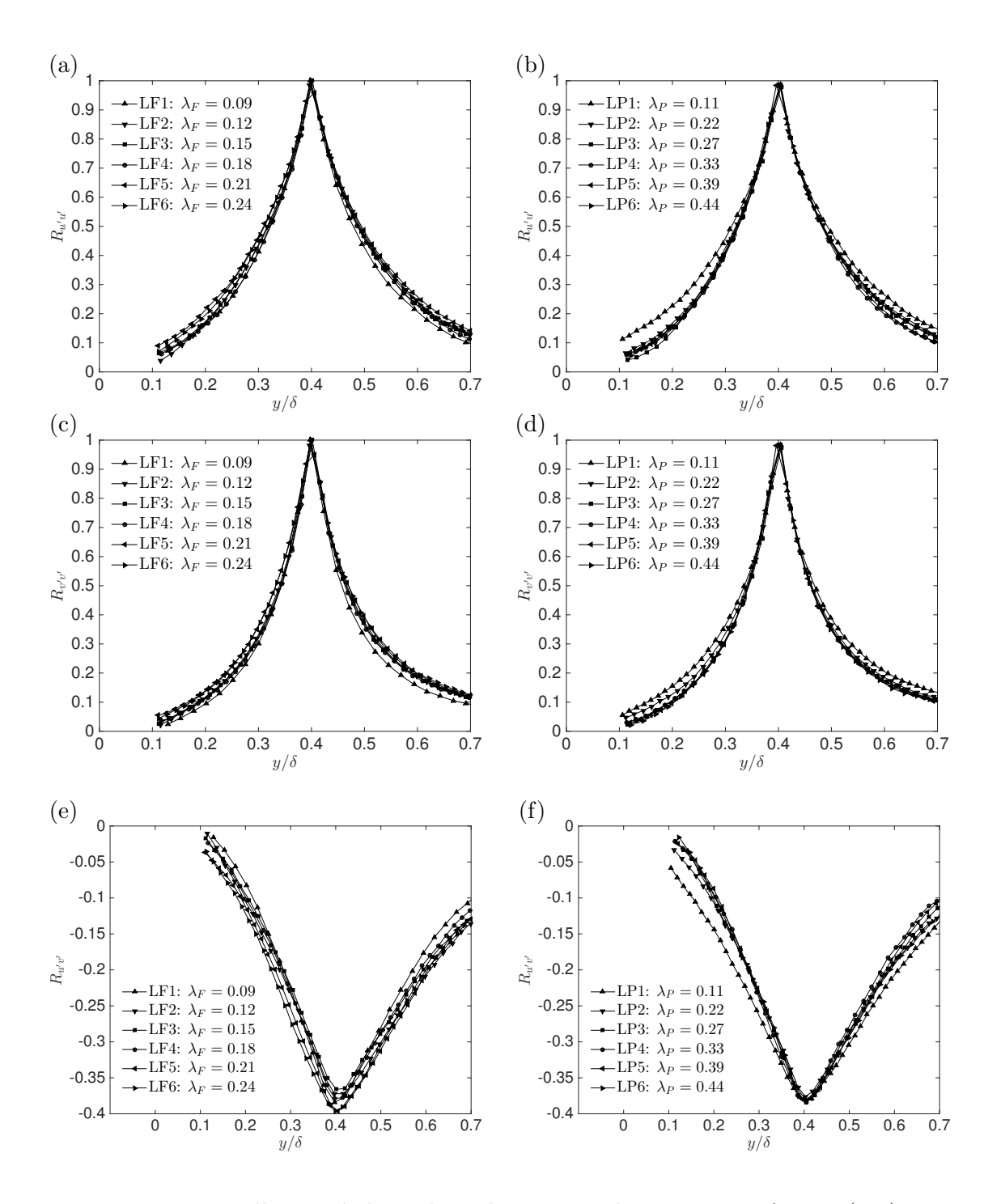


Figure 5.5: Wall-normal slices through auto-correlation points of  $R_{u'u'}$  (top),  $R_{v'v'}$  (centre) and  $R_{u'v'}$  (bottom) as a function of  $\lambda_F$  ( $\lambda_P = const = 0.27$ ) on the left and  $\lambda_P$  ( $\lambda_F = const = 0.15$ ) on the right. Markers are spaced every five vectors for clarity.

(on the right column) compared to the frontal solidity cases, although the shapes are qualitatively the same. The wall-normal fluctuation correlations in figure 5.6(c) & (d), are compact in both directions in the (y,z) plane. Finally, spanwise velocity correlations in figure 5.6(c) also show a very compact structure in both directions. This suggests that both spanwise and wall-normal velocity fluctuations exhibit compact coherence in all three directions. However, the streamwise velocity has extended coherence in the streamwise direction, to a lower extent in the wall-normal direction and is compact in the spanwise direction. When taken together, these findings are in good agreement with Sillero et al. (2014). These are also consistent with the presence of hairpin-packet-type structures that result in forward-leaning elongated low- and high-speed regions that are narrow in the spanwise direction. However, it is important to highlight that, given the nature of the data sets discussed herein (2D velocity planes), these observations should not be considered conclusive of the presence of the hairpin packets.

The cross-correlations  $R_{u'v'}$ ,  $R_{u'w'}$  and  $R_{v'w'}$  have also being calculated in the (y, z) plane and are presented in figure 5.7 at the top, centre and bottom rows, respectively. Again, the left column (a), (c) & (e) indicates results for the frontal solidity, whilst the right column (b), (d) & (f) contains plan solidity cases. The  $R_{u'v'}$  correlation is a compact streamwise structure of negative correlation elongated in the wall-normal direction, as expected since the u'v' products is, on average, negative. Correlation for  $\lambda_F$  and  $\lambda_P$  cases present very similar shapes. The  $R_{u'w'}$  correlations present a four-lobe-shaped structure centred around the auto-correlation peak. Alternating regions of positive and negative correlations are shown. This is consistent with streamwise roll modes, where a positive streamwise velocity fluctuation at the origin is correlated to inward spanwise flow above the reference point, and outward spanwise flow below the reference point. This is agreement with previous findings in smooth-wall studies. The  $R_{v'w'}$  correlation has a very similar structure to the  $R_{u'w'}$  but with inverted sign. This is not surprising since the streamwise and wall-normal velocity components have a negative correlation. This again is consistent with the observations in smooth-wall studies.

The behaviour of the different cases can be further explored by taking a slice through the auto-correlation points for  $R_{u'u'}$ ,  $R_{v'v'}$ ,  $R_{w'w'}$  and  $R_{u'v'}$  along the spanwise direction (dashed lines in figures 5.6 and 5.7). These results are presented in figure 5.8. For the frontal solidity cases (on the left column), an extremely good collapse is shown across cases for all the correlations, although  $R_{w'w'}$  presents slightly higher scatter in dependence upon the solidity. However, no clear trend is discernible. Similar behaviour is reported for the plan solidity cases on the right, although differences between cases are more marked. Cuts along figure 5.7(c) to (f) are not reported as they are not significant. Similar analysis can be carried out when cuts of velocity correlations are taken along the wall-normal direction (solid lines in figures 5.6 and 5.7). These are presented in figure 5.9 for the normal and shear stresses in (d) & (f) and (e) & (g), respectively. Wall-normal cuts along the  $R_{u'u'}$  and  $R_{v'v'}$  are compact across all cases throughout the entire wall-normal extent. Differences are only discernible in the outer region of the

 $R_{w'w'}$  cuts (figure 5.9(e) & (f)) for both frontal and plan solidity cases. This might be due to the extremely low value that this variable assumes in the outer region, hence the uncertainty in determining its correlation is high.

To conclude, the findings presented in this current section strengthen the previous conclusions in chapter 4. Although the different morphologies present a lack of similarity in the turbulence statistics across cases, the underlying spatial structure of the turbulence is only marginally affected, in accordance with most of the literature. A clear universal character of the turbulence is present in both the measurements in (x, y) and (y, z) planes. This supports the presence of a certain similarity in the characteristics of TBLs over smooth and different types of rough-walls. Moreover, these findings tie in well with the literature on the presence of hairpin vortices in TBLs over rough surfaces, as discussed in § 5.1. However, the nature of the data sets (i.e. 2D velocity fields) prevents these findings from being conclusive.

#### 5.4.2 Velocity correlation length scales

The streamwise extent of the turbulence coherence can be further explored by defining a streamwise length scale based on the cross-correlation,  $L_{xu'u'}$ , as twice the distance of the most downstream location on the  $R_{u'u'} = 0.5$  contour (Christensen et al., 2005). In the same fashion, a streamwise length scale for the wall-normal fluctuations,  $L_{xv'v'}$ , can be defined based on the autocorrelation  $R_{v'v'}$ , and so on. Figure 5.10 shows the wallnormal variation of streamwise length scale for  $R_{u'u'} = 0.5$ ,  $R_{v'v'} = 0.5$  and  $R_{u'v'} = 0.15$ contours. The 0.5 contour results are here presented, although similar conclusions can be drawn by choosing the 0.3 to 0.6 contour lines. It can be seen in figure 5.10(a)& (b) that the streamwise length scale across both the frontal and plan solidity cases tend to collapse fairly well in the outer region (i.e.  $y/\delta > 0.3$ ), where it is impossible to highlight trends as a function of the two solidities. Differences appear to be more significant closer to the wall. In particular, an increase in frontal solidity seems to be increasing the coherence of the structure for  $0.1 < y/\delta < 0.3$ . The opposite trend is found in the plan solidity variation, where the sparsest cases (LP1 and LP2 in figure 5.10(b) report the highest coherence closer to the wall  $(0.1 < y/\delta < 0.3)$ . The LP3 case does not show this behaviour for reasons which are at present unclear. These trends are also confirmed in the streamwise extent of  $R_{v'v'}$  and  $R_{u'v'}$  in figure 5.10(c) to (f). An increase in frontal solidity is accompanied by a marginal increase in the streamwise length scale, while the opposite occurs for the plan solidity variation.  $R_{u'v'}$  based length scales present the highest differences across cases. This is probably due to the higher experimental uncertainty in determining these quantities.

A similar procedure can be applied to quantify the wall-normal extent of these correlations. Figure 5.11(a) to (f) present the results for  $R_{u'u'}$ ,  $R_{v'v'}$  and  $R_{u'v'}$  for the frontal

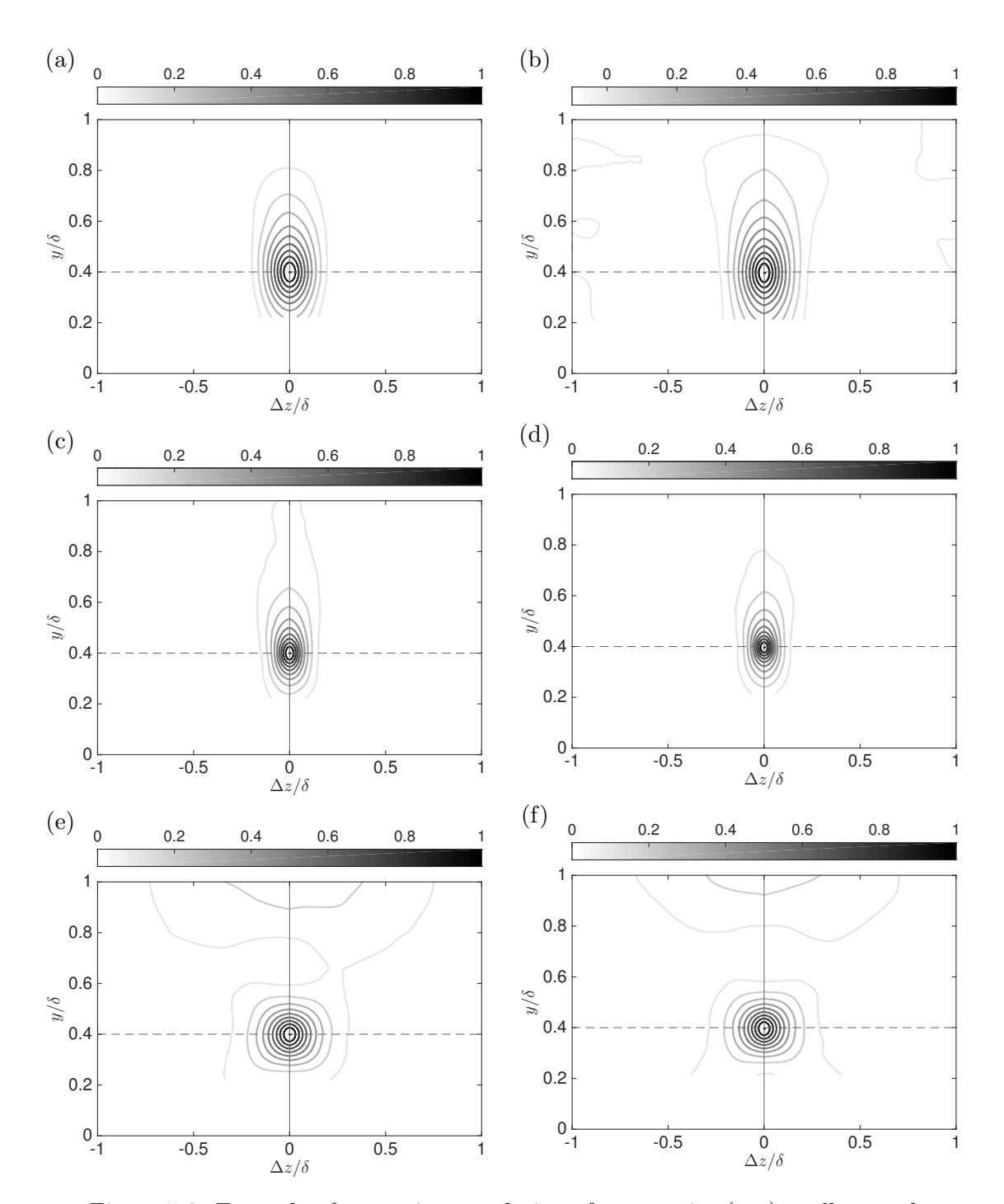


Figure 5.6: Example of two-point correlation of streamwise (top), wall-normal (centre) and spanwise (bottom) fluctuations in the (y,z) plane. Colorbar represents the normalised correlation coefficient,  $R_{u'u'}$ ,  $R_{v'v'}$  and  $R_{w'w'}$  as a function of  $\lambda_F$  ( $\lambda_P = const = 0.27$ ) on the left and  $\lambda_P$  ( $\lambda_F = const = 0.15$ ) on the right. Flow is left to right. Examples cases LF2 and LP2.

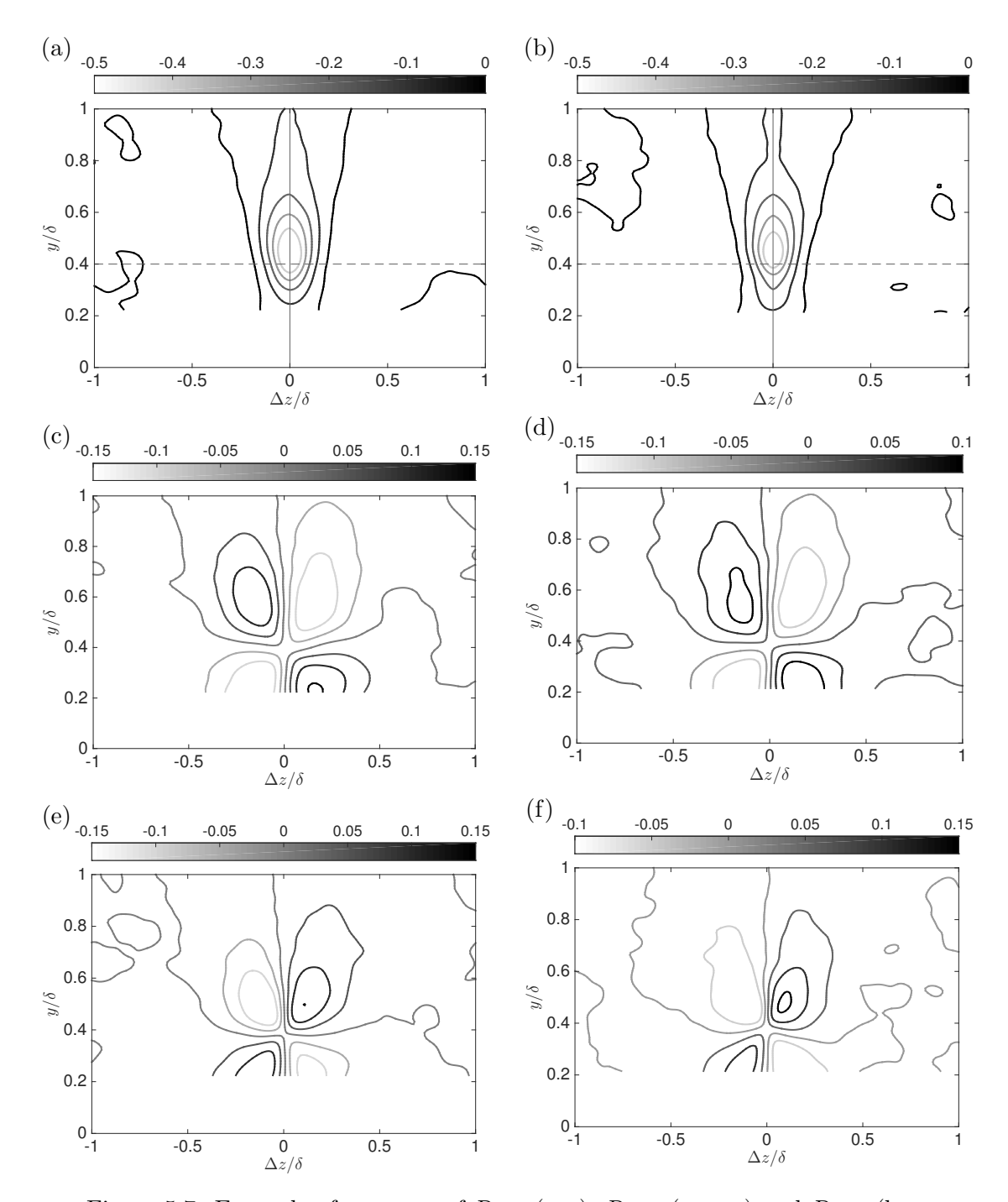


Figure 5.7: Example of contours of  $R_{u'v'}$  (top),  $R_{u'w'}$  (centre) and  $R_{v'w'}$  (bottom) in the (y,z) plane, as a function of  $\lambda_F$  ( $\lambda_P = const = 0.27$ ) on the left and  $\lambda_P$  ( $\lambda_F = const = 0.15$ ) on the right. Flow is left to right. Examples cases LF2 and LP2.

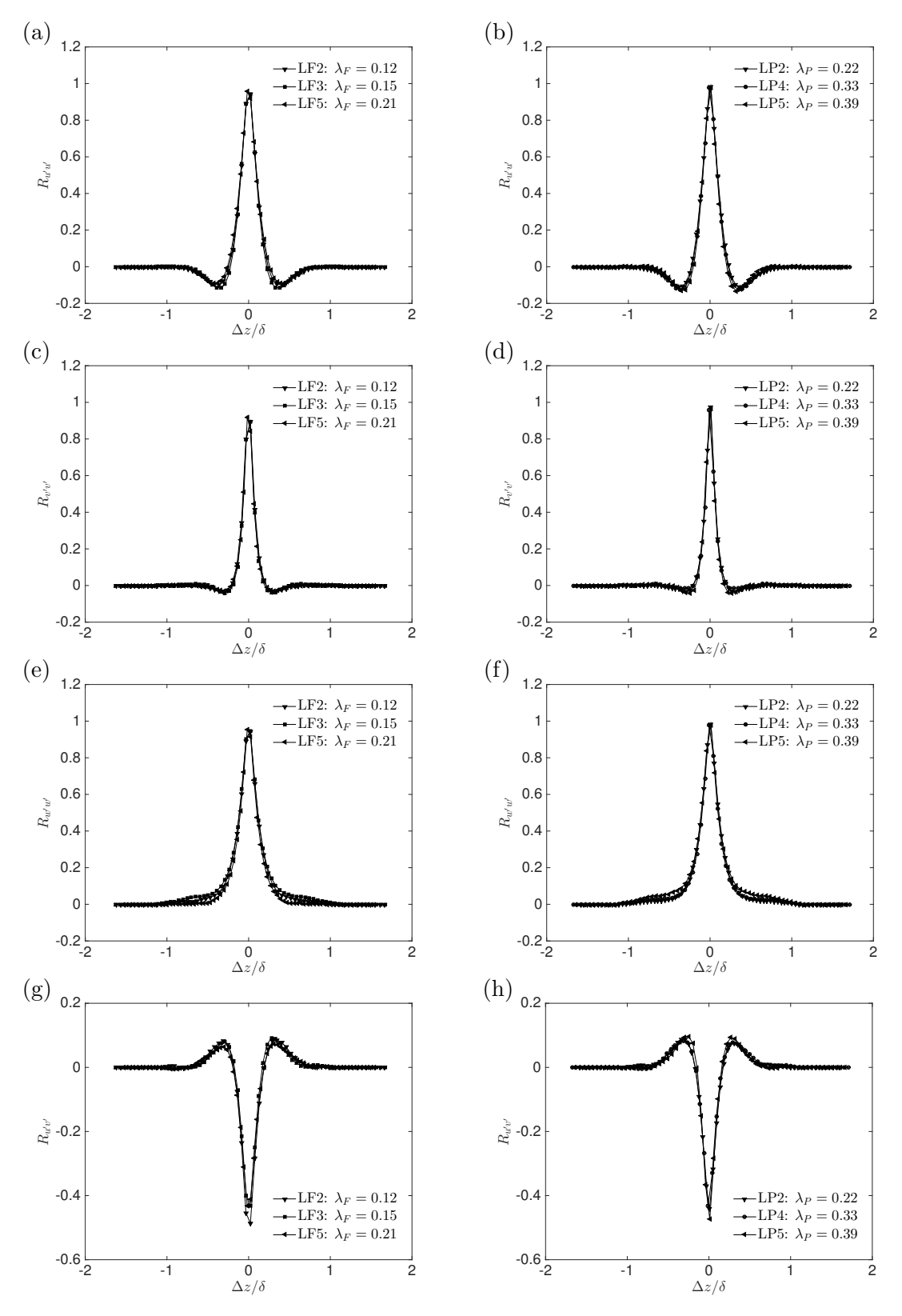


Figure 5.8: Spanwise slices through auto-correlation points of  $R_{u'u'}$ ,  $R_{v'v'}$ ,  $R_{w'w'}$  and  $R_{u'v'}$  (from top to bottom) as a function of  $\lambda_F$  ( $\lambda_P = const = 0.27$ ) on the left and  $\lambda_P$  ( $\lambda_F = const = 0.15$ ) on the right. Flow is left to right. Markers are spaced every five vectors for clarity.

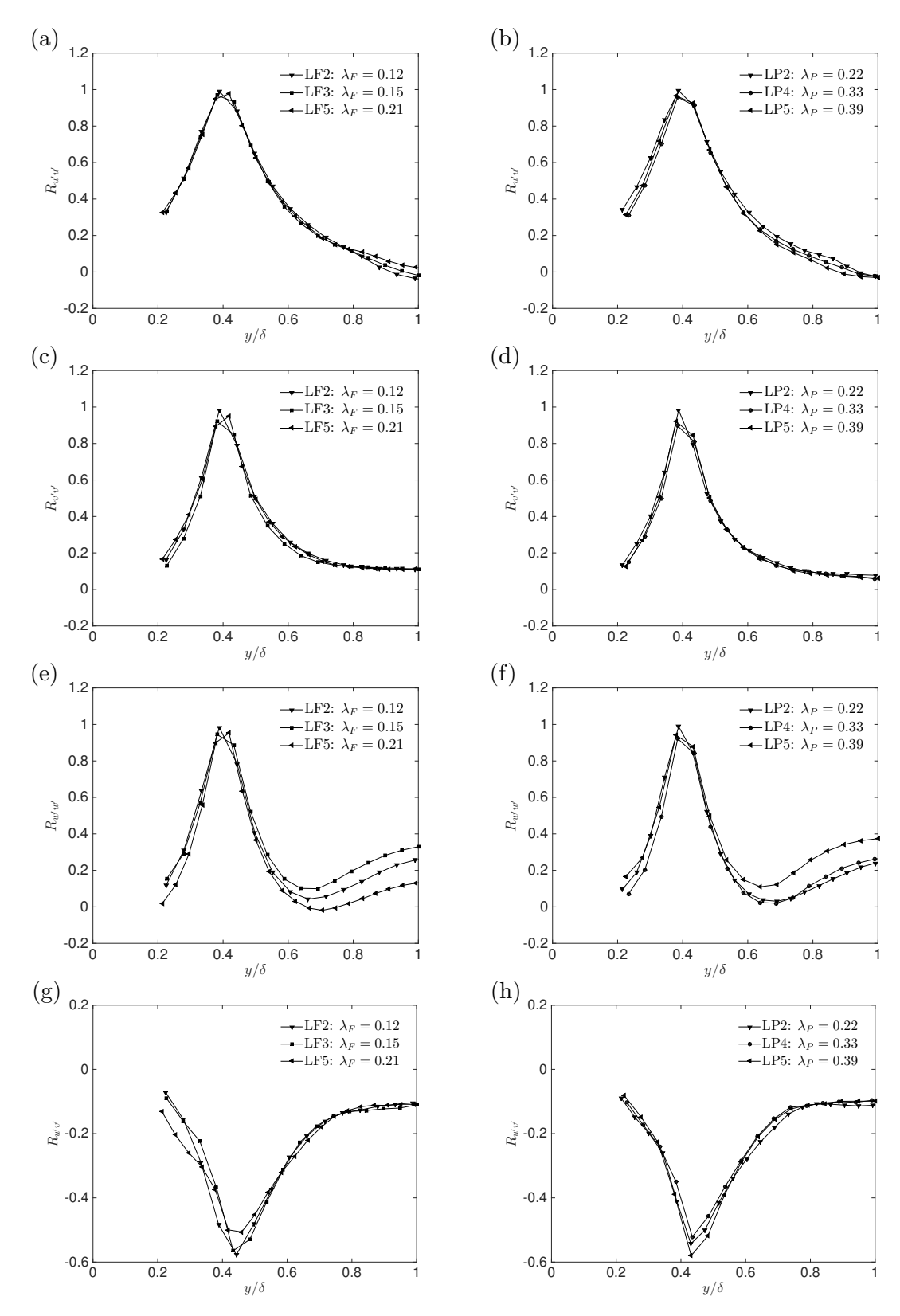


Figure 5.9: Wall-normal slices through auto-correlation points of  $R_{u'u'}$ ,  $R_{v'v'}$ ,  $R_{w'w'}$  and  $R_{u'v'}$  (from top to bottom) as a function of  $\lambda_F$  ( $\lambda_P = const = 0.27$ ) on the left and  $\lambda_P$  ( $\lambda_F = const = 0.15$ ) on the right. Flow is left to right. Markers are spaced every five vectors for clarity.

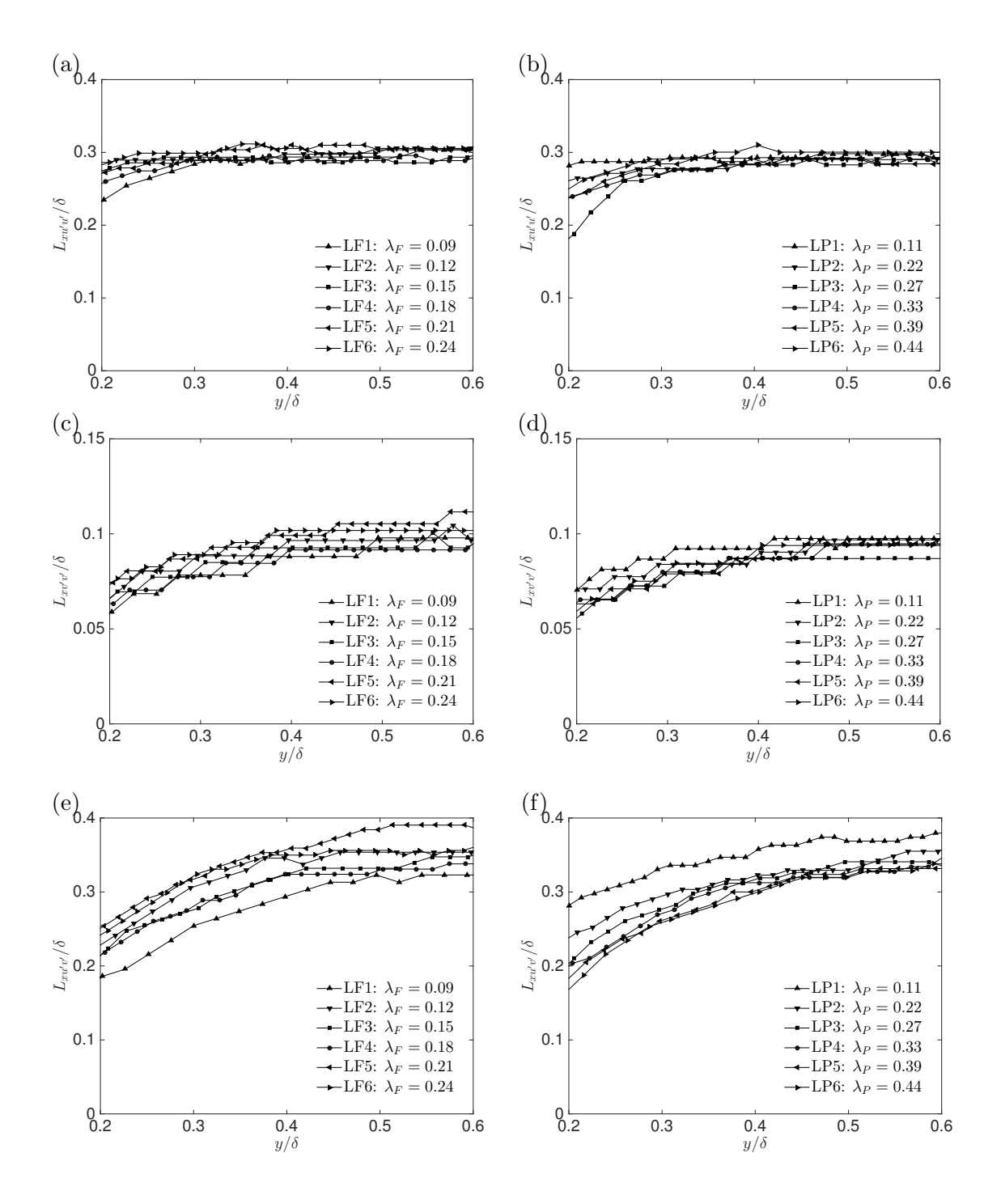


Figure 5.10: Streamwise variation of streamwise length scales based on  $R_{u'u'} = 0.5$ ,  $R_{v'v'} = 0.5$  and  $R_{u'v'} = 0.15$  contours as a function of  $\lambda_F$  ( $\lambda_P = const = 0.27$ ) on the left and  $\lambda_P$  ( $\lambda_F = const = 0.15$ ) on the right. Markers are spaced every five vectors for clarity.

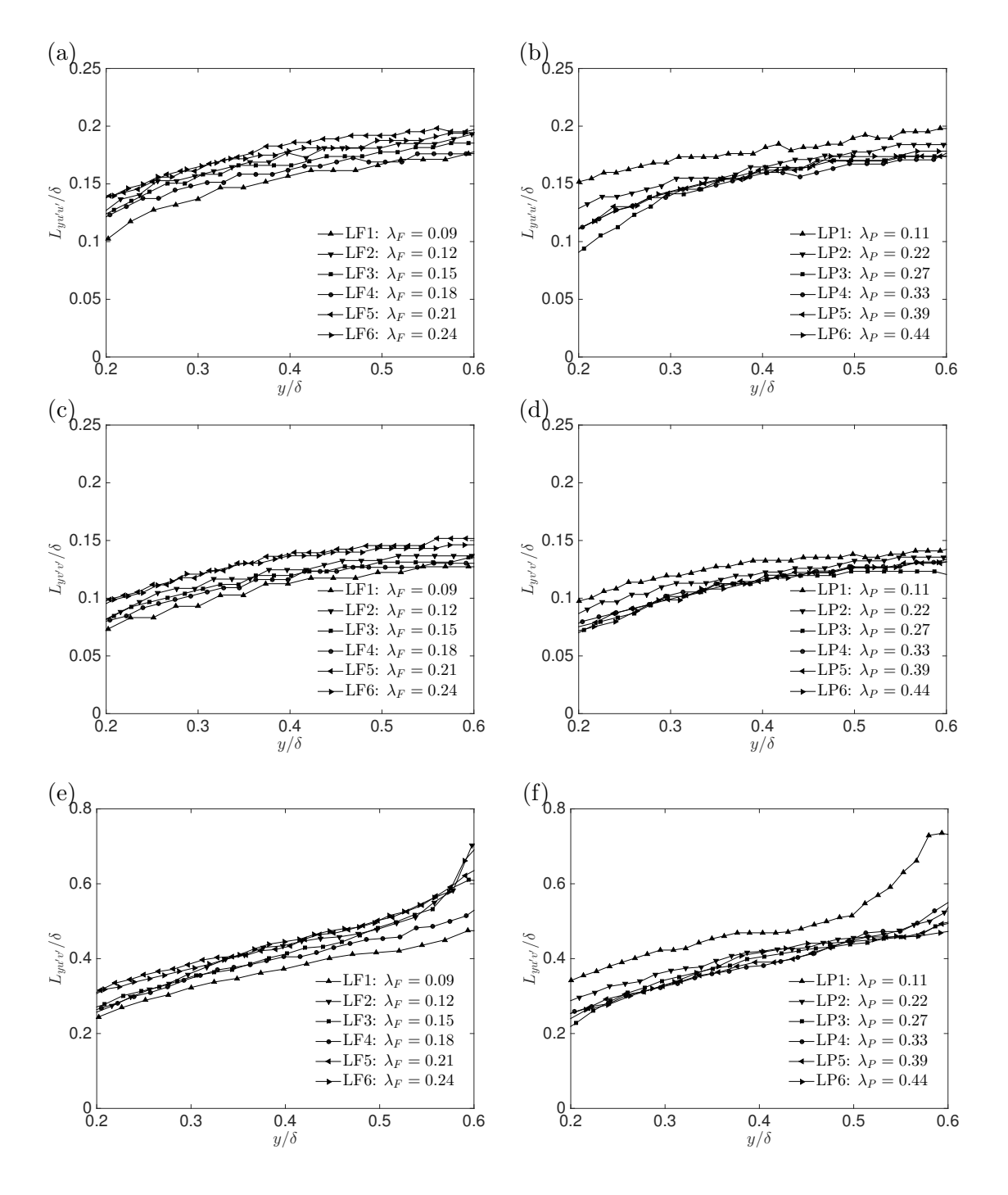


Figure 5.11: Wall-normal variation of wall-normal length scales based on  $R_{u'u'} = 0.5$ ,  $R_{v'v'} = 0.5$  and  $R_{u'v'} = -0.15$  contours as a function of (a)  $\lambda_F$  ( $\lambda_f = const = 0.27$ ) and (b)  $\lambda_P$  ( $\lambda_f = const = 0.15$ ). Markers are spaced every five vectors for clarity.

and plan solidity cases. The results for the plan solidity cases are generally more compact than the frontal solidity ones. Although it is difficult to highlight trends, higher  $\lambda_F$  (i.e. higher frontal blockage) usually results in an increased length scale. As in the previous case, the collapse of  $L_{yu'v'}$  deteriorates, possibly due to the higher experimental uncertainty affecting this quantity. Correlation length scales calculated over the (y, z) plane are here omitted; they would not add any relevant information but would merely confirm the (x, y) plane results.

To summarise the findings presented for the correlation length scales, the data shown in figures 5.10 and 5.11 have been averaged across the wall-normal range to infer trends and facilitate comparison across plan and frontal solidity cases. These results are presented in figure 5.12. It is easy to note, in this format, that the  $L_{xu'u'}$  and  $L_{xu'v'}$  assume very similar values, whilst  $L_{xv'v'}$  is considerably smaller. This ties in well with instantaneous snapshots of velocity fluctuations in figure 5.1. It is also clear that both the streamwise and wall-normal length scales based on  $R_{u'u'}$  and  $R_{v'v'}$  are fairly insensitive, on average, to the wall morphologies, as they appear flat for an increase of both solidities. Remarkably similar results are obtained from frontal and plan solidity cases. A slight sensitivity to the wall conditions seems to be present for length scales based upon  $R_{u'v'}$ . Both streamwise and wall-normal coherencies increase as the frontal solidity grows, while they decrease for variation in plan density. This behaviour closely resembles the effect that the two density parameters have on the bulk drag discussed in chapter 3. These findings predominately show that the correlation length scales and hence the structure of the streamwise and wall-normal fluctuations, are universal across different rough-walls, when scaled with the boundary layer thickness. The shear stress length scale, however, is more sensitive to the morphology of the wall.

#### 5.4.3 Population trends of vortices

Regions of non-zero swirl strength can be associated with hairpin packets (Adrian et al., 2000b; Christensen et al., 2005; Volino et al., 2007). Given that the mean shear in the flow invariably generates negative swirl events (for which  $\omega_z < 0$ ), it is important to quantify the existence and the strength of retrograde vortices ( $\omega_z > 0$ ) that appear in the boundary layer, as they act against the mean shear. Once the vortices have been identified, their occurrence and strength can be studied as a function of the wall-normal location. Figure 5.13(a) & (b) show the fraction of positive (retrograde) and negative (prograde) swirl in black and grey respectively for each wall-normal location for frontal and plan solidity variations. The negative swirl is found to be dominant throughout the entire  $y/\delta$  range as expected, as it is a direct consequence of the mean shear. Given that the latter is stronger near the wall, due to the no-slip condition on the velocity, it is not surprising that the number of prograde vortices is higher in this region, where they reach 25%, to then decrease down to 15% at the boundary layer edge. The rate of change of appearance is rapid from the wall up to  $y/\delta \approx 0.2$ , and then becomes

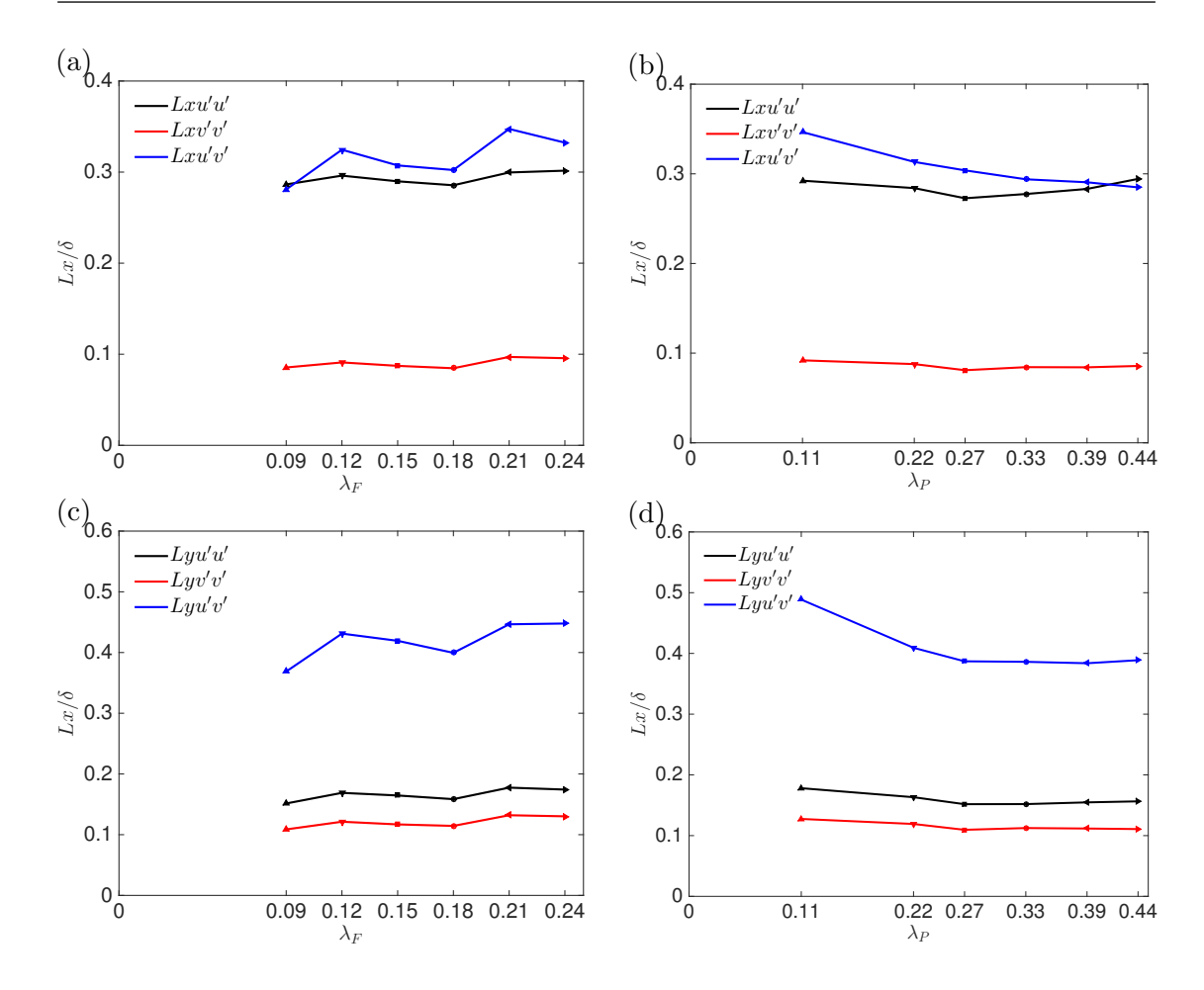


Figure 5.12: (top) Wall-normal variation trends of streamwise correlation length scales for (a) frontal and (b) plan solidities. (bottom) Wall-normal variation trends of wall-normal correlation length scales for (c) frontal and (d) plan solidities. Filled symbols follow previous convention.

more gradual further away from the surface. The opposite behaviour is found in the percentage of occurrence of retrograde vortices, where from about 5% in the near-wall region, grows rapidly up to a stable 13% in the outer region. This is in agreement with previous findings (Wu and Christensen, 2006; Volino et al., 2007). The agreement across the different  $\lambda_F$  cases is very good if one excludes the LF1 case, which generates slightly higher percentage of prograde vortices (up to  $y/\delta = 0.7$ ) and hence, a lower percentage of retrograde vortices. The collapse degrades, however, for the  $\lambda_P$  cases.

Having examined the PDFs of swirl, it is interesting to evaluate the strength of these vortices across the boundary layer. Figure 5.13(c) & (d), presents these results as a function of the frontal and plan solidity variations. It is shown that the prograde vortices (in black) are, on average, stronger that their retrograde counterpart (in grey) over the entire wall-normal range. This is particularly true near to the wall where the mean shear is the strongest. There is better collapse exhibited by the frontal solidity cases when compared to the plan solidity variations, which confirms the greater effect of the

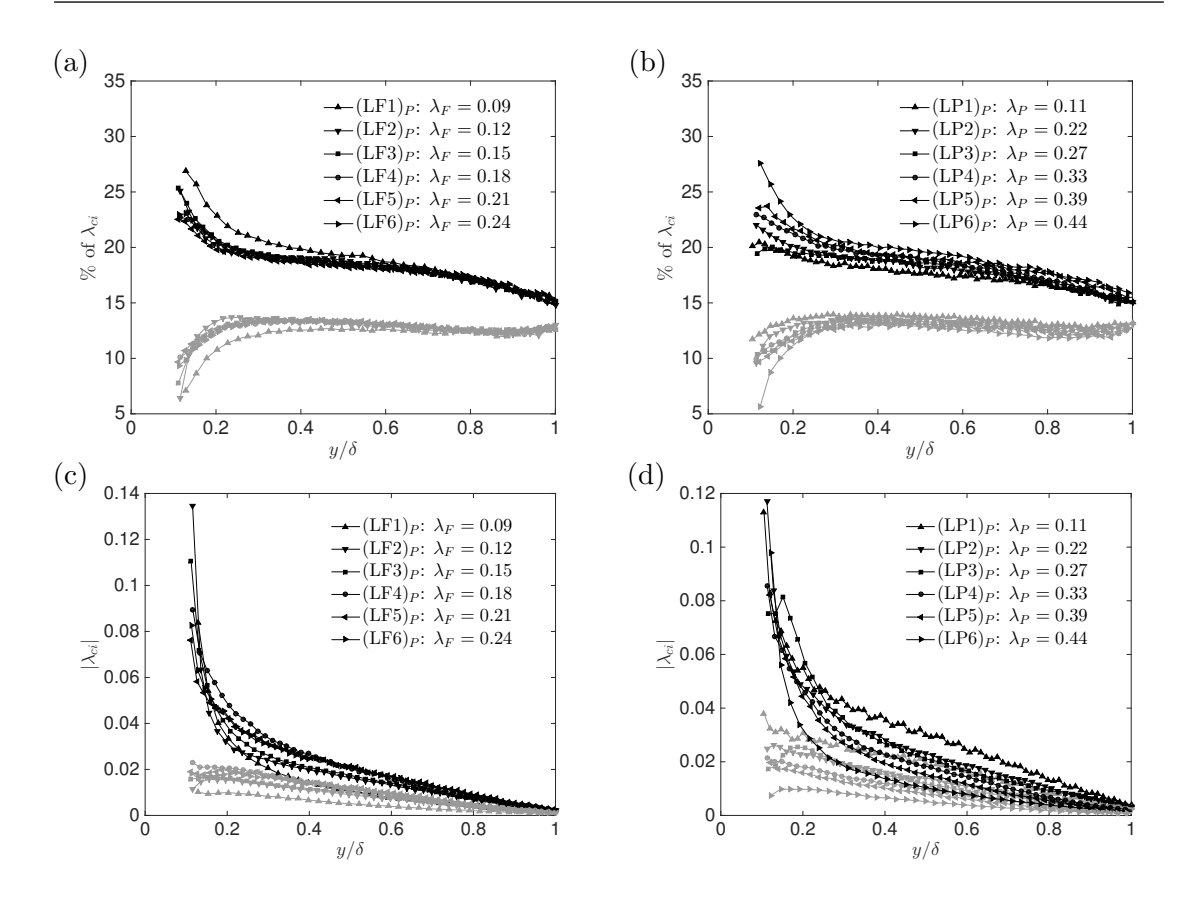


Figure 5.13: Population vortex trend in the (x,y) plane. (Top) Percentage of prograde (black) and retrograde (grey) vortices, (bottom) strength of prograde (black) and retrograde (grey) vortices as a function of (left)  $\lambda_F$  ( $\lambda_P = const = 0.27$ ) and (right)  $\lambda_P$  ( $\lambda_f = const = 0.15$ ). Grey symbols follow the convention of the black ones.

 $\lambda_P$  on the turbulence statistics, and the consequent lack of outer-layer similarity across these cases discussed in chapter 4. This suggests that, for a fixed frontal solidity, a variation in plan solidity introduces changes in the small-scales (scales that are of the size of hairpin vortices), rather than the larger-scale structures. These small-scales are sufficiently strong that they change the second order statistics sufficiently, and hence potentially lead to the breakdown of outer-layer similarity.

The same swirling strength analysis can also be applied to the (y, z) plane measurements. Given that the mean shear is not part of the in-plane gradients, the terms "prograde" and "retrograde" do not really hold. This analysis is, nonetheless, still valid. For this plane, we use the terms "prograde" and "retrograde" to indicate clockwise and counter-clockwise rotation. Figure 5.14 shows the swirling strength results for frontal and plan solidity on the left and right column, respectively. At the top, the percentage of clockwise and counter-clockwise rotating vortices across the wall-normal direction is shown. It is important to note that, although small differences are present across cases, the percentage of positive and negative vortices roughly equalise in each case. This, although far from conclusive, ties in well with the presence of hairpin packets, for which an

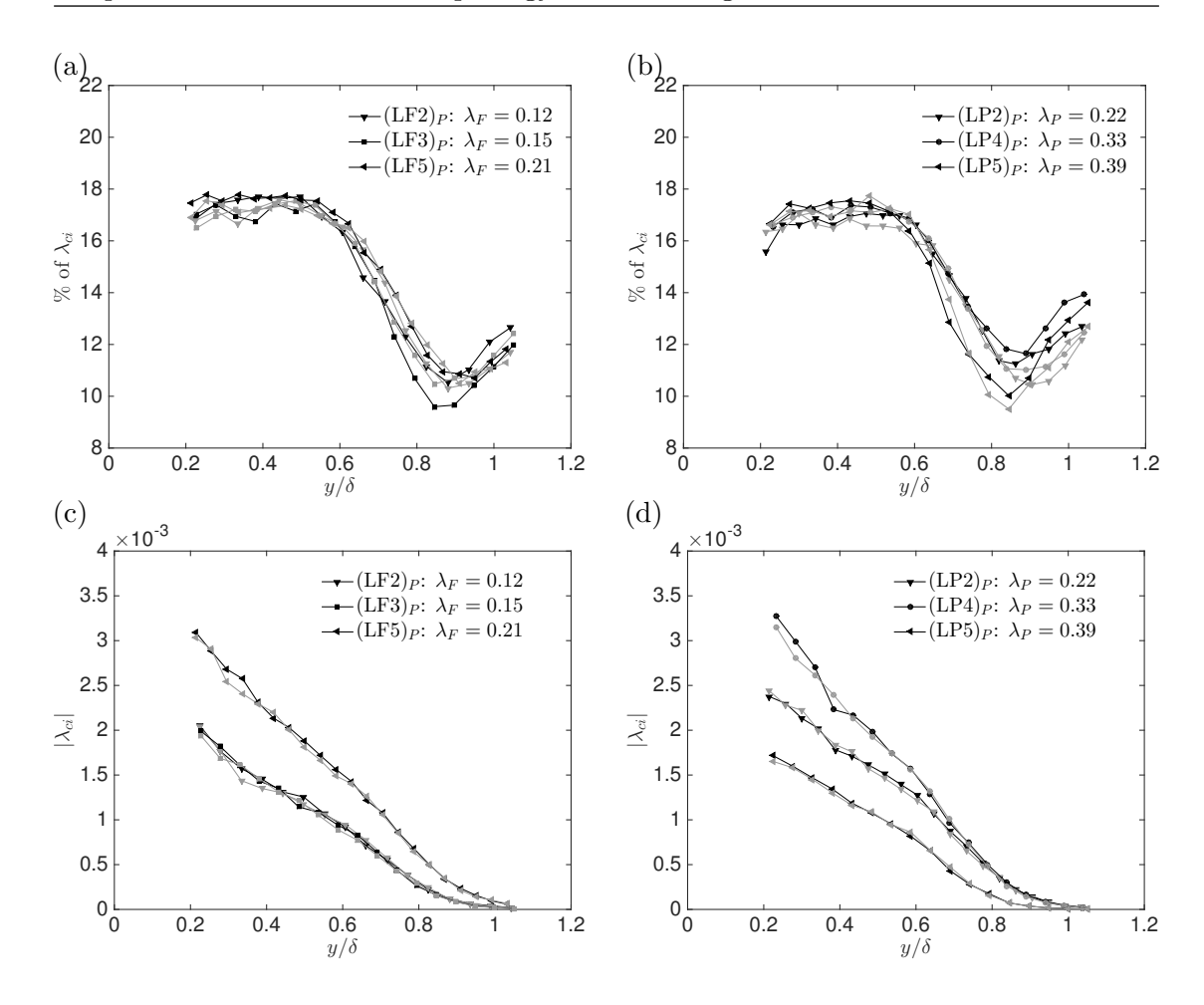


Figure 5.14: Population vortex trends in the (y,z) plane. (Top) Percentage of prograde (black) and retrograde (grey) vortex, (bottom) strength of prograde (black) and retrograde (grey) vortex, as a function of (left)  $\lambda_F$  ( $\lambda_f = const = 0.27$ ) and (right)  $\lambda_P$  ( $\lambda_f = const = 0.15$ ). Grey symbols follow the convention of the black ones.

average vortex is composed of a pair of counter rotating legs (Head and Bandyopadhyay, 1981; Adrian et al., 2000b; Christensen and Adrian, 2001; Ganapathisubramani et al., 2003; Tomkins and Adrian, 2003; Ganapathisubramani et al., 2005; Wu and Christensen, 2010). The different frontal solidity cases (left) are much more compact when compared to the effect of the plan solidity variation (right), which seems to be more dependent upon the solidity, at least in the outer-layer. This is consistent with the observations in the (x, y) plane data previously presented in this section. Just as in the previous case, we can calculate the average strength of these vortices. This is shown in figure 5.14(c) & (d). It appears that the strength of the vortices depends on surface morphology, particularly so for the  $\lambda_P$  cases. It seems that an increase in  $\lambda_P$  is accompanied by increasingly weaker vortices, while the opposite is true for the frontal solidity cases.

It is also worth discussing that, there appears to be a kick up in the number of swirls identified as we go out of the boundary layer  $(y/\delta > 0.8)$  in figure 5.14(a) & (b). This is due to the higher measurement uncertainty in the gradients in this cross-plane data.

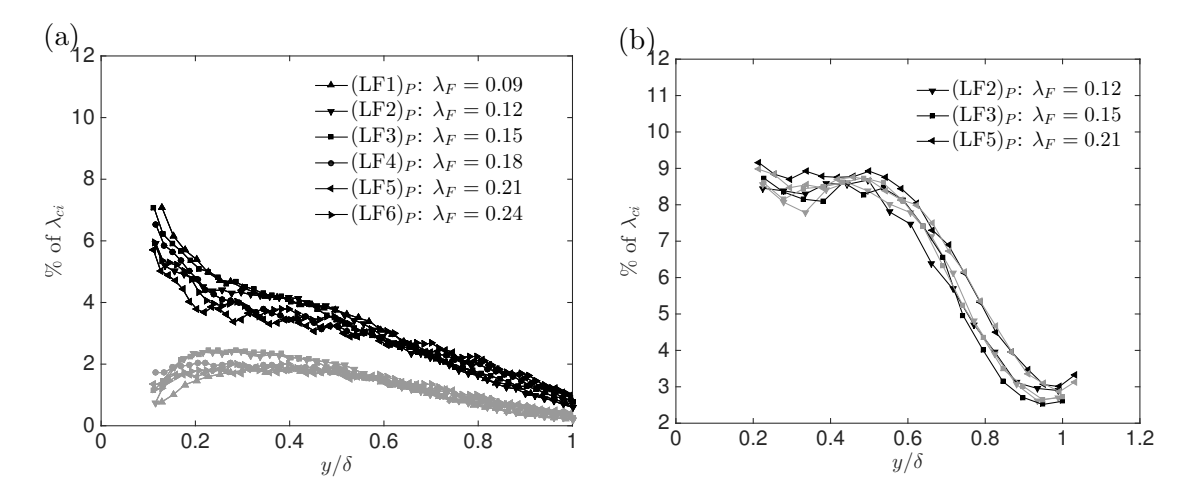


Figure 5.15: Conditioned population vortex trends in the (a) (x, y) and (b) (y, z) planes. Percentage of prograde (black) and retrograde (grey) vortex, as a function of  $\lambda_F$  ( $\lambda_f = const = 0.27$ ). Grey symbols follow the convention of the black ones.

There are no filters set for what we identify to be a vortex. Every point above a certain threshold is used to calculate the PDFs. If a spatial filter is applied to our population statistics, for example, only including a region of adjoining points with swirl greater than zero, then the increasing trend beyond  $y/\delta > 0.8$  disappears. A proof of this behaviour is provided in figure 5.15. Here, after each point (i,j) in the FOV  $(\in \mathbb{R}^{i \times j})$  is conditioned for non-zero  $\lambda_{ci}$  - vortices are considered present only if the adjoining four vectors ((i,j-1),(i,j+1),(i-1,j)) and (i+1,j) also have  $\lambda_{ci} \neq 0$ . Figure 5.15(a) shows results for the (x,y) plane. It is shown here that when appropriate conditioning is used, the occurrence of vortices in the outer-region reduces to be nearly zero, i.e. much smaller that the correspondent trend is figure 5.13(a). Figure 5.15(b) presents conditioned results for the (y,z) plane, where the above-discussed increase of vortex occurrence in the outer region, is significantly attenuated. The occurrence of the vortices in this region is also reduced to values close to zero. Although the utilities of this conditioned swirling strength analysis is evident, most of the results presented herein are based on un-conditioned statistics. This is only to facilitate the comparison with previous studies in the literature.

It is important to point out that the strength of the vortices in the two planes examined herein appears to be significantly different (see figures 5.13 and 5.14). This discrepancy is not due to the flow physics, but it is to do with the way the strength is calculated (see Wu and Christensen (2006) for further details). Therefore, a comparison across the two planes is meaningless.

#### 5.4.4 Swirling strength correlations

Following the methodology described in § 5.2, the correlation coefficient of the signed swirling strength,  $R_{\Lambda\Lambda}$ , can also be calculated. This allows us to examine whether the

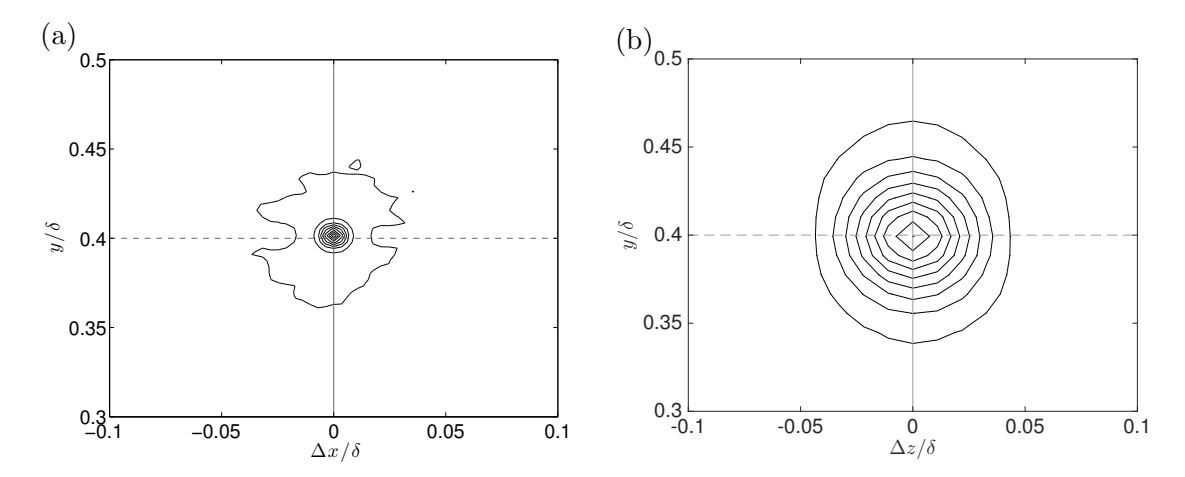


Figure 5.16: Example of swirling strength correlation coefficient,  $R_{\Lambda\Lambda}$ , (a) in the (x,y) plane and (b) in the (y,z) plane. Outermost contour  $R_{\Lambda\Lambda} = 0.1$ , contour spacing 0.1. Solid lines indicate cuts through the wall-normal location while dashed lines indicate cuts through the auto-correlation along the streamwise direction. Example case LF3.

size of the vortices discussed in the previous section change with variations in surface morphology. Contours of the auto-correlation of  $R_{\Lambda\Lambda}$  (at  $y/\delta=0.4$ ) are shown in figure 5.16(a) & (b) for both the (x,y) and the (y,z) planes. These are characterised by a small compact structure in both the streamwise and wall-normal directions. Their extent is fairly small compared to those of streamwise and wall-normal velocity fluctuations, in accordance with previous studies (Volino et al., 2007). When compared to the (x,y) planes, the extent of the correlated data in the (y,z) planes in figure 5.16(b) is much more pronounced, as it reaches a size of 0.1  $y/\delta \times$  0.1  $\Delta z/\delta$  (wall-normal-spanwise) directions. This could purely be an effect of the resolution of the cross-stream data, which is much coarser than the (x,y) plane data.

As for the velocity fluctuations, cuts through the streamwise and wall-normal directions of  $R_{\Lambda\Lambda}$  can be plotted to examine the extent of this coherency across the different cases. These cuts are indicated by the solid and dashed lines in figure 5.16. Streamwise and wall-normal slices through the origin are presented in figure 5.17(a) & (b) and (c) & (d) respectively for both  $\lambda_F$  and  $\lambda_P$ . These show good collapse across all frontal and plan solidity cases, indicating that neither the streamwise nor the wall-normal extent of the swirl coherency are affected by the surface morphology. Similar behaviour is found for cuts in figure 5.16(b), hence not shown. This further strengthens the argument that the characteristic structure of the turbulence (i.e. hairpin) and its population density are not affected by the roughness morphology. However, the strength of these small-scales might be.

Finally, to understand the relationship between a vortex core and its velocity surroundings, the cross-correlation between signed swirling strength,  $\Lambda_{ci}$ , and the streamwise and wall-normal velocity fluctuations can be evaluated (Volino et al., 2007). Figure 5.18(a)

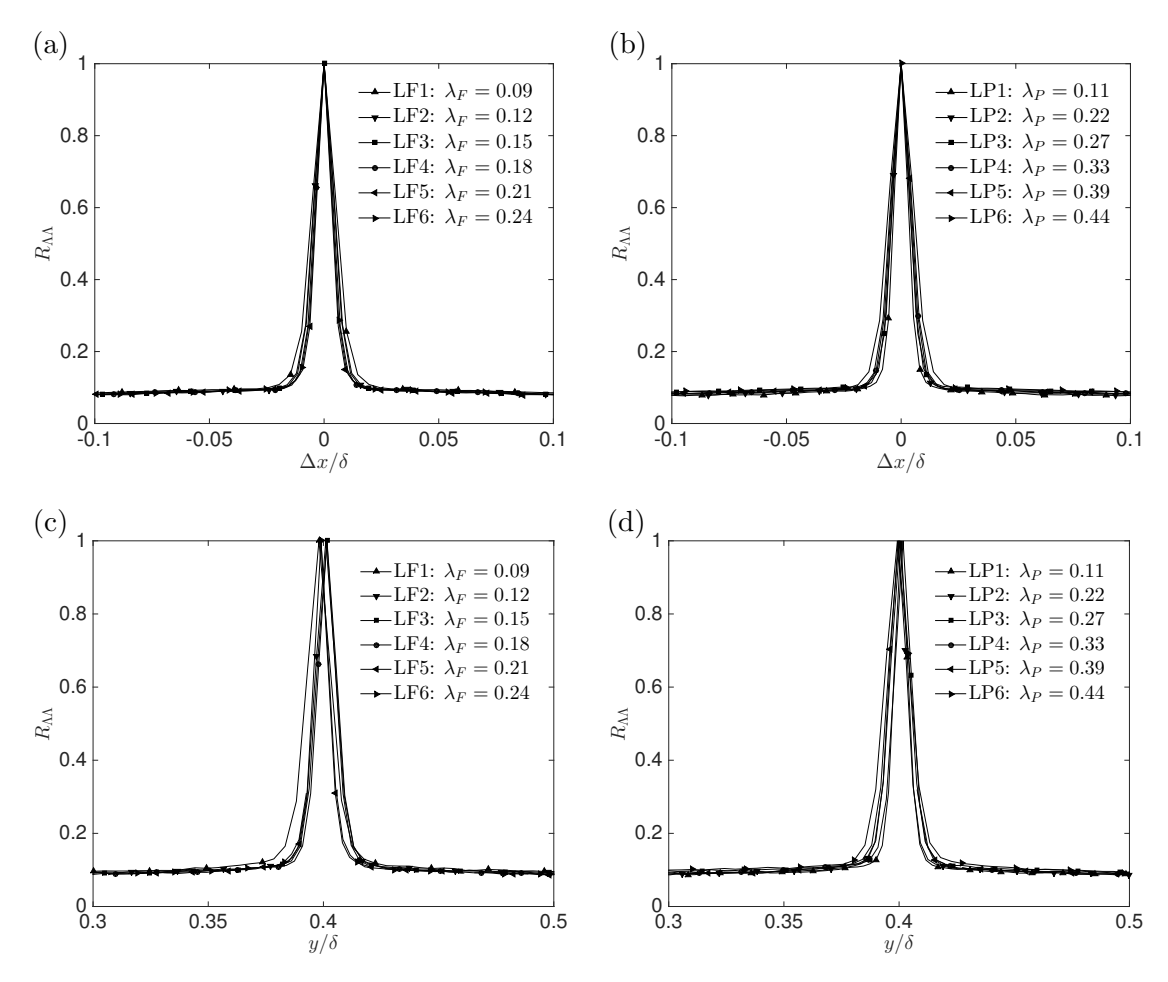


Figure 5.17: (Top) Streamwise and (bottom) wall-normal slices through autocorrelation points of  $R_{\Lambda\Lambda}$  contours in the (y,z) plane as a function of  $\lambda_F$  ( $\lambda_f = const = 0.27$ ) on the left and  $\lambda_P$  ( $\lambda_f = const = 0.15$ ) on the right. Markers are spaced every five vectors for clarity.

& (b) show contours of the cross-correlation of the signed swirl strength and the streamwise and wall-normal velocities in the (x,y) plane,  $R_{\Lambda u'}$  and  $R_{\Lambda v'}$  respectively. Both are centred at  $y=0.4\delta$  for consistency with previous results. If a head of a vortex is considered, this will induce positive u' above itself and negative u' below. Therefore, this will generate positively signed streamwise velocity fluctuation above itself and negatively signed u' below. This is highlighted in figure 5.18(a), where a positive  $R_{\Lambda u'}$  above and a negative  $R_{\Lambda u'}$  region below this vortex are shown. Assuming the presence of hairpin vortices, because they merge to form a more complex vortex packet, the region of streamwise coherence is extended. In the same fashion, a prograde vortex induces wall-normal velocity toward the wall (i.e v' < 0) and away from the wall (i.e v' > 0) downstream and upstream from its core. This behaviour is captured in figure 5.18(b). The shape and extent of these coherencies agree with both Christensen and Adrian (2001) and Volino et al. (2007). The inclination of the inclined positive-negative interface of  $R_{\Lambda u'}$  can be calculated, and it is often considered to represent the vortex packet inclination (Christensen and Adrian, 2001; Volino et al., 2007). The resulting inclination angles for each

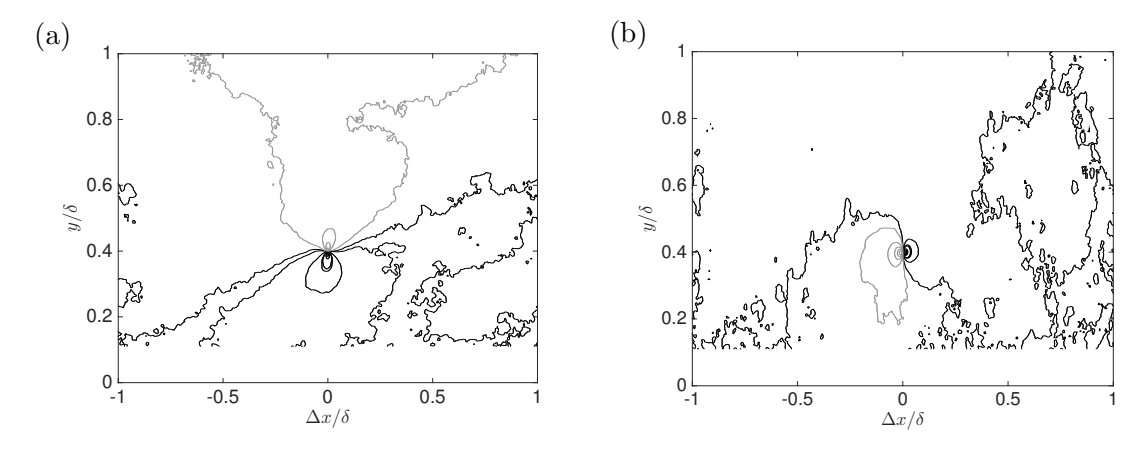


Figure 5.18: Example of contours of (a)  $R_{\Lambda u'}$  and (b)  $R_{\Lambda v'}$  in the (x, y) plane centred at  $y/\delta = 0.4$ . Contour magnitudes  $R_{\Lambda u'} = R_{\Lambda v'} = R_{\Lambda w'} = 0.01, 0.03, 0.07, 0.1$ ; contour signs black, negative; grey, positive. Examples case LF2.

Data set	$\alpha_{R_{\Lambda u'}}$	Data set	$\alpha_{R_{\Lambda u'}}$
LF1	11°	LP1	15°
LF2	$15^{\circ}$	LP2	$11^{\circ}$
LF3	$13^{\circ}$	LP3	$13^{\circ}$
LF4	$16^{\circ}$	LP4	$14^{\circ}$
LF5	$16^{\circ}$	LP5	$19^{\circ}$
LF6	$21^{\circ}$	LP6	$19^{\circ}$

Table 5.2:  $R_{\Lambda u'}$  inclination angles,  $\alpha_{R_{\Lambda u'}}$ , as a function of the surface morphologies.

case is summarised in table 5.2. These angles are fairly consistent with the streamwise correlation angles (in table 5.1) and, therefore, are in agreement with above-mentioned studies.

#### 5.5 Conclusions

The results herein presented have shown the individual effect of frontal and plan solidities on the spatial structure of the turbulence. Findings in agreement with the presence of hairpin packets are observed to be a prominent feature of the TBLs over roughwalls, as previously well-documented in the case of smooth-walls. Two-point spatial correlations of streamwise velocity were found to be coherently inclined in the flow direction, with angles which are comparable with both PIV instantaneous snapshot of the turbulence, and previous observations in both rough and smooth-wall TBLs. The turbulent structures' inclination, in disagreement with Krogstad and Antonia (1994), not only is found to be similar to previous smooth-walls data but also (and perhaps most importantly for the aims of this this thesis), is confirmed to be insensitive (within

experimental uncertainty) to a change in the frontal or plan solidities. Instead, this seems to be a rather universal characteristic of the turbulence.

The extent of the coherence of the turbulent structures, both via cuts of velocity fluctuations, and length scales (based on  $R_{u'u'}$ ,  $R_{v'v'}$  and  $R_{u'v'}$ ) are found to be remarkably similar across all the different walls examined herein. This is interesting, particularly given the lack of outer-layer similarity that was highlighted for the same surfaces in chapter 4. The structure of the turbulence results in good agreement across the surface morphologies, even when examining  $R_{\Lambda u'}$ ,  $R_{\Lambda v'}$  and  $R_{\Lambda w'}$  shapes and cuts.

Swirling strength criteria has allowed a population trends analysis on vortical structures. The results presented indicate that, although the presence of prograde vortices (in the sense of the mean shear) in the (x, y) plane is highly dominant when compared to the retrograde vortices, the latter are found to frequently populate the TBLs studied (up to 15 % statistically). Finally, the frequency of appearance of both kinds of vortices seems to be insensitive to the changes in surface morphology. However, their strength is highly modulated by the solidities. In particular, increasing the plan solidity seems to result in the creation of less effective vortices. This ties in well with the finding presented in chapter 3. The above results show that as the  $\lambda_P$  increases, the weaker the produced vortices, and therefore, as demonstrated at the start of this investigation (chapter 3), the lower the bulk drag.

# Chapter 6

# Further discussion and conclusions

Section 6.1 presents the major findings of this thesis. Some final remarks are also drawn. Section 6.2 critically looks at the analysis contained in this work and highlights limitations and shortcomings. Finally, § 6.3 suggests possible directions for future work.

## 6.1 Summary of the major findings

Some open questions regarding rough-wall boundary layers were presented in § 1.3. The current section summarises and further discusses the answers sought by this thesis.

#### 6.1.1 The bulk quantities

The current results show, for the first time, the individual effect of frontal and plan solidities on various bulk quantities in a controlled experiment. The non-dimensional roughness length (i.e. the bulk drag) reaches a peak value for  $\lambda_F = 0.21$ , while it monotonically decreases with increasing  $\lambda_P$ . This conflicts with previous results presented in the literature, which were obtained by examining the flow over cube roughness, where the effects of  $\lambda_F$  and  $\lambda_P$  are coupled. The results herein presented also highlight limitations of morphometric methods for the skin friction predictions (Macdonald, 1998). This thesis suggests that morphometric studies purely based on the geometry of roughness elements might not be accurate, as proof is provided on the importance of the pattern element distribution and the shape of the roughness itself. Further studies are suggested to identify appropriate correlations relating the geometry of the wall to the generated drag.

The floating-element drag-balance design (Krogstad and Efros, 2010) has been proven to be an indispensable means of calculating the skin friction generated by the different surface morphologies. The total stress methods in any form (Flack et al., 2005; Reynolds and Castro, 2008; Manes et al., 2011) are here confirmed to generally underestimate the drag, as in Cheng et al. (2007). This drag-balance design, although far from being a definitive solution to the skin friction estimation uncertainty, allows the latter to be reduced from 15% (when common methods are used), to approximately 5%.

#### 6.1.2 The roughness sublayer

An investigation into the depth of the roughness sublayer has revealed different behaviours for variation in frontal and plan solidities. The RSL depth, however, is found to follow the same trend in both cases - it appears to be inversely proportional to the bulk drag. A decrease in drag is usually accompanied by a thickening of the RSL and vice-versa. In addition, the relative energy content in the POD modes calculated over the RSL region strongly suggest that the effect of increasing  $\lambda_F$  is to redistribute a larger proportion of the energy to the highest energy POD modes (i.e. the larger scales), while increasing  $\lambda_P$  redistributes the energy toward the smaller scales (or higher-order modes).

The use of POD to infer spatial similarity of flows over different wall morphologies has also been demonstrated. This is inferred by the appearance of the "cut off" mode, which suggests a lack of scale coherency across different wall morphologies.

#### 6.1.3 The validity of Townsend's similarity hypothesis

The individual effect of frontal and plan solidities on the statistics of the turbulence was examined. Mean velocity profiles in defect form conform to outer-layer similarity for different  $\lambda_F$  cases, while the collapse degrades marginally for different  $\lambda_P$  cases. This suggests that for a given frontal blockage, the plan arrangement of the roughness can lead to violation of outer-layer similarity. The streamwise and wall-normal turbulent intensities, as well as Reynolds shear stresses, show a lack of outer-layer similarity for almost all cases considered. This indicates that, for these rough surfaces with a relative roughness height of  $h/\delta \approx 0.1$ , the flow does not seem to follow outer-layer similarity, especially for higher-order quantities. This is in disagreement with the conclusions of Castro (2007) and Amir and Castro (2011) who suggested that outer-layer similarity is valid up to  $h/\delta \approx 0.15$ . Therefore, the maximum relative roughness height for which outer-layer similarity holds depends not only on the ratios  $\delta/h$  or  $\delta/h_s$ , as previously suggested (Jimenez, 2004; Flack et al., 2005), but also on the surface roughness morphology, as well as the geometry of the individual roughness elements.

POD analysis was used to infer information on the spatial structure of the turbulence across the walls examined herein. This revealed that, although the turbulence statistics

showed a lack of outer-layer similarity, some form of spatial universality of the flow is still present, as significantly different rough-walls exhibit virtually identical POD mode shapes and sizes. The different rough surfaces exhibit different absolute energy levels in the modes, in dependence on the solidities. This difference in energy distribution across scales could be responsible for the breakdown of outer-layer similarity.

#### 6.1.4 The roughness characterisation

A comparison between two surfaces with the same  $\lambda_F$  and  $\lambda_P$ , but with different element patterns, shows that the roughness length is different for these two surfaces. Moreover, these two nominally "identical" surfaces (if the roughness is only characterised by  $\lambda_F$  and  $\lambda_P$ ) do not seem to exhibit outer-layer similarity in higher order quantities. This suggests that frontal and plan solidities, along with the mean height of the roughness elements, might not be enough to fully characterise a rough-wall, as the generated drag also depends on the roughness pattern (in accordance with Cheng et al. (2007)). Moreover, preliminary studies on the effect of the geometry of the roughness elements was also carried out and reported increases in bulk drag of the order of 20% when the rough element shape was changed from cylindrical to rectangular bricks. Future studies are required to identify appropriate parameters to fully characterise the roughness, and eventually model it.

#### 6.1.5 The spatial arrangement of the turbulence

Results show the individual effect of frontal and plan solidities on the spatial organisation of the turbulence. Findings in agreement with the presence of hairpin packets are observed to be a prominent feature of the rough-wall boundary layer, as in the well-documented smooth-wall flows. Streamwise velocity correlations are found to coherently incline in the flow direction with angles which are comparable in both rough and smooth-wall boundary layers. This inclination is confirmed to be insensitive to a change in the frontal and plan solidities. Instead, this seems to be a rather universal characteristic of the turbulence, which is in disagreement with Krogstad and Antonia (1994).

The extent of the coherence of the turbulent structures both via cuts of velocity fluctuations and length scales (based on  $R_{u'u'}$ ,  $R_{v'v'}$  and  $R_{u'v'}$ ) are found to be remarkably similar across all the different walls examined herein, throughout the entire wall-normal range. This is interesting, particularly given the lack of outer-layer similarity that was highlighted for the same surfaces. The structure of the turbulence results in good agreement across the surface morphologies, even when examining  $R_{\Lambda u'}$ ,  $R_{\Lambda v'}$  and  $R_{\Lambda w'}$  quantities.

Swirling strength criteria indicate that, although the presence of prograde vortices in the (x, y) plane is highly dominant when compared to the retrograde vortices, the latter are found to frequently populate the boundary layers studied (up to 15 % statistically). Additionally, the frequency of appearance of both kind of vortices seems to be insensitive to the changes in surface morphology; however, their strength is highly modulated by the solidities.

#### 6.1.6 The energy distribution across scales

POD analysis showed that a trend of increasingly smaller structures for higher-order modes is generally found throughout all cases. Therefore, the low-energy modes tend to be associated with large-scale structures, whilst high-energy modes are representative of increasingly smaller scales. Comparison of the first five modes across all the morphologies show identical mode shapes and sizes, indicating that there is a degree of structural similarity regardless of roughness morphology.

It is also found that a redistribution of energy across scales takes place for variation of frontal and plan densities. The two solidities trigger different energy mechanisms. In particular, the effect of an increased frontal solidity would be to redistribute the energy toward the highest energy POD modes (i.e. the large scale), whilst the opposite trend is found for the plan solidity variation. Increasing the  $\lambda_P$  redistributes the energy toward the higher order modes, hence the smaller scales.

## 6.2 Limitations and shortcomings

An inherent limitation of studies on strong relative roughness height  $(h/\delta \approx 0.1)$  is the difficulty in determining whether a canonical logarithmic region is present at all, and if so, what its boundaries are. This problem is common to all rough-wall studies, although its significance scales with the roughness size. Moreover, a choice on the most appropriate von Kármán constant has to be made and this is not a trivial task for such strongly rough-walls. These limitations, although here mitigated where possible, could not be avoided, as the aim of this work has been to investigate the upper limit of the Townsend's similarity hypothesis. Its validity is well accepted and documented for low-relative-roughness height.

Another problem when dealing with TBLs is the fact that the skin friction is generally unknown. This becomes an inconvenience, particularly in rough-walls, given the higher number of unknowns necessary to describe the law of the wall (i.e. virtual origin and roughness function). Nevertheless, the skin friction is used to non-dimensionalise a great number of statistics, hence the best possible accuracy is required when determining it. Although a floating-element drag-balance was designed and manufactured for this

purpose, this has proven accurate only up to 5%. A second iteration design could have reduced this uncertainty to a value of around 3%, as in Krogstad and Efros (2010).

The current work contains a substantial experimental data set. However, as highlighted in § 2.2, the twelve cases here presented are only covering two lines in figure 3.2(a). It remains an open question whether the same conclusions would be drawn if alternative values of  $\lambda_F(\lambda_P)$  and  $\lambda_P(\lambda_F)$  had been chosen (i.e. following different lines in figure 3.2(a)). A much bigger data set, possibly generated by combining efforts across different institutions, should be gathered to extend the conclusions here discussed to the whole  $(\lambda_F, \lambda_P)$  parameter space. More effort into further exploring the effect of the geometry of the roughness is also required to shed light on this topic. In this respect, effects of the presence of the pins on top of the roughness bricks could also be better quantified.

Considering the measurements herein presented, the 3D data set could have matched the depth of the 2D one. This was not possible due to a data storage issue. The 3D setup, having to record information from two cameras, is in principle at least double the size of the 2D equivalent. Therefore, only 1500 realisations (against the 2000 in the 2D measurements) were acquired. A higher number of images would have been beneficial for statistical convergence and if conditionally-averaged statistics were to be presented.

The current work only describes time-averaged fields (i.e. ensemble averaged) as no time-resolved information is available. This means that frequency information is unavailable. On the other hand, using time-resolved PIV would have had a major impact on the spatial resolution (given the current camera's capability).

Finally, due to complications with light reflection associated with PIV measurements, it has been decided to neglect the analysis of the flow within the canopy (i.e. in between the roughness elements). This is not considered critical, given the aims of this thesis, although it could be taken into consideration for future studies.

#### 6.3 Recommendations for future work

Suggested areas of further research that complement or extend the work presented in this thesis are herein suggested.

The roughness fetch for the current work was deliberately chosen to be long enough so that a fully-developed boundary layer could be generated. Nevertheless, given the availability of the floating element friction balance, the effect of a short fetch of roughness onto the skin friction generation would be a worthwhile exercise. It has has been shown in § 4.3.2 that the influence of the Lego<sup>TM</sup> baseboard upstream of the bricks is irrelevant in terms of the bulk properties, however an exploration of the effect of step-change in roughness (similar to Cheng and Castro (2002a)) could prove fruitful for these reduced-fetch cases.

In the same line of investigation on short fetch of roughness, studying continuously varying frontal and plan solidity walls (in the streamwise direction), would highlight the interrelationship between the wall morphology and the adjacent flow. This could result in mapping a threshold (in the  $(\lambda_F, \lambda_P)$  plane), at which the turbulence structure is essentially independent from the surface morphology. In particular, it would be fascinating to explore through synchronised PIV acquisition whether, and to what extent, the characteristic of the turbulence above the Lego<sup>TM</sup> baseboard are retained downstream in the bricks' region. A detailed analysis of what particular features of the turbulence are transferred to the new morphology would be important. Time-resolved PIV could also be employed to study the temporal evolution of these structures.

Finally, in the current quest for an unequivocal definition of a surface morphology, the effect of a number of different parameters should also be tested. This includes further studies on the geometry of the roughness morphology (with detailed analysis of the field in the canopy layer), the introduction of different porosity roughnesses with the aim of replicating natural environments (i.e. presence of trees), and the exploration into flexible roughness to mimic the vegetation in pipes and river beds. An exploration into the possibility of energy harvesting from turbulent flows is also an important line of enquiry.

# Appendix A

## Smooth-wall

#### A.1 Introduction

Although this work primarily aims at comparing different types of rough morphologies, results for smooth-wall are here reported for the sake of completeness. Given the importance of matching the Reynolds number,  $Re_{\tau}$ , to that of the rough-walls in examination, the smooth-wall experiment had to be carried out in a different facility. The same order of magnitude Reynolds number could be recreated in this experiment (i.e.  $Re_{\tau} \approx 4000$ ). A brief experimental facility and details summary is given in section A.2. Similar analysis to that presented so far has been carried out on the smooth-wall case. A brief description of the results (with particular focus on the main differences with the respect of the rough cases) are herein introduced and discussed from section A.3.1 onward. Finally some conclusions are drawn.

## A.2 Experimental facility and details

The smooth-wall experiment took place during 2013 at the R. J. Mitchell Wind Tunnel at the University of Southampton and was carried out by the join effort of Dr. Roeland de Kat and Dr. Grégoire Fourrié. The facility is a low-speed recirculating wind tunnel with a working section of 10.5 m in length, with a 3.5  $m \times 2.4$  m cross-section. Experiments were conducted in nominally ZPG at approximately 15 m/s. 2D PIV measurements were taken 7 m downstream along the test section and resulted in comparable resolution ( $l_{smooth}^+ \approx 35$ ) to the data sets presented herein. The reader is referred to Fourriè et al. (2014) for further details.

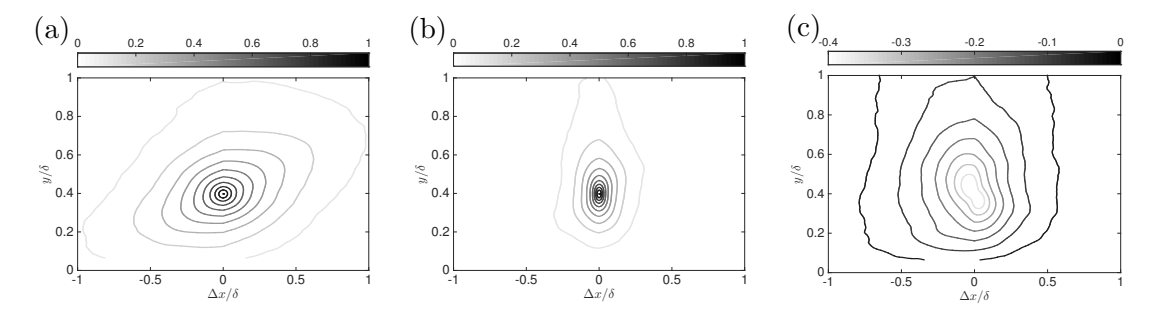


Figure A.1: Two-point correlation of (a) streamwise, (b) wall-normal and (c) Reynolds shear stress fluctuations for smooth-wall case. Colorbar represents the normalised correlation coefficient,  $R_{u'u'}$ ,  $R_{v'v'}$  and  $R_{u'v'}$ . Flow is left to right.

### A.3 Results and discussion

Following the same structure of chapters 4 and 5, results for the smooth-wall case are next presented.

#### A.3.1 Velocity correlations

Firstly, two-point velocity correlations are presented. Figure A.1(a) shows streamwise velocity correlations  $R_{u'u'}$ . As for the rough-wall cases, this results as a strongly elongated forward-leaning structure, which represents the inclination of the vortex packets that populate the boundary layers. When compared to the rough cases in figure 5.3(a), both the streamwise and the wall-normal extents of this correlation are bigger for the smooth-wall case. The streamwise velocity is still strongly correlated at  $y = \delta$  and extend for almost  $2\delta$  in the streamwise direction, which is nearly 25% higher than the correspondent extent for the rough-walls. This is in agreement with Krogstad and Antonia (1994). Figure A.1(b) shows correlations of wall-normal velocity fluctuations. Similar conclusions to the previous case can be drawn when comparing it to the rough cases in examination (see figure 5.3(b)), where both vertical and horizontal coherencies result bigger than in the rough counterpart. Finally, the Reynolds shear stress correlations is plotted in figure A.1(c). A similar trend is registered, where the smooth-wall shows a slightly more extended correlation when compared to the rough-wall (see figure 5.3(c)).

The inclination angle of streamwise velocity correlations is next inferred (Christensen et al., 2005). Results for the smooth-wall cases are shown in table A.1. These values are in the range reported in literature (Volino et al., 2007, 2009; Ganapathisubramani and Schultz, 2011; Christensen et al., 2005; Head and Bandyopadhyay, 1981; Christensen and Adrian, 2001; Adrian et al., 2000b; Tomkins and Adrian, 2003; Nakagawa et al., 2003). Also reported in the same table is the inclination angle for the  $R_{\Lambda u'}$  (inferred from figure A.3(b)), which gives similar information about the turbulence organisation. Differences between the two angles are present, however, the values are in the same range. It can be concluded from this evidence, that the streamwise structure of the turbulence (i.e.

possibly the vortex packets inclination) does not seem to depend of the wall morphology. The smooth-wall case showed a similar inclination as the rough-walls examined herein.

$$\begin{array}{ccc} \text{Data set} & \alpha_{R_{u'u'}} & \alpha_{R_{\Lambda u'}} \\ \hline \text{SMOOTH} & 17^{\circ} & 13^{\circ} \end{array}$$

Table A.1:  $R_{u'u'}$  and  $R_{\Lambda u'}$  inclination angles,  $\alpha_{R_{u'u'}}$  and  $\alpha_{R_{\Lambda u'}}$  for the smoothwall case.

#### A.3.2 Velocity correlation length scales

The streamwise length scale,  $L_{xu'u'}$ , is shown in figure A.2(a). This results much bigger than any of the rough-wall cases previously analysed (figure 5.10(a) & (b)). The smooth case result up to 30% higher throughout the whole wall-normal range. This ties in well with visual comparison of figures 5.3(a) & (b) and A.1(a), where the latter resulted in much bigger correlated region. The wall-normal length scale,  $L_{yu'u'}$ , is presented in figure A.2(b). This results in similar trends as in the previous case, with values for the smooth cases being higher when compared to the rough cases (in figure 5.11(a) & (b)). Next, a similar comparison is directed to the wall-normal correlation lengths,  $L_{xv'v'}$  and  $L_{yv'v'}$ , in figure A.2(c) & (d). The same conclusions as for the streamwise correlation lengths can be drawn, the smooth-wall cases show an enhanced length scales extent, although this is less pronounced than the previous case. Finally, Reynolds shear stress correlation lengths,  $L_{xu'v'}$  and  $L_{yu'v'}$ , are shown in figure A.2(e) & (f). Again, the smooth-wall case presents a bigger correlated region in both streamwise and wall-normal directions, particularly closer to the wall. These results seem to suggest that the roughness act as to degrade the region of correlated velocity.

#### A.3.3 Swirling strength analysis

Contours of the auto-correlation of the signed swirl strength,  $R_{\Lambda\Lambda}$ , are next presented in figure A.3 (a). Its shape is similar to the rough cases, whilst its extent, as for the velocity correlations, is found to be bigger than in the previous surfaces in both streamwise and wall-normal directions. For completeness  $R_{\Lambda u'}$  and  $R_{\Lambda v'}$  correlations are also reported in figure A.3(b) &(c). The results for the smooth-wall resemble the rough-wall cases in figure 5.18(a) & (b). The reader is referred to the latter for a the description of the physical meaning of these shapes.

#### A.3.4 Population trends of vortices

Figure A.4(a) & (b) show the percentage of positive and negative swirl and the strength of these non-zero structure respectively. The percentage of positive swirl is comparable

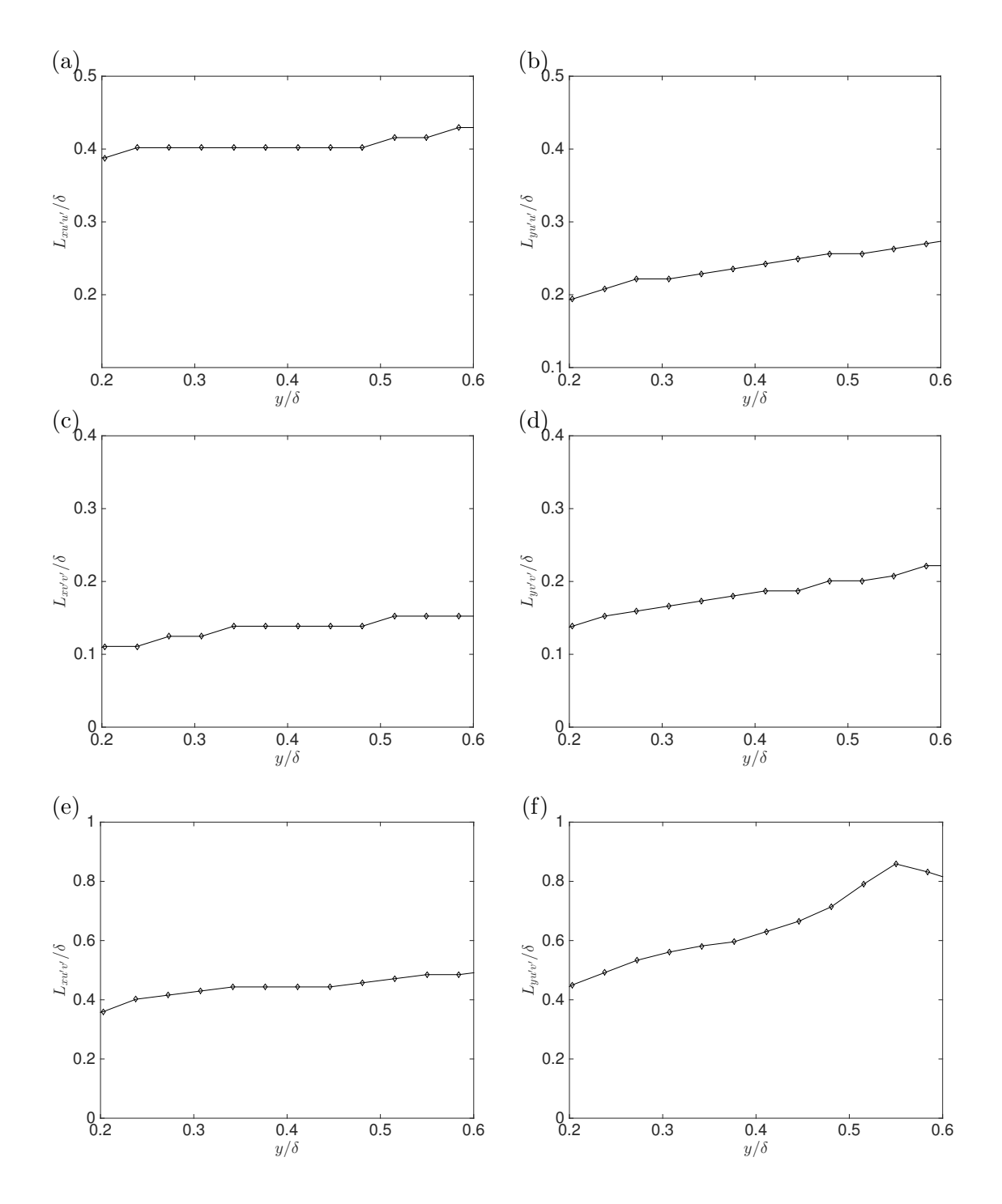


Figure A.2: Streamwise (left) and wall-normal (right) variation of the length scales based on  $R_{u'u'}=0.5$ ,  $R_{v'v'}=0.5$  and  $R_{u'v'}=0.15$  contours (top, centre and bottom respectively) for smooth-wall case.

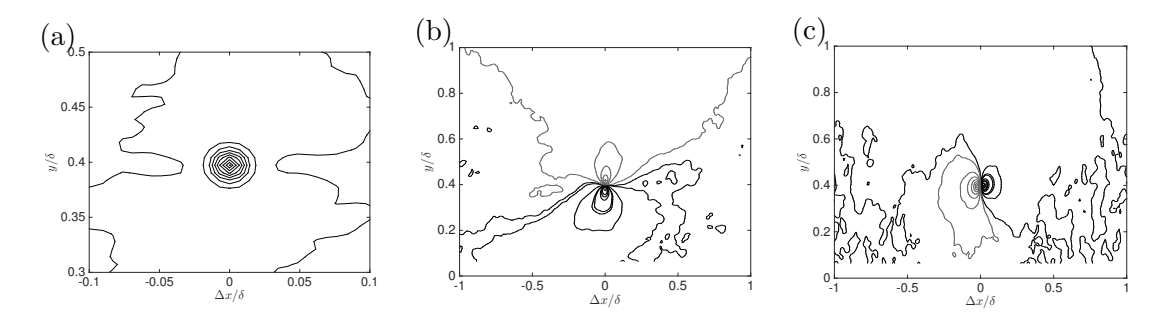


Figure A.3: (a) Swirling strength correlation coefficient,  $R_{\Lambda\Lambda}$ , for smooth-wall case. Outermost contour  $R_{\Lambda\Lambda}=0.1$ , contour spacing 0.1. Contours of (b)  $R_{\Lambda u'}$  and (c)  $R_{\Lambda v'}$  centred at  $y/\delta=0.4$  for smooth-wall case. Contour magnitudes  $R_{\Lambda u'}=R_{\Lambda v'}=0.01,0.03,0.07,0.1$ ; contour signs black, positive; grey, negative.

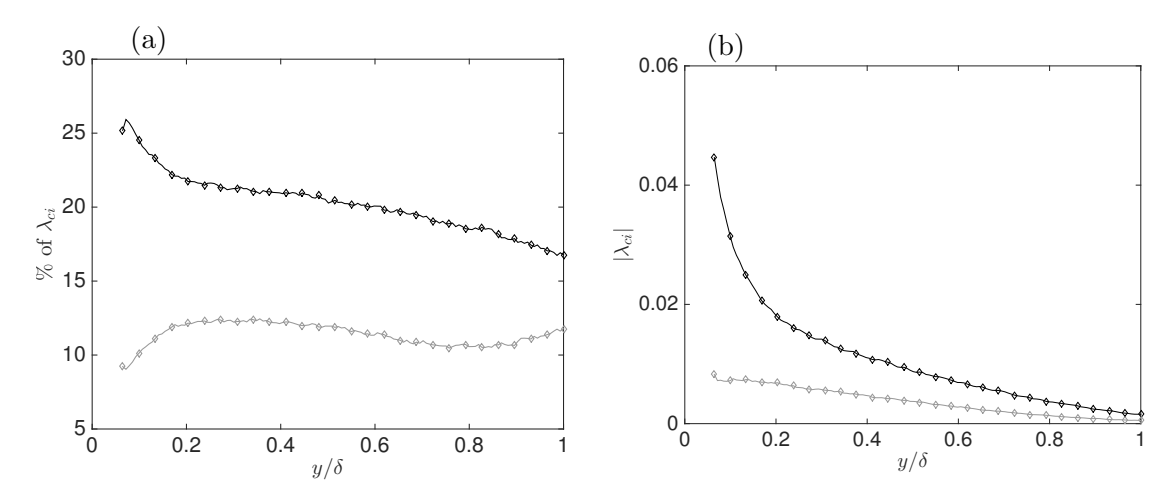


Figure A.4: Population vortex trend in the (x, y) plane. (a) Percentage of prograde (black) and retrograde (grey) vortex, (b) strength of prograde (black) and retrograde (grey) vortices for smooth-wall case.

to the rough-wall cases (in figure 5.13(a) & (b)) with a peak reached in the near-wall region, where the retrograde vortices populate up to 25% of the streamwise field. The population of prograde vortices, on the other hand, is consistently lower than for the previous rough cases in figure 5.13(a) & (b), with maximum values which only reaches approximately 12% against the 14% in the previous cases. This is perhaps not surprising giving that these vortices act against the mean shear. Also not surprising is the fact that the vortical structures' strength in the smooth-wall case results much lower than in rough-walls. It is, in fact, intuitive to attribute some of this swirl to the presence of the roughness elements. Nevertheless, the presence of non zero-swirl in the boundary layer is merely constant across rough and smooth-walls - indication that some of the intrinsic characteristic of the turbulence and its spatial organisation is indeed universal across different surface morphologies.

Data set	Field	$E_1$	$E_2$	$E_3$	$E_4$	$E_5$	$\sum_{i=1}^{5} E_i$	$\sum_{i=1}^{10} E_i$	$0.5\sum_{i=1}^{n} E_i$
SMOOTH	(u',v')	27	10	6	4	3	50	59	5
SMOOTH	(u')	34	12	7	5	3	62	72	3
SMOOTH	(v')	11	8	5	4	3	31	42	16

Table A.2: Fractional TKE,  $E_i$  and cumulative TKE  $\sum_{i=1}^{n} E_i$  content versus mode number.  $0.5\sum_{i=1}^{n} E_i$  refers instead to the number of modes necessary to resolve the 50% of the turbulent kinetic energy contained in the flow.

#### A.3.5 POD modes shape

To conclude this brief comparison between the smooth and the rough cases, a POD analysis is presented. First the POD mode shapes derived from the combined (u', v') field are presented in the left column of figure A.5. These shapes closely resemble the roughwall cases (in both frontal and plan solidities in figure 4.13). Higher-order modes embed information about progressively smaller structure in the flow. For completeness, POD mode shapes derived by the analysis of (v') only field are also reported on right column of figure A.5. These shapes present some differences in the higher-order modes when compared to the rough-walls previously examined. This indicates that, as expected, the (v') component is more sensitive to the surface morphology.

#### A.3.6 POD modes energy content

Perhaps of more use, is to compare the fractional and cumulative TKE across the different modes that characterise the smooth-wall case. Results are summarised in table A.2. When looking at the combined (u',v') field, on average much more energy is contained in the first low-order modes in the smooth case. The lowest order mode reaches 27% of the total TKE for the smooth case against only up to 18% and 19% for frontal and plan solidity cases. A similar trend is found for POD modes calculated upon the streamwise velocity filed, where 34% of the CTKE is contained in mode 1 for the smooth-wall against only 24% for the highest rough case. Similar conclusions can be drawn for the wall-normal field. Also to be noted is that the number of modes necessary to reconstruct the 95% of the CTKE in the smooth-wall case is much lower than the rough cases ( $\approx 500$ ). This confirms a spatially less complex flow.

#### A.4 Conclusions

Rough and smooth-walls boundary layers present numerous similarities in their spatial organisation. These similarities manifest in the form of Reynolds stress and swirling strength correlations and POD mode shapes. The fundamental structure of the boundary layers is consistent with the mutual interaction of vortex packets producing high

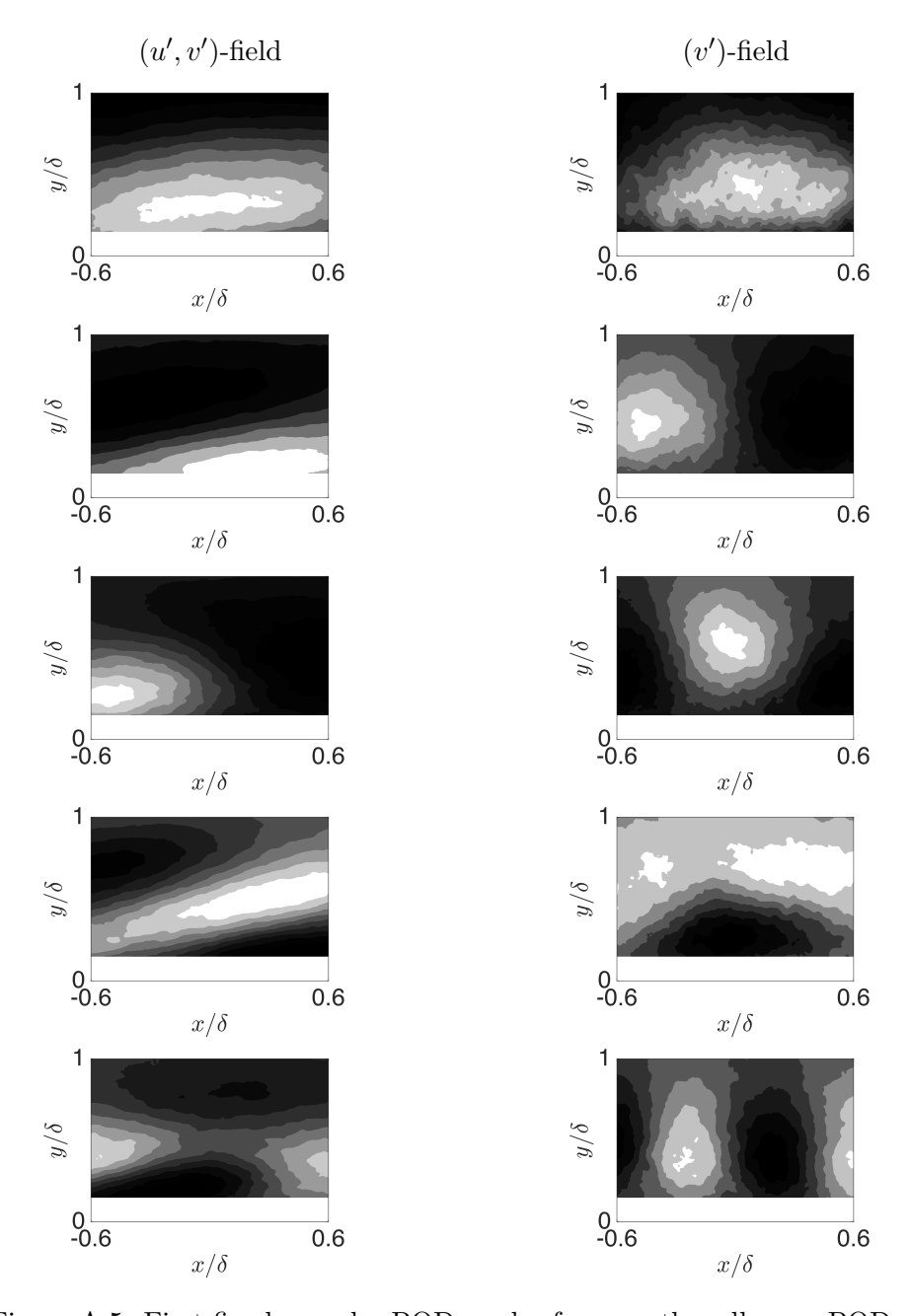


Figure A.5: First five low-order POD modes for smooth-wall case. POD modes are calculated on the combined (u', v') field (left), solely upon (u') field (centre) and solely upon (v') field (right). Flow is left to right.

and low-momentum regions. This is persistent across both rough and smooth-wall cases. The inclination of streamwise velocity correlations is also found to be independent of the surface morphology.

However, the main difference lies within the correlation length scales which are often found to be reduced in both the streamwise and spanwise directions in rough-walls when compared to the smooth case. Due to the higher complexity of the flow, higher-order POD modes (particularly for the wall-normal velocity) often have different shapes and energy contents in between rough and smooth-walls. Generally, more energy is contained in the first few low-order POD modes of smooth-wall TBLs. This is because the small scale structures progressively become more important when the wall becomes rougher. This is also consistent with the lower correlation lengths that characterise the latter.

## Appendix B

# Stereoscopic data validation

#### B.1 Everson and Sirovich's method

Reconstruction methodology based on "gappy" POD has been been shown to produce superior estimations of the missing data, when compared to any other spatial interpolation technique (Raben et al., 2012). Here the methodology highlighted by Everson and Sirovich (1995) based on snapshots POD is applied. The reader is referred to the latter for the technicality of the algorithm but a quick summary and an example is here given. The algorithm follows the following steps:

- 1. the locations of the spurious vectors must be identified. This is achieved comparing the vector in examination both with a local mean and its neighbours;
- 2. the location of the spurious vectors is stored in a "mask";
- 3. the variable of interest is then modified based on the "mask" information so that the spurious vectors are replaced by NaN (i.e. missing vectors);
- 4. POD is applied to this "gappy" data and a reduced model is formed;
- 5. the gaps (i.e. only the spurious vectors) are filled with information given by this newly formed reduced model;
- 6. POD is applied to this reconstructed data set and the modal energy recorded;
- 7. the previous steps are repeated iteratively till convergency is reached in the modal energy (i.e. the solutions at two subsequent iterations are less that  $10^{-4}\%$  apart).

Figure B.1 shows an example of the results following the procedure discussed herein. In particular figure B.1(a) shows the original data set, where spurious vectors are visible at the bottom of the image. Figure B.1(b) shows the same vector field after the "mask" is applied, here spurious vectors are replaced by empty vectors. Finally, B.1(c) shows

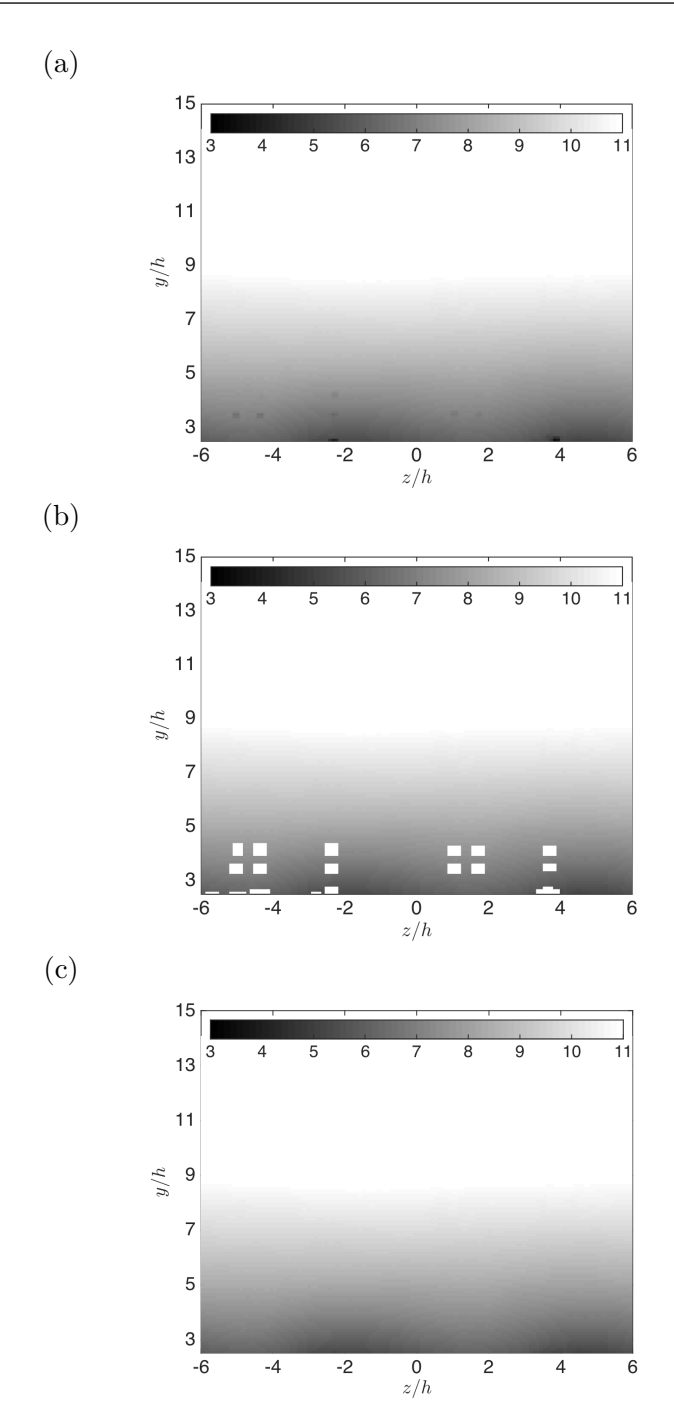


Figure B.1: (a) Streamwise velocity vector field from PIV with spurious vectors. (b) "Gappy" vector field where the spurious vectors are removed after applying the mask. (c) Reconstructed vector field after Everson and Sirovich's (1995) procedure is applied. Flow is left to right. Example case LF5.

the reconstructed velocity field after Everson and Sirovich's (1995) technique is applied. Here the spurious vectors have disappeared and a validated reconstruction was used to fill the gaps, recreating a seamless vector field.

- Acharya, M., Bornstein, J., and Escudier, M. P. (1986). Turbulent boundary layers on rough surfaces. *Experiments in Fluids*, 4:33–47.
- Adrian, R. J., Christensen, K. T., and Liu, Z. C. (2000a). Analysis and interpretation of instantaneous turbulent velocity fields. *Experiments in Fluids*, pages 275–290.
- Adrian, R. J., Meinhart, C. D., and Tomkins, C. D. (2000b). Vortex organization in the outer region of the turbulent boundary layer. *Journal of Fluid Mechanics*, 442:1–54.
- Adrian, R. J. and Westerweel, J. (2011). *Particle Image Velocimetry*. Cambridge University Press.
- Alfredsson, P. H. and Örlü, R. (2010). The diagnostic plot a litmus test for wall bounded turbulence data. *European Journal of Mechanics B/Fluids*, 29(6):403–406.
- Alfredsson, P. H., Segalini, A., and Örlü, R. (2011). A new scaling for the streamwise turbulence intensity in wall-bounded turbulent flows and what it tells us about the "outer" peak. *Physics of Fluids*, 23(4):041702.
- Amir, M. and Castro, I. P. (2011). Turbulence in rough-wall boundary layers: universality issues. *Experiments in Fluids*, 51:313–326.
- Andreopoulos, J. and Bradshaw, P. (1981). Measurements of turbulence structure in the boundary layer on a rough surface. *Boundary-Layer Meteorology*, 20:201–213.
- Arnfield, A. J. (2003). Two decades of urban climate research: a review of turbulence, exchanges of energy and water, and the urban heat island. *International Journal of Climatology*, 23(1):1–26.
- Bakken, O. M., Krogstad, P. A., Ashrafian, A., and Andersson, H. I. (2005). Reynolds number effects in the outer layer of the turbulent flow in a channel with rough walls. *Physics of Fluids*, 17(6):065101.
- Bandyopadhyay, P. R. (1987). Rough-wall turbulent boundary layers in the transition regime. *Journal of Fluid Mechanics*, 180:231–266.

Barros, J. M. and Christensen, K. T. (2014). Observations of turbulent secondary flows in a rough-wall boundary layer. *Journal of Fluid Mechanics*, 748:R1.

- Bechert, D. W., Bruse, M., and Hage, W. (2000). Experiments with three-dimensional riblets as an idealized model of shark skin. *Experiments in Fluids*, 28:403–412.
- Bechert, D. W., Hage, W., VaN Der Hoeven, J. G. T., and Hoppe, G. (1997). Experiments on drag-reducing surfaces and their optimization with an adjustable geometry. *Journal of Fluid Mechanics*, 338:59–87.
- Benedict, L. H. and Gould, R. D. (1996). Towards better uncertainty estimates for turbulence statistics. *Experiments in Fluids*, 22:129–136.
- Berkooz, G., Holmes, P., and Lumley, J. L. (1993). The proper orthogonal decomposition in the analysis of turbulent flows. *Annual Review of Fluid Mechanics*, 25:539–575.
- Best, M. J., Grimmond, C. S. B., and Villani, M. G. (2006). Evaluation of the urban tile in moses using surface energy balance observations. *Boundary-Layer Meteorology*, 118(3):503–525.
- Bhaganagar, K., Kim, J., and Coleman, G. (2004). Effect of Roughness on Wall-Bounded Turbulence. Flow, Turbulence and Combustion, 72:463–492.
- Böhm, M., Finnigan, J., Raupach, M., and Hughes, D. (2012). Turbulence Structure Within and Above a Canopy of Bluff Elements. *Boundary-Layer Meteorology*, 146(3):393–419.
- Bons, J. P., Taylor, R. P., McClain, S. T., and Rivir, R. B. (2001). The Many Faces of Turbine Surface Roughness. *Journal of Turbomachinery*, 123(4):739–748.
- Bottema, M. (1996). Urban roughness modelling in relation to pollutant dispersion. Journal of Wind Engineering and Industrial Aerodynamics, 31(18):3059–3075.
- Britter, R. E. and Hanna, S. R. (2003). Flow And Dispersion In Urban Areas. *Annual Review of Fluid Mechanics*, 35:469–496.
- Calhoun, R., Gouveia, F., Shinn, J., Cheng, H., Stevens, D., Lee, R., and Leone, J. (2004). Flow Around a Complex Building: Comparisons between Experiments and a Reynolds-Averaged Navier Stokes Approach. *Journal of Applied Meteorology*, 43(5):696–710.
- Castro, I. P. (2007). Rough-wall boundary layers: mean flow universality. *Journal of Fluid Mechanics*, 585:469–485.
- Castro, I. P., Segalini, A., and Alfredsson, P. H. (2013). Outer-layer turbulence intensities in smooth- and rough-wall boundary layers. *Journal of Fluid Mechanics*, 727:119–131.

Cheng, H. and Castro, I. P. (2002a). Near-wall flow development after a step change in surface roughness. *Boundary-Layer Meteorology*, 105:411–432.

- Cheng, H. and Castro, I. P. (2002b). Near wall flow over urban-like roughness. *Boundary-Layer Meteorology*, 105:411–432.
- Cheng, H., Hayden, P., Robins, A. G., and Castro, I. P. (2007). Flow over cube arrays of different packing densities. *Journal of Wind Engineering and Industrial Aerodynamics*, 95(8):715–740.
- Chong, M. S., Perry, A. E., and Cantwell, B. J. (1990). A general classification of three-dimensional flow fields. *Physics of Fluids*, 2(5):765–777.
- Christensen, K. T. (2004). The influence of peak-locking errors on turbulence statistics computed from PIV ensembles. *Experiments in Fluids*, 36(3):484–497.
- Christensen, K. T. and Adrian, R. J. (2001). Statistical evidence of hairpin vortex packets in wall turbulence. *Journal of Fluid Mechanics*, 431:433–443.
- Christensen, K. T., Wu, Y., and Y (2005). Characteristics of vortex organization in the outer layer of wall turbulence. In Fourth International Symposium on Turbulence and Shear Flow Phenomena, Williamsburg, Virginia, pages 1025–1030.
- Claus, J., Krogstad, P. A., and Castro, I. P. (2012). Some Measurements of Surface Drag in Urban-Type Boundary Layers at Various Wind Angles. *Boundary-Layer Meteorology*, 145(3):407–422.
- Clauser, F. H. (1954). Turbulent boundary layers in adverse pressure gradients. *J. Aeronaut. Sci.*, 21:91–108.
- Coceal, O. and Belcher, S. E. (2004). A canopy model of mean winds through urban areas. Quarterly Journal of the Royal Meteorological Society, 130(599):1349–1372.
- Coles, D. (1956). The law of the wake in the turbulent boundary layer. *Journal of Fluid Mechanics*, 1(2):191–226.
- Crago, R., Okello, W., and Jasinski, M. (2012). Equations for the Drag Force and Aerodynamic Roughness Length of Urban Areas with Random Building Heights. Boundary-Layer Meteorology, 145(3):423–437.
- Dabberdt, W. F., Hales, J., Zubrick, S., Crook, A., Krajewski, W., Doran, J. C., Mueller, C., King, C., Keener, R. N., R, B., Rodenhuis, D., Kocin, P., Rossetti, M. A., Sharrocks, F., and Stanley SR, E. M. (2000). Forecast Issues in the Urban Zone:Report of the 10th Prospectus Development Team of the U.S. Weather Research Program. Bulletin of the American Meteorological Society, 81(9):2047–2064.
- Darcy, H. (1858). Recherches experimentales relatives au mouvement de l'eau dans les tuyaux. *Mem. Savants etrangers*, 15:1–288.

del Álamo, J. C. and Jimenez, J. (2009). Estimation of turbulent convection velocities and corrections to Taylor's approximation. *Journal of Fluid Mechanics*, 640:5–26.

- Dennis, D. J. C. and Nickels, T. B. (2011). Experimental measurement of large-scale three-dimensional structures in a turbulent boundary layer. Part 1. Vortex packets. *Journal of Fluid Mechanics*, 673:180–217.
- Efros, V. (2011). Scructure of turbulent boundary layer over a 2-D roughness. PhD thesis, Norwegian University of Science and Technology.
- Everson, R. and Sirovich, L. (1995). Karhunen–Loève procedure for gappy data. J. Opt. Soc. Am. A, 12(8):1657–1664.
- Flack, K. A., Schultz, M. P., and Connelly, J. S. (2007). Examination of a critical roughness height for outer layer similarity. *Physics of Fluids*, 19(9):095104.
- Flack, K. A., Schultz, M. P., and Shapiro, T. A. (2005). Experimental support for Townsend's Reynolds number similarity hypothesis on rough walls. *Physics of Flu*ids, 17(3):035102.
- Flores, O., Jimenez, J., and del Álamo, J. C. (2007). Vorticity organization in the outer layer of turbulent channels with disturbed walls. *Journal of Fluid Mechanics*, 591:145–154.
- Fourriè, G., de Kat, R., and Ganapathisubramani, B. (2014). Combined wall shear stress and velocity measurements in a high Reynolds number turbulent boundary layer. In interdisciplinary Turbulence initiative, Bertinoro, Italy September 21-24.
- Ganapathisubramani, B., Hutchins, N., Hambleton, W. T., Longmire, E. K., and Marusic, I. (2005). Investigation of large-scale coherence in a turbulent boundary layer using two-point correlations. *Journal of Fluid Mechanics*, 524:57–80.
- Ganapathisubramani, B., Longmire, E. K., and Marusic, I. (2003). Characteristics of vortex packets in turbulent boundary layers. *Journal of Fluid Mechanics*, 478:35–46.
- Ganapathisubramani, B. and Schultz, M. P. (2011). Turbulent boundary layer structure over sparsely distributed roughness. In 7th International Symposium on Turbulence and Shear flow phenomena, Ottawa, Canada July 28–31.
- Garcia-Mayoral, R. and Jimenez, J. (2011). Drag reduction by riblets. *Philosophical Transactions of the Royal Society A: Mathematical, Physical and Engineering Sciences*, 369(1940):1412–1427.
- Goldstein, D., Handler, R., and Sirovich, L. (1995). Direct numerical simulation of turbulent flow over a modeled riblet covered surface. *Journal of Fluid Mechanics*, 302:333–376.

Grimmond, C. S. B. and Oke, T. R. (1999). Aerodynamic properties of urban areas derived, from analysis of surface form. *Journal of Applied Meteorology*, 38:1262–1292.

- Guala, M., Tomkins, C. D., Christensen, K. T., and Adrian, R. J. (2012). Vortex organization in a turbulent boundary layer overlying sparse roughness elements. *Journal of Hydraulic Research*, 50(5):465–481.
- Hagen, G. (1854). Uber den einfluss der temperatur auf die bewegung des wassers in rohren. Math. Abh. Akad. Wiss.
- Hagishima, A., Tanimoto, J., Nagayama, K., and Meno, S. (2009). Aerodynamic Parameters of Regular Arrays of Rectangular Blocks with Various Geometries. *Boundary-Layer Meteorology*, 132:315–337.
- Hakkinen, R. (2004). Reflections on Fifty Years of Skin Friction Measurement. In *Fluid Dynamics and Co-located Conferences*, pages 2004–2111. American Institute of Aeronautics and Astronautics.
- Hama, F. R. (1954). Boundary layer characteristics for smooth and rough surfaces. Trans. Soc. Nav. Arch. Mar. Engrs, 62:333–358.
- Head, M. R. and Bandyopadhyay, P. (1981). New aspects of turbulent boundary-layer structure. *Journal of Fluid Mechanics*, 107:297–338.
- Holmes, P., Lumley, J. L., and Berkooz, G. (1996). *Turbulence, Coherent Structures, Dynamical Systems and Symmetry*. Cambridge University Press.
- Iyengar, A. K. S. and Farell, C. (2001). Experimental issues in atmospheric boundary layer simulations: roughness length and integral length scale determination. *Journal of Wind Engineering and Industrial Aerodynamics*, 89:1059–1080.
- Jackson, P. S. (1976). The propagation of modified flow downstream of a change in roughness. *Quart. J. Roy. Meteorol. Soc.*, 102:924–933.
- Jackson, P. S. (1981). On the displacement height in the logarithmic velocity profile. Journal of Fluid Mechanics, 111:15–25.
- Jimenez, J. (2004). Turbulent flows over rough walls. *Annual Review of Fluid Mechanics*, 36:173–196.
- Kanda, M., Inagaki, A., Miyamoto, T., Gryschka, M., and Raasch, S. (2013). A New Aerodynamic Parametrization for Real Urban Surfaces. Boundary-Layer Meteorology, 148(2):357–377.
- Kanda, M., Moriwaki, R., and Kasamatsu, F. (2004). Large-eddy simulation of turbulent organized structures within and above explicitly resolved cube arrays. *Boundary-Layer Meteorology*, 112(2):343–368.

Keirsbulck, L., Labraga, L., Mazouz, A., and Tournier, C. (2002). Surface Roughness Effects on Turbulent Boundary Layer Structures. *Journal of Fluids Engineering*, 124:127–135.

- Khanduri, A. C., Stahpopoulos, T., and Bedard, C. (2003). Wind-induced interference effects on buildings- a review of the state-of-the-art. *Engineering Structure*, 7:617–630.
- Kim, K. C. and Adrian, R. J. (1999). Very large-scale motion in the outer layer. *Physics of Fluids*, 11(2):417–422.
- King, M. J. (1982). The measurement of ship hull roughness. Wear, 83(2):385–397.
- Kline, S. J. and McClintock, F. A. (1953). Describing Uncertainties in Single Sample Experiments. *Mech. Enq.*, pages 3–8.
- Kolmogorov, A. N. (1941). The local structure of turbulence in incompressible viscous fluids at very large Reynolds numbers. *Dokl. Akad. Nauk. SSSR. Reprinted in Proc R Soc London A 434*, 9-13 (1991), 30:299–303.
- Krogstad, P. A. and Antonia, R. A. (1994). Structure of turbulent boundary layers on smooth and rough walls. *Journal of Fluid Mechanics*, 227:1–21.
- Krogstad, P. A. and Antonia, R. A. (1999). Surface roughness effects in turbulent boundary layers. *Experiments in Fluids*, 27:450–460.
- Krogstad, P. A., Antonia, R. A., and Browne, L. W. (1992). Comparison between rough and smooth wall turbulent boundary layers. *Journal of Fluid Mechanics*, 245:599–617.
- Krogstad, P. A. and Efros, V. (2010). Rough wall skin friction measurements using a high resolution surface balance. *International Journal of Heat and Fluid Flow*, 31(3):429–433.
- Lee, S.-H., Lee, J. H., and Sung, H. J. (2010). Direct Numerical Simulation and PIV Measurement of Turbulent Boundary Layer over a Rod-Roughened Wall. In Nickels, T. B., editor, IUTAM Symposium on The Physics of Wall-Bounded Turbulent Flows on Rough Walls, pages 1679–1687. Springer Netherlands.
- Leonardi, S. and Castro, I. P. (2010). Channel flow over large cube roughness: a direct numerical simulation study. *Journal of Fluid Mechanics*, 651:519–539.
- Leonardi, S., Orlandi, P., Smalley, R. J., Djenidi, L., and Antonia, R. A. (2003). Direct numerical simulations of turbulent channel flow with transverse square bars on one wall. *Journal of Fluid Mechanics*, 491:229–238.
- Licari, A. M. and Christensen, K. T. (2011). Modeling Cumulative Surface Damage and Assessing its Impact on Wall Turbulence. *AIAA Journal*, 49(10):2305–2320.

Ligrani, P. M. and Moffat, R. J. (1985). Structure of transitionally rough and fully rough turbulent boundary layers. *Journal of Fluid Mechanics*, 162:69–98.

- Lim, C., Thomas, T. G., and Castro, I. P. (2009). Flow Around a Cube in a Turbulent Boundary Layer: LES and Experiment. *Journal of Wind Engineering and Industrial Aerodynamics*, 97(2):96–109.
- Lim, H. C., Castro, I. P., and Hoxey, R. P. (2007). Bluff bodies in deep turbulent boundary layers: Reynolds-number issues. *Journal of Fluid Mechanics*, 571:97–118.
- Lu, S. S. and Willmarth, W. W. (1973). Measurements of the structure of the Reynolds stress in a turbulent boundary layer. *Journal of Fluid Mechanics*, 60(3):481–511.
- Lumley, J. L. (1970). Stochastic tools in turbulence. New York: Academic Press.
- Macdonald, R. W. (1998). An improved method for the estimation of surface roughness of obstacle arrays. *Boundary-Layer Meteorology*, 97:1857–1864.
- Manes, C., Poggi, D., and Ridolfi, L. (2011). Turbulent boundary layers over permeable walls: scaling and near-wall structure. *Journal of Fluid Mechanics*, 687:141–170.
- Marusic, I., Monty, J. P., Hultmark, M., and Smits, A. J. (2013). On the logarithmic region in wall turbulence. *Journal of Fluid Mechanics*, 716:R3–1–R3–11.
- Matheis, B. and Rothmayer, A. (2004). Impact of Surface Roughness on Local Aerodynamics Using a Three-Dimensional Navier-Stokes Solver. In 42nd AIAA Aerospace Science Meeting and Exibit, Reno, Nevada. American Institute of Aeronautics and Astronautics.
- Mejia-Alvarez, R. and Christensen, K. T. (2013). Wall-parallel stereo particle-image velocimetry measurements in the roughness sublayer of turbulent flow overlying highly irregular roughness. *Physics of Fluids*, 25(11):115109.
- Millward-Hopkins, J., Tomlin, A., Ma, L., Ingham, D., and Pourkashanian, M. (2012). Aerodynamic Parameters of a UK City Derived from Morphological Data. Boundary-Layer Meteorology, 146(3):447–468.
- Millward-Hopkins, J. T., Tomlin, A. S., Ma, L., Ingham, D., and Pourkashanian, M. (2011). Estimating Aerodynamic Parameters of Urban-Like Surfaces with Heterogeneous Building Heights. *Boundary-Layer Meteorology*, 141(3):467–490.
- Nagib, H. M. and Chauhan, K. A. (2008). Variations of von Kármán coefficient in canonical flows. *Physics of Fluids*, 20(10):101518.
- Nakagawa, S. and Hanratty, T. J. (2001). Particle image velocimetry measurements of flow over a wavy wall. *Physics of Fluids*, 13(11):3504–3507.
- Nakagawa, S., Na, Y., and Hanratty, T. J. (2003). Influence of a wavy boundary on turbulence. *Experiments in Fluids*, 35(5):422–436.

Nikora, V., McLean, S., Coleman, S., Pokrajac, D., and Walters, R. (2007). Double-Averaging Concept for Rough-Bed Open-Channel and Overland Flows: Theoretical Background. *Journal of Hydraulic Engineering*, 133:873–883.

- Nikuradse, J. (1933). Laws of flow in rough pipes. NACA Tech. Memo. 1292.
- Nugroho, B., Hutchins, N., and Monty, J. P. (2013). Large-scale spanwise periodicity in a turbulent boundary layer induced by highly ordered and directional surface roughness. *International Journal of Heat and Fluid Flow*, 41:90–102.
- Padhra, A. (2010). Estimating the sensitivity of urban surface drag to building morphology. PhD thesis, Department of Meteorology, Reading.
- Pearson, D. S., Goulart, P. J., and Ganapathisubramani, B. (2013). Turbulent separation upstream of a forward-facing step. *Journal of Fluid Mechanics*, 724:284–304.
- Perry, A. E. and Abell, C. J. (1977). Asymptotic similarity of turbulence structures in smooth- and rough-walled pipes. *Journal of Fluid Mechanics*, 79:785–799.
- Perry, A. E. and Li, J. (1990). Experimental support for the attached-eddy hypothesis in zero-pressure-gradient turbulent boundary layers. *Journal of Fluid Mechanics*, 218:405–438.
- Placidi, M. and Ganapathisubramani, B. (2013). Investigation of wall-bounded turbulence over regularly distributed roughness. In 8th International Symposium on Turbulence and Shear flow phenomena, Poitiers, France August 28–30.
- Placidi, M. and Ganapathisubramani, B. (2015a). Effect of large surface roughness on flow statistics in turbulent boundary layer. *Under consideration for publication in Journal of Fluid Mechanics*.
- Placidi, M. and Ganapathisubramani, B. (2015b). Effects of large roughness on aerodynamic parameters and the roughness sublayer in turbulent boundary layers. *Under consideration for publication in Journal of Fluid Mechanics*.
- Poll, D. I. A. (1985). Some observations of the transition process on the windward face of a long yawed cylinder. *Journal of Fluid Mechanics*, 150:329–356.
- Prasad, A. K., Adrian, R. J., Landreth, C. C., and Offutt, P. W. (1992). Effect of resolution on the speed and accuracy of particle image velocimetry interrogation. *Experiments in Fluids*, 13:105–116.
- Raben, S. G., Charonko, J. J., and Vlachos, P. P. (2012). Adaptive gappy proper orthogonal decomposition for particle image velocimetry data reconstruction. *Measurement Science and Technology*, 23(2):025303.
- Raffel, M., Willert, C., and Kompenhans, J. (1998). *Particle Image Velocimetry*. A Practical Guide. Springer Verlag, Berlin, second edition.

Raupach, M. R. (1992). Drag and drag partition on rough surfaces. *Boundary-Layer Meteorology*, 60:375–395.

- Raupach, M. R., Antonia, R. A., and Rajagopalan, S. (1991). Rough-Wall Turbulent Boundary Layers. *Applied Mechanics Reviews*, 44(1):1–25.
- Raupach, M. R. and Shaw, R. H. (1982). Averaging procedures for flow within vegetation canopies. *Boundary-Layer Meteorology*, 22:79–90.
- Reed, H. L. and Saric, W. S. (1996). Linear stability theory applied to boundary layers.

  Annual Review of Fluid Mechanics, 28:389–428.
- Reynolds, R. T. and Castro, I. P. (2008). Measurements in an urban-type boundary layer. *Experiments in Fluids*, 45:141–156.
- Reynolds, R. T., Hayden, P., Castro, I. P., and Robins, A. G. (2007). Spanwise variations in nominally two-dimensional boundary layers. *Experiments in Fluids*, 42:311–320.
- Robinson, S. K. (1991). Coherent Motions in the Turbulent Boundary Layer. *Annual Review of Fluid Mechanics*, 23:601–639.
- Santiago, J. L., Coceal, O., Martilli, A., and Belcher, S. E. (2008). Variation of the Sectional Drag Coefficient of a Group of Buildings with Packing Density. *Boundary-Layer Meteorology*, 128:445–457.
- Schetz, A. J. (1993). Boundary Layer Analysis. Prentice Hall.
- Schlichting, H. (1937). Experimental investigation of the problem of surface roughness. *NACA TM*, 823:1–60.
- Schlichting, H. (1979). Boundary Layer Theory. Springer.
- Schultz, M. P. (2004). Frictional Resistance of Antifouling Coating Systems. *Journal of Fluids Engineering*, 126(6):1039.
- Schultz, M. P. (2007). Effects of coating roughness and biofouling on ship resistance and powering. *Biofouling*, 23(5):331–341.
- Schultz, M. P. and Flack, K. A. (2005). Outer layer similarity in fully rough turbulent boundary layers. *Experiments in Fluids*, 38(3):328–340.
- Schultz, M. P. and Swain, G. W. (1999). The Effect of Biofilms on Turbulent Boundary Layers. *Journal of Fluids Engineering*, 121(1):44–51.
- Segalini, A., Örlü, R., and Alfredsson, P. H. (2013). Uncertainty analysis of the von Kármán constant. *Experiments in Fluids*, 54:1460.

Sillero, J. A., Jimenez, J., and Moser, R. D. (2014). Two-point statistics for turbulent boundary layers and channels at Reynolds numbers up to  $\delta+=2000$ . Physics of Fluids, 26(10):105109.

- Snyder, W. H. and Castro, I. P. (2002). The critical Reynolds number for rough-wall boundary layers. *Journal of Wind Engineering and Industrial Aerodynamics*, 90:41–54.
- Tachie, M. F., Bergstrom, D. J., and Balachandar, R. (2004). Roughness effects on a mixing Properties in open channel Turbulent Boundary Layers. Experiments in Fluids, 35:338–346.
- Tani, I. (1988). Turbulent Boundary Layer Development over Rough Surfaces. *Perspectives in Turbulence Studies*, pages 223–249.
- Theodorsen, T. (1952). Mechanism of turbulence. In Proceedings of the Second Midwestern Conference on Fluid Mechanics, March 17–19. Ohio State University, Columbus, OH.
- Theurer, W., Baechlin, W., and Plate, E. J. (1992). Model study of the development of boundary layers above urban areas. *Journal of Wind Engineering and Industrial Aerodynamics*, 41-44:437–448.
- Tomkins, C. D. and Adrian, R. J. (2003). Spanwise structure and scale growth in turbulent boundary layers. *Journal of Fluid Mechanics*, 490:37–74.
- Townsend, A. A. (1976). The Structure of Turbulent Shear Flow. Cambridge University Press.
- Varano, N. D. (2010). Fluid Dynamics and Surface Pressure Fluctuations of Turbulent Boundary Layers Over Sparse Roughness. PhD thesis, Virginia Polytechnic Institute and State University.
- Volino, R. J., Schultz, M. P., and Flack, K. A. (2007). Turbulence structure in roughand smooth-wall boundary layers. *Journal of Fluid Mechanics*, 592:263–293.
- Volino, R. J., Schultz, M. P., and Flack, K. A. (2009). Turbulence structure in a boundary layer with two-dimensional roughness. *Journal of Fluid Mechanics*, 635:75–101.
- Volino, R. J., Schultz, M. P., and Flack, K. A. (2011). Turbulence structure in boundary layers over periodic two- and three-dimensional roughness. *Journal of Fluid Mechanics*, 676:172–190.
- Webb, R., Eckert, E. R. G., and Goldstein, R. (1971). Heat transfer and friction in tubes with repeated-rib roughness. *International Journal of Heat and Mass Transfer*, 14(4):601–617.

Westerweel, J. (1997). Fundamentals of digital particle image velocimetry. PhD thesis, Delft University Press.

- Wieringa, J. (2014). Representative roughness parameters for homogenous terrain. Boundary-Layer Meteorology, 63:323–363.
- Winter, G. K. (1977). An outline of the techniques available for the measurement of skin friction in turbulent boundary layers. *Progress in Aerospace Sciences*, 18:1–57.
- Wu, Y. (2014). A study of energetic large-scale structures in turbulent boundary layer. *Physics of Fluids*, 26(4):045113.
- Wu, Y. and Christensen, K. T. (2006). Population trends of spanwise vortices in wall turbulence. *Journal of Fluid Mechanics*, 568:55–76.
- Wu, Y. and Christensen, K. T. (2007). Outer-layer similarity in the presence of a practical rough-wall topography. *Physics of Fluids*, 19(8):085108.
- Wu, Y. and Christensen, K. T. (2010). Spatial structure of a turbulent boundary layer with irregular surface roughness. *Journal of Fluid Mechanics*, 655:380–418.
- Zaki, S. A., Hagishima, A., Tanimoto, J., and Ikegaya, N. (2011). Aerodynamic Parameters of Urban Building Arrays with Random Geometries. *Boundary-Layer Meteorology*, 138(1):99–120.
- Zaunon, E., Durst, F., and Nagib, H. (2003). Evaluating the Law of the Wall in two-dimensional fully developed channel flows. *Physics of Fluids*, 15:3079–3089.
- Zhou, J., Adrian, R. J., Balachandar, S., and Kendall, T. M. (1999). Mechanisms for generating coherent packets of hairpin vortices in channel flow. *Journal of Fluid Mechanics*, 387:353–396.